Phenomenology of New Physics Models at Colliders and in Gravitational Waves

Dissertation submitted for the award of the title
"Doctor of Natural Sciences"
to the Faculty of Physics, Mathematics and Computer Science
of Johannes Gutenberg University Mainz in Mainz

Eric Madge Pimentel

born in Ratingen, Germany

Mainz, June 1, 2020

JOHANNES GUTENBERG UNIVERSITÄT MAINZ

date of submission: June 2, 2020
date of defense: October 14, 2020

Abstract

The existence of physics beyond the Standard Model of particle physics is very well motivated. This dissertation studies the phenomenology of models that accommodate such new physics. It mainly covers two aspects: collider phenomenology and gravitational waves.

We first present a search for Higgs-portal dark matter at the *LHC* and its prospective high-luminosity and high-energy upgrades, entertaining the vector-boson fusion channel. We derive the limits on the portal coupling as a function of the dark matter mass, in particular also for masses close to the transition between the on- and off-shell Higgs regime. Subsequently, a study of the $h \to Z\gamma$ decay in top-pair associated production is considered. We evaluate the observational prospects at future proton colliders and derive the corresponding indirect constraints that can be put on the new physics' contribution to the decay rate. Our exploration of collider probes of physics beyond the Standard Model is then concluded with a comprehensive analysis of the phenomenology of a model in which lepton number is gauged. The model automatically provides a candidate for particle dark matter. We investigate the parameter space in which the measured relic abundance is reproduced, impose constraints from direct and indirect dark matter searches, and assess the limits from collider experiments.

We then move on to study the gravitational wave phenomenology of new physics, focusing on stochastic gravitational wave backgrounds generated in cosmological first-order phase transitions. After an introduction to the topic, we return to the gauged-lepton-number-model and investigate the lepton number breaking phase transition. We identify the parameter regions in which the transition is of first order and which are consistent with the collider and dark matter constraints. We then calculate the respective gravitational wave spectrum and evaluate its detectability at *LISA* and other future gravitational wave observatories. Finally, we consider phase transitions occurring in decoupled dark sectors, particularly focusing on sub-MeV hidden sectors. We investigate the interplay between cosmological constraints on the number of relativistic degrees of freedom and the detectability of the gravitational wave background generated by a phase transition in such a sector.

List of Publications

References to collaborators by name have been anonymized in the electronic version.

This thesis is based on the publications and preprints [1–4]. In the following, a brief summary of these works is provided, highlighting the respective contributions of the author.

[1] E. Madge and P. Schwaller, *Leptophilic dark matter from gauged lepton number: Phenomenology and gravitational wave signatures*, *JHEP* **02** (2019) 048, [1809.09110]

We perform a comprehensive study of an extension of the Standard Model in which lepton number is promoted to a gauge group. Additional fermions required to cancel anomalies provide a dark matter candidate. The lepton number gauge group is spontaneously broken using the Higgs mechanism. We assess the collider and dark matter phenomenology of the model and investigate the possibility of observing the lepton number breaking phase transition through gravitational waves.

The paper updates and extends the discussion of the model in ref. [5]. All calculations, simulations and parameter scans, the derivation of the resulting constraints and experimental sensitivity, the creation of the corresponding graphical presentations, as well as the composition of the publication text (except for the introduction) were performed by the author with advise and corrections from the collaborators. Correspondingly, the majority of the contents of chapters 5 and 7 of this dissertation has been copied literally (partially with minor modifications to the text) from the publication, which is subject to the creative commons license CC-BY 4.0 [6].

[2] M. Breitbach, J. Kopp, E. Madge, T. Opferkuch and P. Schwaller, *Dark, Cold, and Noisy: Constraining Secluded Hidden Sectors with Gravitational Waves*, *JCAP* **1907** (2019) 007, [1811.11175]

This work investigates the detectability of stochastic gravitational wave backgrounds generated in cosmological phase transitions in decoupled hidden sectors, particularly focusing on sub-MeV sectors and the interplay with constraints from the effective number of neutrino species.

The parameter scans calculating the phase transition properties were performed independently by a collaborator and the author. All authors contributed to the derivation of the dependence of the gravitational wave spectrum on the temperature ratio between the hidden sector and photon bath, and to the text in the published manuscript. The figures in the publication were created by a collaborator and cross-checked by the author. The author further particularly contributed by the extraction of noise and sensitivity curves of pulsar timing arrays from the literature, as well as by an approximate analytic analysis of the phase transition of the singlet scalars toy model with one or two scalar fields.

[3] F. Goertz, E. Madge, P. Schwaller and V. T. Tenorth, *Discovering the $h \to Z\gamma$ Decay in $t\bar{t}$ Associated Production*, *Phys. Rev. D* **102** (2020) 053004, [1909.07390]

We propose a collider search for the so-far unobserved decay of the Higgs boson into a photon and a Z boson, entertaining the top-pair associated Higgs production channel. The discovery prospects in this channel, as well as the respective bounds on new physics, are investigated for the high-luminosity and high-energy upgrades of the *LHC*, as well as for a 100 TeV *pp* collider (*FCC*), performing a Monte Carlo study.

The Monte Carlo simulations of the signal and irreducible background process as well as the analysis of the corresponding events were performed independently by a collaborator and the author. Additional sub-leading backgrounds were divided up amongst these two and simulated only once. All authors contributed to the derivation of the significance and the corresponding limits on new physics contributions, as well as to the text.

[4] J. Heisig, M. Krämer, E. Madge and A. Mück, *Probing Higgs-portal dark matter with vector-boson fusion*, *JHEP* **03** (2020) 183, [1912.08472]

In this work, a study of Higgs-portal dark matter produced in vector-boson fusion is presented. Constraints from the current *LHC* as well as projections for the *HL-LHC* and *HE-LHC* updates are derived, including an estimate of the systematic uncertainties in the case of data-driven background determination. Particular care is taken to obtain consistent limits in the dark matter mass region close to the Higgs resonance.

The author performed all Monte Carlo simulations of the signal and background processes and their successive analysis, with advice from the collaborators. The plots depicting the respective limits on the portal couping are due to a collaborator and were cross-checked by the author. The author further derived the perturbative unitarity bound on the coupling in the tensor dark matter case, as well as the limits on the portal coupling for different cut-offs on the integral in eq. (3.13). The published text contains contributions from all authors.

All figures depicted in this dissertation are due to the author. Figures from the publications listed above that were produced by collaborators, as well as some of the figures produced by the author himself, have been recreated for this thesis to obtain a (mostly) uniform plot layout.

Contents

Prologue

1. Introduction

The Standard Model (SM) of particle physics is one of the most successful theories ever developed in the field of physics. Since its formulation in the late 1960s [7–9], it correctly describes the known particles as well as their strong, weak and electromagnetic interactions. Undoubtedly, one of its most notable triumphs was the correct prediction of the existence of a massive, neutral scalar particle, the Higgs boson [10–15], which was finally discovered at the *LHC* in 2012 [16, 17]. Over the past decades, an extensive program for experimental tests of the SM has been carried out, which impressively confirmed the validity of its predictions over a variety of processes.

Despite its tremendous success in providing accurate predictions for the *LHC* and other colliders, the SM suffers from various short-comings that require the introduction of new physics beyond the Standard Model (BSM). These open problems include questions motivated from a theoretical point of view, partially based on arguments of philosophical nature, such as the hierarchy or naturalness problem and the strong CP problem, but also puzzles related to experimental observations, mostly astrophysical or cosmological, that are not accommodated within the SM. Examples of the latter category are neutrino masses and oscillations, the generation of a baryon asymmetry in the early Universe, and the existence of dark matter (DM) and dark energy.

A plethora of models has been proposed to potentially solve one or several of the open problems described above, ranging from simple extensions of the SM in which only a single new field is added, over models with rather complicated sectors of new physics, to novel frameworks extending the symmetries of space-time, such as supersymmetry (SUSY), or models of extra dimensions. This dissertation is dedicated to the study of the phenomenology of such models. Particular focus is put on models of DM, which are discussed in chapters 3, 5 and 7, whereas chapters 4 and 8 consider new physics in a more general context. We here choose two different, complementary paths to constrain BSM models. Part I is devoted to collider studies of new physics, mostly focusing on pp machines. In part II we then investigate the gravitational wave (GW) phenomenology of BSM models, in particular regarding cosmological phase transitions (PTs) in the early Universe.

Particle accelerators and colliders have proven to be invaluable discovery tools in elementary particle physics. Since the early scattering experiments by Rutherford, shooting helium nuclei on gold targets in 1911 [18], the procedure of smashing particles into one another and inferring elementary physics from the respective outcome has been refined immensely, leading to the development of giant machines that reach unprecedented energies and precision. Much of the observational confirmation of the SM was provided by collider experiments, as for instance the discovery of various particles predicted on theoretical grounds such as the W and Z bosons, the top quark, and, last but not least, the Higgs boson. Colliders are therefore commonly regarded promising facilities to unveil the nature of new physics.

Since, despite the ample efforts to unravel new physics taken at colliders and other types of experiments, no definite BSM signatures have been found so far, we may have to face the possibility that whatever new physics cures the open problems could interact only very weaky (or maybe even not at all) with the particles of the SM. We however know that, at least in the case of DM, the new physics should feature gravitational interactions. As a consequence, even in this very pessimistic scenario, gravity may provide a handle to probe BSM physics. This is particularly promising in the light of the recent direct observation of GWs by *LIGO* and *Virgo* in 2015 [19], which led to the proposal and elaboration of concrete realizations for various future GW observatories. Most notably, the first-ever space-based GW interferometer, *LISA* [20], will prospectively be launched in the mid 2030's. These future experimental facilities pave the way for a potential detection of new physics via GWs.

In the context of GWs, new physics may be observable in deviations from predictions for astrophysical events such as mergers of black holes (BHs) or neutron stars (NS), or in the form a stochastic gravitational wave background (SGWB) of cosmological origin. A cosmological SGWB can for instance be generated in the era of inflation, from the decays of cosmic strings, or in cosmological first-order PTs. In this thesis, we will focus on the latter case.

According to our current understanding of the history of our Universe, it started with an epoch of exponential expansion, the epoch of inflation, from which the Universe emerged flat, homogeneous, isotropic, and basically empty (except for the inflaton field). During the subsequent epoch of reheating, the inflaton then decayed, repopulating the Universe with a thermal plasma of elementary particles. Due to the expansion of the Universe driven by the energy in the plasma, its temperature dropped during the further evolution. In the course of this cooling process, the Universe may have undergone one or several PTs, which, if these were of first order, could have generated a stochastic background of GWs detectable by future observatories. The SM predicts two transitions: the electroweak PT (EWPT), in which the electroweak (EW) gauge symmetry is broken to electromagnetism (EM), and the confining PT of quantum chromodynamics (QCD), which breaks chiral symmetry. However, in the SM both of these transitions are cross-overs.[1] The observation of the SGWB generated by a cosmological PT would therefore be a clear indication of new physics, potentially providing insight into the nature of the underlying theory.

Laboratory and cosmological probes of new physics provide complementary ways to asses BSM models. Collider experiments may directly detect new particles, e.g. in the form of resonances, or observe them indirectly via their effects on SM observables. Cosmological observations, on the other hand, can for instance provide limits on the number of relativistic degrees of freedom (DOFs) in the early Universe, as we will discuss in chapter 8, or on the mass of DM if it is thermal (we briefly touch upon this bound in section 2.3). While all evidence for DM is of astrophysical and cosmological nature, there is still a good chance that it can be produced at collider experiments. Cosmology and colliders further exhibit a particular interplay in the context of spontaneous symmetry

[1] In a misuse of language, we will nonetheless refer to them as PTs.

breaking (SSB). As pointed out above, the corresponding cosmological PT may be observable in GWs if it is of first order, while indications for the order of the PT can be obtained at colliders, e.g. probing the potential of the Higgs boson in the context of the EWPT, or by the creation of a quark-gluon plasma in the case of the chiral PT. Furthermore, as all elementary SM particles obtain their masses from the Higgs mechanism, it is suggestive to assume that the masses of BSM particles are generated in a similar manner. If the new particles are much heavier than the weak scale, they cannot obtain their full masses via electroweak symmetry breaking (EWSB), potentially indicating the spontaneous breaking of additional symmetries, which may in turn be associated with an observable PT.

This thesis is organized as follows. We first briefly recapitulate the SM and its open problems in chapter 2. Next, in part I, collider studies searching for new physics are considered. We start with a DM search at proton colliders in chapter 3, focusing on Higgs-portal DM in the vector-boson fusion (VBF) channel. In chapter 4 we then assess the prospects of detecting the decay of the Higgs boson into a photon and a Z boson at future collider experiments, and evaluate how this can be used to indirectly constrain the impact of new physics on the decay process. We conclude the part in chapter 5 with a comprehensive study of the DM and collider phenomenology of a model in which lepton number is promoted to a gauge symmetry. Subsequently, part II is devoted to probing BSM physics via GWs. Chapter 6 provides an introduction to SGWBs, their detection, and how they are generated in cosmological first-order PTs. As an example, chapter 7 investigates the lepton number breaking PT of the model we considered in chapter 5. Chapter 8 then considers PTs in general hidden sectors, addressing the question how the corresponding SGWB is affected when the dark sector is sequestered. Finally, conclusions of the thesis are presented in chapter 9.

2. The Standard Model and Beyond

Before diving into the phenomenology of new physics beyond the Standard Model (BSM), let us first very briefly recapitulate the Standard Model (SM) itself, assuming that the reader is mostly familiar with this subject. For a more detailed review, the reader shall be referred to the usual text books, such as refs. [21, 22]. We then proceed in this chapter by pointing out some of the open questions of the SM with emphasis on those related to the models studied in this dissertation.

2.1. The Standard Model of Particle Physics

The SM is a gauge theory describing the strong, weak and electromagnetic forces. It is based on the symmetry group $SU(3)_c \times SU(2)_L \times U(1)_Y$, corresponding to the $SU(3)_c$ color group of quantum chromodynamics (QCD) [23–28] as well as the weak isospin $SU(2)_L$ and hypercharge $U(1)_Y$ gauge groups uniting the electroweak forces [7–9]. The structure of the SM is completely fixed by this gauge symmetry, its particle content, and by requiring renormalizability [29].

Its matter content consists mostly of fermionic fields. The quark fields Q_L, u_R, and d_R transform as triplets upon the $SU(3)_c$ group of QCD, whereas the lepton fields ℓ_L and e_R are QCD singlets. The left-handed fields (with index L) are doublets under the weak gauge group $SU(2)_L$, while the right-handed fields (with index R) are $SU(2)_L$-singlets. Each of these five types of fermions comes in three generations. Hence, the representations and charges of the SM fermions under the $SU(3)_c \times SU(2)_L \times U(1)_Y$ gauge group are

$$\begin{aligned} &Q_L^i \sim \left(\mathbf{3},\, \mathbf{2},\, \frac{1}{6}\right) , \qquad && u_R^i \sim \left(\mathbf{3},\, \mathbf{1},\, \frac{2}{3}\right) , \qquad && d_R^i \sim \left(\mathbf{3},\, \mathbf{1},\, -\frac{1}{3}\right) , \\ &\ell_L^i \sim \left(\mathbf{1},\, \mathbf{2},\, -\frac{1}{2}\right) , && e_R^i \sim (\mathbf{1},\, \mathbf{1},\, -1) , && \end{aligned} \tag{2.1}$$

where $i = 1, 2, 3$ is a generation index.

In addition to the fermions, the SM features an $SU(2)_L$ doublet scalar field H transforming as $H \sim (\mathbf{1},\, \mathbf{2},\, 1/2)$, the Higgs doublet. It spontaneously breaks the electroweak (EW) gauge symmetry to electromagnetism (EM), $SU(2)_L \times U(1)_Y \to U(1)_{\text{EM}}$, via the Higgs mechanism [10–15], acquiring a vacuum expectation value (VEV). Rotating the VEV into the lower real component of the doublet using a global transformation, it can be expanded as $H = (G^\pm,\ (v + h + iG^0)/\sqrt{2})^T$, where h is the physical Higgs mode, v its (space-time independent) VEV, and G^i are the would-be Goldstone bosons that provide the longitudinal degrees of freedom (DOFs) to the massive gauge bosons. The Higgs VEV induces mass terms for the EW gauge bosons from the Higgs' covariant derivative term. The resulting mass eigenstates are the charged $W^\pm$ and neutral Z bosons with masses m_W and m_Z, and the massless photon γ.

Apart from the kinetic and potential terms (as well as gauge-fixing and ghost terms), the SM symmetries allow Yukawa interactions of the form

$$\mathcal{L}_{\text{yuk}} = -(Y_u)_{ij}\, \bar{Q}_L^i\, \tilde{H}\, u_R^j - (Y_d)_{ij}\, \bar{Q}_L^i\, H\, d_R^j - (Y_e)_{ij}\, \bar{\ell}_L^i\, H\, e_R^j + \text{h.c.}\,, \tag{2.2}$$

where $\tilde{H} \equiv i\sigma_2 H^*$ with σ_2 denoting the second Pauli matrix. Upon spontaneous symmetry breaking (SSB), the Yukawa interactions generate mass terms for the quarks and leptons.[1] Writing the doublet fields in their $SU(2)_L$ components $Q_L^i = (u_L^i,\ d_L^i)^T$ and $\ell_L^i = (\nu_L^i,\ e_L^i)$, these mass terms are

$$\mathcal{L}_{\text{yuk}} \supset -(M_u)_{ij}\, \bar{u}_L^i\, \tilde{H}\, u_R^j - (M_d)_{ij}\, \bar{d}_L^i\, H\, d_R^j - (M_e)_{ij}\, \bar{e}_L^i\, H\, e_R^j + \text{h.c.}\,, \tag{2.3}$$

where $M_f = Y_f\, v/\sqrt{2}$ for $f = u, d, e$. The mass matrices M_f can be diagonalized via singular value decomposition, rotating the quark and lepton fields by unitary 3×3 matrices U_C^f, i.e. $f_C^i \to (U_C^f)^{ij} f_C^j$, where $C = L, R$, with left and right-handed fields rotated independently. The resulting mass eigenstates are six massive quarks, to wit, in order of increasing mass, the up (u), down (d), strange (s), charm (c), bottom (b) and top (t) quarks, three massive charged leptons, namely the electron (e), muon (μ) and tau lepton (τ), as well as the corresponding three massless neutrinos ν_e, ν_μ and ν_τ.

The unitary transformations that diagonalize the fermion masses reappear in the kinetic terms $\bar{\psi}^i \not{D} \psi^i$ with $\psi^i = Q_L^i, u_R^i, d_R^i, \ell_L^i, e_R^i$. They however mostly combine to unity, except in the charged current interactions of the left-handed doublets, such as for instance $\bar{u}_L^i \gamma^\mu d_L^i$. In the quark sector, the rotations of the left-handed fields combine to the unitary Cabibbo-Kobayashi-Maskawa (CKM) matrix [30, 31] $V \equiv (U_L^u)^\dagger\, U_L^d$, which describes the quark-flavor-changing charged-current interactions with the W boson. These then take the form $\bar{u}_L^i \gamma^\mu V_{ij} d_L^j W_\mu^+ + \text{h.c.}$, where u^i and d^i now denote the up- and down-type mass eigenstate quarks.

As a unitary matrix, the CKM matrix has 9 DOFs, viz. three rotation angles and six phases. The mass terms are however invariant under phase changes of each of the six quark fields, whereas the CKM matrix is only invariant under a simultaneous change of all six phases. We can therefore absorb five phases in the quark fields, resulting in four physical, real parameters: three mixing angles, and one (CP-violating) phase.

In the lepton sector, on the other hand, no such matrix appears in the SM. As neutrinos remain massless, we can simply transform ν_L in the same way as e_L, so that the matrix disappears. However, when right-handed neutrinos are added, as we will discuss in section 2.3.3, the neutrino mass terms force us to rotate ν_L differently from e_L. The resulting mixing matrix of the leptons is called the Pontecorvo-Maki-Nakagawa-Sakata (PMNS) matrix [32, 33].

As already mentioned, the SM features two potential phase transitions (PTs). The first one comes from the spontaneous breaking of the EW gauge symmetry in which the Higgs field acquires its VEV. Lattice simulations indicate that the electroweak PT (EWPT) of the SM proceeds as a weak cross-over at a temperature around $T \simeq 160\,\text{GeV}$ [34]. However, even simple extensions of the SM by a single scalar field may render the transition first-order [35–37]. The second PT is the chiral PT of QCD, in which the quark-gluon plasma of the early Universe confines into hadrons, with the quark condensate

[1] Note that explicit mass terms are inconsistent with the weak gauge symmetry, as left-handed fields are doublets while the right-handed ones are singlets.

breaking chiral symmetry. This is also a cross-over, occurring at a temperature around $T \simeq 160\,\mathrm{MeV}$ [38]. Due to this low temperature, the chiral PT may also be probed directly in heavy ion collisions at the *LHC* or *RHIC* [39]. Furthermore, the corresponding transition in QCD-like sectors of BSM models may very well be a first-order PT [40, 41].

2.2. New Physics in the Higgs Sector

Many of the motivations to consider BSM physics are to some degree related to the Higgs boson or the spontaneous breaking of the EW gauge symmetry. One particular example which has inspired numerous models of new physics is the EW hierarchy problem. It can be boiled down to the question why the observed mass of the Higgs boson or the EW scale are so much lighter than the scale of gravity, the Planck scale. The extremely tiny ratio $m_h^2/M_P^2 \sim 10^{-34}$ violates 't Hooft's principle of technical naturalness [42], which states that dimensionless parameters of fundamental theories should be $\mathcal{O}(1)$ numbers unless setting them to zero enhances the symmetry of the theory.

The hierarchy problem stems from the observation that the Higgs mass in the SM is additively renormalized, i.e. quantum corrections to the Higgs mass are independent of the Higgs mass itself.[2] This can be realized noting that the loop corrections to the Higgs mass exhibit a quadratic divergence. In the SM, these corrections are [43]

$$\frac{\Delta m_h^2}{m_h^2} = \frac{3\,\Lambda^2}{8\pi^2\,v^2}\left[4\frac{m_t^2}{m_h^2} - \frac{m_Z^2}{m_h^2} - 2\frac{m_W^2}{m_h^2} - 1 + \ldots\right] \approx \left(\frac{\Lambda}{500\,\mathrm{GeV}}\right)^2 , \tag{2.4}$$

where the loop integrals have been regularized imposing a cut-off Λ on the virtual momentum, and $v \simeq 246\,\mathrm{GeV}$ is the Higgs' VEV. Considering the SM as an effective field theory (EFT),[3] this means that the Higgs mass is quadratically sensitive to the scale of new physics, i.e. it is ultraviolet (UV) sensitive. As a result, loop corrections to the Higgs mass exceed its physical value when considering scales above $\Lambda \sim 500\,\mathrm{GeV}$.

Note that the cut-off scale Λ should be interpreted as a placeholder for the mass scale of whatever new physics appears in the UV. If we extend the SM adding a new particle with mass M that couples to the Higgs boson, this particle will induce mass corrections that go like $\Delta m_h^2 \sim M^2$, assuming that we now employ dimensional regularization. Hence, any new massive particle coupled to the Higgs will in general generate corrections on the order of the new physics' scale; heavy particles do not decouple. As a result, we encounter a fine-tuning problem. Suppose that there is new physics UV-completing the SM at some high scale $\Lambda \gg m_h$. The Higgs mass parameter of the theory then needs to be tuned at the level m_h^2/Λ^2 to cancel the quantum corrections and give the observed mass of $m_h = 125\,\mathrm{GeV}$. The higher Λ, the worse the tuning.

Although the fine-tuning problem is in principle mostly an aesthetic problem counteracting our intuition, it is still an inherently unsatisfying feature of the SM, and therefore served as a guideline for the construction of numerous models of new physics. Possible

[2] In contrast, multiplicatively renormalized parameters, such as for instance the electron mass, receive corrections that are proportional to the parameter itself.

[3] Note that the running of the hypercharge gauge coupling in the SM exhibits a Landau pole around $\Lambda \sim 10^{41}\,\mathrm{GeV}$, so that the SM has to be considered an EFT with a cut-off around or below that scale.

solutions to the hierarchy problem include little Higgs [44, 45] or composite Higgs [46–48] models, in which the Higgs boson arises as a pseudo-Goldstone boson from the spontaneous breaking or confinement of a gauge or global symmetry, and where that symmetry protects the Higgs mass from large corrections, or models of supersymmetry (SUSY) [49–51], where bosonic corrections are canceled by the corresponding contributions from their fermionic super-partners and vice-versa.

A further open question directly related to the Higgs potential regards the stability of the EW vacuum. At large field values, the potential of the Higgs field h can be approximated by the quartic term $V(h) \simeq \lambda(h)\, h^4/4$, including the renormalization group (RG) evolution of the quartic coupling $\lambda(\mu)$. The latter is governed by the β function [52, 53]

$$\beta_\lambda \equiv \frac{\mathrm{d}\,\lambda}{\mathrm{d}\,\log\mu} = \frac{1}{16\,\pi^2}\left[12\lambda^2 + 6\lambda y_t^2 - 3y_t^4 + \dots\right], \tag{2.5}$$

where λ is the Higgs quartic and y_t is the top Yukawa coupling. If the top contribution dominates, it drives the quartic coupling negative at high field values. As a consequence, the Higgs potential is not bounded from below and the EW vacuum is not stable. This is indeed the case for the measured values of the Higgs and top masses. The corresponding tunneling rate is however very low, such that the lifetime of the vacuum exceeds the age of the Universe by orders of magnitude, and we live in a meta-stable vacuum very close to the border of stability [52]. New physics contributions to the running of λ may render the EW vacuum absolutely stable, or conversely spoil its (meta-)stability.

Another important motivation for BSM physics is the failure of the SM to provide suitable conditions for the generation of the baryon asymmetry of the Universe. At some point during the history of the Universe, a tiny excess of baryons over anti-baryons of [54]

$$\eta = \frac{n_B - n_{\bar{B}}}{n_\gamma} \simeq 10^{-9} \tag{2.6}$$

must have been generated. The anti-baryons subsequently annihilated with the baryons, leaving the Universe dominated by the excess baryons, eventually leading to our mere existence. Although the baryon asymmetry is not necessarily related to electroweak symmetry breaking (EWSB), one of the standard scenarios for its generation relies on a first-order EWPT.

The generation of a baryon asymmetry from an initially baryon-symmetric Universe requires that the so-called Sakharov conditions [55] are satisfied. These are the non-conservation of baryon number, violation of C and CP invariance, and deviation from thermal equilibrium. The first requirement is obvious, C and CP violation are needed to produce matter and anti-matter at different rates, and non-equilibrium is required as the equilibrium number densities of particles and anti-particles are the same. In principle, the SM could establish all these conditions at the EWPT, generating the asymmetry in a scenario called electroweak baryogenesis (EWBG) [56–58]. The weak interactions of the SM exhibit C and CP violation, baryon number (or $B+L$, to be more precise) is violated by non-perturbative sphalerons, and a first-order EWPT can provide the required out-of-equilibrium conditions. However, the amount of CP violation in the SM is not sufficient, and the EWPT is a cross-over [34]. EWBG therefore requires BSM physics.

All these open problems and their potential solutions more or less directly relate to the Higgs potential and the EWPT. Collider and gravitational wave (GW) experiments therefore provide complementary ways to probe the corresponding BSM extensions. At colliders, we can directly search for additional particles coupled to the Higgs boson or other SM particles. Furthermore, the Higgs potential can be probed directly, e.g. measuring a cubic term via double Higgs production. GW observatories, on the other hand, may detect the stochastic gravitational wave background (SGWB) produced in the EWPT if it is of first order, as for instance required in EWBG, or from additional PTs such as a confining PT in a composite Higgs model.

2.3. Dark Matter

Among the various open problems of the SM, a large fraction of the work presented in this dissertation particularly regards the existence of dark matter (DM). DM is a mysterious form of matter that is non-luminous but interacts gravitationally, and whose existence can be inferred from astrophysical and cosmological observations (see e.g. ref. [59] for a review). Today, it is well established that only roughly 5 % of the energy content of our Universe consists of the baryonic matter we know from the SM, whereas about 27 % is constituted of DM [60]. The remaining 68 % are dark energy, an even more mysterious form of energy, required to accommodate the observed accelerated expansion of our Universe. Both of these non-baryonic components, DM and dark energy, are now incorporated into the ΛCDM Standard Model of cosmology (including cold dark matter (CDM) and a cosmological constant Λ). The SM of particle physics, however, lacks a suitable explanation for these phenomena.

The question about the nature of DM is a long-standing open problem in particle physics, with a history of about 100 years (see ref. [61] for a review). Nowadays, we have ample observational evidence for its existence over a large range of scales [59]. On galactic scales, observations of the rotation curves of spiral galaxies, as for instance the Andromeda galaxy analyzed by Rubin and Ford in 1970 [62], show a flat velocity distribution of the outer stars deviating from the $\propto 1/\sqrt{r}$ expectation, which may be explained by the presence of a DM halo. Similar conclusions can be drawn on the scale of galaxy clusters, for example based on the velocity dispersion in the Coma cluster studied by Zwicky in 1933 [63]. Furthermore, one of the most compelling hints for DM was observed in the Bullet cluster [64], where the collision of two clusters revealed that the bulk mass was mostly unaffected by the collision, while it was clearly visible in the hot baryonic gas component. Finally, measurements of the power spectrum of the cosmic microwave background (CMB) allow for a precise determination of the total energy density of DM of $h^2\Omega_{\mathrm{DM}} = 0.120 \pm 0.001$ [60].

Although the observations indicating the existence of DM may in principle be explained by a population of non-radiating but baryonic astrophysical objects, such as primordial black holes (PBHs) or other types of massive astrophysical compact halo objects (MACHOs),[4] the power spectrum of the CMB [60] as well as the light element abundances

[4] These are however rather strongly constrained and basically ruled out as a main component of DM, see e.g. ref. [65].

predicted by Big Bang Nucleosynthesis (BBN) [66] indicate that the majority of the matter in the Universe is non-baryonic. We therefore here assume that DM consists of elementary or composite particles, potentially having various sub-components.[5] The formation of cosmological structure and the matter power spectrum further imply that the DM mostly consists of cold dark matter (CDM). "Cold" here signifies that the DM is non-relativistic at the times of matter-radiation equality and the onset of structure formation. While density perturbations in the baryonic component cannot collapse to form structures due to radiation pressure until the time of photon decoupling, perturbations in the CDM component can collapse as soon as the Universe becomes matter-dominated, allowing for the early formation of structure at small scales. Hot DM on the other hand is relativistic at matter-radiation equality and has a non-negligible free-streaming length, so that it does not form structures until it becomes non-relativistic. The observed small-scale structure requires that the gross of matter is non-baryonic CDM [68].

Apart from its total abundance, as well as the fact that it is non-luminous (i.e. electromagnetically neutral[6]) and gravitationally interacting, little is known about the nature of DM. The DM particles of course need to be stable, or at least have a lifetime exceeding the age of the Universe [70]. Furthermore, observations of collisions of galaxy clusters, as for instance the Bullet cluster, impose an upper bound on the self-interactions of DM [71]. The possible range of DM masses is almost unconstrained, spanning many orders of magnitude. For bosonic DM, a lower bound on the mass is given by its de Broglie wavelength $\lambda \sim 1/m_{\mathrm{DM}}$: it has to be smaller than the size of the smallest observed structures, i.e. dwarf galaxies. Observations of the Lyman-α forest put a lower bound of $m_{\mathrm{DM}} \gtrsim 10^{-21}\,\mathrm{eV}$ [72]. For fermionic DM on the other hand, the Pauli's exclusion principle sets a much more stringent bound from the mass and size of dwarf galaxies of roughly $m_{\mathrm{DM}} \gtrsim 100\,\mathrm{eV}$ [73]. Thermal DM, i.e. DM that was in thermal equilibrium with the SM plasma in the early Universe, is furthermore required to be heavier than $m_{\mathrm{DM}} \gtrsim 5.3\,\mathrm{keV}$ [74], as it would otherwise erase small-scale structures due to its large free-streaming length at matter-radiation equality. Finally, an upper bound on the DM mass can be obtained from the fact that extremely heavy DM would disrupt star clusters and similar structures when passing through them, imposing a limit of $m_{\mathrm{DM}} \lesssim 5\,M_{\odot}$ [65], where $M_{\odot} = 2 \times 10^{30}\,\mathrm{kg}$ is the solar mass.

The genesis of the abundance of DM particles can be roughly divided into two categories: thermal and non-thermal production [75]. In thermal production, the DM is produced from particles that are in thermal equilibrium, resulting in an energy spectrum that is proportional to that of an equilibrium species. The standard scenario is the so-called thermal freeze-out, in which the DM itself is initially in thermal equilibrium, with an abundance determined by the temperature at which the DM decouples from the plasma. We will discuss this scenario in slightly more detail in section 2.3.1. Commonly employed modifications of or alternatives to thermal freeze-out include co-annihilation with partner particles [76], as well as freeze-in production of a non-equilibrium DM species from

[5] Some of the observations may also be explained by modifications of gravity. These models are however mostly ruled out, in particular in the light of constraints on the deviation of the speed of gravity from the speed of light, derived from the observation of a neutron star (NS) binary merger in GWs and EM radiation [67].

[6] Or at least very close to neutral. A small EM charge (milli-charge) may still be allowed, see e.g. ref. [69].

decays or collisions of thermal-bath particles [77]. Another variation that is particularly interesting in the light of GW signatures is the possibility to produce DM in processes that are only temporarily active due to kinematic thresholds modified by cosmological PTs [78–80]. Furthermore, as in the case of the baryonic matter of the SM, its relic density may be set via an asymmetry in the number of particles and anti-particles. In non-thermal production, on the other hand, the DM abundance does not exhibit a thermal distribution. It may for instance be generated from the decay of out-of-equilibrium particles, or by coherently oscillating scalar fields [75]. Typical examples are axions and sterile neutrinos, which we will briefly discuss in sections 2.3.2 and 2.3.3.

2.3.1. WIMP Dark Matter

An intriguing scenario for thermal particle DM is the so-called weakly interacting massive particle (WIMP) paradigm. In this paradigm, the DM abundance is set via thermal freeze-out. The interactions that change the number density of DM become inefficient when the interaction rate drops below the Hubble rate (the rate at which the Universe expands). The DM then chemically decouples, and its co-moving number density is conserved. This process is called thermal freeze-out. The resulting DM relic abundance can be calculated solving the corresponding Boltzmann equation [81]. We approximately obtain [82]

$$h^2\Omega_{\mathrm{DM}} \simeq \frac{0.1\,\mathrm{pb}\,c}{\langle\sigma v\rangle}\,, \tag{2.7}$$

where $\langle\sigma v\rangle$ is the thermally averaged cross-section times velocity. This is the famous WIMP miracle: the abundance of particle DM with weak-scale masses and cross-sections set via thermal freeze-out coincides roughly with the experimentally observed DM density.

Over the past decades, WIMP DM has evolved into a standard DM paradigm. Numerous models employing this scenario have been constructed. In models for SUSY for instance, the lightest supersymmetric particle (LSP) may constitute a WIMP DM candidate if electrically neutral. The DM models considered in this dissertation also assume thermal freeze-out. WIMP DM has the attractive feature that it provides promising prospects for detecting DM, as the process setting the thermal abundance is generically related to various processes used in astrophysical or laboratory probes. This is depicted in fig. 2.1.

The same annihilation process that determines the DM relic density also leads to the annihilation of DM into SM particles in regions of high local DM densities. Indirect detection experiments aim at observing DM by detecting the annihilation products, searching for γ-rays, cosmic rays of charged antiparticles, or neutrinos. Searches for photons produced either directly in the annihilation or radiated from charged annihilation products are for instance performed at the Cherenkov telescopes *Fermi-LAT*, *H.E.S.S.*, and *MAGIC*, observing nearby dwarf spheroidal galaxies in the Milky Way [83] or the Galactic center [84–86].

Crossing symmetry further relates the annihilation process to DM scattering off SM particles. This allows for direct detection of DM by measuring the corresponding recoil of the scattering partner [87]. Experiments aiming at observing DM based on nuclear recoil provide strong bounds on WIMP DM with masses in the range of a few GeV

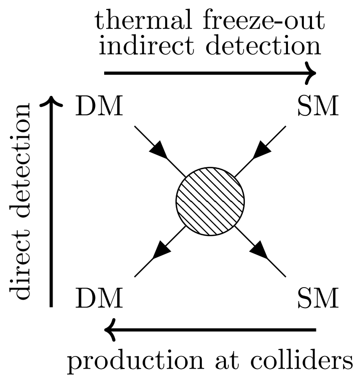

Figure 2.1: Feynman diagram for WIMP DM production and detection processes. For thermal production via freeze-out and indirect detection via DM annihilation into SM particles, the diagram has to be read from left to right. Read from bottom to top, the diagram describes direct detection via DM-nucleus scattering, and read from right to left it corresponds to production at colliders.

to a few TeV. These typically use Xenon or other nobel gases as targets. Currently, the strongest limits are provided by *XENON1T* [88]. Light WIMP DM can further be probed by cryogenic solid-state detectors such as *CRESST* or *SuperCMDS*, which may probe masses as low as 1 MeV using electron recoils [89]. Detectors based on charged coupled devices (CCDs) such as *DAMIC* [90] and *SENSEI* [91] can explore sub-MeV DM via scattering on electrons, and eV-scale dark-photon DM using absorption by electrons.

Finally, inverting the annihilation process, DM can be pair-produced in collisions of SM particles, for example in proton collisions at the *LHC*. The DM then escapes the detector, leading to missing energy signatures. Collider studies of DM therefore search for missing energy recoiling against visible particles such as jets or photons [92–95]

Despite all these efforts to detect WIMP DM, no conclusive observation has been made so far,[7] challenging the standard WIMP scenario which generically predicts promising detection prospects. As a result, alternatives to WIMP DM have become more and more popular over the past years.

2.3.2. Axion-Like Particles

A common alternative to WIMP DM are axion-like particles (ALPs). These are very light, neutral scalar or pseudo-scalar particles with weak couplings to matter and radiation, often arising as (pseudo-)Goldstone bosons of a spontaneously broken $U(1)$ symmetry [68]. If this breaking occurs after inflation, the corresponding PT may again be observable via GWs. The term "axion" typically refers to the QCD axion arising from the $U(1)_{\mathrm{PQ}}$ Peccei-Quinn symmetry, whereas ALPs are more general variants.

[7] Note however that there are some debated hints. For instance, *Fermi-LAT* has observed an excess of γ-rays from the Galactic Center in the few GeV range [96]. Whether this is to be attributed to DM annihilation is an unsolved question (see e.g. ref. [97]). A similar excess can be found in cosmic-ray anti-proton data [98, 99]. Furthermore, the *DAMA/LIBRA* collaboration has reported a controversial detection of an annually-modulated DM annihilation signal [100], which conflicts with the non-observation of this signal in other direct detection experiments [101].

The QCD axion is a potential solution to the strong CP problem, which, similar to the EW hierarchy problem, is a question of naturalness. It comes from the fact that the symmetries of the SM do not forbid the existence of the so-called θ term,

$$\mathcal{L}_\theta = -\frac{g_s^2}{32\pi}\,\theta\,\tilde{G}^a_{\mu\nu}G^{a\,\mu\nu}\,, \tag{2.8}$$

where G ($\tilde{G}$) is the (dual) gluon field strength tensor. The θ term violates CP. Although this term is in principle a total derivative, it cannot be discarded as it gives rise to non-perturbative effects from instantons. The θ parameter can however be moved to a complex phase in the quark mass matrix via a chiral rotation $q \to e^{i\alpha\gamma_5}q$ due to the axial anomaly of QCD. It therefore contributes to the electric dipole moment (EDM) of the neutron [102]. Experimental limits on the neutron EDM [103] thus constrain $|\bar{\theta}| < 10^{-10}$, where $\bar{\theta} = \theta + \arg\det M$ is the physical CP violating parameter originating from the θ parameter and the phase in the quark mass matrix M. This is highly unnatural in the technical sense.

In axion models, the strong CP problem is solved by adding a pseudo-scalar field ϕ_A, the axion, that features a coupling of the form

$$\mathcal{L}_A = -\frac{g_s^2}{32\pi}\left(\bar{\theta} + \frac{\phi_A}{f_A}\right)\tilde{G}^a_{\mu\nu}G^{a\,\mu\nu}\,, \tag{2.9}$$

where f_A the axion decay constant. Such a field can arise as a Goldstone boson from the spontaneous breaking of a global symmetry, the so-called Peccei-Quinn symmetry $U(1)_{\mathrm{PQ}}$ [104, 105]. To understand how the axion solves the strong CP problem, let us consider the vacuum energy of QCD, $E(\bar{\theta}) = -m_\pi^2 f_\pi^2 \cos(\bar{\theta})$ [22], where m_π and f_π are the pion mass and decay constant. In the presence of the axion field, the vacuum energy is modified to $E(\bar{\theta}) = -m_\pi^2 f_\pi^2 \cos(\bar{\theta} + \phi_A/f_A)$, i.e. the energy is now minimized if the axion acquires a VEV that cancels the $\bar{\theta}$ parameter. The θ term therefore vanishes in the vacuum.

The mass of the QCD axion is approximately given by $m_A \approx m_\pi f_\pi / f_A$ [68], i.e. the weaker it couples to the SM (the greater f_A) the smaller the axion mass. Accelerator, reactor, and cosmological constraints generally require $f_A > 10^7\,\mathrm{GeV}$, resulting in axion masses below $m_A \lesssim 10\,\mathrm{meV}$ [106]. Axions and ALPs therefore typically constitute very light DM, mostly produced non-thermally [107].

Axions with such low coupling to the SM are referred to as invisible axions and are inherently difficult to probe experimentally. Interestingly, axions or ALPs with extremely large decay constants, $f_A \sim 10^{17}\,\mathrm{GeV}$, that are coupled to dark photons may again be probed via GWs. If the axion was initially misaligned from its minimum in the early Universe, it will roll down its potential and start to oscillate around the minimum once the Hubble rate has dropped to the axion's mass. One of the dark photon's helicities then experiences a tachionic instability, which exponentially amplifies vacuum fluctuations and thereby generates a chiral SGWB [108, 109].

2.3.3. Sterile Neutrinos

Another possible DM candidate are sterile neutrinos, i.e. right-handed fermions that are complete singlets under the SM. In contrast, the left-handed neutrinos in the SM lepton doublets are referred to as active neutrinos, as they interact via the weak force. Indeed, the addition of right-handed singlet neutrinos is a well motivated extension of the SM. Given the particle content of the SM, one would intuitively like to amend it by three generations of right-handed neutrinos. Furthermore, and much more importantly, their addition allows for the generation of masses for the SM neutrinos.

The origin and nature of neutrino masses is also an open problem of the SM. While the left-handed neutrinos incorporated in the SM are exactly massless, the discovery of neutrino flavor oscillations, for which Kajita and McDonald were awarded the Physics Nobel Prize in 2015, necessarily requires that neutrinos have masses. Fits to oscillation data allow to determine the differences of the squared neutrino masses, and therefore establish a lower bound on their sum of $\sum m_\nu > 0.06\,\mathrm{eV}$ in the case of normal ordering, and $\sum m_\nu > 0.1\,\mathrm{eV}$ for inverted ordering [110]. Observations of the CMB power spectrum and baryon acoustic oscillations by *Planck*, on the other hand, impose an upper limit of $\sum m_\nu < 0.12\,\mathrm{eV}$ [60].[8] Measurements of the end point of the electron energy spectrum in β decays with *KATRIN* [113] further yield an upper bound on the effective anti-electron-neutrino mass $m_\nu^{\mathrm{eff}} < 1.1\,\mathrm{eV}$.

Normal and inverted ordering refer to the different scenarios for the neutrino mass hierarchy allowed by the mass squared differences measured from oscillations. These indicate one small mass splitting of $\Delta m^2 \sim 10^{-5}\,\mathrm{eV}^2$, and a larger one of $\Delta m^2 \sim 10^{-3}\,\mathrm{eV}^2$ [114]. In the normal ordering scenario, the small splitting is between the two lighter neutrino mass eigenstates, whereas in the inverted hierarchy, it is between the two heavier ones. The question which of the orderings is realized in nature is still on debate, however with a preference for normal ordering in the fits [114].

The addition of N_s right-handed[9] sterile neutrinos ν_R^i, $i = 1, \ldots, N_s$, provides a simple way to generate mass terms for the active neutrinos. The SM Lagrangian can then be extended by the terms

$$\Delta\mathcal{L} = -(Y_\nu)_{\alpha i}\,\bar{\ell}_L^\alpha\,\tilde{H}\,\nu_R^i - \frac{1}{2}(M_M)_{ij}\,\bar{\nu}_R^i\,\nu_R^{c\,j} + \text{h.c.}\,, \tag{2.10}$$

where $\alpha = e, \mu, \tau$ is a flavor index, and ν_R^c denotes the charge conjugate sterile neutrinos. After SSB, the first term generates Dirac masses of the form $(m_D)_{i\alpha}\,\bar{\nu}_R^i\nu_L^\alpha$ with $(m_D)_{i\alpha} = (Y_\nu^*)_{i\alpha}\,v/\sqrt{2}$, in the same way as the masses of the charged leptons and quarks are generated. In the absence of the second term, the neutrino masses and mass eigenstates are simply given by the eigenvalues and -vectors of m_D. For $N_s = 3$, we then obtain three Dirac neutrinos. Why may however wonder why the neutrinos are so much lighter than all other SM fermions, despite obtaining their masses via the same mechanism.

[8] This bound assumes three mass-degenerate neutrinos with no additional relativistic DOFs at low temperatures. It may for instance be altered by the presence of additional neutrino species. Including variations of N_{eff} (see section 8.1.2 for a definition) still yields the same constraint [60], while also fitting further parameters can relax the bound to $\sum m_\nu < 0.515\,\mathrm{eV}$ [111]. Furthermore, as higher neutrino masses lead to a lower Hubble rate today, including the data of [112], which is discrepant with the *Planck* data at the 4.4σ level and conversely predicts a higher Hubble rate, leads to tighter constraints [60].

[9] Note that the assumption that the sterile neutrinos are right-handed is not a restriction. Adding left-handed sterile neutrinos leads to the same interactions terms with ν_R replaced by the charge conjugate ν_s^c, while adding both chiralities corresponds to adding twice as many single-handed fields.

If, on the other hand, the Majorana mass term for the sterile neutrinos (the second term in eq. (2.10)) is included, the masses and eigenstates are obtained by diagonalizing the combined mass matrix

$$\Delta\mathcal{L} \supset -\frac{1}{2}\begin{pmatrix}\bar{\nu}_L^c & \bar{\nu}_R\end{pmatrix}\begin{pmatrix}0 & m_D^T \\ m_D & M_M\end{pmatrix}\begin{pmatrix}\nu_L \\ \nu_R^c\end{pmatrix} + \text{h.c.}\,, \tag{2.11}$$

where we suppressed flavor indices. This induces a mixing between the active and charge-conjugated sterile neutrinos. In general, we then obtain $3 + N_s$ Majorana neutrinos,[10] i.e. the mass eigenstates n_k, $k = 1, \ldots, 3 + N_s$, satisfy the Majorana condition $n_k^c = n_k$.[11] Including the Majorana mass term has the attractive feature that it may explain the smallness of the active neutrino masses via the (type-I) seesaw mechanism [116]. If we take the Majorana masses much higher than the weak scale, i.e. $M_M \gg m_D$, we typically obtain three light neutrinos with masses $m_\nu \simeq -m_D^T M_M^{-1} m_D$ and N_S heavy neutrinos with masses $\sim M_M$ [110].

At least two sterile neutrinos are needed to generate the masses required to explain the oscillation data. The lightest neutrino then remains massless. Adding a third right-handed neutrino allows to provide masses for all three active flavors. We can thus arrange a third or fourth right-handed neutrino to remain (mostly) sterile. As suggested in [117], it may then constitute a non-thermal DM candidate with keV scale masses. This is for instance incorporated in the neutrino minimal SM (νMSM) [118, 119], which extends the SM by three right-handed neutrinos, of which two provide masses for the active neutrinos, and the third one constitutes DM. The model can further generate the baryon asymmetry of the Universe.

[10] Whether neutrinos are Dirac or Majorana states is another open question. An observation of neutrinoless double-β-decay can shed light on this problem [115].

[11] Diagonalizing the mass matrix in eq. (2.11), we obtain $\Delta\mathcal{L} = -\sum_k \frac{m_k}{2}\,\bar{\nu}_L^{c\,k}\nu_L^k + \text{h.c.} = -\sum_k \frac{m_k}{2}\,\bar{n}_k^c n_k$, where $n_k = \nu_L^k + \nu_L^{c\,k}$. If M_M has vanishing eigenvalues, some of these combine to Dirac fields.

Part I

New Physics at Colliders

Prelude

In this first part of the dissertation we are going to consider various collider probes of new physics. We will mostly focus on proton-proton collisions.

Currently, the most prominent and important collider facility is the *LHC (Large Hadron Collider)* at *CERN*. It is the largest and most powerful accelerator in the world, colliding protons or heavy ions at center-of-mass energies up to 13 TeV. The *LHC* features the four major experiments *ATLAS*, *CMS*, *LHCb* and *ALICE*, where the first two are the ones most relevant in the following. During its second operational run that terminated recently in the end of 2018, it has delivered an integrated luminosity around $\sim 150\,\mathrm{fb}^{-1}$ of proton-proton collision data at $\sqrt{s} = 13$ TeV to *ATLAS* and *CMS* each. In the first run in 2011 and 2012, roughly $6\,\mathrm{fb}^{-1}$ and $23\,\mathrm{fb}^{-1}$ were collected per experiment at energies of $\sqrt{s} = 7$ TeV and 8 TeV, respectively. After the current maintenance shut-down, the *LHC* is planned to resume operation in 2021 at a center-of-mass energy of 14 TeV, with the aim to record $300\,\mathrm{fb}^{-1}$ of pp collisions in run three until the end of 2024.

For the post-*LHC* era, various successor projects have been proposed. The *LHC* itself will prospectively be upgraded to the *HL-LHC (high-luminosity LHC)* and subsequently continue running at 14 TeV around 2027, intending to reach an integrated luminosity of $3\,\mathrm{ab}^{-1}$ within a decade. More speculative future plans include for instance a *HE-LHC (high-energy LHC)* with a center-of-mass energy of 27 TeV, or an even more futuristic 100 TeV proton collider denoted FCC_{hh} *(Future Circular Collider)*.

In addition, future electron-positron colliders are also in debate. From 1989 to 2000, electrons and positrons with energies up to $\sqrt{s} = 209$ GeV were collided at *LEP (Large Electron-Positron Collider)* at *CERN*, providing data for precise determinations of the properties of the Z and W boson. Although energy losses via Bremsstrahlung preclude the acceleration of electrons to the energies reached in hadron machines, the cleaner experimental conditions, in particular the information of the total momentum in the events along the beam line, render electron colliders promising alternatives for future experiments. As a consequence, proposals for new e^+e^- machines have been elaborated, including both, linear accelerators such as the *ILC (International Linear Collider)* with center-of-mass energies up to $\sqrt{s} = 1$ TeV, as well as circular colliders like an FCC_{ee} with up to $\sqrt{s} = 350$ GeV. Further ideas such as electron-hadron or muon colliders may also be conceived. We will here however mostly focus on pp collisions.

Physics beyond the Standard Model (BSM) can be probed at colliders via two different paths. It can be searched for directly, trying to encounter new particles or their corresponding missing-energy signature if they do not interact with the detector, or indirectly via its effects on Standard Model (SM) processes. For the former case, a variety of studies have been conducted by *ATLAS* and *CMS*, for historical reasons often presented in the context of models of supersymmetry (SUSY). To obtain the corresponding limits on a specific model, these searches then need to be adapted and reinterpreted, typically involving a recasting based on Monte Carlo (MC) simulations. In the latter case, on the other hand, the limits obtained from data or projections are usually presented as bounds on higher-dimensional operators contributing to the processes under consideration, employing the framework of effective field theories (EFTs).

In the following, we will present examples of both of these two approaches. Chapter 3 performs a direct search for Higgs-portal dark matter (DM). We reinterpret a *CMS* study of invisible Higgs decays in vector-boson fusion (VBF) and provide a forecast for the *HL-LHC* and *HE-LHC* sensitivity. In chapter 4 we entertain the top-pair associated Higgs production channel to search for the $h \to Z\gamma$ decay at future colliders and investigate the corresponding indirect constraints on the new-physics contribution to the decay process. We then conclude this part with a comprehensive study of an extension of the SM in which lepton number is gauged, exploring the DM and collider phenomenology of the model in chapter 5.

3. Probing Higgs-Portal Dark Matter with Vector-Boson Fusion

This chapter is based on the publication [4] elaborated in collaboration with Jan Heisig, Michael Krämer, and Alexander Mück. It mostly duplicates the structure and logic of the publication.

To start our discussion of collider probes of new physics, we here present a search for Higgs-portal dark matter (DM) at the *LHC* as well as its high-luminosity and high-energy upgrades, entertaining the vector-boson fusion (VBF) Higgs production channel. We reinterpret a study of invisible Higgs decays in VBF [120] and recast the corresponding projections for the *HL-LHC* [121] by *CMS*. The latter is also used as a basis to obtain a sensitivity forecast at the *HE-LHC*, including estimates of systematic uncertainties.

The discovery of the Higgs boson by *ATLAS* [16] and *CMS* [17] in 2012 marks one of the greatest successes of the Standard Model (SM) of particle physics. Due to the relative recency of its first observation, it is suggestive to assume that the SM Higgs sector may reveal insights into new physics beyond the Standard Model (BSM). Indeed, the Higgs bilinear $H^\dagger H$ is the lowest-dimensional, Lorentz and gauge invariant operator in the SM, allowing for a coupling to singlet extensions of the SM even at the renormalizable level. This provides motivation for so-called Higgs-portal models [122, 123], which are DM models in which the dark sector communicates with the SM primarily via its interaction with the Higgs boson, i.e. the Higgs boson constitutes a portal between SM and dark sector.

In this chapter we primarily focus on the scalar singlet Higgs-portal model [124–126], in which the SM is augmented by a scalar DM field interacting exclusively[1] via the Higgs boson. The discussion of other DM spins is deferred to appendix 3.A. Regarding its DM phenomenology, the parameter space of the model is rather strongly constrained by direct detection bounds [88] on one hand and the DM abundance [60] on the other hand, limiting the scalar mass to values close to half of the Higgs mass, $m_S \sim m_h/2$, or values above $m_S \gtrsim 1\,\text{TeV}$. Throughout this chapter we take the mass of the SM Higgs boson to be $m_h = 125.09\,\text{GeV}$ [127].

While collider searches cannot reach the low portal couplings required to reproduce the full DM relic density close to the Higgs resonance around $m_S \simeq m_h/2$ in the standard thermal freeze-out scenario, the respective limits can still exclude a part of the viable parameter space, for instance in the case that the Higgs-portal scalar only constitutes a fraction of the total amount of DM. Such a scenario may be preferred when fitting the model to the γ-ray Galactic center excess [128] or cosmic-ray anti-proton excess [129]. Furthermore, direct detection limits can be mitigated considering minimal extensions of the model [130–132], potentially reopening larger regions of the parameter space above the threshold, accessible to collider searches.

[1] Except for its quartic self-interaction.

While previous collider studies of Higgs-portal DM have either focused on the mass region constrained by invisible Higgs decays [120, 133], or on the far off-shell (in terms of the Higgs' width) regime [123, 134, 135], we here also obtain limits for scalar masses close to the resonance. For sizeable DM couplings and masses very close to $m_S \simeq m_h/2$, we encounter an unphysical enhancement of the DM production cross-section caused by the break-down of the fixed-width prescription of the propagator. This effect is fixed using a running width in the propagator, giving consistent limits on the portal coupling.

This chapter proceeds as follows. Section 3.1 revisits the scalar singlet Higgs portal model and the DM constraints on its parameter space. We then provide further details on the failure of the fixed-width propagator arising in the vicinity of the Higgs resonance in section 3.2. In section 3.3 we consider a 13 TeV *CMS* search for invisible Higgs decays in VBF [120]. We present the corresponding limits on the portal coupling in section 3.3.1 and validate our Monte Carlo (MC) setup for the following sections in section 3.3.2. Based on ref. [121], section 3.4 then derives the prospective sensitivity of the *HL-LHC* as well as *HE-LHC*. A careful estimate of the systematic uncertainties is obtained in section 3.4.1, and the resulting constraints are presented in section 3.4.2. We conclude in section 3.5. Appendix 3.A provides a reinterpretation for Higgs-portal models with other types of DM fields.

3.1. The Scalar Singlet Higgs-Portal Model

In this chapter we are mainly going to focus on the scalar singlet Higgs-portal model [124–126]. It is one of the simplest possible, ultraviolet (UV) complete extensions of the SM, adding only a real scalar field S that transforms as a singet under the SM symmetries. To render S a valid DM candidate we further have to impose a $\mathbb{Z}_2$ symmetry under which S is odd and all other particles are even, assuring the stability of S. The Lagrangian of this model then reads

$$\mathcal{L} = \mathcal{L}_{\mathrm{SM}} + \frac{1}{2}\,\partial_\mu S\,\partial^\mu S - \frac{1}{2}\,m_{S,0}^2\,S^2 - \frac{1}{4}\,\lambda_S\,S^4 - \frac{1}{2}\,\lambda_{\mathrm{HP}}\,S^2 H^\dagger H\,, \tag{3.1}$$

where the only possible interaction with SM fields at the renormalizable level is the portal coupling $\sim \lambda_{\mathrm{HP}}\,S^2\,H^\dagger H$ to the Higgs bilinear. When the Higgs field acquires its vacuum expectation value (VEV), $\langle H\rangle = (0,\, v/\sqrt{2}\,)^T$ with $v \simeq 246\,\mathrm{GeV}$, the portal term contributes to the physical scalar mass $m_S^2 = m_{S,0}^2 + \frac{1}{2}\lambda_{\mathrm{HP}} v^2$, and induces the interactions

$$\mathcal{L} \supset -\frac{1}{2}\,\lambda_{\mathrm{HP}} v\,h\,S^2 - \frac{1}{4}\,\lambda_{\mathrm{HP}}\,h^2 S^2\,, \tag{3.2}$$

where h is the SM Higgs boson and we use unitary gauge. The first term in eq. (3.2) then allows the Higgs boson to decay into a pair of DM particles if $m_S < m_h/2$. The corresponding invisible decay width of the Higgs boson is given by

$$\Gamma_{\mathrm{inv}} = \Gamma(h \to SS) = \frac{\lambda_{\mathrm{HP}}^2 v^2}{32\pi\, m_h}\sqrt{1 - 4\,\frac{m_S^2}{m_h^2}}\,. \tag{3.3}$$

The phenomenology of the model is primarily determined by two parameters: the DM mass m_S and the portal coupling λ_{HP}. The third parameter of the model, the scalar self-coupling λ_S, only plays a minor role.[2] As a result, the model is very simple and highly predictive, but also rather strongly constrained. It has been studied extensively in the literature (see e.g. ref. [123] and references therein).

The strongest constraints on the model arise from the combination of the DM relic density measured by *Planck* [60] and direct detection limits on the scattering of DM off heavy nuclei as for instance searched for by *XENON1T* [88]. In the thermal freeze-out scenario, the abundance of DM is set by its annihilation into SM particles. Once the annihilation rate drops below the expansion rate of the Universe, the DM cannot maintain equilibrium with the SM. It then freezes out, i.e. decouples, and its number density per co-moving volume is conserved. The lower the interaction cross-section the earlier the freeze-out occurs, leading to a higher relic abundance as the DM experiences less Boltzmann suppression (assuming that decoupling happens when the DM is non-relativistic). The requirement that we do not produce more DM than observed therefore places a lower bound on the annihilation cross-section as a function of the DM mass. Direct detection experiments on the other hand put an upper bound on the DM-nucleus scattering cross-section. In our simple model, both cross sections are controlled by the portal coupling, so that λ_{HP} is constrained from above and below.

Figure 3.1 shows the relic density[3] and direct detection constraints on the DM mass m_S and the portal coupling λ_{HP} in the scalar singlet Higgs-portal model, calculated using MicrOMEGAs v5 [140, 141]. The solid black line depicts the parameters for which the abundance of S coincides with the DM relic abundance $h^2\Omega_{\text{DM}} = 0.1200 \pm 0.0012$ measured by *Planck* [60]. For couplings above this line, S can only account for a fraction of the DM density, whereas couplings below the line are excluded as they lead to an overproduction of DM. This constrains the portal coupling to values above $\lambda_{\text{HP}} \gtrsim 0.04$, unless the scalar mass is around the Higgs resonance $m_S = m_h/2$ where the annihilation of S through an s-channel Higgs boson is very efficient, allowing for portal couplings as low as $\lambda_{\text{HP}} \simeq \text{few} \times 10^{-4}$.

The current 90 % confidence level (CL) upper limit from the *XENON1T* direct detection experiment is indicated by the solid blue line in fig. 3.1, excluding the blue shaded region above the line. The direct detection bound severely limits the viable parameter space of the model, leaving only two regions in which S is neither over-abundant nor excluded by direct detection: the high-mass region with $m_S \gtrsim 1\,\text{TeV}$, and the resonance region where $m_S \simeq m_h/2$.[4] Future experiments will further narrow down these regions. The projected sensitivities for *LZ* [142] and *DARWIN* [143] are indicated by the dashed green and dotted purple lines, respectively. In addition to the direct detection constraints, fig. 3.1 also depicts the current *LHC* limit from searches for invisible decays of the Higgs boson, excluding $\text{Br}(h \to SS) > 19\,\%$ at 95 % CL [120]. Indirect detection experiments may impose further limits in a very narrow region around $m_S \simeq m_h/2$ [146].

Note that the direct detection limits in fig. 3.1 assume that the scalar S accounts for the full measured DM abundance. If it constitutes only a fraction of the total relic density,

[2]This parameter is however relevant in the context of DM self-interactions [136] or the stability of the electroweak vacuum [137].

[3]See refs. [138, 139] for a more careful calculation, in particular regarding the region close to the Higgs resonance.

[4]These are also the regions favored by global fits of the model, see e.g. refs. [144, 145].

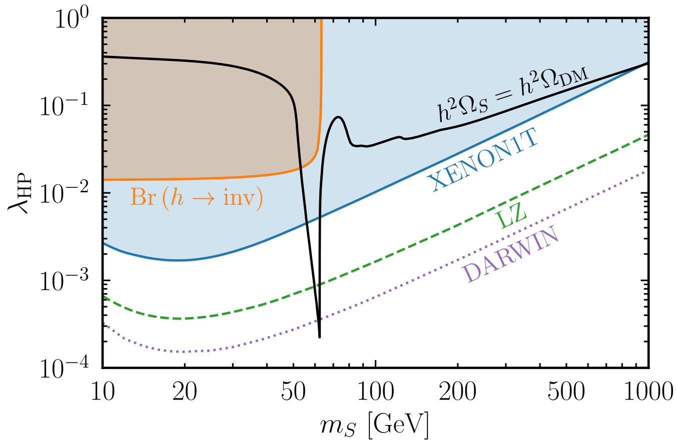

Figure 3.1: DM constraints on the scalar singlet Higgs-portal model as a function of the DM mass m_S and portal coupling $\lambda_{\rm HP}$. Along the solid black line, the scalar S accounts for the full DM relic abundance measured by *Planck* [60], whereas the region below the line is excluded as DM is overproduced. The current 90 % CL exclusion reach of *XENON1T* [88] is shown in blue. The dashed green and dotted purple lines indicate the prospective reach of *LZ* [142] and *DARWIN* [143], respectively. The orange line corresponds to the 95 % upper bound on the invisible Higgs branching ratio by *CMS* [120].

as it is the case in the region above the black line, the constraints are relaxed. Taking this into account further opens up the parameter space of larger portal couplings in the region of the resonance.

3.2. Threshold at Resonance

Previous studies of collider searches for Higgs-portal DM have focused either on the mass region below the Higgs resonance, $m_S < m_h/2$, where the Higgs boson can decay invisibly into a DM pair (see e.g. refs. [120, 133]) or on DM masses lying at least a few GeV above $m_h/2$, where the DM can only be produced from an off-shell Higgs boson (see e.g. refs. [123, 134, 135]). In this chapter, we will also consider the transition between the two regions with $m_S \simeq m_h/2$. In order to obtain consistent results in this region, special care needs to be taken regarding the treatment of the Higgs-boson propagator. This is due to the failure of the fixed-width prescription of the propagator caused by the invisible decay channel opening just above the resonance. Before investigating current and future collider limits on the model, let us therefore first review this problem in more detail and explain how it is fixed by using a running width in the Higgs-boson propagator.

Neglecting electroweak (EW) corrections and higher-order corrections in the portal coupling, the DM production cross-section factorizes into the production of an off-shell Higgs boson and its subsequent decay into a DM pair, i.e.

$$\sigma_{\rm inv} = \int \frac{\mathrm{d}q^2}{2\pi}\, \sigma_h(q^2)\, |P(q^2)|^2\, 2\,q\,\Gamma_{\rm inv}(q^2)\, \Theta(q^2 - 4m_S^2)\,. \tag{3.4}$$

Here, $\sigma_h(q^2)$ is the production cross-section of an off-shell Higgs with invariant mass q^2, $P(q^2)$ is the Higgs-boson propagator, and $\Gamma_{\text{inv}}(q^2)$ is the off-shell decay width given by eq. (3.3) with m_h replaced by $\sqrt{q^2}$.

To obtain accurate predictions for s-channel resonances at momentum q^2 around the resonance, we need to resum one-particle irreducible (1PI) loop-corrections to the propagator. The resulting dressed propagator can be written as

$$P(q^2) = \frac{i}{q^2 - m_R^2 + \Sigma(q^2) + i\varepsilon}\,, \tag{3.5}$$

where m_R is the renormalized mass and $\Sigma(q^2)$ is the 1PI self-energy of the propagating particle. For momenta close to the resonance, we can usually approximate the self-energy as constant, replacing $\Sigma(q^2)$ by $\Sigma(m_P^2)$, where m_P is the pole mass defined by $m_P^2 = m_R^2 + \operatorname{Re}\Sigma(m_P^2)$, i.e. the real part of Σ enters the definition of the pole mass. The imaginary part of Σ on the other hand is related to the total decay width of the (off-shell) particle via the optical theorem, $\operatorname{Im}\Sigma(q^2) = q\,\Gamma_{\text{tot}}(q^2)$. We therefore obtain the Breit-Wigner propagator

$$P_f(q^2) = \frac{i}{q^2 - m_P^2 + i\,m_P\,\Gamma_{\text{tot}}}\,, \tag{3.6}$$

where $\Gamma_{\text{tot}} = \Gamma_{\text{tot}}(m_P^2)$, which is the propagator commonly used for s-channel resonances. This expression is typically valid if the width is sufficiently small, $\Gamma_{\text{tot}} \ll m_p$. If the propagating particle is kinematically allowed to go on-shell, i.e. if $m_S < m_h/2$ in our case, we can further use the narrow-width approximation (NWA) and take

$$|P_f(q^2)|^2 \approx \frac{\pi}{m_P\,\Gamma_{\text{tot}}}\,\delta(q^2 - m_P^2)\,, \tag{3.7}$$

so that the DM cross-section eq. (3.4) simply becomes the on-shell cross-section times branching ratio, $\sigma_{\text{DM}} = \sigma_h(m_h^2) \times \text{Br}_{\text{inv}}$ with $\text{Br}_{\text{inv}} = \Gamma_{\text{inv}}/\Gamma_{\text{tot}}$. In particular, the total Higgs production cross-section is then equal to the on-shell production cross-section,

$$\sigma_f^{\text{tot}} = \int \frac{\mathrm{d}q^2}{2\pi}\,\sigma_h(q^2)\,\frac{2\,q\,\Gamma_{\text{tot}}(q^2)}{(q^2 - m_h^2)^2 + m_h^2\Gamma_{\text{tot}}^2(m_h^2)} \simeq \sigma_h(m_h^2)\,. \tag{3.8}$$

The fixed-width propagator eq. (3.6) presumes that the total decay rate is a smooth function around the resonance and can be approximated as a constant. This is however not the case if a large decay channel opens up close to the resonance, as it is the case in the Higgs-portal model for $m_S \simeq m_h/2$ and $\lambda_{\text{HP}} \gtrsim 0.1$. If this assumption is violated, the fixed-width prescription breaks down and the total cross-section calculated using eq. (3.8) can exceed the on-shell production cross-section. This effect is demonstrated in fig. 3.2, where we show the fiducial DM production cross-section in VBF at the 13 TeV *LHC* (see section 3.3 for details) calculated using a fixed-width propagator (solid red line) for $\lambda_{\text{HP}} = 1$ and DM masses close to $m_h/2$. With such a large portal coupling, the Higgs boson decays 100 % invisibly if $m_S < m_h/2$, such that the DM cross-section is equal to the on-shell Higgs cross-section below the resonance, whereas it falls off quickly for

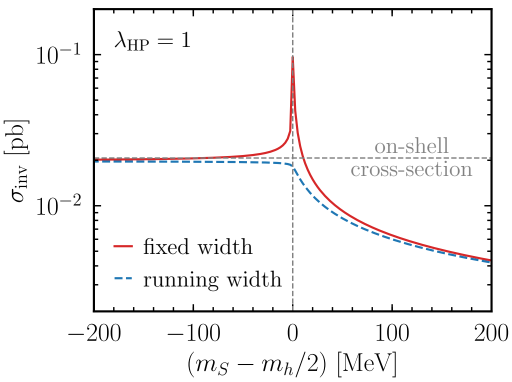

Figure 3.2: Fiducial cross-section for DM production in VBF for $\lambda_{\rm HP} = 1$ in the fixed-width (solid red) and running-width (dashed blue) prescription.

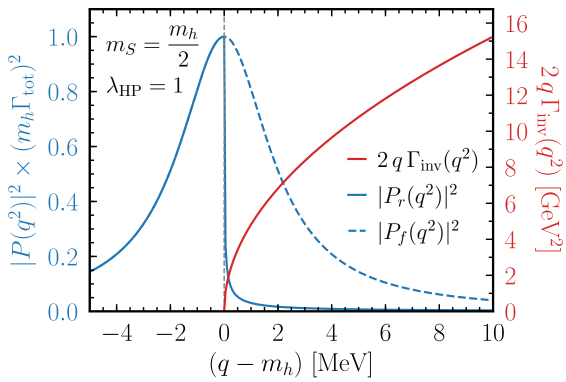

Figure 3.3: Squared fixed-width (dashed blue) and running-width (solid blue) propagator and decay width (red) as a function of the invariant mass of the Higgs boson.

DM masses above the resonance. However, for $m_S \simeq m_h/2$ the cross section displays an unphysical feature, exceeding the on-shell cross-section by almost an order of magnitude.

This unphysical behavior can be fixed by using the running-width propagator which keeps the momentum dependence in the imaginary part of the self-energy,

$$P_r(q^2) = \frac{i}{q^2 - m_P^2 + i\sqrt{q^2}\,\Gamma_{\rm tot}(q^2)}\,, \tag{3.9}$$

where we use $\Gamma_{\rm tot}(q^2) = \Gamma_h^{\rm SM} + \Gamma_{\rm inv}(q^2)$ with $\Gamma_h^{\rm SM} = 4.1\,\text{MeV}$ (i.e. we neglect the momentum dependence of the visible width) as the dominant effect originates from the opening of the invisible channel. As shown by the blue dashed line in fig. 3.2, the DM cross-section is well-behaved if calculated using a running-width propagator, with $\sigma_{\rm inv} \leq \sigma_h(m_h^2)$ for all DM masses.

To further illustrate why the fixed-width prescription breaks down, let us consider the squared propagators as well as the numerator $2\,q\,\Gamma_{\rm inv}(q^2)$ from eq. (3.4) in the resonance region $q^2 \simeq m_h^2$ for $m_S = m_h/2$ and $\lambda_{\rm HP} = 1$ depicted in fig. 3.3. If the fixed-width propagator (dashed blue line) is used, the suppression of off-shell momenta sightly above the resonance is insufficient to overcome the rapidly-growing invisible width in the numerator (red line). For momenta close to the resonance, $q^2 \approx m_h^2$, we therefore obtain (cf. eq. (3.4))

$$2\,q\,\Gamma_{\rm inv}(q^2)\,|P_f(q^2)|^2 \simeq \frac{2\,q\,\Gamma_{\rm inv}(q^2)}{m_h^2\,\Gamma_{\rm tot}^2(m_h^2)} \gg 1\,, \tag{3.10}$$

which can grow arbitrarily large and lead to an enhancement of the DM production cross-section to values above the cross-section for on-shell Higgs production. If, on the other hand, the running Higgs-width is used in the propagator (solid blue line), the denominator also grows with q^2. As a result, the opening invisible channel leads to an

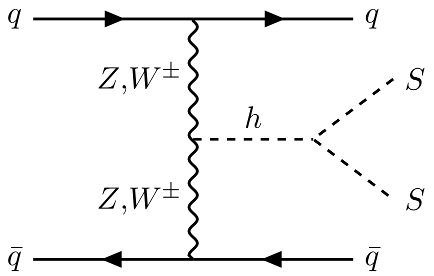

Figure 3.4: Feynman diagram for Higgs-portal DM production in VBF at the *LHC*.

additional suppression of momenta above the threshold for DM pair production in the denominator and we obtain

$$2\,q\,\Gamma_{\text{inv}}(q^2)\,|P_r(q^2)|^2 \simeq \frac{2\,q\,\Gamma_{\text{inv}}(q^2)}{q^2\,\Gamma^2_{\text{tot}}(q^2)} \sim \frac{2}{q\,\Gamma_{\text{inv}}(q^2)}\,, \tag{3.11}$$

where we assumed that $\Gamma_{\text{inv}}(q^2)$ dominates the total width. This additional suppression of momenta above the resonance prohibits the uncontrolled growth of the cross section and restores $\sigma_{\text{inv}} \leq \sigma_h(m_h^2)$.

3.3. Current LHC Limits

Let us now investigate the constraints we can put on the Higgs-portal coupling λ_{HP} from current *LHC* data. We will base our analysis on a search for invisible Higgs decays in the VBF channel by *CMS* [120] using $35.9\,\text{fb}^{-1}$ of data recorded at a center-of-mass energy of 13 TeV.

Vector-boson fusion (VBF) [147, 148] is one of the primary Higgs production-channels at the *LHC*. In this channel, the Higgs boson is produced from the fusion of two Z or W bosons radiated off quarks from the colliding protons in the process $pp \to h + 2\,\text{jets}$. The corresponding Feynman diagram is depicted in fig. 3.4. It features a very characteristic signature of two hard forward jets separated by a large gap in pseudo-rapidity and with a large dijet invariant mass. While the cross section for VBF Higgs production is roughly an order of magnitude below the cross section for Higgs production in gluon fusion, its distinct topology allows for an efficient suppression of background processes via phase-space cuts, which is of particular importance in searches for invisible decays at proton colliders as the Higgs boson cannot be reconstructed from its decay products in this case. VBF hence constitutes the most promising channel in searches for Higgs-portal DM and other primarily Higgs-mediated DM models [123, 134, 135, 149–151]. In the following we will therefore focus on the VBF channel only.

The *CMS* search [120] presents limits derived from a cut-and-count analysis, as well as a shape analysis with respect to the jet-pair invariant mass and pseudo-rapidity difference distributions, posing a 95 % CL observed upper bound on the invisible branching ratio of the SM Higgs-boson of $\text{Br}(h \to \text{inv}) < 58\,\%$ and $\text{Br}(h \to \text{inv}) < 33\,\%$, respectively.[5] *CMS* further interprets their results as limits on the signal strength of an additional Higgs

[5] Note that the cut-and-count limit is alleviated compared to the expected limit of $\text{Br}(h \to \text{inv}) < 30\,\%$ due to a $\sim 2.5\sigma$ excess of events in the signal region with respect to the background-only prediction,

boson $\mathcal{H}$ with mass $m_{\mathcal{H}}$ that is produced SM-like, decays invisibly, and does not mix with the SM Higgs. We will use these limits to reinterpret the *CMS* search in the context of the scalar singlet Higgs-portal model in section 3.3.1 based on eq. (3.4). This allows us to impose limits on the Higgs-portal coupling λ_{HP} for DM masses below, around, and above the resonance without the need of any MC simulation. In section 3.3.2 we then perform a leading order (LO) MC recasting of the cut-and-count analysis, validating the MC setup used for our *HL-* and *HE-LHC* projections.

3.3.1. Reinterpretation of Upper Limits

In this section, we will reinterpret the *CMS* search [120] in the context of the scalar singlet Higgs-portal model to obtain upper limits on the portal coupling λ_{HP}. For DM masses below the threshold for production from on-shell Higgs decays, $m_S < m_h/2$, these bounds can be trivially obtained directly from the 95 % CL upper limit on the invisible branching ratio $\mathrm{Br}_{\mathrm{inv}}^{95\%}$. For masses in the vicinity and beyond the threshold on the other hand, we use eq. (3.4) to calculate the VBF DM-production cross-section σ_{inv}, where in this context $\sigma_h(q^2)$ denotes the fiducial cross-section at detector-level (including acceptance times efficiency) for the VBF production of an off-shell Higgs boson with invariant mass $\sqrt{q^2}$. In the case of a cut-and-count analysis, the upper bound on λ_{HP} can then be computed by equating σ_{inv} to the limit on the signal cross-section $\sigma_{\mathrm{inv}}^{95\%} = \mathrm{Br}_{\mathrm{inv}}^{95\%} \times S/\mathcal{L}$, where $S = 743$ [120] is the predicted number of signal events for $\mathrm{Br}_{\mathrm{inv}} = 1$, and $\mathcal{L} = 35.9\,\mathrm{fb}^{-1}$ is the integrated luminosity.

To obtain the off-shell Higgs production cross-section $\sigma_h(q^2)$ from the experimental analysis, we here use the limits on the signal strength $\mu_{\mathcal{H}} = \sigma_{\mathcal{H}}/\sigma_{\mathcal{H}}^{\mathrm{SM}} \times \mathrm{Br}(\mathcal{H} \to \mathrm{inv})$ of an additional Higgs boson $\mathcal{H}$ with mass $m_{\mathcal{H}}$ that does not mix with the 125 GeV Higgs boson and is produced as in the SM (cf. fig. 7 of ref. [120]). If next-to-leading order (NLO) EW corrections are neglected, the SM prediction for the on-shell production of $\mathcal{H}$ simply corresponds to the off-shell production of the 125 GeV Higgs at $q^2 = m_{\mathcal{H}}^2$, i.e. $\sigma_{\mathcal{H}}^{\mathrm{SM}} = \sigma_h(q^2 = m_{\mathcal{H}}^2)$. We can therefore relate the 95 % CL limit on $\mu_{\mathcal{H}}$ from the cut-and-count analysis to the off-shell Higgs production cross-section $\sigma_h(q^2)$,

$$\mu_{\mathcal{H}}^{95\%}(m_{\mathcal{H}}^2) = \frac{\sigma_{\mathrm{inv}}^{95\%}}{\sigma_h(q^2 = m_{\mathcal{H}}^2)}\,, \tag{3.12}$$

so that eq. (3.4) can be rewritten as

$$\frac{\sigma_{\mathrm{inv}}}{\sigma_{\mathrm{inv}}^{95\%}} = \int \frac{\mathrm{d}q^2}{2\pi}\, \frac{1}{\mu_{\mathcal{H}}^{95\%}(q^2)}\, |P(q^2)|^2\; 2\,q\,\Gamma_{\mathrm{inv}}(q^2)\; \Theta(q^2 - 4m_S^2)\,. \tag{3.13}$$

As a given parameter point is excluded at 95 % CL if $\sigma_{\mathrm{inv}} > \sigma_{\mathrm{inv}}^{95\%}$, the corresponding limit on λ_{HP} as a function of the DM mass can be obtained by equating eq. (3.13) to one and solving the equation numerically.

attributed to a statistical fluctuation (see section 7.2 of ref. [120]). A similarly strong bound of $\mathrm{Br}(h \to \mathrm{inv}) < 53\,\%$ can be obtained from the recent measurement of the total Higgs boson width, $\Gamma_{\mathrm{tot}} = 3.2^{+2.8}_{-2.2}\,\mathrm{MeV}$ [152].

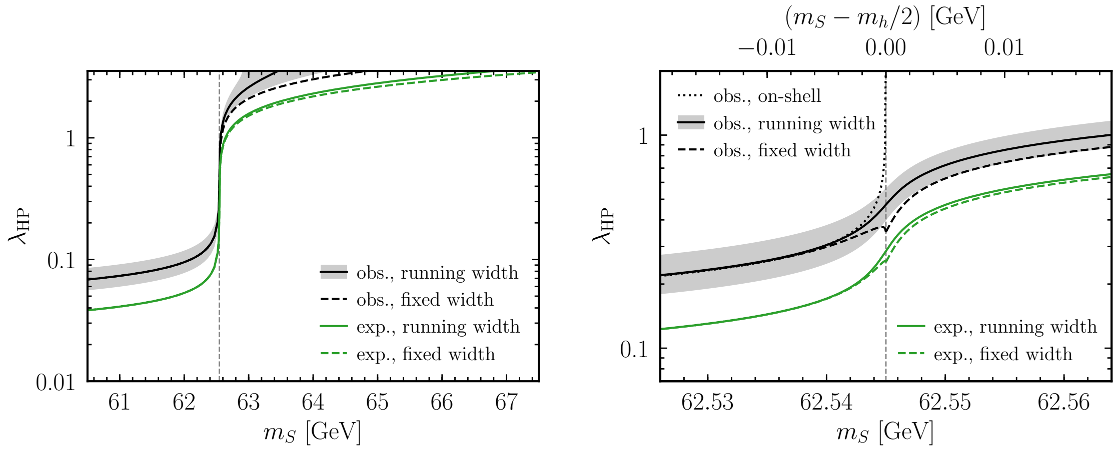

Figure 3.5: Observed (black) and expected (green) 95 % CL upper limits on the Higgs-portal coupling λ_{HP} from the cut-and-count analysis for a wide range of DM masses (left) and very close to the resonance (right). The solid lines use the running-width prescription, whereas the dashed lines indicate the corresponding limits if a fixed width is used. The gray band reflects the uncertainty on the signal cross-section in ref. [120]. The dotted line in the right panel indicates the limits from the invisible branching ratio.

The resulting 95 % CL limits on the portal coupling λ_{HP} as a function of the DM mass m_S from the cut-and-count analysis are shown in fig. 3.5. The black (green) line indicates the observed (expected) limit. The solid lines correspond to limits obtained employing the running-width prescription of the propagator, whereas the dashed lines use a fixed width. We also indicate the 17 % uncertainty on the on-shell Higgs production cross-section in ref. [120], reflected by the gray band obtained by solving $\sigma_{\mathrm{inv}}/\sigma_{\mathrm{inv}}^{95\%} = 1 \pm 0.17$. The left panel covers a mass range of several GeV around the resonance $m_S = m_h/2$, whereas the right panel focuses on the very resonance.

For DM masses below the Higgs resonance, portal couplings as low as $\lambda_{\mathrm{HP}} \sim 0.1$ can be excluded. In this region both descriptions of the width in the propagator give consistent results that perfectly agree with the limits obtained from the invisible branching fraction (i.e. using the NWA) shown as a dotted line in the right panel of fig. 3.5. However, as we approach the resonance, for masses $m_S \gtrsim m_h/2 - \Gamma_h^{\mathrm{SM}}$ the fixed-width approximation (as well as the NWA) breaks down. The limits obtained using a fixed-width propagator (dashed lines) exhibit an unphysical feature at the resonance (cf. right panel), whereas the running-width calculation yields the proper bounds, excluding $\lambda_{\mathrm{HP}} > 0.47$ at $m_S = m_h/2$. Above the threshold, the search rapidly becomes less sensitive and only $\lambda_{\mathrm{HP}} \gtrsim 1$ can be probed, entering the non-perturbative regime. The loss of perturbative control is further indicated by the large deviations in the observed limits between the two calculations at DM masses well above the threshold, where a difference between the descriptions is not expected. This difference is formally of higher-order in λ_{HP} and can be interpreted as a lower bound on the theoretical uncertainty.

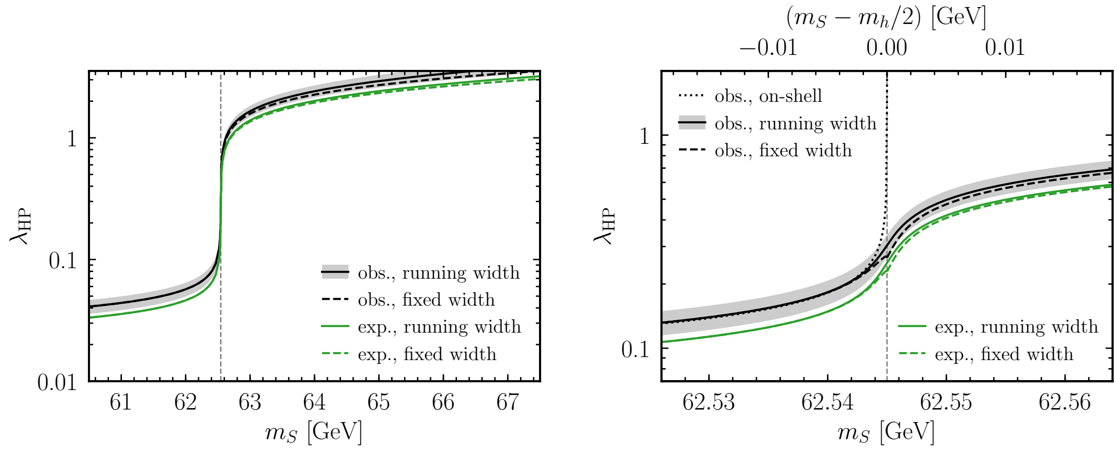

Figure 3.6: Same as fig. 3.5, but for the shape analysis.

We further apply eq. (3.13) to derive limits from the shape analysis in [120], assuming that the dependence of the distributions of the dijet invariant-mass and pseudo-rapidity difference on q^2 can be neglected. The resulting bounds are shown in fig. 3.6. The analysis excludes $\lambda_{\rm HP} > 0.30$ for $m_S = m_h/2$ and yields limits in the perturbative regime up to $m_S \lesssim 67\,\mathrm{GeV}$. As the couplings constrained in the shape analysis are lower than in the cut-and-count case, the effects of the breakdown of the fixed-width description are less pronounced and both calculations agree well within the uncertainties.

3.3.2. Recasting of the Cut-and-Count Analysis

To validate the Monte Carlo (MC) setup we use for the *HL-LHC* and *HE-LHC* projections in section 3.4, let us now perform a MC recasting of the cut-and-count analysis of ref. [120]. We again calculate the DM cross-section using eq. (3.4), but we now obtain the cross section for off-shell Higgs production from MC simulation. Since NLO EW corrections are neglected, the off-shell cross-sections can be calculated from the on-shell cross-section in the SM, setting the Higgs mass to the corresponding value of $\sqrt{q^2}$.

We use the following setup for our MC simulation. Events for VBF Higgs production in the SM with different masses of the Higgs boson are generated at LO using MadGraph5_aMC@NLO v2.6 [153] in the 5-flavor scheme. We employ the NNPDF3.0 [154] LO parton distribution function (PDF) set with $\alpha_s(m_Z) = 0.118$ provided by the LHAPDF6 [155] library. The renormalization and factorization scales are set to the W mass, $\mu_R = \mu_F = m_W$ [156]. The generated events are passed to Pythia v8.235 [157] to model parton shower and hadronization. Detector effects are subsequently simulated in Delphes v3.4.2 [158] with the *CMS* detector card. Jet clustering is performed by FastJet v3.3.1 [159] using the anti-k_T algorithm [160] with $R = 0.4$.

We adapt the cuts used in the *CMS* analysis [120], listed in the corresponding column in table 3.1. At least two jets with $|\eta_j| < 4.7$ and a minimum p_T of 80 GeV (40 GeV) for the (second-)hardest jet are required. To single out VBF Higgs production events, the leading jet pair is further required to be separated in pseudo-rapidity, $|\Delta\eta_{jj}| = |\eta_{j_1} - \eta_{j_2}| > 4.0$,

$\sqrt{s}$	13 TeV	14 TeV / 27 TeV
$p_T^{j_1}$	$> 80\,\text{GeV}$	$> 80\,\text{GeV}$
$p_T^{j_2}$	$> 40\,\text{GeV}$	$> 40\,\text{GeV}$
$\lvert\eta_j\rvert$	< 4.7	< 5.0
$\min(\lvert\eta_{j_1}\rvert, \lvert\eta_{j_2}\rvert)$	< 3.0	–
M_{jj}	$> 1.3\,\text{TeV}$	$> 2.5\,\text{TeV}$ / $> 6\,\text{TeV}$
$\eta_{j_1} \cdot \eta_{j_2}$	< 0	< 0
$\lvert\Delta\eta_{jj}\rvert$	> 4.0	> 4.0
$\lvert\Delta\phi_{jj}\rvert$	< 1.5	< 1.8
$\not{E}_{\mathrm{T}}$	$> 250\,\text{GeV}$	$> 190\,\text{GeV}$
$\lvert\Delta\phi_{j\not{E}_{\mathrm{T}}}\rvert$	> 0.5 ($p_T^j > 30\,\text{GeV}$)	> 0.5 ($p_T^j > 30\,\text{GeV}$)
photon veto	$p_T^\gamma > 15\,\text{GeV}$, $\lvert\eta_\gamma\rvert < 2.5$	–
electron veto	$p_T^e > 10\,\text{GeV}$, $\lvert\eta_e\rvert < 2.5$	$p_T^e > 10\,\text{GeV}$, $\lvert\eta_e\rvert < 2.8$
muon veto	$p_T^\mu > 10\,\text{GeV}$, $\lvert\eta_\mu\rvert < 2.4$	$p_T^\mu > 10\,\text{GeV}$, $\lvert\eta_\mu\rvert < 2.8$
τ-lepton veto	$p_T^\tau > 18\,\text{GeV}$, $\lvert\eta_\tau\rvert < 2.3$	$p_T^\tau > 20\,\text{GeV}$, $\lvert\eta_\tau\rvert < 3.0$
b-jet veto	$p_T^b > 20\,\text{GeV}$, $\lvert\eta_b\rvert < 2.4$	$p_T^b > 30\,\text{GeV}$, $\lvert\eta_b\rvert < 5.0$

Table 3.1: Analysis cuts used in this paper. The cuts for 13 TeV and 14 TeV are taken from refs. [120] and [121], respectively. The cuts for the 27 TeV *HE-LHC* are identical to the ones for the 14 TeV *HL-LHC* except for the cut on M_{jj}.

with $\eta_{j_1} \cdot \eta_{j_2} < 0$ (i.e. the jets are in different hemispheres of the detector), to have a large invariant mass, $M_{jj} > 1.3\,\text{TeV}$, as well as to be close in azimuthal angle, $|\Delta\phi_{jj}| < 1.5$. As the DM particles are invisible to the detector, a lower cut on the missing transverse energy (MET) of $\not{E}_{\mathrm{T}} > 250\,\text{GeV}$ is applied. Additional jets with $p_T > 30\,\text{GeV}$ are allowed if they are well separated from the MET, $|\Delta\phi_{j\not{E}_{\mathrm{T}}}| > 0.5$. Photons, electrons, muons, as well as b- and τ-tagged jets are vetoed.

To account for the contribution of gluon-initiated Higgs production to the signal, as well as to profit from the NLO corrections and more sophisticated detector effects included in the *CMS* simulation, we rescale our results for the cross section to match the *CMS* prediction for on-shell Higgs production. For $\mathrm{Br}(h \to \mathrm{inv}) = 1$, *CMS* predicts a total of 743 ± 129 signal events [120], corresponding to a fiducial cross-section of $(20.7 \pm 3.6)\,\text{fb}^{-1}$, whereas our LO simulation yields $14.2\,\text{fb}^{-1}$ with a scale uncertainty around 25 %. We therefore rescale our cross sections by a factor 1.46 for the 13 TeV *LHC*.

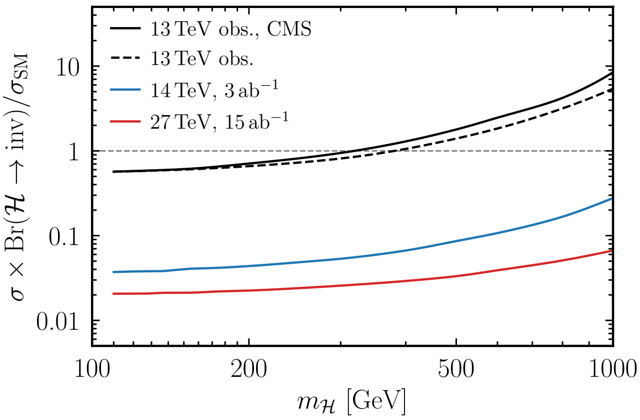

Figure 3.7: Observed 95 % CL upper limit on the signal strength $\mu_{\mathcal{H}} = \sigma \times \mathrm{Br}(\mathcal{H} \to \mathrm{inv})/\sigma_h(m_{\mathcal{H}})$ for an invisibly decaying Higgs boson with mass $m_{\mathcal{H}}$ from the *CMS* cut-and-count analysis in ref. [120] (solid black), as well the predictions from our simulation for the current *LHC* (dashed black), *HL-LHC* (blue), and *HE-LHC* (red).

Our (rescaled) cross-section predictions are presented in terms of the corresponding 95 % CL upper limits on the signal strength $\mu_{\mathcal{H}}$ for additional Higgs bosons with mass $m_{\mathcal{H}}$ in fig. 3.7. The dashed black line depicts our result, whereas the *CMS* limit from fig. 7 of ref. [120] is indicated by the solid black line. For $m_{\mathcal{H}}$ below 150 GeV, the limits agree within the percent level, whereas the deviation between the two becomes larger for higher $m_{\mathcal{H}}$. However, for the DM masses constrained by the *CMS* analysis, the integral in eq. (3.4) is dominated by values of q^2 well below $(200\,\mathrm{GeV})^2$. For $m_S \simeq 70$ GeV for instance, more than 75 % of the cross section arises from contributions with $q^2 < (200\,\mathrm{GeV})^2$. Therefore, the limits on λ_{HP} derived using our MC simulation agree with those presented in fig. 3.5 within the statistical MC uncertainty (~ 1 %), both below and above the Higgs threshold.

3.4. HL-LHC and HE-LHC Projections

We will now derive the projected upper limits on the Higgs-portal coupling λ_{HP} at the 14 TeV *HL-LHC* with an integrated luminosity of 3 ab^{-1} and the 27 TeV *HE-LHC* with 15 ab^{-1} of luminosity. Our projections are based on the sensitivity forecast for the search for invisible Higgs decays in VBF at the *HL-LHC* by *CMS* [121], which predicts a prospective 95 % CL upper bound on the invisible branching ratio of the Higgs boson of $\mathrm{Br}(h \to \mathrm{inv}) < 3.8$ %. This *CMS* limit is obtained from a cut-and-count analysis applying the cuts listed in the right column of table 3.1. The cuts resemble those used in the 13 TeV analysis [120], with a lower MET cut of $\not{E}_{\mathrm{T}} > 190$ GeV and an increased cut on the invariant mass of the leading jet pair, $M_{jj} > 2.5$ TeV.

We calculate the LO cross-section $\sigma_h(q^2)$ for off-shell Higgs production in VBF at center-of-mass energies of 14 TeV and 27 TeV with the same MC setup as used for our 13 TeV limits described in section 3.3.2, now using the *HL-LHC* detector card in Delphes. For the *HL-LHC* predictions we adopt cuts from the corresponding *CMS* study [121]. The same cuts are also applied for our *HE-LHC* study, with the invariant jet mass cut raised to $M_{jj} > 6$ TeV to benefit from the higher center-of-mass energy and increased luminosity (see section 3.4.1 for details). To incorporate gluon-inititiated production, NLO corrections, and the more refined detector simulation of *CMS*, our fiducial detector-level cross-section for on-shell Higgs production is again rescaled to match the *HL-LHC CMS* prediction of 16.3 fb [121]. Our MC simulation yields $\sigma_h(m_h^2) = 10.6\,\text{fb}$ at $\sqrt{s} = 14\,\text{TeV}$, corresponding to a rescaling factor of 1.54, which differs from the 13 TeV rescaling factor by 5 %. We take this as an indication that the rescaling factor does not vary substantially with the center-of-mass energy and the applied cuts, and therefore use the same factor to rescale our 27 TeV results.

The resulting 95 % CL projected *HL-LHC* upper limits on the signal strength $\mu_{\mathcal{H}}$ of additional Higgs bosons are depicted by the blue line in fig. 3.7. These bounds are derived based on the corresponding limit on the invisible branching ratio of the 125 GeV Higgs boson, $\text{Br}(h \to \text{inv}) < 3.8\,\%$ [121]. The red line denotes the projected sensitivity of the *HE-LHC*, using $\text{Br}(h \to \text{inv}) < 2.1\,\%$ obtained as explained in the following sections. The respective limits on the portal coupling λ_{HP} derived using eq. (3.13) are discussed in section 3.4.2 (cf. fig. 3.10).

3.4.1. Background Predictions and Systematic Uncertainties

While we could base our *HL-LHC* limits on the *CMS* predictions in ref. [121], there is no corresponding experimental projection for a 27 TeV machine. Therefore, to obtain the *HE-LHC* limit on the invisible Higgs branching ratio and the signal strength $\mu_{\mathcal{H}}$, as well as the corresponding bounds on the portal coupling λ_{HP} via eq. (3.13), further steps are required. In particular, we need to predict the number of background events, estimate the systematic uncertainty, and adapt the analysis to the detector setup (i.e. center-of-mass energy and luminosity).

We generate events for the dominant backgrounds $pp \to V + \text{jets}$ at LO, where V is either a Z or W boson decaying into two neutrinos ($Z \to \nu\nu$) or a neutrino-lepton-pair ($W \to \ell\nu$), respectively. The same MC tool-chain as for the signal simulation is used. Samples with two and three jets in the final state are merged employing the MLM matching procedure [161, 162]. For comparison with the *CMS* predictions at 14 TeV, we separately simulate processes in which the jets originate from EW interactions and quantum chromodynamics (QCD) radiation, neglecting interference effects. To improve our LO prediction, we also generate the background events at the *HL-LHC* and determine rescaling factors to match the *CMS* predictions in ref. [121] for each of the four contributions. Furthermore, the subleading background originating from top pair production (below 4 %) is obtained by rescaling the W+jets background, assuming similar kinematic distributions. The same factors are then used to rescale the background cross-sections at the *HE-LHC*.

Figure 3.8 shows the jet-pair invariant mass distribution of our simulated events for the Z+jets (blue), W+jets (red) and top (green) backgrounds at the *HL-LHC* (left) and *HE-LHC* (right). For the Z and W backgrounds, the EW (QCD) contributions are shown in deep (light) colors. Our prediction for the distribution of events for on-shell Higgs production in VBF is depicted by the solid thick line. In the *HL-LHC* case, the signal (thick) and total background (thin) predictions of *CMS* [121] are indicated by dashed lines. A good agreement between *CMS* and our (rescaled) simulation can be observed.

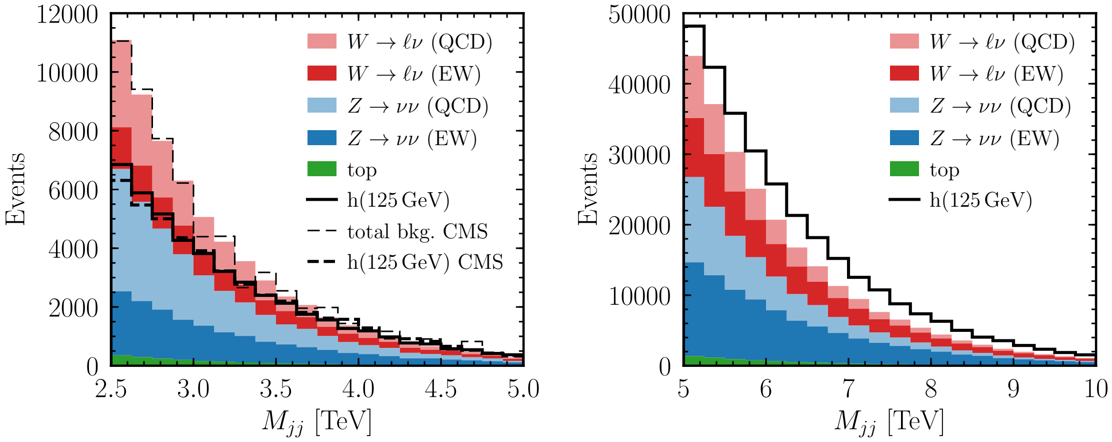

(a) 14 TeV *HL-LHC*, 3 ab^{-1} (b) 27 TeV *HE-LHC*, 15 ab^{-1}

Figure 3.8: Jet-pair invariant mass distribution of the main backgrounds (histograms) and on-shell Higgs production (solid line) at the *HL-LHC* (left) and *HE-LHC* (right). The thick and thin dashed lines in the left panel indicate the CMS prediction for the signal and total background, respectively.

Based on our predictions for the signal and background cross-sections, we derive the 95 % CL upper limit on the number of signal events in the Gaussian limit from the condition

$$\frac{S}{\sqrt{S+B+(\Delta_B^{\rm sys})^2}} = 1.96\,, \tag{3.14}$$

where S and B are the number of signal and background events, respectively, and $\Delta_B^{\rm sys}$ is the systematic uncertainty on the background. For the latter we employ a simple uncertainty model,

$$\Delta_B^{\rm sys} = \sqrt{f_1 B + (f_2 B)^2}\,, \tag{3.15}$$

consisting of one part scaling with $\sqrt{B}$, i.e. like a statistical Poisson uncertainty, and one part scaling with B, i.e. a luminosity-independent relative uncertainty, added in quadrature.

Equation (3.15) is motivated by data-driven background determination methods used in experimental analyses, as it is case in the 13 TeV analysis [120] and the 14 TeV projections [121] by *CMS*. The background originating from a Z boson produced in association with jets and decaying into neutrinos can for instance be obtained by measuring the same process with the Z boson decaying into charged leptons in a control region. If statistics dominated, the uncertainty on the number of events in the control region scales with the square root of the number of events, giving rise to the first contribution in eq. (3.15). A prefactor $f_1 > 1$ then corresponds to control regions with smaller statistics than the signal region. The second contribution in eq. (3.15) accounts for the systematic uncertainty on the transfer factors relating the event numbers in the control and signal regions.

As the two contributions to the uncertainty scale differently with the integrated luminosity, the *HL-LHC* limits on the invisible Higgs branching ratio for 300 fb^{-1}, 1 ab^{-1} and

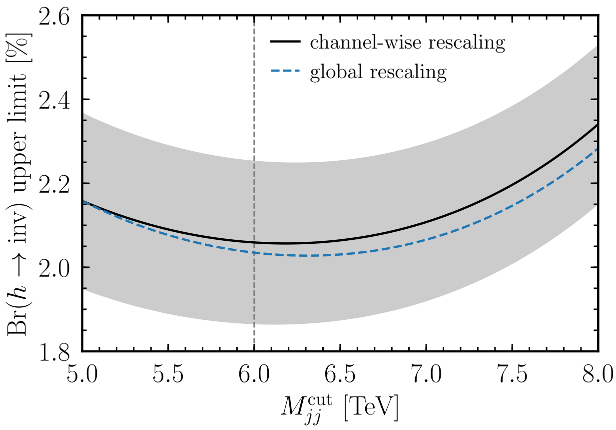

Figure 3.9: Projected 95 % CL upper limit on the invisible branching ratio of the 125 GeV Higgs boson at the *HE-LHC* as a function of the cut on the invariant mass M_{jj}^{cut} of the leading jet pair, using a channel-wise (solid black) and global (dashed blue) rescaling of the background. The gray band depicts the variation of the limit if the number of background events is changed by 10 %.

3 ab^{-1} provided in fig. 5b of ref. [121] can be used to extract the coefficients f_1 and f_2. This yields $f_1 = 1.5$ and $f_2 = 1.3\,\%$. We use these results to estimate the systematic uncertainty at the *HE-LHC*.

We now adapt the cut-and-count search from ref. [121] to the *HE-LHC* using eq. (3.14). Due to the increased center-of-mass energy, we find the biggest potential for gaining sensitivity in strengthening the cut on the invariant mass M_{jj} of the jet pair. Since the higher M_{jj} cut is also the most notable difference between the cuts used at 13 TeV and 14 TeV shown in table 3.1, we optimize this cut only and keep all other cuts as in the *HL-LHC* case. Although further improvement may be achieved applying a higher cut on the pseudo-rapidity difference of the leading jets, $|\Delta\eta_{jj}|$, we here refrain from doing so as we cannot estimate the detector performance at high η_j reliably.

Figure 3.9 shows the 95 % CL upper limit on the invisible branching ratio of the Higgs boson as a function of the jet-pair invariant-mass cut M_{jj}^{cut} at the *HE-LHC*, obtained from eq. (3.14) and based on the distributions depicted in fig. 3.8b. The black line indicates the limits obtained with the background event numbers rescaled for each contribution individually, as described above. For comparison, the dashed blue line shows the bound we get rescaling all background contributions with the same factor. This global rescaling factor is again determined from the 14 TeV simulations, requiring that the total number of background events coincides with the *CMS* prediction [121]. The boundaries of the gray band correspond to the limits (using channel-wise rescaling) if the systematic background uncertainty eq. (3.15) is varied by ±10 %.

The strongest limit on the invisible branching fraction is obtained for an invariant mass cut around $M_{jj}^{\mathrm{cut}} \simeq 6\,\mathrm{TeV} - 6.5\,\mathrm{TeV}$, with only marginal variation of the limit within this range. We therefore adopt $M_{jj} > 6\,\mathrm{TeV}$ to derive our limits, yielding a total of $\sim 120\,000$ background and $\sim 150\,000$ signal events for on-shell Higgs production with $\mathrm{Br}(h \to \mathrm{inv}) = 100\,\%$ at an integrated luminosity of 15 ab^{-1}. The relative systematic uncertainty on the background from eq. (3.15) is 1.4%, dominated by the luminosity-independent contribution f_2. From eq. (3.14) we obtain the 95 % CL upper limit on the invisible branching ratio of the Higgs boson $\mathrm{Br}(h \to \mathrm{inv}) < 2.1\,\%$.

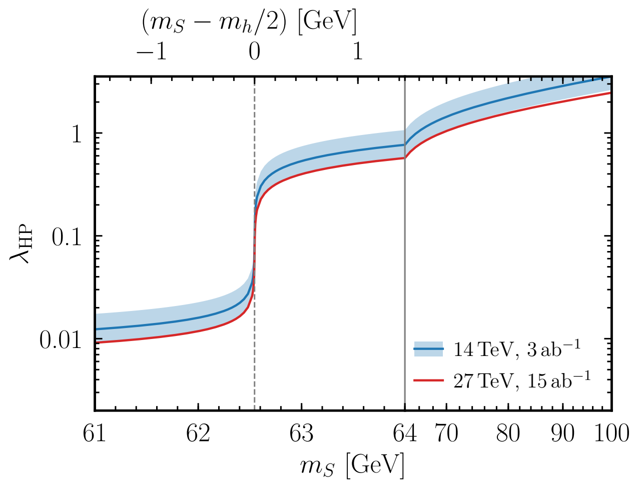

Figure 3.10: Projected 95 % CL upper limits on the Higgs-portal coupling $\lambda_{\rm HP}$ at the *HL-LHC* (blue curve) and *HE-LHC* (red curve) with integrated luminosities of 3 ab^{-1} and 15 ab^{-1}, respectively. The shaded band indicates the *HL-LHC* sensitivity if the systematic uncertainty on the background is multiplied or divided by two. Note that the plot changes from linear to logarithmic scaling of the abscissa at $m_S = 64$ GeV.

3.4.2. Sensitivity Projections

The *HL-LHC* and *HE-LHC* limits on the signal strength $\mu_{\mathcal{H}}$ of an additional Higgs boson with mass $m_{\mathcal{H}}$ that does not mix with the 125 GeV Higgs are indicated by the blue and red line in fig. 3.7. Figure 3.10 shows the corresponding 95 % CL upper limits on the Higgs-portal coupling $\lambda_{\rm HP}$ obtained from eq. (3.13). The blue curve corresponds to the prospective *HL-LHC* sensitivity assuming an integrated luminosity of 3 ab^{-1}, whereas the red line denotes the *HE-LHC* projection from 15 ab^{-1} of data. The shaded band shows the shift of the *HL-LHC* bound if the systematic uncertainty on the background is varied between half and twice the value obtained from eq. (3.15).

For DM masses less than $m_S \lesssim 61$ GeV, portal couplings around $\lambda_{\rm HP} \sim 0.01$ can be excluded. At the resonance $m_S \simeq m_h/2$, the *HL-LHC* can probe $\lambda_{\rm HP} \simeq 0.09$, whereas the *HE-LHC* may reach $\lambda_{\rm HP} \simeq 0.07$. Above the resonance, perturbative couplings $\lambda_{\rm HP} < \sqrt{4\pi}$ are accessible up to $m_S < 100$ GeV at the *HL-LHC* and $m_S < 120$ GeV at the *HE-LHC*, respectively.

As the uncertainty of our cut-and-count analysis is dominated by systematic uncertainties, only little improvement on the limits can be seen comparing the *HL-LHC* and *HE-LHC* results. Our projections can however be viewed as conservative. Stronger limits may be achieved if more a sophisticated analysis e.g. using shape or multivariate techniques is applied.

3.5. Conclusion

In this chapter we have presented a study of Higgs-portal DM at proton colliders, focusing on the VBF channel. We have derived the 95 % CL limits on the portal coupling $\lambda_{\rm HP}$ in the scalar singlet Higgs-portal model from current *LHC* data and provide forecasts for the sensitivity at the *HL-* and *HE-LHC*. Our observed and projected constraints are based on a 13 TeV search for invisible Higgs decays in VBF [120] and the corresponding *HL-LHC* simulation [121] by *CMS*. The limits incorporate an estimate of the systematic uncertainties achievable via data-driven background-determination methods. Particular care was taken to consistently derive the bounds for DM close to the Higgs resonance, requiring the use of the running Higgs-width in the propagator to avoid an unphysical enhancement of the DM production cross-section. While this enhancement would lead to an overestimation of the constraining power by 15 % – 30 % when the 13 TeV *LHC* limits are considered, the effect is negligible for the size of couplings constrained by the *HL*- or *HE-LHC*.

The 95 % CL upper limits on the invisible branching ratio of the Higgs boson provided by *CMS* are $\mathrm{Br}_{\mathrm{inv}} < 33\,\%$ from current data [120] and $\mathrm{Br}_{\mathrm{inv}} < 3.8\,\%$ for the *HL-LHC* [121]. For the *HE-LHC* we obtain the corresponding limit of $\mathrm{Br}_{\mathrm{inv}} < 2.1\,\%$. Note that the projected limits are based on cut-and-count analyses and may be improved if more sophisticated methods are employed. Using $35.9\,\mathrm{fb}^{-1}$ of pp collisions recorded at $\sqrt{s} = 13\,\mathrm{TeV}$ we can establish an upper limit on the portal coupling in the singlet scalar model around $\lambda_{\mathrm{HP}} \simeq 0.04$ below the resonance (at $m_S = 61\,\mathrm{GeV}$), while the limit rapidly degrades when masses above the resonance are considered, excluding for instance $\lambda_{\mathrm{HP}} \gtrsim 2.5$ at $m_S = 64\,\mathrm{GeV}$. At $m_S = m_h/2$, we obtain an upper bound of $\lambda_{\mathrm{HP}} \simeq 0.3$. The *HL-LHC* with $3\,\mathrm{ab}^{-1}$ improves these limits by a factor of ~ 0.3, and we can gain another 25 % in sensitivity at the *HE-LHC* with $15\,\mathrm{ab}^{-1}$. Currently, perturbative couplings $\lambda_{\mathrm{HP}} \leq \sqrt{4\pi}$ can be probed for DM masses below $m_S \lesssim 67\,\mathrm{GeV}$, whereas the *HL*- and *HE-LHC* may reach $m_S \lesssim 100\,\mathrm{GeV}$ and $m_S \lesssim 120\,\mathrm{GeV}$, respectively.

We also present our limits as upper bounds on the signal strengh for the invisible decay of an additional Higgs boson with mass $m_{\mathcal{H}}$ that is produced SM-like and does not mix with the 125 GeV Higgs. The corresponding results allow for a simple reinterpretation of the search for other models with invisible particles coupled to the Higgs boson only. This is illustrated in appendix 3.A for the case of Higgs portal models with different spin-choices for the DM field. Our numerical results are available in digital form as supplementary material to the publication [4].

Appendix of Chapter 3

Appendix 3.A. Reinterpretation for Other Higgs-Portal Models

Based on eq. (3.13) and the limits on the signal strength $\mu_{\mathcal{H}}$ shown in fig. 3.7, our results can be easily reinterpreted for any other DM model in which the DM is produced from an s-channel Higgs boson exclusively, simply by replacing Γ_{inv} in eq. (3.13) by the respective expression for the invisible decay width of an off-shell Higgs boson. To conclude this chapter, we therefore here present limits on the portal coupling for other simple Higgs-portal models with different types of DM fields. In particular, we consider DM described by a Majorana fermion χ, a vector field X^μ, and an anti-symmetric rank-two tensor field[6] $\mathcal{B}^{\mu\nu}$, all singlets under the SM gauge groups. Further details on the models can be found in refs. [134, 163, 165]. The respective portal interactions are given by

$$\mathcal{L}_{\text{HP}}^{\chi} = -\frac{\lambda_{\text{HP}}}{\Lambda}\, H^\dagger H\, \bar{\chi}\chi\,, \tag{3.16a}$$

$$\mathcal{L}_{\text{HP}}^{X} = -\frac{\lambda_{\text{HP}}}{2}\, H^\dagger H\, X^\mu X_\mu\,, \tag{3.16b}$$

$$\mathcal{L}_{\text{HP}}^{\mathcal{B}} = -\frac{\lambda_{\text{HP}}}{2}\, H^\dagger H\, \mathcal{B}^{\mu\nu}\mathcal{B}_{\mu\nu}\,. \tag{3.16c}$$

We here neglect other possible interactions with SM fields such as a pseudo-scalar coupling $i\,\bar{\chi}\gamma_5\chi\, H^\dagger H$, or couplings to the hypercharge field strength tensor $F^{\mu\nu}$. The corresponding decay rates of the Higgs boson into a DM pair are [134, 165]

$$\Gamma\left(h \to \chi\bar{\chi}\right) = \frac{\lambda_{\text{HP}}^2 v^2}{4\pi\,\Lambda^2}\, m_h \left(1 - 4\,\frac{m_\chi^2}{m_h^2}\right)^{\frac{3}{2}}\,, \tag{3.17a}$$

$$\Gamma\left(h \to XX\right) = \frac{\lambda_{\text{HP}}^2 v^2}{128\pi\, m_h}\, \frac{m_h^4 - 4\, m_h^2\, m_X^2 + 12\, m_X^4}{m_X^4} \sqrt{1 - 4\,\frac{m_X^2}{m_h^2}}\,, \tag{3.17b}$$

$$\Gamma\left(h \to \mathcal{B}\mathcal{B}\right) = \frac{\lambda_{\text{HP}}^2 v^2}{16\pi\, m_h}\, \frac{m_h^4 - 4\, m_h^2\, m_{\mathcal{B}}^2 + 6\, m_{\mathcal{B}}^4}{m_{\mathcal{B}}^4} \sqrt{1 - 4\,\frac{m_{\mathcal{B}}^2}{m_h^2}}\,. \tag{3.17c}$$

In contrast to the scalar DM model discussed before, the models in eq. (3.16) are not UV complete. They are non-renormalizable, as apparent in the fermion case from the dimension of the portal-operator in eq. (3.16a), and violate perturbative unitarity

[6] We here consider the transverse mode of the anti-symmetric rank-two tensor, which can be used to describe a massive spin-one resonance. Compared to the other Higgs-portal models studied here, this model has the additional feature that no $\mathbb{Z}_2$ symmetry is required to stabilize the DM candidate. See refs. [163, 164] and references therein for further details.

at high energies. To restore renormalizability and unitarity, additional fields need to be introduced [166–170]. As a consequence, the invisible decay rates grow rapidly with q^2, and the integral in eq. (3.4) or eq. (3.13) receives large contributions from off-shell Higgs momenta $q^2 \gg (2m_{\mathrm{DM}})^2$, in particular in the vector and tensor case. In UV completions of the models, these unitarity violating contributions[7] are expected to be suppressed, e.g. via destructive interference with additional degrees of freedom (DOFs) that unitarize the theory. We therefore impose an upper cut-off on the q^2 integral in eqs. (3.4) and (3.13) at the perturbative unitarity bound from Higgs-to-DM scattering, $hh \to XX \,/\, \mathcal{BB}$. For vector DM we use $q^2 < 32\pi m_X^2/\lambda_{\mathrm{HP}}$ [172], and for the tensor field we obtain $q^2 < 16\pi m_X^2/\lambda_{\mathrm{HP}}$ following the conventions of ref. [163]. In the fermion case, no strong dependence of the portal-coupling limits on the upper bound of the integral is observed.

The 95 % CL upper limits on the portal couplings in the effective Higgs-portal models are shown in fig. 3.11. The vector and tensor model are displayed in the left and right lower panel, whereas the fermion case is shown in the upper right corner. For comparison, we also show the singlet scalar model on the upper left. The black lines depict the current limits from the *CMS* shape analysis [120], whereas the blue and red curves denote the projected sensitivity at the *HL-LHC* and *HE-LHC* with $3\,\mathrm{ab}^{-1}$ and $15\,\mathrm{ab}^{-1}$ of integrated luminosity, respectively. For the current bound, we also show the uncertainty on the signal projections as a gray band. To illustrate the dependence of the limits on the upper cut-off on the off-shell Higgs momentum, we also indicate the corresponding limits applying a cut-off of $q^2 < 1\,\mathrm{TeV}$ and without cut-off by the dashed and dotted light-red curves for *HE-LHC* case.

Note that the lines indicating the 13 TeV limits in the vector and tensor model end at DM masses around $\sim 70\,\mathrm{GeV}$. This is caused by the running width dominating the propagator for large portal couplings λ_{HP}. The cross section in eq. (3.4) then reaches a maximum, and a further increase of λ_{HP} leads to a suppression of the cross section. To obtain reliable limits in this parameter region, a more detailed study would be required, taking into account the high-energy behavior of the models.

[7] Note that the running width in the Higgs propagator also has a unitarizing effect as it suppresses large-q^2 contributions when the total Higgs-width dominates the propagator. This has for instance been exploited in the context of the Higgsplosion mechanism in ref. [171].

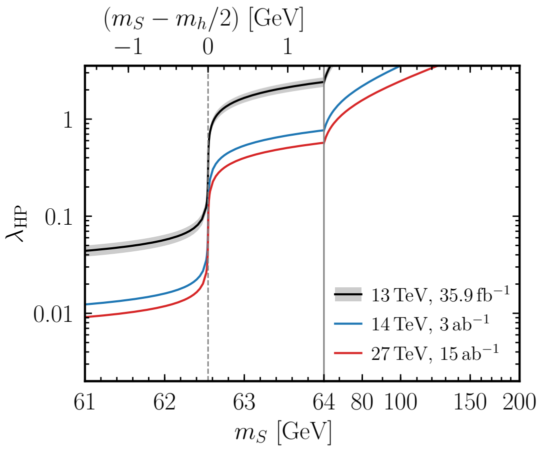

(a) scalar DM

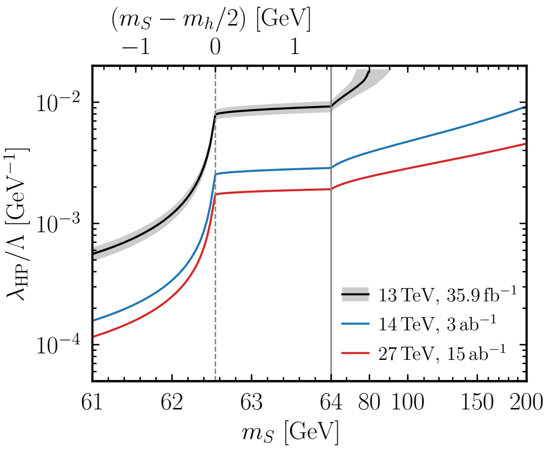

(b) Majorana fermion DM

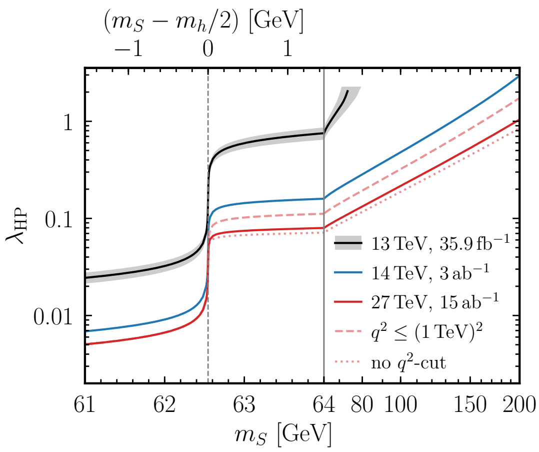

(c) vector DM

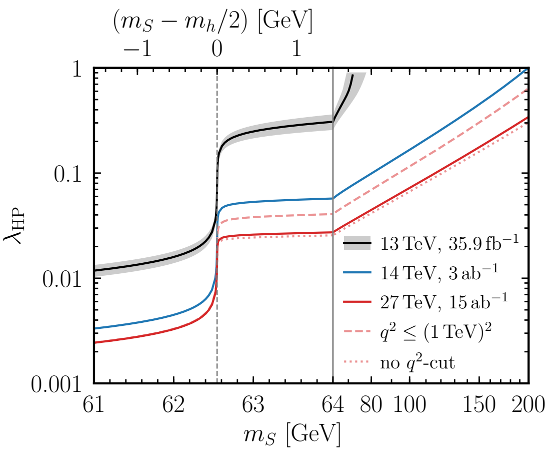

(d) tensor DM

Figure 3.11: Current 95 % CL upper limits (black, with gray band indicating the signal uncertainty) as well as *HL-LHC* (blue) and *HE-LHC* (red) projected sensitivity on the portal coupling $\lambda_{\rm HP}$ in Higgs-portal models with different types of DM fields. For the vector and tensor case in the lower panel, the dashed and dotted light-red curves depict the *HE-LHC* limits if the upper bound of the integral in eq. (3.13) is set to 1 TeV and ∞, respectively, whereas the solid lines cut the integral at the unitarity bound.

4. Discovering the $h \to Z\gamma$ Decay in $t\bar{t}$ Associated Production

The following chapter is based on the work [3] in collaboration with Florian Goertz, Pedro Schwaller and Valentin Tenorth. The chapter resembles the publication in structure and logic.

In continuation of our exploration of collider probes of physics beyond the Standard Model (BSM), we now indirectly constrain new physics via its contribution to the decay of the Higgs boson into a Z boson and a photon. Nowadays, almost a decade after the first observation of the Higgs boson in 2012 [16, 17], the data collected in proton-proton collisions at the *CERN LHC* has provided measurements of various Higgs properties, in particular many of its production and decay modes. The $h \to Z\gamma$ decay considered in this chapter has however not been measured so far. It furnishes a promising channel for the determination of spin [173, 174] and CP [175, 176] properties of the Higgs, and can potentially probe new physics that could be hidden in other observables [176–184].

Similar to the decay into a pair of photons, which, despite its low branching ratio of $\mathrm{Br}(h \to \gamma\gamma) = 2.27 \times 10^{-3}$ [156], was one of the primary channels in the Higgs discovery, the $h \to Z\gamma$ decay is a loop-induced process, mainly mediated by top and W loops. Although the corresponding branching fraction, $\mathrm{Br}(h \to Z\gamma) = 1.54 \times 10^{-3}$ [156], amounts to roughly two thirds of the diphoton one, this decay is significantly harder to observe as the Z boson decays predominantly to hadrons and therefore suffers from large backgrounds at the *LHC*. An accurate reconstruction of the Z boson with a relatively low background is possible if leptonic decays are considered, however at the price of the additional factor $\mathrm{Br}(Z \to \ell^+\ell^-) = 6.67\,\%$ [68], where here and henceforth ℓ denotes an electron or muon. As a consequence, even the most recent search for the $h \to \ell^+\ell^-\gamma$ decay by *ATLAS*, using $139\,\mathrm{fb}^{-1}$ of data collected at a center-of-mass energy of $13\,\mathrm{TeV}$, only provides an upper bound on the cross section for $h \to Z\gamma$ of 3.6 times the Standard Model (SM) prediction [185]. At $\sqrt{s} = 14\,\mathrm{TeV}$ and with an integrated luminosity of $100\,\mathrm{fb}^{-1}$, a significance of 2σ can be reached [173], while even at the *HL-LHC* with $3\,\mathrm{ab}^{-1}$ a 5σ observation will be challenging [186]. A future electron-positron collider, such as the FCC_{ee} with $\sqrt{s} = 240\,\mathrm{GeV}$ and $10\,\mathrm{ab}^{-1}$ luminosity, may reach a significance of 3.6σ [187].

In this chapter we entertain the $pp \to t\,\bar{t}\,h$ production mode to search for the $h \to Z\gamma$ decay, taking advantage of the presence of the top-pair in the final state to enhance the signal-to-background ratio. The observation of top-pair associated Higgs-production has been established recently [188–190], motivating its further use in collider studies, such as the search for invisible Higgs decays [191] or the $h \to Z\gamma$ decay considered here. Due to the large top-Yukawa-coupling, only a modest penalty is payed when radiating a Higgs boson from a top-quark pair. Top-associated Higgs production therefore provides a significantly larger signal-to-background ratio compared to the dominant production from gluon-fusion for instance, rendering it a promising channel in searches for rare Higgs decays.

On the other hand, as the top quark is the heaviest particle in the SM, a large partonic center-of-mass energy is required to produce the $t\,\bar{t}\,h$ state. The corresponding inclusive cross-section for top-associated Higgs production in proton collisions is therefore roughly two orders of magnitude lower then the $pp \to h$ channel from gluon-fusion. Hence, a high integrated luminosity is required to observe the $h \to Z\gamma$ decay in this channel, impeding its potential in searches based on currently available data.

In the following, we thus investigate the potential to measure $h \to Z\gamma$ with a leptonically decaying Z in top-pair associated production at the *HL-LHC* with an integrated luminosity of $3\,\mathrm{ab}^{-1}$, as well as the 27 TeV *HE-LHC* and a 100 TeV hadron collider such as the FCC_{hh} with luminosities of $15\,\mathrm{ab}^{-1}$ and $30\,\mathrm{ab}^{-1}$, respectively. We first provide a rough estimate of the expected number of signal and background events at the *HL-LHC* in section 4.1. Subsequently, we setup a simple cut-and-count analysis and calculate the expected significance based on Monte Carlo (MC) event simulations in section 4.2, also considering projections for the *HE-LHC* and FCC_{hh}. Finally, in section 4.3, we examine constraints on new physics via the corresponding limits on the $hZ\gamma$ coupling. We provide a summary of this chapter in section 4.4.

4.1. HL-LHC Sensitivity Estimate

The total cross-section for top-pair associated Higgs production at $\sqrt{s} = 14\,\mathrm{TeV}$ including quantum chromodynamics (QCD) and electroweak (EW) next-to-leading order (NLO) corrections is [156]

$$\sigma(pp \to t\bar{t}h) = 613\,\mathrm{fb}\ {}^{+6.0\,\%}_{-9.2\,\%}\ (\text{scale})\ \pm 3.5\,\%\ (\text{PDF} + \alpha_s)\,, \tag{4.1}$$

where the first uncertainty reflects the change of the cross section when varying the factorization and renormalization scales between half and twice the central value, and the second one combines the uncertainty on the parton distribution functions (PDFs) and strong coupling strength. Assuming an integrated luminosity of $3\,\mathrm{ab}^{-1}$, and taking the branching ratios [68, 156]

$$\mathrm{Br}(h \to Z\gamma) = 1.54 \times 10^{-3} \qquad \text{and} \qquad \mathrm{Br}(Z \to \ell^+\ell^-) = 6.67\,\% \tag{4.2}$$

for the Higgs and Z decays, we obtain a total of $S_0 \approx 190$ signal events.

While the decay products of the Higgs boson, i.e. the photon and the electron or muon pair from the Z decay, can be reconstructed efficiently, requirements imposed to tag top-pair-associated production will degrade the signal count. To retain an observable number of events after selection cuts have been applied, the analysis needs to be designed as inclusive as possible. For our first estimate, let us here assume a selection efficiency of $10\,\% - 15\,\%$, in the same ballpark as the corresponding efficiency in the diphoton case ($\sim 12\,\%$ [192]). We therefore expect roughly $S = (20 - 30)$ signal events in the analysis.

The dominant irreducible background is $t\bar{t}Z$ production with the radiation of an additional photon. The corresponding cross section at $\sqrt{s} = 14\,\text{TeV}$ including NLO QCD (but not EW) corrections is

$$\sigma(pp \to t\bar{t}Z\gamma) = 9.3\,\text{fb}\ {}^{+10.4\,\%}_{-11.5\,\%}\ (\text{scale})\ \pm 3.4\,\%\ (\text{PDF} + \alpha_s)\,, \tag{4.3}$$

where we used MadGraph5 [153] for the calculation and applied $p_T^\gamma > 10\,\text{GeV}$ and $|\eta_\gamma| < 4$ at generator-level. This amounts to $B_0 \approx 1860$ background events (with the Z boson decaying leptonically) at the *HL-LHC*, i.e. roughly an order-of-magnitude more than the number signal events.

In addition, further background events originate from reducible backgrounds, where we expect the most important contribution to be $pp \to t\bar{t}Zj$ with the jet misidentified as a photon. This misidentification may for instance occur if most of the jet energy is carried by a π^0 or η meson decaying to a collimated pair of photons. In an experimental analysis, this background will be determined using data-driven methods, e.g. applying a two-dimensional side-band method based on the photon isolation criterion [193], or floating the background normalization and fitting the invariant mass distribution of the reconstructed $Z\gamma$ pair below and above $M_{Z\gamma} \sim m_h$. Since a reliable simulation of this background is challenging, we here simply enhance the number of background events by 50 % to account for non-simulated backgrounds. Assuming the same selection efficiency as for the signal, we obtain (280 – 420) background events. We here neglect further background contributions that arise depending on the respective top-pair decay channel considered, as we expect these to be sub-leading.

Due to the extremely narrow width of the Higgs boson, $\Gamma_h = 4.1\,\text{MeV}$ [156], the invariant mass distribution of the $Z\gamma$ pair in the signal events is sharply peaked at the Higgs mass, whereas the background has a smooth distribution. To obtain a large signal-to-background ratio we therefore restrict the invariant mass to lie within a 10 GeV window around the Higgs mass, $120\,\text{GeV} < M_{Z\gamma} < 130\,\text{GeV}$. While the signal is basically unaffected by this cut, the background is reduced to roughly 7 % of its original size, based on the corresponding distribution in the MadGraph events. We therefore expect $B = (20 - 30) \approx S$ background events, resulting in a significance of $S/\sqrt{B} \simeq 4.5\,\sigma - 5.5\,\sigma$. Further improvement of the sensitivity compared to this simple cut-and-count analysis may be achieved fitting the invariant mass distribution in the signal-plus-background and background-only hypothesis. The $t\bar{t}h$ channel therefore provides promising prospects for an observation of the $h \to Z\gamma$ decay.

4.2. Analysis

In this section we corroborate our estimated sensitivity, setting up a toy analysis for the *HL-LHC* using MC simulations. The analysis in section 4.2.1 focuses on the semi-leptonic top-pair decay channel, with $t \to bjj$ and $\bar{t} \to \bar{b}\ell^-\bar{\nu}_\ell$ or vice versa. In section 4.2.2, our results are then extrapolated to also include the all-leptonic and all-hadronic channel, assuming the same efficiency as obtained for our analysis in the semi-leptonic case. We extend the projections to the *HE-LHC* and *FCC$_{hh}$* in section 4.2.3.

4.2.1. Semi-Leptonic Channel

We generate events at the *HL-LHC* with $\sqrt{s} = 14\,\text{TeV}$ and an integrated luminosity of $3\,\text{ab}^{-1}$ for the signal process $pp \to t\bar{t}h$ and the irreducible background $pp \to t\bar{t}Z\gamma$ (without the corresponding Higgs contribution) at NLO in QCD using MadGraph5_aMC@NLO [153, 194]. The renormalization and factorization scale are set to $\mu_R = \mu_F = m_t + m_h/2$ [156]. We use the PDF4LHC15 NLO PDF set [195] accessed via the LHAPDF6 interface [155]. Our inclusive cross-section reproduces the corresponding NLO QCD prediction of 603 fb in ref. [156]. The subsequent $h \to Z\gamma$ and $Z \to \ell^+\ell^-$ decays, as well as parton-shower simulation and hadronization are performed in Pythia8 [157], assuming the branching ratios in eq. (4.2). The events are then passed to Delphes v3.4.2 [158] for detector simulation with the *HL-LHC* detector card. Jets are reconstructed in FastJet 3 [159] using the anti-k_t algorithm [160] with $R = 0.4$, imposing $p_T > 25\,\text{GeV}$ and $|\eta| < 2.5$.

Our analysis for the semi-leptonic channel is loosely based on ref. [192], which is a 8 TeV cut-and-count search for $h \to \gamma\gamma$ in top-pair associated production. Since we expect two leptons (electrons or muons) from the Z boson decay and one lepton from the leptonically decaying (anti-)top quark, we require exactly three leptons satisfying the reconstruction criteria $p_T > 15\,\text{GeV}\,(10\,\text{GeV})$ and $|\eta| < 2.47\,(2.7)$ for electrons (muons). We further require at least three jets with $p_T > 30\,\text{GeV}$ and $|\eta| < 2.5$ and impose a minimum missing transverse energy (MET) cut of $\not{E}_\text{T} > 20\,\text{GeV}$. Furthermore, we demand the presence of at least one b-tagged jet, as well as at least one photon with $p_T > 15\,\text{GeV}$ and $|\eta| < 2.37$. For the reconstruction of the Z boson, a pair of opposite-sign same-flavor (OSSF) leptons with an invariant mass $76\,\text{GeV} < M_{\ell\ell} < 106\,\text{GeV}$ is required. This lepton pair is then used along with the hardest photon to reconstruct the Higgs boson. If more than one such lepton pair is found, the pair with the invariant mass closest to the Z mass is used. To suppress the irreducible background we finally restrict the invariant mass of the $\gamma\,\ell^+\ell^-$ system to a 10 GeV window around the Higgs mass, $120\,\text{GeV} < M_{\gamma\ell\ell} < 130\,\text{GeV}$.

Table 4.1 lists the cut-flow for the signal and background events. The spectrum of the invariant mass $M_{\gamma\ell\ell}$ of the reconstructed Higgs boson after applying the selection cuts (except for the cut on $M_{\gamma\ell\ell}$) are shown in fig. 4.1. The signal is broken down into the respective contributions with all-leptonic (light orange), semi-leptonic (orange) and all-hadronic (red) decays of the $t\bar{t}$ pair, and stacked on top of the irreducible background (blue). It can be seen that the analysis indeed picks out the semi-leptonic channel with negligible contamination from the other top-pair decays. The signal is sharply peaked around $M_{\gamma\ell\ell} \approx m_h$, so that we obtain a signal-to-background ratio of $S/B \simeq 1$ after cutting on $M_{\gamma\ell\ell}$. Note that the signal-to-background ratio remains constant during the cut flow except for the last cut on the mass of the reconstructed Higgs boson, as these cuts are meant to suppress the reducible backgrounds which we did not simulate.[1] The corresponding selection efficiencies for signal and background in the semi-leptonic channel are $\epsilon_N = N_\text{final}/(\text{Br(semi-lept.)} \times N_\text{initial})$, where $N = S, B$ are the number of signal and

[1] We however confirmed in a leading order (LO) simulation that the reducible backgrounds $t\bar{t}W^\pm\gamma$, $W^\pm b\bar{b}jZ\gamma$, and $t\bar{t}t\bar{t}\gamma$ are negligible, as well as that the background $tZ\gamma jj$ ($\sim 30\,\%$ of the irreducible background) is within the 50 % enhancement used in our naive estimate and the extrapolation to all top-channels.

Cut	14 TeV, 3 ab^{-1} S	B	27 TeV, 15 ab^{-1} S	B	100 TeV, 30 ab^{-1} S	B
Initial	186	1862	4.4k	47k	112k	1.3M
$N(\ell) = 3$	25	273	539	6.2k	16k	210k
$N(j) \geq 3,\ p_T^j > 30\,\text{GeV}$	15	170	344	4.1k	12k	160k
$\not{E}_\text{T} > 20\,\text{GeV}$	14	160	322	3.9k	11k	150k
$N(b) \geq 1$	12	137	276	3.3k	10k	140k
$N(\gamma) \geq 1,\ p_T^\gamma > 15\,\text{GeV}$	8.1	83	180	2.0k	6.7k	84k
Z-reconstruction	7.6	80	166	1.9k	6.3k	82k
Higgs-reconstruction	7.3	5.2	160	101	6.1k	3.2k

Table 4.1: Number of signal and background events after each selection cut for the *HL-LHC* (14 TeV, 3 ab^{-1}), *HE-LHC* (27 TeV, 15 ab^{-1}) and *FCC$_{hh}$* (100 TeV, 30 ab^{-1}).

background events taken from table 4.1, and Br(semi-lept.) = 28.8 % [68] is the branching ratio into semi-leptonic decays of the top-pair. We obtain $\epsilon_S = 14\,\%$ and $\epsilon_B = 0.97\,\%$.

4.2.2. All-Hadronic and All-Leptonic Channel

Let us now assume that the selection efficiencies are the same for all top channels. Taking the initial number of signal and background events from table 4.1 we then arrive at the total numbers of

$$S = 186 \times \epsilon_S \approx 25 \qquad \text{and} \qquad B = 1.5 \times 1862 \times \epsilon_B \approx 27\,. \tag{4.4}$$

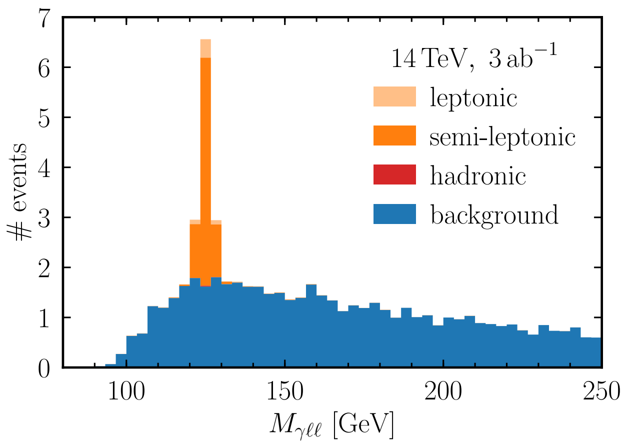

Figure 4.1: Invariant mass distribution of the photon and OSSF lepton-pair system (before Higgs-reconstruction cut) for the background (blue) and signal events with fully-hadronic (red, not visible), semi-leptonic (orange) and fully-leptonic (light orange) decays of the top-quark pair at the *HL-LHC*.

In other words, we enhance the final numbers in table 4.1 by a factor 1/Br(semi-lept.) to mimic an analysis that also considers the all-leptonic and all-hadronic decay channels. In addition, we here emend the background by 50 % to account for reducible backgrounds, such as $pp \to t\bar{t}Zj$. The result agrees well with our estimate from section 4.1.

Considering the statistical uncertainty $\Delta B = \sqrt{B} \approx 5$ only, our cut-and-count analysis establishes a significance of $S/\sqrt{B} \approx 4.8$ for the observation of the $h \to Z\gamma$ decay in $t\,\bar{t}$ associated production alone. Top-pair associated Higgs production may therefore contribute significantly to establish an experimental observation of this Higgs decay. The sensitivity may be further improved employing top-reconstruction algorithms based on boosted decision trees, as used in the observation of top-associated Higgs production in other Higgs decay channels [188–190], with which hadronic top-decays can be reconstructed at high efficiency. Our results may therefore be seen as a conservative estimate, even in the case that the non-simulated background processes are underestimated.

4.2.3. Predictions for 27 and 100 TeV Colliders

Next we derive the corresponding prospective signficance at the 27 TeV *HE-LHC* [196] and the 100 TeV *FCC*$_{hh}$ [197] with the respective integrated luminosities of 15 ab^{-1} and 30 ab^{-1}. Events are simulated with the same MC setup as in section 4.2.1, using the *HL-LHC* (*FCC*$_{hh}$) Delphes detector card for the 27 TeV (100 TeV) collider. The signal cross-sections for $pp \to t\bar{t}h$ production are 2.9 pb at the *HE-LHC* [198] and 33 pb at the *FCC*$_{hh}$ [199], which we reproduce in our simulations. For the irreducible $t\,\bar{t}\,Z\,\gamma$ background we obtain cross sections of 46 fb (at $\sqrt{s} = 27$ TeV) and 670 fb (at $\sqrt{s} = 100$ TeV), respectively, again requiring $p_T > 10$ GeV and $|\eta| < 4$ for the photons in MadGraph.

For simplicity and comparability with the *HL-LHC* case, we apply the same selection cuts as in section 4.2.1 for the analysis of the semi-leptonic top-pair channel. The resulting event numbers are listed in the respective columns of table 4.1, and the $M_{\gamma\ell\ell}$ invariant mass spectra are depicted in fig. 4.2. In the semi-leptonic channel, we obtain signal and background efficiencies of $\epsilon_S = 13\,\%$ (19 %) and $\epsilon_B = 0.75\,\%$ (0.85 %) at the *HE-LHC* (*FCC*$_{hh}$). Enhancing the background by 50 % and extrapolating to the other top decays we therefore expect $S \approx 555$ and $B \approx 526$ at the *HE-LHC* over all channels. For the *FCC*$_{hh}$ we obtain $S \approx 21\,000$ and $B \approx 17\,000$ in total.

4.3. Constraints on New Physics

Measurements of (or limits on) the $h \to Z\gamma$ decay can be used to indirectly constrain new physics via its effects on the decay rate. Since the $h\,Z\,\gamma$ coupling is already loop-suppressed in the SM, it provides particularly promising prospects for the observation of BSM effects, e.g. from additional heavy states running in the loop.

Within the effective field theory (EFT) framework, the impact of new physics on SM observables can be parameterized in terms of higher-dimensional operators. Let us here

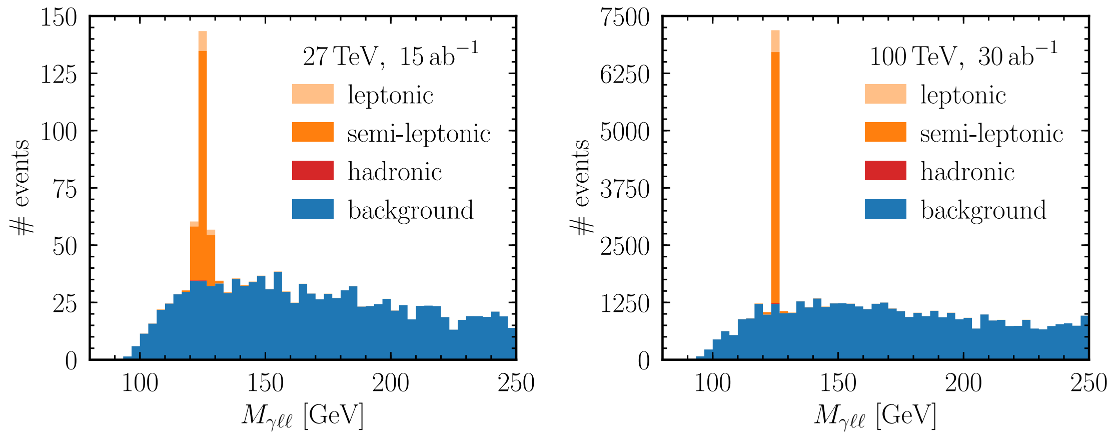

(a) *HE-LHC* (b) FCC_{hh}

Figure 4.2: Same as fig. 4.1 for the *HE-LHC* (left) with a center-of-mass energy of 27 TeV and an integrated luminosity of 15 ab^{-1}, as well as the FCC_{hh} (right) with 100 TeV and 30 ab^{-1} of luminosity.

neglect possible new physics in the production of the Higgs boson and consider the leading dimension-six operators relevant for the $h \to Z\gamma$ decay rate,

$$\begin{aligned} \mathcal{O}_{HW} &= \frac{i\,g_2}{m_W^2}\,(D^\mu H)^\dagger\,\sigma_a\,(D^\nu H)\;W^a_{\mu\nu}\,, \\ \mathcal{O}_{HB} &= \frac{i\,g_1}{m_W^2}\,(D^\mu H)^\dagger\,(D^\nu H)\;B_{\mu\nu}\,, \\ \mathcal{O}_\gamma &= \frac{g_1^2}{m_W^2}H^\dagger H\,B_{\mu\nu}B^{\mu\nu}\,, \end{aligned} \tag{4.5}$$

where H is the SM Higgs doublet, $W^a_{\mu\nu}$ and $B_{\mu\nu}$ are the weak and hypercharge field-strength tensors, and g_2 and g_1 are the respective gauge couplings. We here neglect CP odd operators. After electroweak symmetry breaking (EWSB) we can expand the Higgs field around its vacuum expectation value (VEV), $\langle H\rangle = (0, v/\sqrt{2})^T$. The operators in eq. (4.5) then contribute to the tree-level term

$$\mathcal{L} \supset c_{Z\gamma}\frac{h}{v}Z_{\mu\nu}F^{\mu\nu}\,, \tag{4.6}$$

where h is the physical Higgs mode, $F_{\mu\nu}$ is the electromagnetic (EM) field strength tensor, and $Z_{\mu\nu}$ the equivalent for the Z boson. In terms of the Wilson coefficients c_{HW}, c_{HB} and c_γ of the dimension-six operators,[2] the $c_{Z\gamma}$ coupling is given by

$$c_{Z\gamma} = -\tan\theta_W\,\Big[(c_{HW} - c_{HB}) + 8\sin^2\theta_W\,c_\gamma\Big] \tag{4.7}$$

with θ_W denoting the weak mixing angle.

[2] We amend the SM Lagrangian by the terms $\Delta\mathcal{L} = c_{HW}\mathcal{O}_{HW} + c_{HB}\mathcal{O}_{HB} + c_\gamma\mathcal{O}_\gamma$.

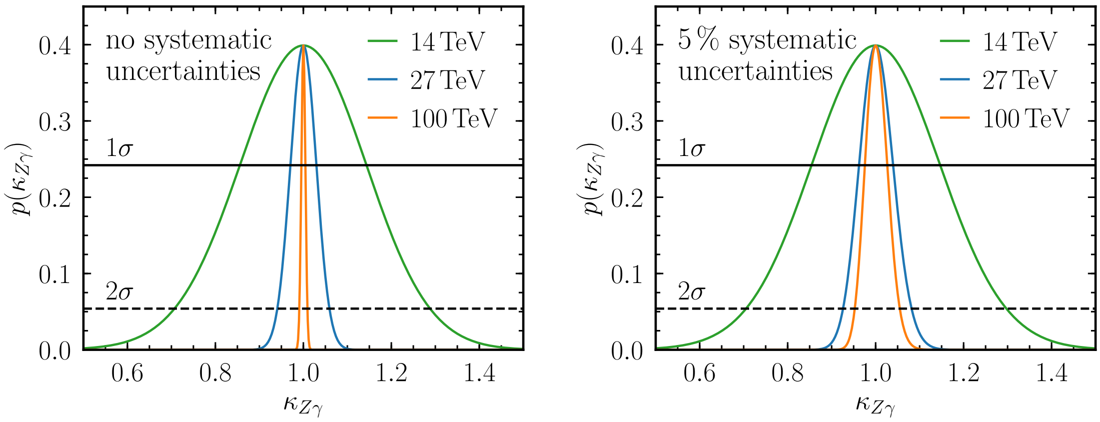

(a) without systematic uncertainty

(b) 5 % systematic uncertainty

Figure 4.3: Expected p-value for $\kappa_{Z\gamma}$ at the *HL-LHC* (green), *HE-LHC* (blue) and FCC_{hh} (orange), assuming that the SM value is observed. In the left panel systematic uncertainties are neglected, whereas the right panel includes a 5 % uncertainty.

To constrain the new physics effects in the $h \to Z\gamma$ decay, we employ the so-called coupling strength modifier or κ framework [200]. In this framework, the absolute value of each coupling of the Higgs boson is modified by a factor κ_i, while the corresponding tensor structure is assumed to be SM-like. The SM is therefore reproduced if all $\kappa_i = 1$. Experimentally the coupling modifiers can be extracted from the ratios of production cross-sections or decay rates to the respective SM prediction. In particular, the squared modifier of the $h\,Z\,\gamma$ coupling can be obtained from the $h \to Z\gamma$ decay rate and expressed in terms of the new-physics coupling $c_{Z\gamma}$ in eq. (4.7) as [179]

$$\kappa_{Z\gamma}^2 = \frac{\Gamma(h \to Z\gamma)}{\Gamma(h \to Z\gamma)_{\text{SM}}} \simeq 1 - 0.146 \frac{4\pi}{\alpha \cos\theta_W} c_{Z\gamma} \,, \tag{4.8}$$

where α is the EM fine-structure constant and the second equality only holds for small $c_{Z\gamma}$. Again, we neglect modifications of the production cross-section.

We now obtain our limits on the coupling modifier $\kappa_{Z\gamma}$ from the $h \to Z\gamma$ decay in $t\bar{t}$ associated Higgs production as follows. The predicted total number of events for a given value of $\kappa_{Z\gamma}$ is $N(\kappa_{Z\gamma}) = \kappa_{Z\gamma}^2 S + B$, where S and B are the SM signal and background event counts over all top decays, given by eq. (4.4) in the *HL-LHC* case or by the respective numbers in section 4.2.3 for the *HE-LHC* and FCC_{hh}. We then assume that the measured number of events corresponds to the SM prediction, $N(\kappa_{Z\gamma}{=}1)$, and exclude values of $\kappa_{Z\gamma}$ at a significance of $n\,\sigma$ if $N(\kappa_{Z\gamma})$ deviates from the SM value by more than n times the uncertainty.

Figure 4.3 shows the corresponding probability (times uncertainty) as a function of $\kappa_{Z\gamma}$ in the Gaussian approximation,

$$p(\kappa_{Z\gamma}) = \frac{1}{\sqrt{2\pi}} \exp\left[-\frac{\Delta N^2(\kappa_{Z\gamma})}{2\,\sigma_N^2}\right] , \tag{4.9}$$

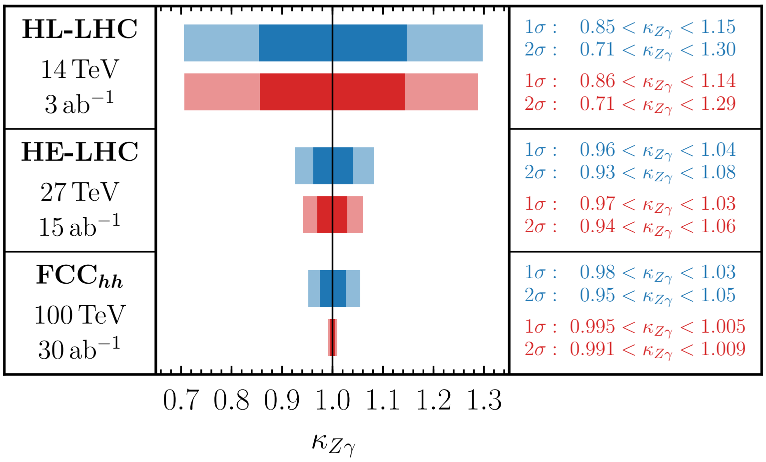

Figure 4.4: Prospective 1σ and 2σ constraints on the coupling modifier $\kappa_{Z\gamma}$ from the process $pp \to t\bar{t}h$, $h \to Z\gamma$ at the *HL-LHC* (top), *HE-LHC* (center) and *FCC$_{hh}$* (bottom), assuming statistical uncertainties only (red) as well as a 5 % systematic uncertainty on the signal (blue).

where $\Delta_N(\kappa_{Z\gamma}) \equiv N(\kappa_{Z\gamma}) - N(1) = (\kappa_{Z\gamma}^2 - 1)S$, and σ_N is the uncertainty. The colored lines correspond to the *HL-LHC* (green), *HE-LHC* (blue) and *FCC$_{hh}$* (orange). The intersections with the solid (dashed) black line indicate the values excluded with a significance of 1σ (2σ).

If only statistical uncertainties are considered (fig. 4.3a), i.e. taking $\sigma_N^2 = N(\kappa_{Z\gamma})$, the 1σ (2σ) limits on $\kappa_{Z\gamma}$ are obtained as

$$\begin{aligned}
&\textit{HL-LHC}: && 0.86 \leq \kappa_{Z\gamma} \leq 1.14 && (\,0.71 \leq \kappa_{Z\gamma} \leq 1.29\,)\,, \\
&\textit{HE-LHC}: && 0.97 \leq \kappa_{Z\gamma} \leq 1.03 && (\,0.94 \leq \kappa_{Z\gamma} \leq 1.06\,)\,, \\
&\textit{FCC}_{hh}: && 0.995 \leq \kappa_{Z\gamma} \leq 1.005 && (\,0.991 \leq \kappa_{Z\gamma} \leq 1.009\,)\,,
\end{aligned} \tag{4.10}$$

which are displayed as red bars in fig. 4.4. With the low-background process considered here, the signal can be established at the future *HE-LHC* and *FCC$_{hh}$* hadron colliders with a significance far beyond 5σ, allowing for the measurement of the effective $h\,Z\,\gamma$ coupling at the percent-level and thus for a determination of spin and CP properties of the Higgs boson.

At this level of precision, the assumption of considering statistical uncertainties only is questionable and systematic errors need to be incorporated. We therefore take into account an estimate of the theoretical uncertainties on the prediction of the signal cross-section $\sigma(pp \to t\bar{t}h)$. Currently, this uncertainty is around 10 % (cf. eq. (4.1)). Anticipating some progress in the theoretical predictions, we assume a relative systematic uncertainty of 5 %, added to the statistical error in quadrature. The corresponding limits are depicted as blue bars in fig. 4.4, and the p-values are plotted in fig. 4.3b. For the 1σ (2σ) constraints we then obtain

$$\begin{aligned} &\textit{HL-LHC}: && 0.85 \leq \kappa_{Z\gamma} \leq 1.15 && (\, 0.71 \leq \kappa_{Z\gamma} \leq 1.30 \,)\,, \\ &\textit{HE-LHC}: && 0.96 \leq \kappa_{Z\gamma} \leq 1.04 && (\, 0.93 \leq \kappa_{Z\gamma} \leq 1.08 \,)\,, \\ &\textit{FCC}_{hh}: && 0.98 \leq \kappa_{Z\gamma} \leq 1.03 && (\, 0.95 \leq \kappa_{Z\gamma} \leq 1.05 \,)\,. \end{aligned} \tag{4.11}$$

Our projections are competitive to limits from other production modes [198], which are around 10 % at the *HL-LHC* and 3 % − 4 % at the *HE-LHC* (at 1σ), as well as to prospective constraints from the *ILC* of $\sim 5\,\%$ [201].

The systematic uncertainties may be further reduced considering ratios of couplings, such as $\kappa_{Z\gamma}/\kappa_{\gamma\gamma}$, where uncertainties on the production mode cancel to a large extend. Since the $h \to Z\gamma$ rate in the SM is dominated by the W loop, so that heavy charged fermions for instance have a larger effect on the $h \to \gamma\gamma$ rate, this ratio is still highly sensitive to BSM physics.

4.4. Conclusion

We have investigated the prospects for discovering the Higgs decay to a Z boson and a photon in top-pair associated production at future proton colliders. Our projections are based on a MC analysis of the semi-leptonic top channel. Assuming the same selection efficiency for the fully-leptonic and fully-hadronic channel, we have demonstrated that $t\bar{t}$ associated production can contribute significantly to establishing an observation of the $h \to Z\gamma$ decay at the *HL-LHC*. Improved analysis techniques may even permit a $\sim 5\sigma$ discovery in this production channel alone. The higher event rates at a potential *HE-LHC* or *FCC*$_{hh}$ should definitely lead to a 5σ observation in the considered channel.

We further evaluated the corresponding bounds on the modifier $\kappa_{Z\gamma}$ of the effective $h\,Z\,\gamma$ coupling, constraining $\kappa_{Z\gamma}$ at the level of 15 %, 4 % and 2 % at the *HL-LHC*, *HE-LHC*, and *FCC*$_{hh}$, respectively, if a systematic uncertainty of 5 % is assumed. Our limits are competitive to those obtained from other production channels, including electron-positron colliders [187, 198, 201, 202]. It can be expected that a more sophisticated analysis, for instance using advanced top-tagging techniques based on machine learning, will strengthen these bounds.

5. Leptophilic Dark Matter from Gauged Lepton Number

This chapter is based on the publication [1]. Since the text in the paper (except for the introduction) has been composed by the author, the sections 5.1 to 5.4 are copied word-for-word. Minor modifications have been made to adjust to the structure, conventions and style of this thesis.

While the previous chapters have described two rather generic searches for physics beyond the Standard Model (BSM), let us now conduct a dedicated study of a specific model of new physics with particular focus on dark matter (DM).

As discussed in section 2.3.1, DM models with a relic abundance set via thermal freeze-out are in tension. Searches for DM at the *LHC* as well as direct detection experiments based on DM scattering on nuclei strongly constrain its interactions with quarks, while non-negligible interactions with at least a subset of the Standard Model (SM) particles are required to reproduce the observed abundance. In this chapter we therefore consider a model of leptophilic dark matter [203–205], i.e. DM that couples predominantly to leptons. Further motivation for new physics primarily interacting with leptons is provided by models of neutrino mass generation, the persistence of the muon $g-2$ anomaly, as well as by current hints for lepton-flavor-universality violation in B-physics observables.[1]

We here extend the SM by promoting lepton number to a $U(1)_\ell$ gauge group. Since lepton number is anomalous if only the SM particle content is assumed, this requires the introduction of additional fields to cancel the anomalies.[2] In the model considered in this chapter, anomaly cancellation is achieved adding two generations of fermions that are vector-like under the SM gauge groups but have chiral interaction with respect to lepton number [5]. A residual global symmetry surviving spontaneous symmetry breaking (SSB) then ensures the stability of the lightest additional lepton, automatically providing a candidate for leptophilic DM.

Since no massless gauge boson other than the photon is observed experimentally, a mass term for the lepton number gauge boson needs to be generated. We therefore break lepton number spontaneously. This may potentially lead to the generation of a stochastic gravitational wave background (SGWB) in the early Universe if the corresponding phase transition (PT) is of first-order, which might then be observable at *LISA* or other future gravitational wave (GW) experiments. We will thus discuss the lepton number breaking PT in this model as an example of how new physics can be probed via GWs in chapter 7 of part II of this thesis. Particular focus will be put on the interplay between the detectability of the SGWB and constraints from the collider and DM phenomenology of the model.

[1] Recent work in this direction can for instance be found in refs. [206–218].

[2] Various ways of anomaly free gauging of lepton number can be found in the literature [5, 219–228].

This chapter is organized as follows. The model is introduced in section 5.1, discussing constraints on the lepton number gauge coupling from renormalization group (RG) running. The corresponding DM phenomenology is investigated in section 5.2, and section 5.3 studies constraints from collider experiments. Intermediate conclusions are presented in section 5.4. A discussion of the lepton number breaking PT, the resulting GW signal and its detectability is deferred to chapter 7.

5.1. The Model

The model considered here has been introduced in [5]. In this model, the SM gauge group is extended by an additional $U(1)_\ell$ lepton number gauge group under which all SM leptons including three generations of right-handed neutrinos carry unit charge, whereas the other SM fields are neutral. Lepton number is spontaneously broken by an SM singlet scalar field, giving mass to the lepton number gauge boson. Additional fermionic fields are added to cancel gauge anomalies. These additional fields are vector-like under the SM gauge group.

5.1.1. Gauge Sector

The model is based on the gauge group[3] $SU(3)_c \otimes SU(2)_W \otimes U(1)_Y \otimes U(1)_\ell$. Omitting quantum chromodynamics (QCD), the gauge sector of the Lagrangian is given by

$$\mathcal{L} \supset -\frac{1}{4} W^a_{\mu\nu} W^{a\,\mu\nu} - \frac{1}{4} \hat{B}_{\mu\nu} \hat{B}^{\mu\nu} - \frac{1}{4} \hat{Z}_{\ell\,\mu\nu} \hat{Z}^{\mu\nu}_\ell + \frac{\epsilon}{2} \hat{B}_{\mu\nu} \hat{Z}^{\mu\nu}_\ell \,, \tag{5.1}$$

where W^a and $\hat{B}$ are the gauge bosons of the SM weak and hypercharge gauge group, respectively, and $\hat{Z}_\ell$ is the lepton number gauge boson. The $\frac{\epsilon}{2} \hat{B}_{\mu\nu} \hat{Z}^{\mu\nu}_\ell$ term leads to kinetic mixing between the hypercharge and lepton number $U(1)$ gauge bosons. The kinetic terms can be diagonalized by a $GL(2,\mathbb{R})$ transformation [229]

$$\begin{pmatrix} \hat{B} \\ \hat{Z}_\ell \end{pmatrix} = \begin{pmatrix} 1 & \frac{\epsilon}{\sqrt{1-\epsilon^2}} \\ 0 & \frac{1}{\sqrt{1-\epsilon^2}} \end{pmatrix} \begin{pmatrix} B \\ Z_\ell \end{pmatrix} . \tag{5.2}$$

The hats denote fields in the gauge basis and the unhatted fields are in the basis where the kinetic terms are diagonal and canonically normalized.

The model further features two scalar fields: the SM Higgs doublet transforming under $SU(2)_W \otimes U(1)_Y \otimes U(1)_\ell$ as $H \sim (\mathbf{2}, 1/2, 0)$, and a complex scalar $\Phi \sim (\mathbf{1}, 0, L_\Phi)$ which is an SM singlet with lepton number L_Φ. We let both fields acquire a vacuum expectation value (VEV) given by $\langle H \rangle = (0, v_H/\sqrt{2})$ and $\langle \Phi \rangle = v_\Phi/\sqrt{2}$, thus breaking the electroweak (EW) and lepton number gauge group $SU(2)_W \otimes U(1)_Y \otimes U(1)_\ell$ to $U(1)_{\text{EM}}$ electromagnetism (EM). The gauge bosons then obtain masses from the kinetic terms of the scalar fields, with the covariant derivative given by

$$\mathrm{D}_\mu = \partial_\mu - i g_2 W^a_\mu T^a - i g_1 Y \hat{B}_\mu - i g_\ell L \hat{Z}_\ell . \tag{5.3}$$

[3] To avoid confusion between the L denoting the weak gauge group of left-handed fields and lepton number, we here use $SU(2)_W$ instead of the standard $SU(2)_L$ notation.

Here, g_2, g_1 and g_ℓ are the gauge couplings of the $SU(2)_W$, $U(1)_Y$ and $U(1)_\ell$ gauge groups, respectively. The W mass is the same as in the SM, $m_W = \frac{1}{2}g_2 v_H$, whereas the mass matrix for the remaining gauge fields in the kinetic eigenbasis (W^3, B, Z_ℓ) is given by

$$M^2_{\mathrm{GB}} = \begin{pmatrix} \frac{g_2^2 v_H^2}{4} & -\frac{g_1 g_2 v_H^2}{4} & -\frac{\epsilon g_1 g_2 v_H^2}{4\sqrt{1-\epsilon^2}} \\ -\frac{g_1 g_2 v_H^2}{4} & \frac{g_1^2 v_H^2}{4} & \frac{\epsilon g_1^2 v_H^2}{4\sqrt{1-\epsilon^2}} \\ -\frac{\epsilon g_1 g_2 v_H^2}{4\sqrt{1-\epsilon^2}} & \frac{\epsilon g_1^2 v_H^2}{4\sqrt{1-\epsilon^2}} & \frac{g_\ell^2 L_\Phi^2 v_\Phi^2}{1-\epsilon^2} + \frac{\epsilon g_1^2 v_H^2}{4(1-\epsilon^2)} \end{pmatrix} . \tag{5.4}$$

The upper-left 2×2 submatrix is diagonalized rotating by the SM weak mixing angle. If $\epsilon \neq 0$, the resulting Z_{SM} boson is mixing with the Z_ℓ boson. The kinetic eigenstates are related to the physical mass eigenstates by

$$\begin{pmatrix} W^3 \\ B \\ Z_\ell \end{pmatrix} = \begin{pmatrix} c_W c_\xi & s_W & -c_W s_\xi \\ -s_W c_\xi & c_W & s_W s_\xi \\ s_\xi & 0 & c_\xi \end{pmatrix} \begin{pmatrix} Z \\ A \\ Z' \end{pmatrix} , \tag{5.5}$$

where $c_W = \cos\theta_W = g_2/\sqrt{g_1^2 + g_2^2}$ and $s_W = \sin\theta_W = g_1/\sqrt{g_1^2 + g_2^2}$ are sine and cosine of the weak mixing angle θ_W, whereas $c_\xi = \cos\xi$ and $s_\xi = \sin\xi$ are sine and cosine of the $Z - Z'$ mixing angle ξ. Defining $M^2_{Z_{\mathrm{SM}}} = (g_1^2 + g_2^2)v_H^2/4$, $M^2_{Z_\ell} = g_\ell^2 L_\Phi^2 v_\Phi^2$, $M_B^2 = g_1^2 v_H^2/4$ and $\eta = \epsilon/\sqrt{1-\epsilon^2}$, the $Z - Z'$ mixing angle and the neutral gauge boson masses are

$$\tan(2\xi) = \frac{2M^2_{Z_{\mathrm{SM}}} \sin\theta_W \epsilon\sqrt{1-\epsilon^2}}{M^2_{Z_\ell} - M^2_{Z_{\mathrm{SM}}}(1-\epsilon^2) + M^2_{Z_{\mathrm{SM}}} \sin^2\theta_W \epsilon^2} \approx 2\epsilon \sin\theta_W \frac{M^2_{Z_{\mathrm{SM}}}}{M^2_{Z_\ell}} , \tag{5.6}$$

and

$$\begin{aligned} m^2_{Z^{(\prime)}} &= \frac{1}{2}\left(M^2_{Z_\ell} + M^2_{Z_{\mathrm{SM}}} + \eta^2 M_B^2 \pm \sqrt{\left(M^2_{Z_\ell} + M^2_{Z_{\mathrm{SM}}} + \eta^2 M_B^2\right)^2 - 4M^2_{Z_\ell} M^2_{Z_{\mathrm{SM}}}} \right) \\ &\approx M^2_{Z_{\mathrm{SM}}} \left(M^2_{Z_\ell}\right) , \end{aligned} \tag{5.7}$$

where the approximate expressions are expansions up to linear order in ϵ. Note that the definition of the weak mixing angle θ_W and the EM coupling e in terms of the SM gauge couplings g_1 and g_2 is not altered by the kinetic mixing.

5.1.2. Scalar Sector

The model has two scalar fields: the SM Higgs $H \sim (\mathbf{2}, 1/2, 0)$ and the $U(1)_\ell$ breaking SM singlet scalar $\Phi \sim (\mathbf{1}, 0, L_\Phi)$, where we choose $L_\Phi = 3$ as will be discussed in section 5.1.3. The corresponding potential is given by

$$V(H,\Phi) = -\mu_H^2 H^\dagger H + \lambda_H \left(H^\dagger H\right)^2 - \mu_\Phi^2 \Phi^\dagger \Phi + \lambda_\Phi \left(\Phi^\dagger \Phi\right)^2 + \lambda_p H^\dagger H\, \Phi^\dagger \Phi . \tag{5.8}$$

Expanding the fields around their VEVs,

$$H = \begin{pmatrix} G^+ \\ \frac{1}{\sqrt{2}}\left(v_H + \hat{h} + \hat{G}^0\right) \end{pmatrix} \quad \text{and} \quad \Phi = \frac{1}{\sqrt{2}}\left(v_\Phi + \hat{\phi} + \hat{\omega}^0\right) , \tag{5.9}$$

the would-be Nambu-Goldstone bosons $G^\pm$, $\hat{G}^0$ and $\hat{\omega}^0$ become the longitudinal degrees of freedom of the $W^\pm$, Z and Z' gauge bosons. The mass matrix for the remaining scalars is

$$M_H^2 = \begin{pmatrix} -\mu_H^2 + 3\lambda_H v_H^2 + \frac{\lambda_p}{2} v_\Phi^2 & \lambda_p v_H v_\Phi \\ \lambda_p v_H v_\Phi & -\mu_\Phi^2 + 3\lambda_\Phi v_\Phi^2 + \frac{\lambda_p}{2} v_H^2 \end{pmatrix} . \tag{5.10}$$

The Higgs portal term $\lambda_p \, H^\dagger H \, \Phi^\dagger \Phi$ induces a mixing between the $\hat{h}$ and $\hat{\phi}$ fields. The mass eigenstates are defined by

$$\begin{pmatrix} h \\ \phi \end{pmatrix} = \begin{pmatrix} \cos\theta_H & -\sin\theta_H \\ \sin\theta_H & \cos\theta_H \end{pmatrix} \begin{pmatrix} \hat{h} \\ \hat{\phi} \end{pmatrix} \tag{5.11}$$

with the corresponding masses

$$m_{h,\phi}^2 = \left(\lambda_H v_H^2 + \lambda_\Phi v_\Phi^2\right) \pm \sqrt{\left(\lambda_H v_H^2 - \lambda_\Phi v_\Phi^2\right)^2 + \lambda_p^2 v_H^2 v_\Phi^2} \, , \tag{5.12}$$

where we eliminated μ_H^2 and μ_Φ^2 using the condition that the potential (5.8) has a minimum for $\hat{h} = v_H$ and $\hat{\phi} = v_\Phi$. Here, h is the SM-like Higgs with $m_h = 125\,\text{GeV}$, and ϕ is the lepton number Higgs which will typically have a mass $m_\phi > m_h$ due to the VEV hierarchy imposed by *LEP* constraints (see section 5.3.1).

5.1.3. Fermion Sector

With the SM fermion content only, lepton number is an anomalous symmetry. The lepton-gravity $U(1)_\ell$ and pure lepton $[U(1)_\ell]^3$ anomalies are canceled by the presence of three generations of right-handed neutrinos $\nu_R \sim (\mathbf{1}, 0, 1)$, whereas the cancellation of the remaining anomalies requires additional fermions, to which we refer as exotic or dark[4] leptons in the following. This can be realized in various ways (see e.g. refs. [219–228]). Here, we add two sets of chiral fermions that combine to transform vector-like under the SM gauge group, and thus do not spoil the cancellation of anomalies in the SM gauge sector.

$$\begin{aligned} \ell'_L &= \begin{pmatrix} N'_L \\ E'_L \end{pmatrix} \sim \left(\mathbf{2}, -\frac{1}{2}, L'\right) , & \ell''_R &= \begin{pmatrix} N''_R \\ E''_R \end{pmatrix} \sim \left(\mathbf{2}, -\frac{1}{2}, L''\right) , \\ \nu'_R &\sim (\mathbf{1}, 0, L') , & \nu''_L &\sim (\mathbf{1}, 0, L'') , \\ e'_R &\sim (\mathbf{1}, -1, L') , & e''_L &\sim (\mathbf{1}, -1, L'') \ . \end{aligned} \tag{5.13}$$

[4]Strictly speaking, the additional leptons are not "dark" in the typical sense since most of them carry EW charge. However, as we will discuss in section 5.2, the lightest exotic lepton constitutes a candidate for DM, so that, in a slight abuse of language, we also denote the other anomaly-canceling fermions as dark.

L'	L''	$\Delta\mathcal{L}$
-5	-2	$\bar{\ell}''_R \Phi^* \ell_L\,,\ \bar{e}''_L \Phi^* e_R\,,\ \bar{\nu}''_L \Phi^* \nu_R$
-4	-1	$\bar{\ell}''_R \tilde{H} \nu^c_R\,,\ \bar{\nu}''_L H^\dagger \ell^c_L\,,\ \bar{\nu}'_R \Phi^* \nu^c_R$
-3	0	$\bar{\nu}''_L \nu''^c_L$
-2	1	$\bar{\ell}''_R \ell_L\,,\ \bar{e}''_L e_R\,,\ \bar{\nu}''_L \nu_R$
-3/2	3/2	$\bar{\ell}''_R \tilde{H} \nu'^c_R\,,\ \bar{\nu}''_L H^\dagger \ell'^c_L\,,\ \bar{\nu}''_L \Phi \nu''^c_L\,,\ \bar{\nu}'_R H^\dagger \ell''^c_R\,,\ \bar{\nu}'_R \Phi^* \nu'^c_R\,,\ \bar{\ell}'_L \tilde{H} \nu''^c_L$
-1	2	$\bar{\nu}'_R \nu^c_R$
0	3	$\bar{\nu}'_R \nu'^c_R$
1	4	$\bar{\ell}''_R \Phi \ell_L\,,\ \bar{e}''_L \Phi e_R\,,\ \bar{\nu}''_L \Phi \nu_R\,,\ \bar{e}'_R H^\dagger \ell_L\,,\ \bar{\nu}'_R \tilde{H}^\dagger \ell_L\,,\ \bar{\ell}'_L H e_R\,,\ \bar{\ell}'_L \tilde{H} \nu_R$
2	5	$\bar{\nu}'_R \Phi \nu^c_R$

Table 5.1: Lepton number charge assignments for L' and L'' that allow for the additional terms $\Delta\mathcal{L}$ in the Lagrangian.

The first set corresponds to a 4th generation of SM-like leptons but with lepton number L', whereas the second set has opposite chirality and lepton number L''. Imposing the condition $L' - L'' = 3$, the remaining $[SU(2)_W]^2 \otimes U(1)_\ell$, $[U(1)_Y]^2 \otimes U(1)_\ell$ and $U(1)_Y \otimes [U(1)_\ell]^2$ anomalies cancel.

In order to write Yukawa terms for the additional fermions involving the lepton number breaking scalar Φ, $L_\Phi = 3$ must be chosen. The Yukawa sector is then given by

$$\begin{aligned} \mathcal{L} \supset & - c_\ell \bar{\ell}''_R \Phi \ell'_L - c_e \bar{e}''_L \Phi e'_R - c_\nu \bar{\nu}''_L \Phi \nu'_R \\ & - y'_e \bar{\ell}'_L H e'_R - y''_e \bar{\ell}''_R H e''_L - y'_\nu \bar{\ell}'_L \tilde{H} \nu'_R - y''_\nu \bar{\ell}''_R \tilde{H} \nu''_L + \text{h.c.}\,, \end{aligned} \tag{5.14}$$

Note that specific values of L' allow for additional terms in the Lagrangian. For example if $(L', L'') = (1, 4)$ or $(-2, 1)$, the dark fermions can mix with the SM ones, potentially leading to flavor-changing neutral currents and threatening the stability of our DM candidate. Table 5.1 lists the lepton number charges that allow additional terms. We will exclude these choices in the following. For any other pair of real numbers with $L'' = L' + 3$, the Yukawa interactions of the exotic leptons are fully described by eq. (5.14).

After spontaneous symmetry breaking, mass terms for the additional fermions are generated,

$$\mathcal{L} \supset - \begin{pmatrix} \bar{N}'_L & \bar{\nu}''_L \end{pmatrix} \mathcal{M}^\nu_{LR} \begin{pmatrix} N''_R \\ \nu'_R \end{pmatrix} - \begin{pmatrix} \bar{E}'_L & \bar{e}''_L \end{pmatrix} \mathcal{M}^e_{LR} \begin{pmatrix} E''_R \\ e'_R \end{pmatrix} + \text{h.c.}\,, \tag{5.15}$$

with the mass matrices given by

$$M_{LR}^{\nu} = \frac{1}{\sqrt{2}} \begin{pmatrix} c_\ell^* v_\Phi & y_\nu' v_H \\ y_\nu''^* v_H & c_\nu v_\Phi \end{pmatrix} , \quad M_{LR}^{e} = \frac{1}{\sqrt{2}} \begin{pmatrix} c_\ell^* v_\Phi & y_e' v_H \\ y_e''^* v_H & c_e v_\Phi \end{pmatrix} . \tag{5.16}$$

The matrices can be diagonalized via singular value decomposition, yielding the diagonal matrices $M_D^\nu = U_L^{\nu\dagger} M_{LR}^\nu U_R^\nu$ and $M_D^e = U_L^{e\dagger} M_{LR}^e U_R^e$, where U_C^a are unitary matrices.

For simplicity, and to avoid CP violating phases, let us assume that the Yukawa couplings c_i and $y_i^{\prime(\prime)}$ are real. The diagonalization matrices then become orthogonal. The fermions combine to two charged (e_4 and e_5) and two neutral (ν_4 and ν_5) Dirac fields, which are given in terms of the original fields by

$$\begin{aligned} \begin{pmatrix} \nu_4 \\ \nu_5 \end{pmatrix} &= \begin{pmatrix} \cos\alpha_\nu & \sin\alpha_\nu \\ -\sin\alpha_\nu & \cos\alpha_\nu \end{pmatrix} \begin{pmatrix} N_L' \\ \nu_L'' \end{pmatrix} + \begin{pmatrix} \cos\beta_\nu & \sin\beta_\nu \\ -\sin\beta_\nu & \cos\beta_\nu \end{pmatrix} \begin{pmatrix} N_R'' \\ \nu_R' \end{pmatrix} , \\ \begin{pmatrix} e_4 \\ e_5 \end{pmatrix} &= \begin{pmatrix} \cos\alpha_e & \sin\alpha_e \\ -\sin\alpha_e & \cos\alpha_e \end{pmatrix} \begin{pmatrix} E_L' \\ e_L'' \end{pmatrix} + \begin{pmatrix} \cos\beta_e & \sin\beta_e \\ -\sin\beta_e & \cos\beta_e \end{pmatrix} \begin{pmatrix} E_R'' \\ e_R' \end{pmatrix} . \end{aligned} \tag{5.17}$$

The right- and left-handed fields mix with different mixing angles unless we choose $y_\nu' = y_\nu''$ and $y_e' = y_e''$. Thus, the resulting fermions in general are chiral with respect to both the SM and $U(1)_\ell$.

In the absence of the Yukawa terms (5.14), the Lagrangian exhibits a global $[U(1)]^6$ symmetry at the classical level, consisting of a $U(1)$ symmetry for each additional lepton field in eq. (5.13). The Φ Yukawa terms break this to three $U(1)$ symmetries (one for the doublets, one for the charged singlets, and one for the neutral singlets), whereas the H Yukawa terms (in the absence of the Φ Yukawas) break the symmetry to $U(1)_{L'} \otimes U(1)_{L''}$. Hence, small values of $c_i \ll 1$ and $y_i^{\prime(\prime)} \ll 1$ are technically natural, rendering vector-like masses $c_i v_\Phi \ll v_\Phi$. Similarly, $y_{\nu\, i}^{\mathrm{SM}} \ll 1$ are technically natural. As we will see later, $v_\Phi \gtrsim 2\,\mathrm{TeV}$, therefore we typically have $c_i v_\Phi \gg y_i^{\prime(\prime)} v_H$. Consequently, the mixing angles $\alpha_{e/\nu}$ and $\beta_{e/\nu}$ are usually small, and the masses are approximately given by $m_{e_{4/5}} = c_{\ell/e} v_\Phi/\sqrt{2}$ and $m_{\nu_{4/5}} = c_{\ell/\nu} v_\Phi/\sqrt{2}$.

To simplify the discussion of the model we will restrict to the case of symmetric mass matrices, i.e. $y_{e/\nu} \equiv y_{e/\nu}' = y_{e/\nu}''$, in the following, so that $\alpha_{e/\nu} = \beta_{e/\nu}$. Let us further assume that $c_e = c_\ell$. The masses are then given by

$$m_{\nu_{4/5}} = \frac{1}{2\sqrt{2}} \left((c_\ell + c_\nu) v_\Phi \pm \sqrt{(c_\ell - c_\nu)^2 v_\Phi^2 + 4 y_\nu^2 v_H^2} \right) , \tag{5.18}$$

$$m_{e_{4/5}} = \frac{1}{\sqrt{2}} \left(c_\ell v_\Phi \pm y_e v_H \right) . \tag{5.19}$$

In particular, $m_{\nu_4} = (m_{e_4} + m_{e_5})/2$ if $y_\nu v_H \ll c_{l/\nu} v_\Phi$, and e_4 and e_5 are maximally mixed with $\alpha_e = \beta_e = \pi/4$.

Note that the SM neutrino masses in our model are pure Dirac masses generated from small Yukawa couplings to the SM Higgs doublet. Majorana mass terms are forbidden by the lepton number gauge symmetry, whereas mass terms arising from mixing with the exotic leptons would spoil the DM stability and are therefore avoided by suitable choices of the lepton number charges.

5.1.4. RG Running

Before exploring the phenomenology of the model, let us first consider the renormalization group running of the lepton number gauge coupling g_ℓ.

The running of a gauge coupling g is governed by the beta function

$$\beta = \frac{\partial g}{\partial \log \mu}\,. \tag{5.20}$$

For a $U(1)$ gauge group, the one-loop beta function is

$$\beta = \frac{g^3}{16\pi^2}\left[\frac{2}{3}\sum_f Q_f^2 + \frac{1}{3}\sum_s Q_s^2\right]\,, \tag{5.21}$$

where the sums run over all Weyl fermions and complex scalars charged under the gauge group with charge $Q_{f/s}$, respectively.

For the lepton number gauge group we get contributions from the SM leptons (with unit charge), the two additional generations of vector-like leptons (with charge L' and L''), and the lepton number breaking scalar (with charge L_Φ). Thus,

$$\beta = \frac{g_\ell^3}{16\pi^2}\left[\frac{8}{3}\Big(N_f + L'^2 + L''^2\Big) + \frac{1}{3}L_\Phi^2\right] = \frac{g_\ell^3}{16\pi^2}\left[35 + 16L' + \frac{16}{3}L'^2\right]\,, \tag{5.22}$$

where we used the lepton number charges $L'' = L' + 3$, $L_\Phi = 3$ and the number of SM flavors $N_f = 3$.

The dependence of the gauge coupling on the scale μ is consequently given by

$$g_\ell^2(\mu) = \frac{g_0^2}{1 - \frac{g_0^2}{8\pi^2} b \log\frac{\mu}{\mu_0}} \simeq g_0^2\Big[1 + \frac{g_0^2}{8\pi^2} b \log\frac{\mu}{\mu_0}\Big]\,, \tag{5.23}$$

where $g_0 = g_\ell(\mu_0)$ and $b = \Big[35 + 16L' + \frac{16}{3}L'^2\Big]$. $U(1)_\ell$ has a Landau pole when the second term in the bracket in eq. (5.23) is of order unity, i.e. at the scale $\mu = \Lambda$ with

$$\Lambda = \mu_0 \exp\left(\frac{8\pi^2}{b g_0^2}\right)\,. \tag{5.24}$$

We now choose $\mu_0 = m_{Z'} = 3 g_0 v_\Phi$. Figure 5.1 shows the Landau pole Λ normalized to the scalar VEV v_Φ as a function of $g_0 = g_\ell(m_{Z'})$ for different values of the charge L'. Certainly, we want the Landau pole to occur significantly above the Z' mass and above v_Φ, otherwise the validity of our perturbative results would be questionable. This requires choosing $g_\ell(m_{Z'}) \lesssim 0.5$ for most values of L'. The slowest running is obtained for $L' = -3/2$, which we however excluded since it allows for Majorana mass terms.

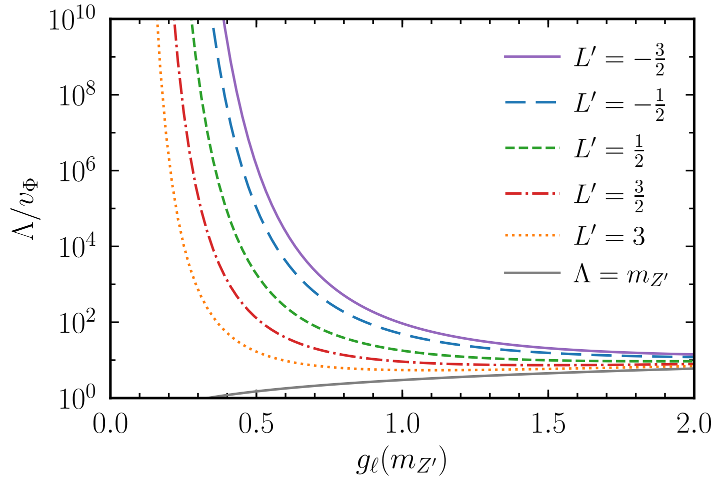

Figure 5.1: Landau pole Λ normalized to the scalar VEV v_Φ as a function of $g_0 = g_\ell(m_{Z'})$ for different values of the charge L'. The gray, solid line indicates the value of the Z' mass corresponding to g_0.

To prevent the gauge coupling from running into a Landau pole at low scales, we choose $L' = -1/2$ in the remainder of this paper.[5] In this case $g_\ell(m_{Z'}) \approx 1$ is acceptable, with the Landau pole located almost two orders of magnitude above v_Φ. For $v_\Phi = 2\,\text{TeV}$ this implies an upper bound of $m_{Z'} \lesssim 6\,\text{TeV}$ for the mass of the Z' boson. For most of the considerations that follow, the exact value of L' merely matters anyway. An exception are the DM constraints discussed in section 5.2, where we therefore also consider different values for L'.

5.2. Leptophilic Dark Matter

Provided that we avoid the specific choices of L' and L'' discussed in section 5.1.3, the model features a global $U(1)_{L'+L''}$ symmetry under which all SM fermions are neutral whereas the exotic leptons have unit charge, and which is free of anomalies. This symmetry persists when the EW and $U(1)_\ell$ gauge symmetries are broken and ensures the stability of the lightest dark lepton. If neutral, it is a candidate for dark matter.

For the remainder we identify ν_5 as the DM candidate (which can always be achieved by defining the mixing angles in eq. (5.17) accordingly) and relabel it as $\nu_{\text{DM}} \equiv \nu_5$. Since direct detection experiments exclude DM candidates with unsuppressed couplings to the SM Z boson, ν_{DM} should be composed predominantly of the SM singlets ν''_L and ν'_R. Consequently α_ν and β_ν should be small. In particular, this requires $c_\nu < c_\ell$. Finally, at least one of y'_ν and y''_ν should be non-vanishing, otherwise an additional global $U(1)$ symmetry remains unbroken and the next-to-lightest dark fermion (either ν_4 or $e_{4/5}$) would be stable as well.

The model is implemented in FeynRules [230], and subsequently mircOMEGAs [140] was used to calculate the relic density as well as direct and indirect detection constraints.

[5] Note that picking a half-integer value is mostly for aesthetic reasons. We could have chosen any real number not listed in table 5.1. Further requiring $\Lambda \lesssim 100\,\text{TeV}$ for $g_\ell = 1$ and $v_\Phi = 2\,\text{TeV}$ restricts the viable choices to $L' \in [-5/2, -1/2]$.

scalar sector	gauge sector	fermion sector	
$v_\Phi = 2\,\mathrm{TeV}$	$m_{Z'} = 1.5\,\mathrm{TeV}$	$m_{\mathrm{DM}} = 640\,\mathrm{GeV}$	$m_{e_4} = 2.0\,\mathrm{TeV}$
$m_\phi = 2.5\,\mathrm{TeV}$	$\epsilon = 0$	$\sin(\theta_{\mathrm{DM}}) = 0$	$m_{e_5} = 1.5\,\mathrm{TeV}$
$\sin(\theta_H) = 0$	$L' = -\frac{1}{2}$		

Table 5.2: Default values for the model parameters (assuming $y'_{\nu/e} = y''_{\nu/e}$ and $c_e = c_l$) used throughout this paper, unless specified otherwise. For negligible $\sin(\theta_{\mathrm{DM}})$, the mostly-doublet, heavy neutrino mass is given by $m_{\nu_4} \simeq (m_{e_4} + m_{e_5})/2 = 1.75\,\mathrm{TeV}$.

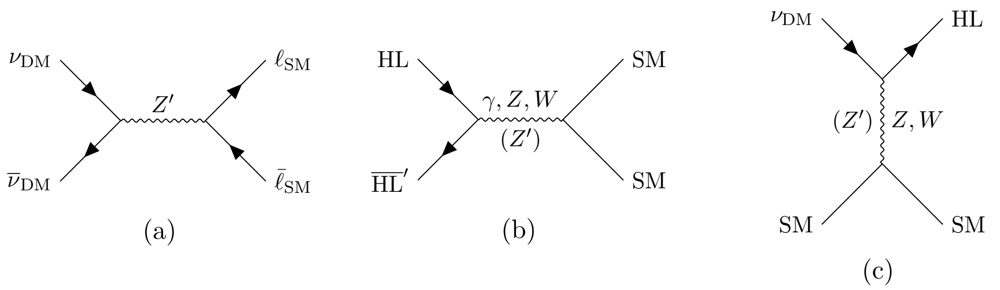

Figure 5.2: Processes contributing to the depletion of the DM relic abundance.

Unless specified otherwise, we use the parameters listed in table 5.2. We here relabelled $\theta_{\mathrm{DM}} \equiv \alpha_\nu = \beta_\nu$.

5.2.1. Relic Abundance

Assuming that ν_{DM} is a thermal relic, its abundance is predominantly set by its annihilation cross-section to two leptons through an s-channel Z' (fig. 5.2a). Other possible channels are annihilation to gauge or scalar bosons through an intermediate h or ϕ, or to fermions via a Z boson. The former is suppressed by the $h - \phi$ mixing, whereas the latter can arise from $Z - Z'$ mixing or by an admixture of the SM component in the DM. The doublet-singlet mixing further allows for t-channel annihilation to two bosons, and a small mass splitting between the DM and the other exotic leptons can lead to co-annihilation. See ref. [5] for more details.

The parameter regions in the $m_{\mathrm{DM}} - v_\Phi$ and $m_{\mathrm{DM}} - m_{Z'}$ planes that reproduce the DM relic abundance of $h^2\Omega_{\mathrm{DM}} = 0.1200 \pm 0.0012$ measured by the *Planck* satellite [60] are shown in fig. 5.3 for different values of L'. We assume a lepton number gauge coupling of $g_\ell = 0.1$ and a scalar self-coupling of $\lambda_\Phi = 0.5$, as well as Yukawa couplings $c_\ell = 1.5$ and $y_e = 0$ when scanning over the VEV (left panel), and a scalar VEV of $v_\Phi = 2\,\mathrm{TeV}$ when varying the Z' mass (right panel). The remaining parameters are set to the values specified in table 5.2.

The colored regions yield a DM abundance that lies within two standard deviations around the *Planck* measurement. For each value of $m_{Z'}$ we typically obtain two viable

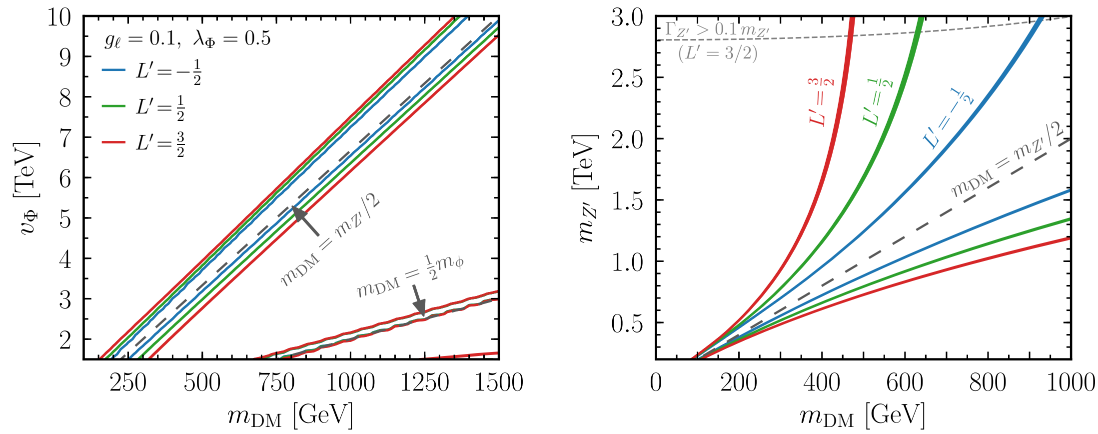

(a) $g_\ell = 0.1$, $\lambda_\Phi = 0.5$

(b) $v_\Phi = 2\,\mathrm{TeV}$

Figure 5.3: Parameter regions reproducing the DM relic density $h^2\Omega_{\mathrm{DM}} = 0.120 \pm 0.001$ measured by *Planck* [60] within two standard deviations for different values of L', fixing the gauge coupling (left) or scalar VEV (right). The dashed gray lines in the right plot indicate the parameters for which the Z' width exceeds 10 % of its mass.

values for the DM mass, one below and one above the $m_{\mathrm{DM}} = m_{Z'}/2$ resonance. In fig. 5.3a, we can in addition also see the scalar resonance at $m_{\mathrm{DM}} = m_\phi/2$. To guide the eye, the resonances are indicated by dashed dark-gray lines.

Since the Z' predominantly decays into ν_{DM} and the other dark leptons, its width increases with L'. For $L' = -1/2$, the Z' is rather narrow and the DM mass is restricted to values close to half of the Z' mass. For larger charges, the resonance becomes broader and the DM mass can be lower. The light gray, dashed line in fig. 5.3b indicates the regions in which the width of the Z' exceeds 10 % of its mass for $L' = 3/2$.

The dependence of the DM relic density on the masses of the non-DM exotic leptons e_4, e_5, and ν_4, denoted as heavy leptons (HLs) in the following, is shown in fig. 5.4, assuming that they all have the same mass m_{HL}. The colored regions again yield the measured DM abundance, now assuming $L' = -1/2$. The colors correspond to a relative mass splitting $\Delta_m \equiv (m_{\mathrm{HL}} - m_{\mathrm{DM}})/m_{\mathrm{DM}}$ of 1 % (blue), 2 % (red), 5 % (green), and 10 % (purple) between the DM and the HLs.

For high DM masses, the HL masses affect the relic density only by changing the Z' width. However, for lower DM masses the abundance is no longer set by annihilation of the DM to SM leptons as depicted in fig. 5.2a, but via co-annihilation. In this case, the HL abundance is depleted by annihilation of e_4, e_5 and ν_4 to SM particles through electroweak processes as shown in fig. 5.2b. This depletion is transferred to the DM abundance by the EW processes depicted in fig. 5.2c in which a DM particle scatters off SM particles and changes into a HL. These processes require $\sin\theta_{\mathrm{DM}} \neq 0$, but we need this assumption anyways to ensure that there is only a single DM component. As the diagram 5.2b is dominanted by EW processes, the relic density in this regime is independent of the Z' mass. Figure 5.4 assumes $\sin\theta_{\mathrm{DM}} = 0$. However, modifying the

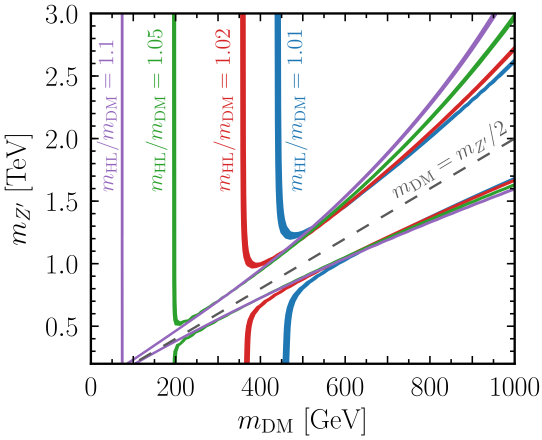

Figure 5.4: Same as fig. 5.3b fixing $L' = -1/2$, but including co-annihilation with the heavy leptons (HLs) for a mass splitting of $\Delta_m = 1\,\% - 10\,\%$, assuming that e_4, e_5 and ν_4 have equal mass $m_{\rm HL}$. The colored regions reproduce the measured relic abundance, the colors correspond to different values of $m_{\rm HL}/m_{\rm DM} = 1 + \Delta_m$.

mixing within the range allowed by direct detection (see section 5.2.2) does not alter the result.

Varying the remaining parameters of the model only has a minor effect on these results. The scalar mass m_ϕ and the $h - \phi$ mixing angle θ_H only have an effect in the region of the ϕ resonance $m_{\rm DM} = m_\phi/2$ (or the h resonance).

5.2.2. Direct and Indirect Detection

Direct detection experiments strongly constrain DM couplings to the SM Z boson via scattering off nuclei. For small values of the kinetic mixing parameter ϵ, the coupling is given by

$$Z \to \nu_{\rm DM}\,\bar{\nu}_{\rm DM}: \qquad s^2_{\rm DM}\frac{ie}{2c_W s_W}\gamma_\mu + s_\xi \frac{ig_\ell}{2}\gamma_\mu \left[(L'+L'') + (L'-L'')(c^2_{\rm DM} - s^2_{\rm DM})\gamma_5\right], \quad (5.25)$$

where $s_W = \sin\theta_W$, $s_\xi = \sin\xi$, $s_{\rm DM} = \sin\theta_{\rm DM}$ and $c_{\rm DM} = \cos\theta_{\rm DM}$. The first term originates from the heavy doublet neutrino $N = N'_L + N''_R$ (which has vector-like couplings to the SM Z) mixing into the DM, whereas the second part comes from the chiral DM $-$ Z' coupling. The axial part of the latter is also modified by the DM mixing via the $\bar{\nu}_4\nu_4 Z'$ vertex, while the vector part remains untouched by $\theta_{\rm DM}$ since it here enters as $(c^2_{\rm DM} + s^2_{\rm DM})$.

Figure 5.5 shows the constraints on the $Z - Z'$ and DM mixing as a function of the Z' mass, obtained from direct detection limits on spin-independent DM-nucleus scattering. The solid lines correspond to current constraints from the *XENON1T* experiment based on one tonne times year of data acquisition [88], the long dashed lines indicate the prospective sensitivity of *LZ* [142], and the dash-dotted lines show the projected reach of *DARWIN* [143]. At each parameter point, the DM mass is fixed to a value reproducing $h^2\Omega_{\rm DM} = 0.12$ (chosing the value below the Z' resonance). The charges are taken to be $L' = -1/2$ (blue) or $L' = 3/2$ (red), and the VEV is set to $v_\Phi = 2\,\text{TeV}$.

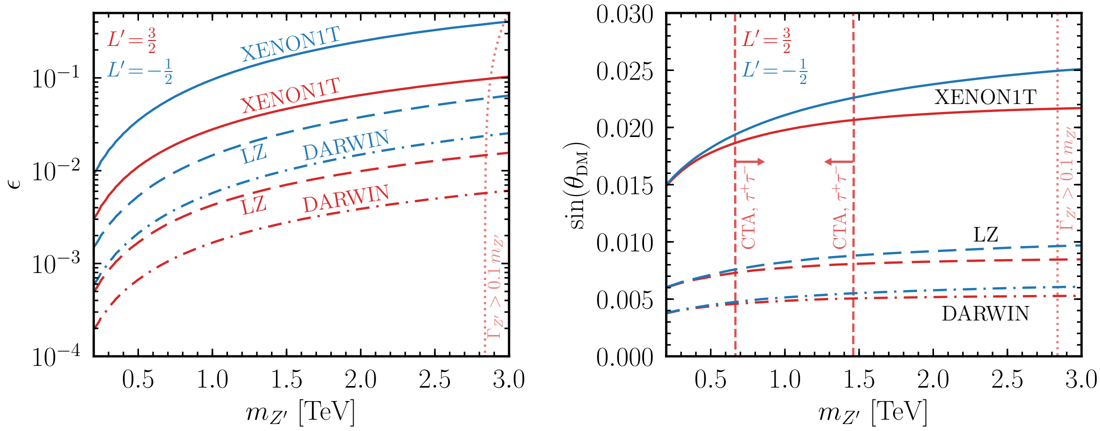

(a) kinetic mixing parameter ϵ ($\theta_{\rm DM} = 0$)   (b) DM mixing angle $\sin\theta_{\rm DM}$ ($\epsilon = 0$)

Figure 5.5: Direct detection limits on the $Z - Z'$ and $\nu_{\rm DM} - \nu_4$ mixing for $L' = -1/2$ (blue) and $L'' = 3/2$ (red). Current constraints from the *XENON1T* experiment [88] are shown as solid lines, the long-dashed lines indicate the projected sensitivity of *LZ* [142], and the dash-dotted lines correspond to *DARWIN* [143]. The DM mass is fixed by the requirement to reproduce the *Planck* relic density; all other parameters are set according to table 5.2. The short-dashed lines in 5.5b indicate the prospective reach of the *CTA* [231] indirect detection experiment. The light dotted lines show the region where the Z' width grows above 10 % of the mass.

Current direct detection experiments can probe kinetic mixing parameters in the percent range and DM mixing angles of $\sin\theta_{\rm DM} \gtrsim 0.015 - 0.025$, depending on the Z' mass. With *LZ*, DM mixing angles around $\sin\theta_{\rm DM} \gtrsim 0.006 - 0.01$ as well as kinetic mixing in the sub-percent range can be reached, while *DARWIN* can prospectively exclude $\sin\theta_{\rm DM} \gtrsim 0.004 - 0.006$, and sub-per-mill kinetic mixing for $m_{Z'} \lesssim 1\,\text{TeV}$. The constraints for $L' = 3/2$ are stronger than for $L' = -1/2$ since the latter case leads to higher DM masses, whereas the former case gives DM masses below 500 GeV.

Beside Z-mediated DM-quark interactions, nuclear scattering can also proceed via Higgs (or ϕ) exchange, either through $h - \phi$ mixing or by direct DM-Higgs couplings. However, since the Higgs only weakly couples to nuclei, the direct detection constraints on the Higgs mixing angle are much weaker than on $\theta_{\rm DM}$ or ξ. For $m_\phi = 2.5\,\text{TeV}$, *XENON1T* can currently exclude $\sin\theta_H \gtrsim 0.1 - 0.4$. *LZ* and *DARWIN* can prospectively probe $\sin\theta_H \gtrsim 0.02 - 0.06$ and $\sin\theta_H \gtrsim 0.007 - 0.02$, respectively. Here, direct detection experiments are more sensitive for $L' = -1/2$ since the Yukawa couplings are proportional to the DM mass, i.e. we benefit from the higher DM masses in the $L' = -1/2$ case. For lower ϕ masses on the other hand, the scattering cross section is reduced due to $\phi - h$ interference effects, leading to weaker direct detection limits. The corresponding constraints are shown in fig. 5.6.

A further, indirect way of probing DM is via its annihilation to SM particles. Since the observation of charged particles suffers from large uncertainties associated with their propagation through the Galactic halo, we here only consider indirect detection constraints

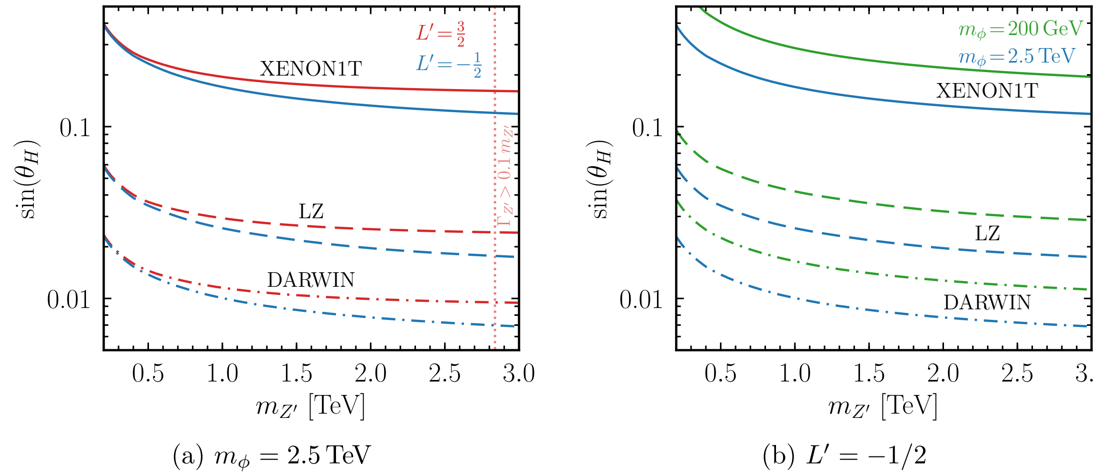

Figure 5.6: Direct detection limits on the Higgs mixing angle θ_H for lepton number charges (left plot, $m_\phi = 2.5\,\mathrm{TeV}$) of $L' = -1/2$ (blue) and $L' = 3/2$ (red), and scalar masses (right plot, $L' = -1/2$) of $m_\phi = 200\,\mathrm{GeV}$ (green) and $m_\phi = 2.5\,\mathrm{TeV}$ (blue). The current constraints from the *XENON1T* experiment [88] are shown as solid lines, the long-dashed and dash-dotted lines indicate the projected sensitivities of *LZ* [142] and *DARWIN* [143], respectively. As before, the DM mass is set to the value reproducing the measured relic abundance.

from γ-ray searches. As photons travel unperturbed by Galactic magnetic fields, they can be traced back to their production site, allowing for constraints on DM annihilation by observing photons from regions with a high DM density.

In our model, the DM typically annihilates through the lepton number gauge boson Z' into SM leptons with equal branching ratios. Photons are thus predominantly produced as secondary products from annihilation to charged leptons. Direct production of monochromatic photons is possible via annihilation through the scalar bosons h and ϕ, however, this is suppressed unless resonant.

We tested the annihilation of thermally produced DM (i.e. satisfying the relic density constraint) in our model against current limits from observations of dwarf spheroidal galaxies by *MAGIC* and *Fermi-LAT* [83], and of the inner Galactic halo by *H.E.S.S.* [85], as well as against γ line searches from *Fermi-LAT* [84] and *H.E.S.S.* [86]. The strongest limits come from secondary produced photons from annihilation into τ leptons. However, the current sensitivity reaches the level of the annihilation cross section required for thermal production (which in addition is reduced by the branching ratio of 1/6 into tauons) only for DM below 100 GeV, which, even for light Z' masses, is below the DM masses predicted by our model (cf. fig. 5.3). This also holds for the projected sensitivity of *Fermi-LAT*, assuming a 15-year data set of 60 dwarf spheroidal galaxies [232]. On the other hand, a next-generation γ-ray observatory such as the *CTA* [231] will be able to exclude Z' masses between roughly 670 GeV and 1.46 TeV if $L' = 3/2$. The corresponding limit is indicated by the vertical dashed lines in fig. 5.5b.

In principle, our model can furthermore be probed through its neutrino sector. Modifications of the neutrino interactions with the SM leptons arise from Z' exchange or kinetic mixing, and DM-neutrino interactions can be mediated by a Z or Z' boson. Neutrino couplings to the lepton number breaking scalar and SM Higgs boson are suppressed by the neutrino Yukawa couplings. For the range of Z' and DM masses considered here, no constraints are obtained from current data [233, 234].

5.3. Collider Phenomenology

While new physics that couples directly to quarks and gluons is nowadays severly constrained by direct searches at the *LHC*, the situation is different for the leptophilic new physics model we are considering here. In this model, constraints predominantly arise from a combination of *LEP* limits as well as direct and indirect *LHC* measurements, such as e.g. Higgs data. In the following we present an overview of the most important constraints on the lepton number gauge boson, the extended Higgs sector and the new leptons introduced in our model, and comment on the prospects for detection at the *HL-LHC* and future colliders.

5.3.1. Z' Constraints

Since in the absence of kinetic mixing the lepton number gauge boson does not couple to quarks, the strongest constraints on the Z' boson come from *LEP II*. These exclude Z' masses below the maximal *LEP* center-of-mass energy of 209 GeV (except for tiny gauge couplings $g_\ell < 10^{-2}$ [235, 236]) and severely restrict the lepton number breaking VEV v_Φ through 4-lepton contact interactions.

A heavy Z' induces effective contact interactions between electrons and charged (SM) leptons. Since the Z' couplings to SM fermions are vector-like, the corresponding contact interactions are given by (neglecting kinetic mixing)

$$\mathcal{L}_{\text{eff}} \supset -\frac{g_\ell^2}{2m_{Z'}^2}\,\bar{e}\gamma_\mu e\,\bar{e}\gamma^\mu e - \frac{g_\ell^2}{m_{Z'}^2}\,\bar{e}\gamma_\mu e\,\bar{\mu}\gamma^\mu \mu - \frac{g_\ell^2}{m_{Z'}^2}\,\bar{e}\gamma_\mu e\,\bar{\tau}\gamma^\mu \tau\,, \tag{5.26}$$

which interfere destructively with the SM Z boson for center-of-mass energies above the Z-pole. *LEP* puts a 95 % lower bound of $\Lambda > 20\,\text{TeV}$ [237] on the scale suppressing this contact interaction, related to the model parameters by $\Lambda^2 = 4\pi\, m_{Z'}^2/g_\ell^2$. Using $m_{Z'} = L_\Phi g_\ell v_\Phi$ with $L_\Phi = 3$, this gives a lower bound on the scalar VEV of

$$v_\Phi \gtrsim 1880\,\text{GeV}\,. \tag{5.27}$$

To be conservative, we set the VEV to $v_\Phi = 2\,\text{TeV}$ in the following.

Future e^+e^- colliders have the potential to substantially tighten these bounds. For instance, the *ILC* with a center-of-mass energy of $\sqrt{s} = 1\,\text{TeV}$ can exclude Z' masses below 1 TeV (unless the gauge coupling is below $g_\ell \lesssim 7.6\times 10^{-8}$), and constrain the VEV to be above $v_\Phi \gtrsim 15\,\text{TeV}$ at 90 % confidence level (CL) using muon contact interactions [208].

At the *LHC*, the Z' is rather hard to produce. In particular, in the absence of kinetic mixing it is predominantly produced by pair-producing SM leptons that radiate off a Z'. The Z' can then be detected from its decays to charged SM leptons.

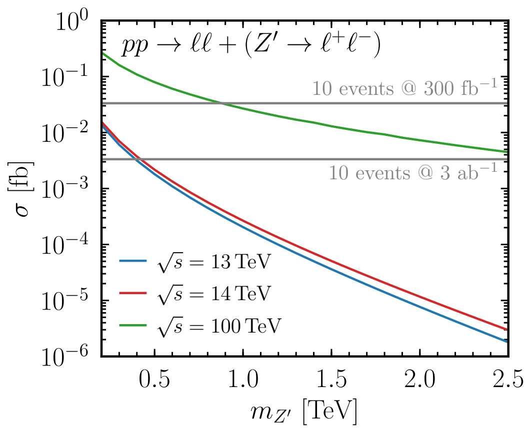

Figure 5.7: Z' production cross-section in the absence of kinetic mixing for the *LHC-13* (blue), *LHC-14* (red), as well as *FCC-100* (green).

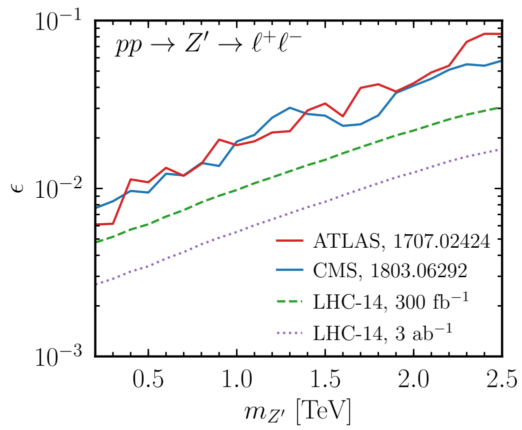

Figure 5.8: Current *LHC* limits in the Z' mass vs. kinetic mixing parameter-plane from *ATLAS* (solid red) and *CMS* (solid blue), as well as projections for the 14 TeV *LHC* with 300 fb^{-1} (dashed green) and 3 ab^{-1} (dotted purple).

To obtain a rough estimate of the detection prospects, we calculate the parton-level cross-section for $pp \to \ell\ell Z'$ with CalcHEP 3.6 [238], where ℓ can be any SM lepton, including neutrinos. For the decay we use the narrow-width approximation (NWA), assuming that the Z' decays into SM leptons only. In this case, the corresponding branching ratio to charged leptons is $\mathrm{Br}\left(Z' \to \ell^+\ell^-\right) = 50\,\%$. The cross section as a function of the Z' mass is shown in fig. 5.7 for the *LHC* with center-of-mass energies of 13 TeV (blue) and 14 TeV (red), as well as for a 100 TeV *FCC* (green). The gray lines indicate the cross sections that would produce 10 Z's, assuming integrated luminosities of 300 fb^{-1} and 3 ab^{-1}.

With the current *LHC* data, no constraints can be put on the Z' mass if kinetic mixing is absent. With 300 fb^{-1}, the *LHC* would not produce a sufficient amount of Z's. At the *HL-LHC*, Z' masses below $\lesssim 400$ GeV can be reached. The prospects for a 100 TeV collider are more promising. With 3 ab^{-1}, more than 10 events are produced for masses up to 2.5 TeV, extending the reach into the multi-TeV region.

In the presence of kinetic mixing the situation is different. The lepton number gauge boson then couples to quarks with couplings proportional to the kinetic mixing parameter ϵ and the quark hypercharge. It can thus be produced directly in proton-proton collisions and be searched for as a dilepton resonance, giving constraints in the $m_{Z'}$ vs. ϵ plane.

Figure 5.8 shows constraints from current searches for dilepton resonances using 36 fb^{-1} of data collected at a center-of-mass energy of $\sqrt{s} = 13$ TeV by *ATLAS* [133] (solid red line) and *CMS* [239] (solid blue line). Projections for the *LHC* at a center-of-mass energy of $\sqrt{s} = 14$ TeV with an integrated luminosity of 300 fb^{-1} (dashed green) and 3 ab^{-1} (dotted purple) are also shown. Currently, kinetic mixing can be probed in the percent range, the *HL-LHC* can prospectively reach the sub-percent range for light Z'. Again, the cross sections have been calculated with CalcHEP [238], assuming a narrow Z' width with a branching ratio of 1/3 to light charged leptons (e or μ). The projections have been obtained assuming that the limits on cross-section ratios provided by *CMS* [239] do not change when increasing the center-of-mass energy from 13 TeV to 14 TeV, and that the exclusion reach scales with the square root of the luminosity.

The kinetic mixing can also be probed via its effects on SM precision measurements at electron-positron colliders [240]. However, as these effects are suppressed for high Z' masses, the *LHC* provides the strongest constraints in the mass range considered here.

5.3.2. Higgs Constraints

The scalar sector of our model is subject to constraints from measurements of the properties of the 125 GeV Higgs boson at *ATLAS* and *CMS*, as well as from null-results of searches for scalar bosons at different masses.

In our model, the SM Higgs properties can be modified by three effects: the $h-\phi$ mixing which modifies all SM Higgs couplings, modifications of Higgs couplings to EW gauge bosons (in particular to two photons) by loops of heavy charged leptons, and decays to BSM states (if kinematically accessible). However, given the lower bound on the lepton number breaking VEV (5.27), the new states are typically too heavy for the SM Higgs to decay into, so that the last effect is absent in most of the parameter space.

The mixing between the lepton number breaking scalar and the SM Higgs boson given by equation (5.11) reduces the Higgs couplings to SM fields by $\cos\theta_H$. *ATLAS* and *CMS* provide limits on modifications of Higgs couplings compared to the SM values in terms of signal strengths, defined by

$$\mu_X = \frac{\sigma\,(pp\to h)\times \mathrm{Br}\,(h\to X)}{\sigma^{\mathrm{SM}}\,(pp\to h)\times \mathrm{Br}^{\mathrm{SM}}\,(h\to X)}\,. \tag{5.28}$$

Neglecting additional Higgs decay channels and further modifications of loop-induced Higgs couplings discussed below, the production cross-sections are modified by a factor $\cos^2\theta_H$, whereas the branching ratios remain unchanged as the cosine factors in the partial and total widths cancel. Thus, the signal strengths are $\mu=\cos^2\theta_H$. An estimate of the limit on the mixing angle can be obtained from the global signal strength. The current *CMS* measurement is $\mu = 1.17\pm 0.10$ [241]. This gives a 95 % exclusion of

$$|\sin\theta_H| < 0.16\,. \tag{5.29}$$

Loops of the dark electrons e_4 and e_5 can contribute sizeably to the $h\to\gamma\gamma$ and $h\to Z\gamma$ rate. In the SM, these rates are given by [242]

$$\Gamma(h\to\gamma\gamma) = \frac{\alpha^2 m_h^3}{256\pi^3 v_H^2}\left|\sum_f N_c^f Q_f^2 A_{1/2}(\tau_f) + A_1(\tau_W)\right|^2, \tag{5.30}$$

$$\Gamma(h\to Z\gamma) = \frac{\alpha m_W^2 m_h^3}{128\pi^4 v_H^4}\left(1-\frac{m_Z^2}{m_h^2}\right)^3 \left|\sum_f N_c^f \frac{Q_f \hat{v}_f}{c_W} A_{1/2}(\tau_f,\lambda_f) + A_1(\tau_W,\lambda_W)\right|^2, \tag{5.31}$$

where α is the electromagnetic coupling constant, $\tau_i = 4m_i^2/m_h^2$, and $\lambda_i = 4m_i^2/m_Z^2$. The expressions for the form factors A_s for a spin s particle running in the loop can be found in ref. [242]. The sums run over all charged fermions that couple to the Higgs. N_c^f is the color-representation of the fermion, Q_f is its electric charge, and $\hat{v}_f$ is the fermion's (reduced) vector-coupling to the Z boson. In the SM, the dominant contribution from fermions comes from the top quark with $N_c^t = 3$, $Q_t = 2/3$, and $\hat{v}_t = 1 - \frac{8}{3}s_W^2$.

Equations (5.30) and (5.31) assume that the fermions couple to the Higgs with a vertex factor proportional to their masses. The top quark in the SM for instance has a vertex factor $-i\frac{y_t}{\sqrt{2}} = -i\frac{m_t}{v_H}$. This is not true for the heavy charged leptons. The corresponding vertex factors are

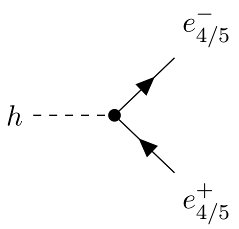

$$-\frac{i}{\sqrt{2}}\mathcal{Y}_{he_{4/5}}, \qquad \mathcal{Y}_{he_{4/5}} = \pm c_H y_e - s_H c_\ell\,, \tag{5.32}$$

for the SM-like Higgs.[6] The correct result can then be obtained by rescaling the dark electron contributions by a factor $\frac{\mathcal{Y}_{sf}v_H}{\sqrt{2}m_f}$, where $s = h, \phi$ and $f = e_4, e_5$. Due to the scalar mixing, the SM contributions further get a factor of c_H or s_H for h and ϕ, respectively. We thus obtain

$$\begin{aligned}\Gamma(h \to \gamma\gamma) = \frac{\alpha^2 m_h^3}{256\pi^3 v_H^2}\Bigg| &\frac{4}{3}c_H A_{1/2}(\tau_t) + c_H A_1(\tau_W) \\ &+ \frac{\mathcal{Y}_{he_4}v_H}{\sqrt{2}m_{e_4}}A_{1/2}(\tau_{e_4}) + \frac{\mathcal{Y}_{he_5}v_H}{\sqrt{2}m_{e_5}}A_{1/2}(\tau_{e_5})\Bigg|^2,\end{aligned} \tag{5.33}$$

$$\begin{aligned}\Gamma(h \to Z\gamma) = \frac{\alpha m_W^2 m_h^3}{128\pi^4 v_H^4}\left(1 - \frac{m_Z^2}{m_h^2}\right)^3 \Bigg| &\frac{6 + 16s_W^2}{3c_W}c_H A_{1/2}(\tau_t, \lambda_t) + c_H A_1(\tau_W, \lambda_W) \\ &+ \frac{1 - 4s_W^2}{c_W}\frac{v_H}{\sqrt{2}}\left(\frac{\mathcal{Y}_{he_4}}{m_{e_4}}A_{1/2}(\tau_{e_4}, \lambda_{e_4}) + \frac{\mathcal{Y}_{he_5}}{m_{e_5}}A_{1/2}(\tau_{e_5}, \lambda_{e_5})\right)\Bigg|^2.\end{aligned} \tag{5.34}$$

The corresponding widths for the ϕ scalar can be obtained by replacing $m_h \to m_\phi$, $c_H \to s_H$, $\mathcal{Y}_{he_i} \to \mathcal{Y}_{\phi e_i}$, and $\tau_i = 4m_i^2/m_\phi^2$. The leading QCD corrections can be included by multiplying the top contribution by $(1 - \alpha_s/\pi)$ [242].

We evaluated constraints from direct Higgs searches using HiggsBounds 4.3.1 [243]. The corresponding limits from *LEP* [244, 245] (purple), $\sqrt{s} = 7\,\text{TeV}$ and $\sqrt{s} = 8\,\text{TeV}$ searches with *ATLAS* and *CMS* for a Higgs boson in the $h \to ZZ/WW$ channel [246–249] (blue), and a combination of *CMS* 7 TeV and 8 TeV searches in various final states [250] (green) are shown as colored regions in fig. 5.9. The red line indicates limits from signal strength measurements. These include measurements of Higgs boson properties in the $h \to 4\ell$ and $h \to \gamma\gamma$ channels by *ATLAS* [251, 252], and a *CMS* analysis combining different

[6] The corresponding interactions of ϕ are obtained by replacing $c_H \to s_H$ and $s_H \to -c_H$.

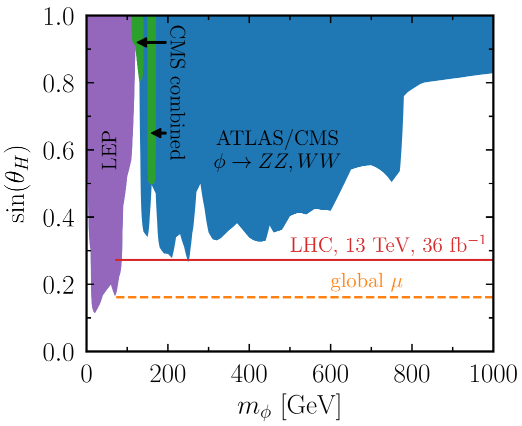

Figure 5.9: Exclusion bounds on the mass of the lepton number breaking scalar ϕ and the Higgs mixing angle θ_H from direct searches (colored regions) and signal strength measurements (colored lines).

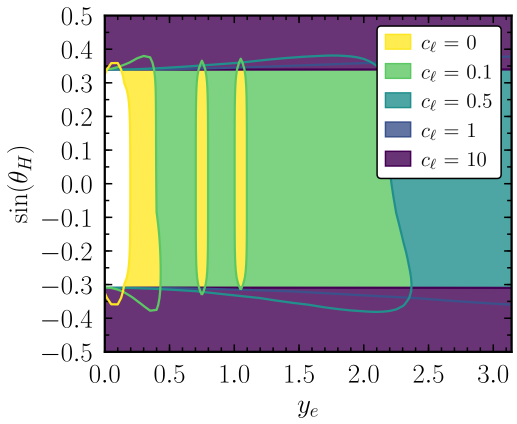

Figure 5.10: 95 % exclusion limits from signal strength measurements by *ATLAS* and *CMS* on the Higgs mixing angle and the heavy electron Yukawa couplings.

channels [241], both at a center-of-mass energy of 13 TeV, as well as the combination of 7 TeV and 8 TeV results from *ATLAS* and *CMS* [253]. The dashed orange line corresponds to the naive estimate (5.29).

The constraints on the Higgs mixing angle θ_H are shown in fig. 5.9 for the parameter values given in table 5.2. Signal strength measurements exclude $\sin\theta_H \gtrsim 0.27$, i.e. the limit in eq. (5.29) from the global signal strength overestimates the exclusion reach. Direct searches for additional scalars provide somewhat weaker constraints of around $\sin\theta_H \gtrsim 0.4$ for a large range of m_ϕ, but are stronger for scalar masses below the Higgs mass. The Higgs signal strength fits are more involved for m_ϕ near 125 GeV and for $m_\phi < 62.5$ GeV where the Higgs may decay into ϕ-pairs. The signal strength constraint shown in fig. 5.9 should be taken with a grain of salt in those regions.

If the new leptons have sizeable couplings to the Higgs boson, the Higgs signal strengths in different channels can vary due to the loop contributions to $h \to \gamma\gamma$ and $h \to Z\gamma$ decays. Figure 5.10 shows the current *LHC* limits from refs. [241, 251–253] as a function of the mixing angle and the heavy electron Yukawa couplings c_ℓ and y_e. If the Φ Yukawa coupling c_ℓ is small, the dark electrons gain their mass predominantly from EW symmetry breaking and hence strongly contribute to the $h \to \gamma\gamma$ rate. Thus, the Yukawa coupling to the Higgs doublet y_e is also restricted to be small. For large c_ℓ, the heavy electron contributions in eq. (5.33) are mass-suppressed, so that y_e can take large values without modifying $\Gamma(h \to \gamma\gamma)$ beyond the experimentally allowed limits.

Note that for $c_\ell = 0$ the charged heavy lepton masses are given by $m_{e_{4/5}} = \frac{y_e v_H}{\sqrt{2}}$. The *LEP* limit on the mass (see section 5.3.3) then constrains the Yukawa coupling to $y_e > 0.57$, hence the entire region allowed by $h \to \gamma\gamma$ and $h \to Z\gamma$ is excluded in this case. Similarly, section 5.1.3 implies $|y_e| < 0.24$ for $c_\ell = 0.1$ and $v_\Phi = 2$ TeV. Further

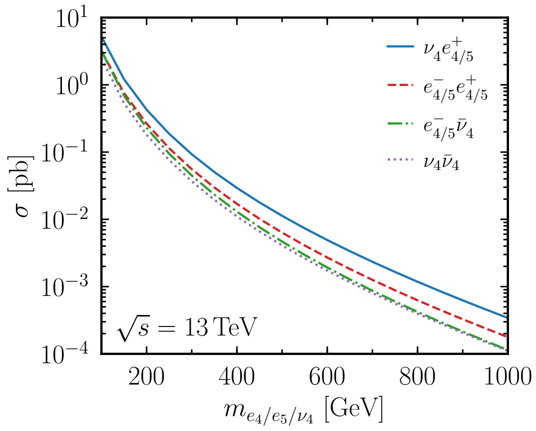

Figure 5.11: Production cross-sections for HL pairs at the *LHC* with a center-of-mass energy of 13 TeV, assuming equal masses for all HLs.

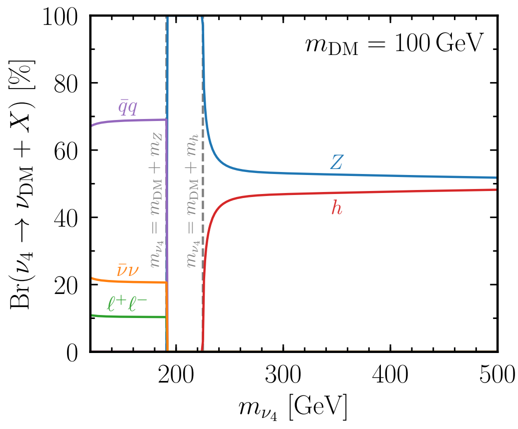

Figure 5.12: Branching ratios of the neutral HL, assuming $m_{e_4} = m_{e_5} \approx m_{\nu_4}$, $\sin\theta_{\text{DM}} = 0.01$, and a DM mass of 100 GeV.

note that the exclusion for $c_\ell = 10$ is shown despite severly challenging the bounds of perturbativity to illustrate the constraints in the limit of large c_ℓ.

5.3.3. Constraints on Heavy Leptons

Whereas the DM candidate is mostly an SM singlet, the remaining heavy leptons (HLs) carry EW charge and can hence be produced at colliders. Direct searches for heavy, charged leptons at *LEP* set a lower limit of roughly 100 GeV on the e_4 and e_5 mass [254]. *LHC* limits on the HLs can be obtained by recasting supersymmetry (SUSY) searches for electroweakly produced charginos and neutralinos.

Figure 5.11 shows the cross section for the production of two charged heavy leptons (dashed red), heavy positrons with a heavy neutrino (solid blue), heavy electrons with a heavy anti-neutrino (dash-dotted green), and pairs of heavy neutrinos (dotted purple) in proton-proton collisions at $\sqrt{s} = 13\,\text{TeV}$ calculated using CalcHep [238]. We here take the most optimistic scenario for HL production in which all HLs have the same mass. As the DM mixing angle θ_{DM} is restricted to be small by the direct detection constraints in section 5.2.2, and therefore only has a negligible effect on the production cross-section, it can be set to zero.

Due to the $U(1)$ symmetry that stabilizes the DM, the HLs can only decay amongst themselves or to dark matter. Consequently, to allow the lighter dark electron to decay, $\theta_{\text{DM}} \neq 0$ is required. Otherwise the model would have a charged DM population and therefore be excluded. However, even a (negligibly) small amount of DM mixing is sufficient to let the exotic particles decay fast enough to avoid this problem.

The charged HLs typically decay into DM and a (potentially off-shell) W boson. Depending on the masses, decays to other exotic leptons can also be possible. These are however suppressed by phase space. The heavy neutrino can decay to DM and a(n off-shell) Z boson or, if $m_{\nu_4} > m_{\text{DM}} + m_h$, to DM and an SM Higgs boson. In the latter case,

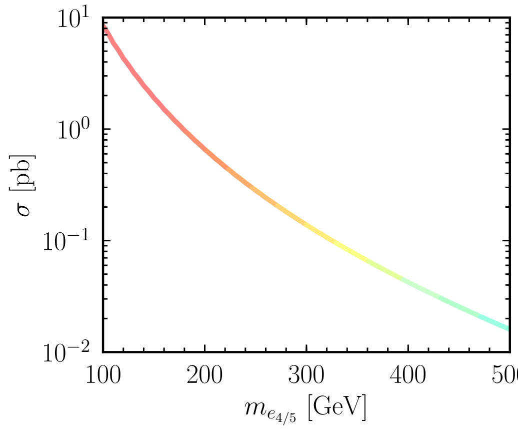

Figure 5.13: Total cross section for $pp \to e^{\pm}_{4/5}\nu_4$ production at $\sqrt{s} = 13\,\text{TeV}$ as a function of the HL mass. The colors resemble the color-coding of the cross section in [256].

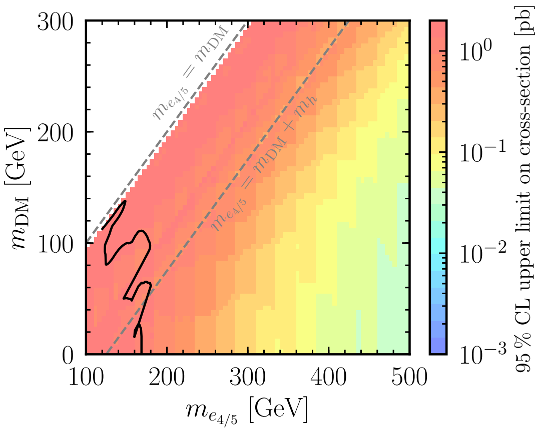

Figure 5.14: CMS 95 % exclusion limits from [256], assuming equal masses for all HLs and that they decay within the detector.

the branching rations to DM + Z and DM + h are roughly 50 %. Figure 5.12 shows the branching ratios of ν_4 as a function of the mass for a DM mass of 100 GeV and a mixing angle of $\sin\theta_{\text{DM}} = 0.01$.

At the *LHC*, the HLs can be searched for by looking for missing transverse energy (MET) in association with W, Z, or h bosons (or SM lepton pairs in the off-shell case). These searches have been performed by *ATLAS* [255] and *CMS* [256] in the context of simplified SUSY models, using $36\,\text{fb}^{-1}$ of data recorded at the *LHC* with $\sqrt{s} = 13\,\text{TeV}$. They assume that the lightest neutralino $\tilde{\chi}^0_1$ is the lightest supersymmetric particle (LSP) and consider the process $pp \to \tilde{\chi}^{\pm}_1\tilde{\chi}^0_2$, where the lightest chargino $\tilde{\chi}^{\pm}_1$ decays to the LSP plus a W boson, and the next-to-lightest neutralino $\tilde{\chi}^0_2$ to the LSP plus Z or h. The respective 95 % CL exclusion bounds from *CMS* can be found in fig. 8 of ref. [256].

The production cross-section for the corresponding process in our model is depicted in fig. 5.13, again assuming $\sin\theta_{\text{DM}} = 0$ and $m_{\text{HL}} \equiv m_{e_4} = m_{e_5} = m_{\nu_4}$. The respective exclusion bounds from *CMS* [256] are shown in fig. 5.14, taking the limits with $\text{Br}\left(\tilde{\chi}^0_2 \to \tilde{\chi}^0_1 Z\right) = 100\,\%$ for $m_{\text{DM}} < m_{\text{HL}} < m_{\text{DM}} + m_h$, and the limits assuming $\text{Br}\left(\tilde{\chi}^0_2 \to \tilde{\chi}^0_1 Z\right) = \text{Br}\left(\tilde{\chi}^0_2 \to \tilde{\chi}^0_1 h\right) = 50\,\%$ for $m_{\text{HL}} > m_{\text{DM}} + m_h$. The *LHC* can currently exclude HL masses below $m_{\text{HL}} \lesssim 180\,\text{GeV}$ and DM masses below $m_{\text{DM}} \lesssim 140\,\text{GeV}$. For the co-annihilation region discussed in section 5.2.1, the mass splitting between the charged states and the DM candidate becomes very small, so that the searches used here become inefficient. Instead it has been shown that these regions can be probed by mono-jet, mono-Z and disappearing track searches, with masses of up to 200 GeV reachable at the *LHC* and up to 1 TeV at a future hadron collider [257–262].

5.4. Intermediate Conclusion

We have presented a comprehensive study of the DM and collider phenomenology of a model in which lepton number is gauged, extending and updating the limits in ref. [5]. A mass for the lepton number Z' boson is generated via spontaneous breaking of the corresponding gauge symmetry, induced by the VEV of an SM singlet scalar field Φ with lepton number charge $L_\Phi = 3$. The model further features additional leptonic states, the presence of which is forced upon us by the necessity to cancel gauge anomalies associated with $U(1)_\ell$. These exotic leptons naturally give rise to a candidate of leptophilic DM.

Assuming that the DM is a thermal relic, we identified the regions of the parameter space in which the DM candidate can account for the full abundance measured by *Planck*. We found that the correct relic density can be reproduced for a broad extent of DM masses in the $\mathcal{O}(100\,\mathrm{GeV})$ to TeV range. This typically requires choosing $m_{Z'} \sim 2m_{\mathrm{DM}}$.

Direct and indirect detection experiments put limits on the DM interactions with SM fields. Direct detection constrains the various mixings that can give rise to DM-quark interactions. These are the SM doublet admixture into the singlet DM characterized by θ_{DM}, the kinetic mixing parameter ϵ of the lepton number and hypercharge gauge groups, and the mixing angle θ_H between the SM and the lepton-number Higgs. *XENON1T* can exclude ϵ and θ_{DM} in the percent range, and $\sin\theta_H \gtrsim \mathcal{O}(0.1)$; *LZ* and *DARWIN* can improve the limits by roughly an order of magnitude. Indirect detection on the other hand mainly probes Z' mediated DM-SM interactions. However, even the next-generation *CTA* is only sensitive for lepton number charges as large as $L' = 3/2$.

We also investigated collider constraints. The most important ones are *LEP* limits. These put a lower bound on the lepton number breaking scalar VEV $v_\Phi \gtrsim 1.88\,\mathrm{TeV}$, and exclude Z' masses below $m_{Z'} \simeq 200\,\mathrm{GeV}$, as well as charged exotic leptons below 100 GeV. The *LHC* can only put limits on the Z' mass if the kinetic mixing is $\epsilon \gtrsim \mathcal{O}(0.01 - 0.1)$, the *HL-LHC* with $3\,\mathrm{ab}^{-1}$ can reach $\epsilon \sim 10^{-3}$ for low Z' masses and even exclude $m_{Z'} \lesssim 500\,\mathrm{GeV}$ if $\epsilon = 0$. Current *LHC* measurements further exclude Higgs mixing angles $\sin\theta_H \gtrsim 0.27$ and constrain the exotic leptons' Yukawa couplings.

Having mapped out the phenomenologically viable parameter space of the model, we can now proceed and investigate the lepton number breaking PT as well as the detectability of the corresponding SGWB in chapter 7. Let us therefore hereby conclude part I of this thesis and move on to part II on constraining new physics using GWs generated in cosmological first-order PTs.

Part II

Gravitational Waves from Cosmological Phase Transitions

Prelude

Gravitational waves (GWs) are perturbations in the metric of space-time propagating at the speed of light, following as a consequence of Einstein's theory of general relativity (GR). Their existence was predicted by Albert Einstein in 1916 [263, 264].

First indirect evidence of GWs was provided in 1979 [265] through measurements of the Hulse-Taylor binary [266], a binary system of a pulsar and a neutron star (NS), for which Hulse and Taylor were awarded the 1993 Nobel prize in physics. Pulsars (see e.g. ref. [267] for a review) are highly magnetized NS that rotate rapidly and emit electromagnetic (EM) radiation along their magnetic axis. This beam of radiation then hits Earth periodically, resulting in light-house-like pulse signals that provide very accurate clocks. Timing of these pulses over a sufficiently large period of observation allows for a precise determination of the masses and orbit of the binary system. As the system looses energy due to emission of GWs, the orbit is expected to decay. The corresponding decrease of the orbital period could be observed in the Hulse-Taylor binary at a rate consistent with the predictions of GR [268] and is now established to agree with the GR prediction at a level of a few per mill [269].

On September 14, 2015, almost a century after Einstein's prediction, the first direct observation of GWs was achieved by the *Advanced LIGO (Laser Interferometer Gravitational-Wave Observatory)* interferometers [19]. The physics Nobel prize 2017 was awarded to Rainer Weiss, Barry Barish, and Kip Thorne for this ground-breaking discovery. The observed GW signal originated from the merger of two black holes (BHs) into a single BH. Since then, the *LIGO* and *Virgo* collaborations have reported 9 further observations of BH merger events as well as one NS merger during their first two observational runs, and 56 detection candidates from their third run. The direct detection of GWs has inspired a drastic increase in the interest in GW physics and the various ways it can be used to probe fundamental physics. It opens a new and unique window to the early Universe, allowing us to see much further into the past than ever before.

We prevalently observe our Universe through light. The potential for direct observations is therefore limited to the eras during which the Universe was transparent to EM radiation, to wit, the time after photon decoupling, a few hundred thousand years after the Big Bang at a temperature of roughly 1 eV [270].[1] When electrons and protons form neutral hydrogen atoms in the so-called recombination epoch, the number density of free electrons in the Universe drops rapidly and the processes that keep the photons in thermal equilibrium with the plasma of the early Universe (mainly Thompson scattering, $e^- + \gamma \to e^- + \gamma$) become inefficient. The photon interaction rate then drops below the

[1] Still, we have a reliable probe of an even earlier stage of the Universe — Big Bang Nucleosynthesis (BBN). The concordance of the observed abundances of light elements with the corresponding prediction of BBN indicates that it indeed proceeded as predicted in the Standard Models of particle physics and cosmology at a temperature around 1 MeV.

Hubble rate, the rate at which the Universe expands. As a consequence the photons decouple and are no longer in thermal equilibrium with the rest of the plasma; they now stream freely through the Universe. The relic photons from the time of recombination are today observed in the form of the cosmic microwave background (CMB). Although direct observations via photons are limited to the time after photon decoupling, even much earlier processes such as inflation may still be observable indirectly through their imprints in the CMB.

Due to the very weak coupling strength of gravity, GWs on the other hand decouple very early in the history of the Universe. The interaction rate Γ of particles in the early Universe is $\Gamma = n\sigma v$, where σ is the cross section, n is the number density (of the interaction partner), and v the (relative) velocity. As all species are relativistic at high temperatures, we can take $n \sim T^3$ and $v \sim c$, and the cross section for gravitons can be estimated as $\sigma \sim T^2/M_P^4$, where $M_P \sim 2 \times 10^{18}\,\text{GeV}$ is the Planck mass. The Hubble rate during radiation domination on the other hand is roughly given by $H \sim T^2/M_P$. Comparing the interaction rate of gravitons to the expansion rate of the Universe therefore yields

$$\frac{\Gamma(T)}{H(T)} \sim \left(\frac{T}{M_P}\right)^3 ,$$

i.e. gravitons decouple around the Planck scale. After that, they can propagate freely from the time of their production until today, therefore allowing us to directly observe the very early Universe.

Whereas the GWs observed so far all originate from single events at specific positions in the sky, namely mergers of BH or NS binaries, we are here interested in stochastic backgrounds of GWs, i.e. the superposition of many statistically independent GW events. In particular, GWs produced in the early Universe are typically of stochastic nature due to causality, as the correlation length of the source is limited by the horizon size at the time of production. A GW signal produced at a temperature of $100\,\text{GeV}$ (around the time of the electroweak (EW) phase transition) for instance could today be observed from $\sim 10^{24}$ independent regions on the sky [271]. Since the early Universe is (assumed to be) homogeneous and isotropic on large scales, the initial conditions for generating GWs are the same in all these patches, resulting in a stochastic gravitational wave background (SGWB).

The following part of this thesis is focused on the SGWB from cosmological phase transitions (PTs), and its potential for providing insights into new physics. The possibility to probe dark sector physics using GW signals from PTs was proposed in [272] and explored further in [273–281]. An introduction to SGWBs is provided in chapter 6, describing its main characteristics and detection prospects. We explain how PTs generate GWs and how the corresponding spectrum is calculated. As an example for the potential of probing new physics via GWs, chapter 7 considers the lepton number breaking PT in the gauged lepton number model introduced in chapter 5. Chapter 8 subsequently investigates PTs in decoupled hidden sectors, with particular focus on sub-MeV sectors and the interplay with constraints on the effective number of neutrino species.

6. Stochastic Gravitational Wave Backgrounds

A stochastic gravitational wave background (SGWB) is a gravitational wave (GW) signal produced by a large number of independent, unresolved, and weak sources, characterized only statistically (see e.g. refs. [271, 282–285]). It can be viewed as the GW equivalent of the cosmic microwave background (CMB). SGWBs can be generated by astrophysical sources, such as compact binaries of white dwarfs and super-massive black hole binaries (SMBHBs), or be of cosmological origin, such as quantum fluctuations of the vacuum generated during inflation, the decay of cosmic string loops, and cosmological first-order phase transitions (PTs).

The main characteristics of SGWBs are summarized in section 6.1. We then give a brief overview of current and future GW detectors in section 6.2, mostly focusing on those that are sufficiently sensitive to detect SGWBs, and describe how the sensitivity is evaluated in section 6.3. Section 6.4 subsequently focuses on SGWBs generated in cosmological first-order PTs, explaining the generation mechanism and how the corresponding spectrum is calculated. An integral ingredient for the calculation is the finite-temperature effective potential, which is shortly reviewed in section 6.5.

6.1. Characterization

SGWBs generated in the early Universe are usually assumed to be

isotropic. Since the early Universe was homogeneous and isotropic, as reflected in the isotropy of the CMB, a cosmological SGWB should also share this property.

unpolarized. As the Standard Model (SM) exhibits parity violation in the weak interactions only, there is no reason why a generic SGWB should be polarized. There are however mechanisms that can produce a polarized SGWB.

stationary. In other words, the statistical properties of the SGWB only depend on time differences, but not on absolute time. Comparing the age of the Universe of roughly 14 Gyr [60] to the maximal realistic observation period or around 10 yr, this assumption is almost certain to be true.

Gaussian. According to the central limit theorem, the sum of a large number of statistically independent random variables follows a Gaussian distribution. Some production mechanisms may however result in a non-Gaussian SGWB.

Based on these assumptions, SGWBs are typically described in terms of their fractional energy density (or density parameter) power spectrum, i.e. the energy density ρ_{GW} per logarithmic frequency interval normalized to the critical energy density $\rho_c = 3M_P^2 H^2$, where M_P is the reduced Planck mass and H is the Hubble rate,

$$\Omega_{\rm GW}(f) \equiv \frac{1}{\rho_c} \frac{\mathrm{d}\,\rho_{\rm GW}(f)}{\mathrm{d}\,\log f}\,. \tag{6.1}$$

As eq. (6.1) depends on the value of the Hubble rate due to the normalization to ρ_c, one typically rewrites the Hubble rate as $H = h \times 100\,\mathrm{km}\,\mathrm{Mpc}^{-1}\,\mathrm{s}^{-1}$ and reports limits on the quantity $h^2\Omega_{\rm GW}$.

6.2. Gravitational Wave Experiments

Over the past century, several methods for detecting GWs have been proposed and developed, ranging from simple resonant mass detectors to sophisticated interferometers in space.

The first GW detector was the Weber bar, proposed in 1960 [286] and constructed in 1966 [287] by Joseph Weber. It consisted of a 1.5 t aluminium cylinder with a length of ~ 150 cm and a resonance frequency of 1660 Hz. The basic idea was that an incident GW with a frequency close to the resonance frequency would induce a detectable change in the length of the cylinder. Using several of these cylinders, Weber claimed a detection of GWs in 1969 [288]. However, his claim could eventually not be supported.

Nowadays, we have two important classes of GW observatories at our disposal: GW interferometers and pulsar timing arrays (PTAs). The former can be subdivided into ground- and space-based observatories. Each of these types of experiments covers a different frequency range.

GW interferometers detect GWs by measuring the GW-induced motion of free-falling test masses via laser interferometry. The best-known, currently operating,[1] ground-based observatories are *LIGO* [289, 290] and *Virgo* [291, 292], which were recently joined on February 25, 2020, by the Japanese underground detector *KAGRA* [293, 294]. They have arm lengths of a few kilometers and are sensitive in the high-frequency range around $10\,\mathrm{Hz} - 10^4\,\mathrm{Hz}$. Whereas the sensitivity of the current experiments is typically insufficient to detect the SGWB from cosmological PTs, the next generation of ground-based interferometers, such as *ET* [295] or *CE* [296], will have a much higher sensitivity.

Space-based interferometers have the advantage that they overcome the limitation of ground-based interferometers to frequencies $f \gtrsim 1\,\mathrm{Hz}$ due to seismic noise. They can also have much longer arms and may therefore probe lower frequencies. The first space-based GW observatory is *LISA* [20], which will prospectively be launched in the mid 2030s [271].[2] It consists of three satellites arranged in a regular triangle with a side-length of 2.5×10^9 m, orbiting the sun roughly 20° behind Earth. *LISA* will be sensitive in the frequency range $0.1\,\mathrm{mHz} - 0.1\,\mathrm{Hz}$. Various successor experiments targeting the deci-Hertz region have already been proposed, including *BBO* [299], *DECIGO* [300, 301],

[1] Actually, the third observational run of *LIGO* and *Virgo* was suspended on March 27, 2020, (about a month before the scheduled end of the run) due to the COVID-19 pandemic.

[2] There are also plans for *LISA*-like Chinese projects, *Taiji* [297] and *TianQin* [298], which aim at a similar launch date.

and its scaled-down version *B-DECIGO* [302], the former two consisting of four copies of *LISA* (with shorter arms).

PTAs are a network of millisecond pulsars that detects GWs by monitoring the pulsars' times of arrival. An incident GW would emerge as a correlated change in the timing residuals of the pulsars. PTAs are sensitive to SGWBs in the low frequency range around $10^{-9}\,\mathrm{Hz} - 10^{-7}\,\mathrm{Hz}$, set by the total time of observation. Currently operating observatories are *EPTA* [303, 304], *NANOGrav* [305, 306], and *PPTA* [307], as well as their combination, *IPTA* [308, 309]. A planned, next-generation observatory, *SKA* [310], will prospectively start taking data in 2028 [311].

6.3. Detection and Sensitivity

The detectability of a given SGWB power spectrum $h^2\Omega_{\mathrm{GW}}$ is assessed based on the signal-to-noise ratio (SNR) ρ. We consider an SGWB detectable if the corresponding SNR exceeds a threshold value, $\rho > \rho_{\mathrm{thr}}$, where ρ_{thr} depends on the experiment under consideration.

For a network of detectors, such as PTAs or the *LIGO-Virgo* network, the optimal-filter cross-correlated SNR is given by

$$\rho^2 = 2\,T_{\mathrm{obs}} \int\limits_{f_{\mathrm{min}}}^{f_{\mathrm{max}}} \mathrm{d}f \left[\frac{h^2\Omega_{\mathrm{GW}}(f)}{h^2\Omega_{\mathrm{eff}}(f)}\right]^2 , \tag{6.2}$$

where T_{obs} is the observation period, $(f_{\mathrm{min}}, f_{\mathrm{max}})$ is the frequency bandwidth of the detectors, and $h^2\Omega_{\mathrm{eff}}$ is the effective noise of the network (see appendix 6.A for details) in fractional energy density. The auto-correlated SNR for a single detector can be obtained by omitting the factor 2 in eq. (6.2). The effective noise of various GW observatories is shown in fig. 6.1, along with the expected background from SMBHBs [306, 312]. Analytic expressions for the noise spectra as well as the corresponding values of the SNR threshold used in this dissertation can be found in ref. [2].

While eq. (6.2) allows us to calculate whether a given GW spectrum is detectable or not, the effective noise curves $h^2\Omega_{\mathrm{eff}}$ are not suitable for a graphical evaluation of the detectability. To provide a simple way to visualize if a SGWB spectrum can be detected by a given experiment, one usually employs so-called power-law integrated (PLI) sensitivity curves [313]. To construct the PLI curves, the signal is assumed to follow a simple power-law,

$$h^2\Omega_{\mathrm{GW}} = h^2\Omega_\beta \left(\frac{f}{f_{\mathrm{ref}}}\right)^\beta , \tag{6.3}$$

where f_{ref} is an arbitrary reference frequency. For a fixed value of the exponent β and a given experiment, one can then invert eq. (6.2) to calculate the minimal detectable amplitude $h^2\Omega_\beta^{\mathrm{thr}}$ for which $\rho = \rho_{\mathrm{thr}}$. The PLI sensitivity $h^2\Omega_{\mathrm{PLI}}$ is obtained by taking the envelope of the minimal detectable power-law spectra over all values of β,

$$h^2\Omega_{\mathrm{PLI}}(f) = \max_\beta \left[h^2\Omega_\beta^{\mathrm{thr}} \left(\frac{f}{f_{\mathrm{ref}}}\right)^\beta\right] . \tag{6.4}$$

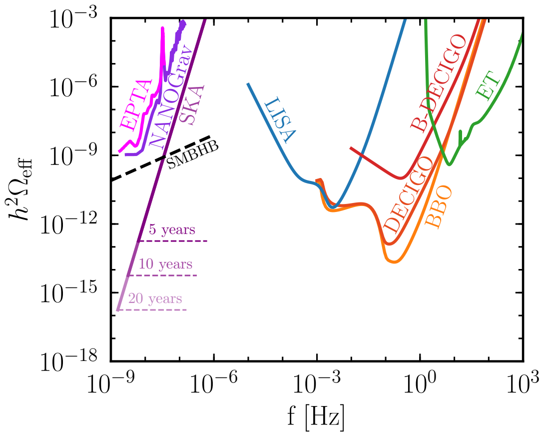

Figure 6.1: Energy density noise $h^2\Omega_{\text{eff}}$

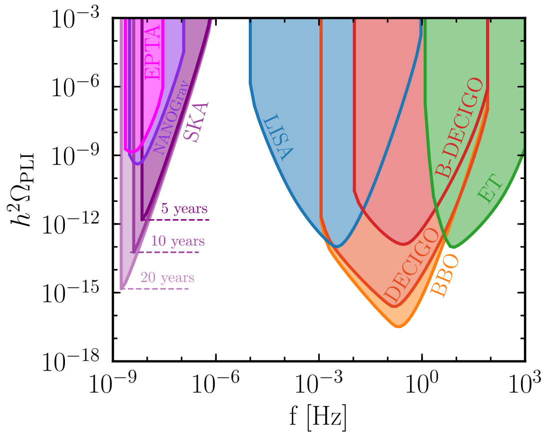

Figure 6.2: PLI sensitivity $h^2\Omega_{\text{PLI}}$

The region enclosed by the PLI curve is then interpreted as the region to which the experiment is sensitive, i.e. a spectrum that reaches into the region above the PLI sensitivity curve is detectable. Although this is strictly speaking only true for simple power-law spectra of the form in eq. (6.3), SGWBs can typically be approximated by power-laws at least over a large fraction of the experiment's frequency band, so that this method is applicable.

Figure 6.2 shows the PLI spectra corresponding to the noise curves in fig. 6.1 along with some example spectra (see section 6.4.3 for details). Note that we assume that the SMBHB background can be resolved and subtracted. Throughout this work, we will use the SNR, eq. (6.2), to assess the detectability of an SGWB numerically, and the PLI curves in eq. (6.4) for graphical representation of the sensitivity.

6.4. Cosmological Phase Transitions

Throughout most of its evolution, our Universe is very well described as a hot plasma of particles in local thermal equilibrium at a temperature T.[3] As the Universe keeps expanding adiabatically, its temperature decreases at a rate determined by the energy content. During this process it most probably went through at least two PTs: the electroweak PT (EWPT), and the confining PT of quantum chromodynamics (QCD).

A cosmological PT is a transition between different vacua, often associated with the breaking of a global or local symmetry. More generally, PTs can be defined as "a line in the (T, μ)-plane across which the grand canonical free energy density $f(T, \mu)$ is non-analytic" [314], where μ is the chemical potential. This non-analyticity across the line separating the phases is typically related to the change in an order parameter given by the vacuum expectation value (VEV) of an elementary or composite field, such as the Higgs' VEV in the case of the EWPT, spontaneously breaking $SU(2)_L \times U(1)_Y \to U(1)_{\text{EM}}$, or the quark condensate of QCD confinement breaking chiral symmetry.

[3] As we will discuss in chapter 8, the various components of the plasma do not need to be in thermal contact with one-another and may therefore have different temperatures.

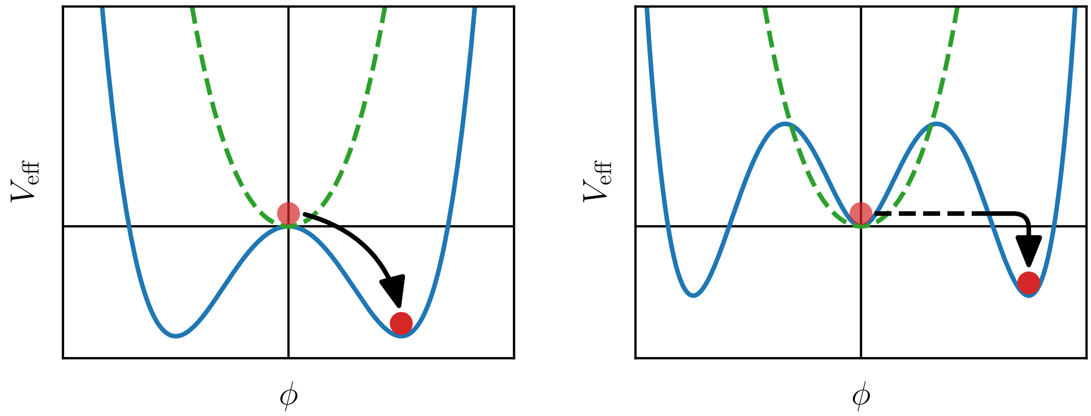

(a) cross-over (b) first-order

Figure 6.3: Illustration of a cross-over (left) and first-order PT (right).

In quantum field theory (QFT), vacua are given by the minima of the effective potential $V_{\rm eff}(\phi, T)$, which is the potential of the order parameter[4] $\langle\phi\rangle$ incorporating quantum and thermal corrections. Further details on the effective potential shall be deferred to section 6.5. At high temperatures, it is typically dominated by terms of the form $\phi^2 T^2$, which then restore spontaneously broken symmetries. As a consequence, theories that experience spontaneous symmetry breaking (SSB) have generically undergone a symmetry-breaking PT in the early Universe, as understood by Kirzhnits and Linde in 1972 [315].

We commonly distinguish between two types of PTs: first-order and higher-order transitions. Formally, a first-order PT is a PT in which the derivative of the free energy density with respect to a thermodynamic parameter, e.g. temperature, is discontinuous. Similarly, higher-order PTs have discontinuities in higher-order derivatives (and are continuous in the lower-order ones). Finally, in a cross-over all derivatives are continuous.[5] Since only first-order PTs can generate GWs, we will henceforth only distinguish between first-order and cross-over transitions, including all higher-order transitions in the latter category. In the SM, both, the electroweak (EW) and QCD PT, are cross-overs. Their nature may however change if new physics contributions are taken into account.

The important distinction between first-order and cross-over PTs lies in the way the order parameter, i.e. the VEV of ϕ, changes. This is illustrated in fig. 6.3, where the effective potential $V_{\rm eff}$ is shown as a function of ϕ. The dashed green lines depict the potential at high temperatures, which has a single minimum at the origin, whereas the solid blue lines are the low-temperature potential.

In a cross-over (fig. 6.3a), as the Universe cools down, the high-temperature minimum turns into a maximum at low temperatures and the potential develops a minimum at non-vanishing field values. The field ϕ can then smoothly "roll down" the potential to transition from the high- to the low-temperature vacuum. In the case of a first-order

[4]For simplicity, we here assume a single order parameter and vanishing chemical potential.

[5]Strictly speaking, a cross-over does therefore not correspond to a PT according to the definition above.

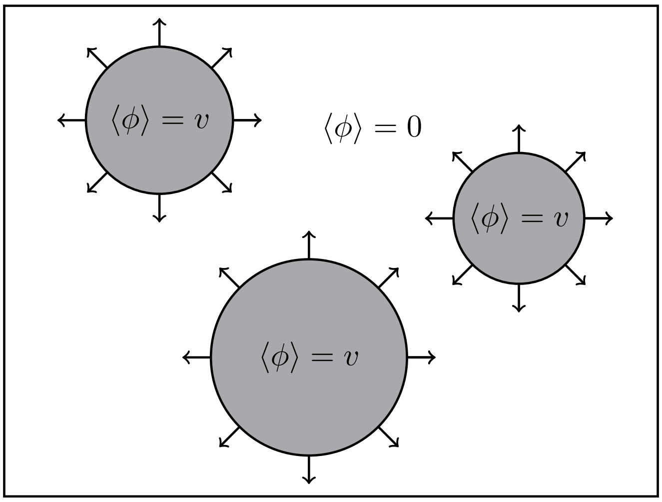

Figure 6.4: Illustration of a first-order PT via the nucleation of bubbles of the true vacuum inside the false-vacuum phase.

PT (fig. 6.3b) on the other hand, the high-temperature minimum still persists at low temperatures as a local minimum, but the global minimum again lies at non-vanishing field values. However, the two minima are now separated by a potential barrier, such that the field cannot smoothly evolve from the false (local) vacuum to the true (global) one. Instead, in a first-order PT the field has to thermally fluctuate over or quantum tunnel through the barrier.

It is this tunneling process through which first-order PTs generate a SGWB. We therefore provide more details on the process in section 6.4.1. Subsequently, section 6.4.2 introduces the parameters used to characterize the PTs. Finally, the corresponding generation mechanisms for the SGWB is explained in section 6.4.3.

6.4.1. Bubble Nucleation

A cosmological first-order PT proceeds through the nucleation of bubbles of the true vacuum in the sea of the false vacuum. At high temperatures, the Universe, depicted as a box in fig. 6.4, is in the false-vacuum phase, which we here assume to be characterized by a vanishing VEV, $\langle\phi\rangle = 0$. As the Universe cools down, a second minimum, the true vacuum, starts to form at $\langle\phi\rangle = v$. When the true vacuum becomes energetically favorable, the field tunnels at random points of the Universe, forming spherical bubbles inside of which the fields is in the true vacuum, shown in gray in fig. 6.4.

Driven by the energy release from the potential difference in the tunneling, the bubbles subsequently expand, provided that the energy gain exceeds the surface energy of the bubbles (otherwise they collapse). The nucleation of the expanding vacuum bubbles then competes against the expansion of the Universe. If the bubbles are nucleated sufficiently fast to overcome the Hubble expansion, the bubbles will collide and merge, and eventually fill the whole Universe with the true vacuum.

The bubble nucleation rate per unit volume is given by [316–320]

$$\Gamma = \begin{cases} R_0^{-4} \left(\frac{S_{E,4}}{2\pi}\right)^2 \exp\left(-S_{E,4}\right) & \text{for quantum tunneling,} \\ T^4 \left(\frac{S_{E,3}}{2\pi T}\right)^{\frac{3}{2}} \exp\left(-\frac{S_{E,3}}{T}\right) & \text{for thermal fluctuations,} \end{cases} \tag{6.5}$$

where R_0 is the radius of the nucleated bubble, and the d-dimensional Euclidean action $S_{E,d}$ is given by

$$S_{E,d} = \Omega_d \int_0^\infty \mathrm{d}r \left[\frac{1}{2}\left(\frac{\mathrm{d}\,\phi_b}{\mathrm{d}\,r}\right)^2 + V(\phi_b)\right], \tag{6.6}$$

evaluated at the $O(d)$ symmetric bounce solution ϕ_b that satisfies the differential equation

$$\frac{\mathrm{d}^2\,\phi_b}{\mathrm{d}\,r^2} + \frac{d-1}{r}\frac{\mathrm{d}\,\phi_b}{\mathrm{d}\,r} = V'(\phi_b)\,. \tag{6.7}$$

Here, Ω_d is the solid angle in d dimensions ($\Omega_3 = 4\pi$ and $\Omega_4 = 2\pi^2$), V is given by the effective potential at finite or zero temperature, respectively, shifted such that $V = 0$ in the false vacuum, and V' is its derivative with respect to ϕ.

Let us now define two characteristic temperatures of first-order PTs: the critical temperature T_c and the nucleation temperature T_n. The critical temperature is simply the temperature at which the true and the false vacuum become degenerate, i.e. $V_{\text{eff}}(\phi_t, T_c) = V_{\text{eff}}(\phi_f, T_c)$, where ϕ_t and ϕ_f are the field values of the true and false vacuum, respectively. This is the temperature below which it is in principle possible to nucleate bubbles of the true vacuum. However, as discussed above, the transition does not occur unless bubbles are nucleated sufficiently fast to overcome the Hubble expansion. This defines the nucleation temperature, at which the probability that on average one bubble has been nucleated per Horizon volume is of order one.

The nucleation temperature can be roughly estimated by taking $\Gamma(T_n)/H^4(T_n) \sim 1$. Assuming thermal tunneling with $\Gamma \sim T^4 \exp\left(-S_{E,3}/T\right)$ and a radiation dominated Universe with Hubble rate and energy density given by

$$H^2(T) = \frac{\rho_{\text{rad}}(T)}{3M_P^2}\,, \qquad \text{and} \qquad \rho_{\text{rad}}(T) = \frac{\pi^2}{30}\, g_\star(T)\, T^4\,, \tag{6.8}$$

where $g_\star$ is the effective number of relativistic degrees of freedom (DOFs), we obtain

$$\frac{S_{E,3}(T_n)}{T_n} \sim 146 - 4\log\left(\frac{T_n}{100\,\text{GeV}}\right) - 2\log\left(\frac{g_\star(T_n)}{100}\right). \tag{6.9}$$

Unless specified otherwise, we therefore use the condition $S_{E,3}(T)/T = 140$ to determine the nucleation temperature T_n.

We can further define the temperature at which the transition is completed as the temperature at which an order one fraction of the Universe has transitioned to the true vacuum. However, in this dissertation we are only going to deal with PTs with no significant super-cooling (i.e. the Universe is not going to be dominated by vacuum energy), transitioning fast enough to assume an instant transition and ignore the change of temperature during the PT.

6.4.2. Phase Transition Parameters

A cosmological first-order PT can be characterized by four parameters: the temperature T_* at which the transition occurs, the energy budget α, the inverse duration β, and the wall velocity v_w at which the bubble walls move. Here, we will only consider fast transitions for which we can take $T_* = T_n$. In the remainder of this section, all functions of T should be understood to be evaluated at $T = T_*$.

The energy budget of a PT is defined by the energy released in the tunneling, given by the latent heat $\mathcal{E}$,[6] normalized to the energy density in radiation at the time of the transition,

$$\alpha = \frac{\mathcal{E}}{\rho_{\rm rad}} = \frac{1}{\rho_{\rm rad}} \left(\Delta V_{\rm eff} - T \, \frac{\partial \, \Delta V_{\rm eff}}{\partial T} \right) , \tag{6.10}$$

where $\Delta V_{\rm eff} \equiv V_{\rm eff}(\phi_f(T), T) - V_{\rm eff}(\phi_t(T), T)$ is the potential difference between the false and true vacuum at temperature T. This can be interpreted as the strength of the PT.

The inverse duration of the transition is approximately given by the relative change of the nucleation rate, $\beta = \dot{\Gamma}/\Gamma$. This parameter is usually normalized to the Hubble rate at the time of the transition. Using $H \equiv \dot{a}/a$, and assuming an adiabatically expanding Universe with $s(T)a^3 \sim T^3 a^3 = \text{const}$, we obtain

$$\frac{\beta}{H} = \frac{1}{H} \frac{\mathrm{d} \, \log \Gamma}{\mathrm{d}\, t} = \frac{\mathrm{d} \, \log \Gamma}{\mathrm{d} \, \log a} = - \frac{\mathrm{d} \, \log \Gamma}{\mathrm{d} \, \log T} = T \frac{\mathrm{d}}{\mathrm{d}\, T} \frac{S_{E,3}}{T} , \tag{6.11}$$

where we neglected the time/temperature dependence of the prefactor of the thermal tunneling rate in eq. (6.5).

While the quantities discussed above only depend on equilibrium properties and can be directly calculated from the effective potential or the tunneling rate, the velocity v_w at which the bubble walls move is a more complicated beast. It depends on the friction exerted on the bubble walls by the particles of the plasma that gain a mass in the transition. The wall velocity therefore depends on microscopic properties of the plasma and out-of-equilibrium dynamics [321–323]. However, the generation of an observable SGWB requires the PT to be strongly first-order, which typically comes along with large wall velocities. Unless specified otherwise, we will therefore simply assume $v_w \simeq 1$ throughout this thesis.

Although we can be ignorant about the exact value of v_w, the wall dynamics have an important impact on the way GWs are generated in the transition, as it determines the amount of latent heat that is transferred into bulk motion of the primordial plasma. One therefore distinguishes between two regimes: runaway and non-runaway [324, 325]. In the runaway regime, the friction exerted by the plasma is insufficient to prevent the bubble walls from accelerating perpetually. As a consequence, only little energy is transferred to the plasma and most of the energy release goes into the acceleration of the bubbles. If, on the other hand, the friction is sufficiently strong, the bubbles reach a terminal boost factor. The latent heat is then efficiently converted into plasma motion.

[6] Alternatively, one often defines α via the change in the trace of the energy-momentum tensor, $\alpha \equiv \left(\Delta V_{\rm eff} - \frac{1}{4} \frac{\partial}{\partial T} \Delta V_{\rm eff} \right) / \rho_{\rm rad}$. For strong PTs, the $\Delta V_{\rm eff}$ part dominates and both definitions coincide.

At leading order (LO), the latent heat required to enter a runaway regime (normalized to the radiation energy density) can be estimated as [321, 324]

$$\alpha_\infty = \frac{1}{\rho_{\mathrm{rad}}} \left(\sum_{\mathrm{bosons}} n_i \, \frac{T^2}{24} \, \Delta m_i^2 \; + \sum_{\mathrm{fermions}} n_i \, \frac{T^2}{48} \, \Delta m_i^2 \right) , \tag{6.12}$$

where n_i and Δm_i^2 are the number of DOFs and squared mass difference of species i between the two phases, respectively. Transitions with $\alpha > \alpha_\infty$ run away, whereas the ones with $\alpha < \alpha_\infty$ do not. However, it has been shown that in the case that the particles gaining a mass are coupled to gauge bosons, next-to-leading order (NLO) corrections due to transition radiation from the particles crossing the wall produce a friction proportional to the wall boost factor γ [325]. Therefore, a runaway is prevented in this case. We can, however, still treat $v_w \simeq 1$ [325].

6.4.3. Generation of a Stochastic Gravitational Wave Background

The possibility of generating GWs in a cosmological first-order PT was realized in the mid 1980's by Witten [326] and Hogan [327]. The generation of the GWs occurs via three mechanisms: collisions of the vacuum bubbles, collisions of sound waves in the primordial plasma of the Universe, and turbulence. Each of these mechanisms results in a contribution to the GW power spectrum,

$$h^2\Omega_{\mathrm{GW}}(f) = h^2\Omega_\phi(f) + h^2\Omega_{\mathrm{sw}}(f) + h^2\Omega_{\mathrm{turb}}(f) \, . \tag{6.13}$$

Recall that a first-order PT proceeds via the nucleation of bubbles of the true vacuum inside the false vacuum. The energy freed in the tunneling process can, however, not be released into GWs due to the spherical symmetry of the bubbles. According to the famous quadrupole formula, the generation of GWs requires a quadrupole moment that varies in time. The latent heat can therefore only drive the expansion of the bubbles. However, as soon as two of these bubbles collide, the spherical symmetry is broken and GWs are generated. This yields the first contribution to the spectrum, the scalar field contribution $h^2\Omega_\phi$. It is commonly calculated using the envelope approximation [328], which assumes that most of the energy is stored in a thin shell around the bubble walls and only considers the envelope of the collided bubbles as illustrated in black in fig. 6.5.

For the other two contributions we need to take into account that the transition happens in the early Universe, where a thermal plasma of particles is present. If the scalar field (or operator) that acquires a VEV couples to this plasma, the expanding bubbles will induce acoustic waves in it. These sound waves also form bubbles, that expand at the speed of sound, depicted in red in fig. 6.5. The sound bubbles then emit GWs upon collision, producing the sound wave contribution $h^2\Omega_{\mathrm{sw}}$. As the collisions of acoustic waves provide a much longer lasting source than the initial vacuum bubble collisions, this contribution typically dominates the spectrum if present.

Finally, the expanding bubbles also induce vortical motions and eddies in the fluid, depicted in blue in fig. 6.5. These give rise to GWs generated from magnetohydrodynamic (MHD) turbulence. The corresponding GW spectrum is denoted as $h^2\Omega_{\mathrm{turb}}$. This

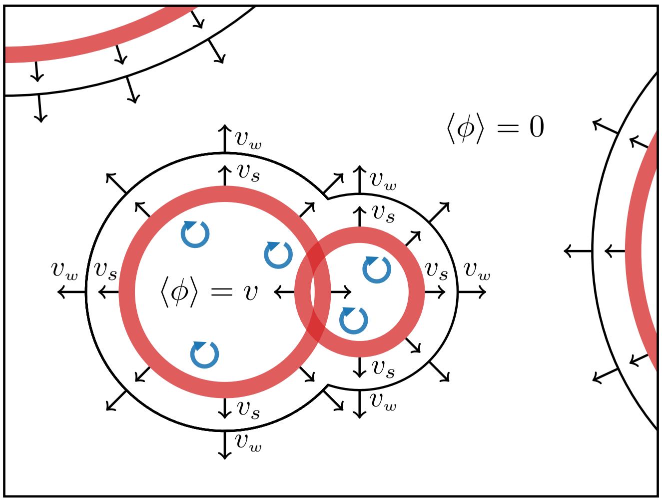

Figure 6.5: Illustration of the generation of GWs in a first-order PT from vacuum bubble collisions (black), sound waves (red), and turbulences (blue).

contribution is typically negligible compared to the sound wave contribution, unless the sound waves last less than a Hubble time.

The spectra for the respective contributions are obtained from analytic arguments and numerical simulations. In terms of the parameters introduced in section 6.4.2, we will use the following expressions throughout this work [329–332].

$$h^2\Omega_\phi(f) = \mathcal{R}\,\frac{0.11 v_w^3}{0.42+v_w^2}\left(\frac{H}{\beta}\right)^2\left(\frac{\kappa_\phi\,\alpha}{1+\alpha}\right)^2\,\mathcal{S}_\phi(f)\,, \tag{6.14a}$$

$$h^2\Omega_{\rm sw}(f) = \mathcal{R}\;\;0.159\,v_w\left(\frac{H}{\beta}\right)\left(\frac{\kappa_{\rm sw}\,\alpha}{1+\alpha}\right)^2\,\mathcal{S}_{\rm sw}(f)\,, \tag{6.14b}$$

$$h^2\Omega_{\rm turb}(f) = \mathcal{R}\;\;20.1\,v_w\left(\frac{H}{\beta}\right)\left(\frac{\kappa_{\rm turb}\,\alpha}{1+\alpha}\right)^{\frac{3}{2}}\,\mathcal{S}_{\rm turb}(f)\,. \tag{6.14c}$$

The spectral shapes $\mathcal{S}$ are given by

$$\mathcal{S}_\phi(f) = \frac{3.8\,(f/f_\phi)^{2.8}}{1+2.8\,(f/f_\phi)^{3.8}}\,, \tag{6.15a}$$

$$\mathcal{S}_{\rm sw}(f) = \left(\frac{f}{f_{\rm sw}}\right)^3\left[\frac{7}{4+3\,(f/f_{\rm sw})^2}\right]^{\frac{7}{2}}\,, \tag{6.15b}$$

$$\mathcal{S}_{\rm turb}(f) = \left(\frac{f}{f_{\rm turb}}\right)^3\left[\frac{1}{1+(f/f_{\rm turb})^2}\right]^{\frac{11}{3}}\frac{1}{1+8\pi f/h_*}\,. \tag{6.15c}$$

The corresponding peak frequencies at production are roughly set by the transition time scale β. After red-shifting to today they become

$$f_\phi = \frac{0.62\,h_*}{1.8-0.1v_w+v_w^2}\left(\frac{\beta}{H}\right)\,,\qquad f_{\rm sw} = \frac{2\,h_*}{\sqrt{3}\,v_w}\left(\frac{\beta}{H}\right)\,,\qquad f_{\rm turb} = \frac{3.5\,h_*}{2\,v_w}\left(\frac{\beta}{H}\right)\,. \tag{6.16}$$

The Hubble rate at production red-shifted to today, h_*, and the red-shift factor $\mathcal{R}$ for the amplitude (also accounting the change of the critical energy density $\rho_c = 3\,M_P^2 H^2$) are

$$h_* = \frac{a_*}{a_0} H_* = 3.2 \times 10^{-32} \left(\frac{g^0_{\star S}}{g^*_{\star S}}\right)^{\frac{1}{3}} \sqrt{g^*_\star}\, T_* = 16.5\,\mu\mathrm{Hz} \left(\frac{T_*}{100\,\mathrm{GeV}}\right) \left(\frac{g^*_\star}{100}\right)^{\frac{1}{6}}, \tag{6.17a}$$

$$\mathcal{R} = \left(\frac{a_*}{a_0}\right)^4 \left(\frac{H_*}{H_{100}}\right)^2 = 2.473 \times 10^{-5} \left(\frac{g^0_{\star S}}{g^*_{\star S}}\right)^{\frac{4}{3}} \left(\frac{g^*_\star}{g^0_\star}\right) = 1.67 \times 10^{-5} \left(\frac{g^*_\star}{100}\right)^{-\frac{1}{3}}, \tag{6.17b}$$

where quantities with index '0' ('$*$') are evaluated today (at emission), $g_\star$ and $g_{\star S}$ are the relativistic and entropic effective DOFs, respectively, and $H_{100} = 100\,\mathrm{km\,Mpc^{-1}\,s^{-1}}$. We have inserted eq. (6.8) and assumed conservation of co-moving entropy, $a^3(T)s(T) \propto a^3(T) g_{\star S}(T) T^3 = \mathrm{const}$, as well as $T_0 = 2.35 \times 10^{-13}\,\mathrm{GeV}$ [68, 333], $g^0_\star = 2$ and $g^0_{\star S} = 3.909$ [334] for the photon temperature and effective DOFs today. In the last step we have assumed that the number of entropic and radiation DOFs at the time of the transition do not differ, i.e. $g^*_\star = g^*_{\star S}$.

Finally, we need the efficiency factors κ_ϕ, κ_{sw}, and κ_{turb} for the conversion of latent heat into acceleration of the bubble walls, bulk motion of the plasma, and MHD turbulence, respectively. Whether the GW spectrum is dominated by the vacuum bubble collisions or the plasma contributions depends on the behavior of the bubble walls. If the coupling to the plasma is sufficiently strong to prevent runaway, the contribution $h^2\Omega_\phi$ from the collisions of vacuum bubbles can be neglected and only the plasma contributions are relevant. In this case, we can set $\kappa_\phi = 0$, and the efficiency factor for the sound wave contribution is [321]

$$\kappa_{\mathrm{sw}} = \kappa(\alpha) = \frac{\alpha}{0.73 + 0.083\sqrt{\alpha} + \alpha}\,, \tag{6.18}$$

provided that $v_w \sim 1$. If, on the other hand, the bubbles enter the runaway regime, only a fraction α_∞/α of the latent heat can be converted into bulk motion of the plasma, with α_∞ given by eq. (6.12). The surplus energy is then goes into the acceleration of the bubble walls. The efficiency factors for the vacuum bubble and sound wave collisions then become

$$\kappa_\phi = 1 - \frac{\alpha_\infty}{\alpha}\,, \qquad \text{and} \qquad \kappa_{\mathrm{sw}} = \frac{\alpha_\infty}{\alpha}\,\kappa(\alpha_\infty)\,. \tag{6.19}$$

In both cases, the amount of latent heat converted to turbulence is only a fraction of the sound wave efficiency, $\kappa_{\mathrm{turb}} = \varepsilon_{\mathrm{turb}} \kappa_{\mathrm{sw}}$, where $\varepsilon_{\mathrm{turb}} \simeq 5\,\% - 10\,\%$.

The reader should be aware that the expressions for the GW spectrum quoted above reflect the state of the art around the time the works [1] and [2] were published. As the field is currently developing quickly, further progress has been achieved, including more recent simulations of the scalar field and sound wave contributions [335, 336] and improved perceptions regarding the energy budget of the transition and the life time of sound waves in the plasma [320, 337–339] .

6.5. The Effective Potential

When being introduced to SSB, one typically studies the vacuum of a theory by minimizing the potential (i.e. the non-derivative part of the negative Lagrangian) with respect to the fields, assuming that the vacuum states of the fields are constant in space-time. While this is correct in classical field theory, the quantum nature of the fields in a QFT gives rise to quantum corrections, which need to be taken into account. In the early Universe, the presence of a thermal bath of particles further requires the incorporation of thermal effects. This is done by the effective potential V_{eff}, which is the potential of the fields including quantum and thermal corrections. As should be apparent from the previous section, the effective potential plays an integral role in the determination of the parameters characterizing a cosmological PT and the corresponding GW spectrum.

In the following, the most important formulae for the calculation of the effective potential will be summarized. Further details, including a formal definition of the effective potential, are included in appendix 6.B.

At the one-loop level, the finite-temperature effective potential including daisy-resummation[7] is given by

$$V_{\text{eff}}(\phi, T) = V_{\text{tree}}(\phi) + V_{\text{CW}}(\phi) + \Delta V_{\text{ct}}(\phi) + V_{\text{T}}(\phi, T) + V_{\text{ring}}(\phi, T)\,, \tag{6.20}$$

where ϕ denotes the classical background fields (potentially more than one), V_{tree} is the tree-level potential, V_{CW} are the one-loop zero-temperature or Coleman-Weinberg [340] corrections, ΔV_{ct} includes counter-terms, V_{T} are the one-loop thermal corrections, and V_{ring} resums the leading contributions from higher-loop diagrams (ring diagrams).

The dimensionally regularized and renormalized Coleman-Weinberg [340] corrections in Landau gauge evaluate to

$$V_{\text{CW}}(\phi) = \sum_i \frac{\eta_i\, n_i}{64\pi^2} m_i^4(\phi) \left[\log\left(\frac{m_i^2(\phi)}{\mu_R^2}\right) - C_i\right]\,, \tag{6.21}$$

where the sum runs over all particle species that couple to the fields ϕ, $m_i^2(\phi)$ and n_i are the field-dependent squared masses and DOFs[8] of species i, $\eta_i = +1\ (-1)$ for bosons (fermions), and $C_i = 3/2\ (5/6)$ for scalars and fermions (gauge bosons). The renormalization scale μ_R is typically chosen to be the magnitude of the zero-temperature VEV of ϕ. In eq. (6.21), ultraviolet (UV) divergences are canceled using $\overline{\text{MS}}$ counter-terms. If further renormalization conditions are imposed, we need to include the finite part of the counter-terms (or the difference to the $\overline{\text{MS}}$ ones, to be more precise) represented by $\Delta V_{\text{ct}}(\phi)$ in eq. (6.20).

The finite-temperature one-loop corrections are given by [341]

$$V_{\text{T}}(\phi, T) = \sum_i \frac{\eta_i\, n_i\, T^4}{2\pi^2} \int_0^\infty \mathrm{d}x\, x^2 \log\left[1 - \eta_i \exp\left(-\sqrt{x^2 + \frac{m_i^2(\phi)}{T^2}}\right)\right]\,, \tag{6.22}$$

[7] I.e. resumming the leading higher-loop corrections, see appendix 6.B.3.

[8] Note that, as we are working in Landau gauge, both, massive gauge bosons and the corresponding would-be Goldstone bosons, contribute with three and one polarization DOF, respectively.

which can be expanded for high temperatures as [341]

$$V_{\mathrm{T}}(\phi,T) = T^4 \sum_{\mathrm{bosons}} n_i \left[\frac{1}{24}\frac{m_i^2(\phi)}{T^2} - \frac{1}{12\pi}\left(\frac{m_i^2(\phi)}{T^2}\right)^{\frac{3}{2}} \right] - T^4 \sum_{\mathrm{fermions}} n_i \left[\frac{1}{48}\frac{m_i^2(\phi)}{T^2} \right] + \dots\,, \quad (6.23)$$

where field-independent and higher-order terms in m^2/T^2 have been dropped. As the squared masses typically grow with the square of the fields, $m^2(\phi) \sim \phi^2$, the dominant field-dependent part at high temperatures then goes like $T^2\phi^2$ and therefore restores broken symmetries in the early Universe.

In addition to the thermal one-loop corrections, we also take into account the so-called ring or daisy contributions. These arise from the inclusion of the leading higher-loop corrections by resumming the high-temperature thermal mass corrections to the Matsubara zero-mode propagator in the one-loop potential. The corresponding corrections are [342]

$$V_{\mathrm{ring}}(\phi,T) = -\frac{T}{12\pi} \sum_{\mathrm{bosons}} n_i \left[\Big(m^2(\phi) + \Pi(T)\Big)_i^{\frac{3}{2}} - \Big(m^2(\phi)\Big)_i^{\frac{3}{2}} \right]\,, \quad (6.24)$$

where $\Pi(T)$ are the thermal Debye masses evaluated in the high-temperature limit, and $(m^2(\phi) + \Pi(T))_i$ is the i-th eigenvalue of the full (tree-level + thermal) mass matrix [343]. Note that for gauge bosons only the longitudinal mode receives thermal mass corrections, whereas the Debye mass of the transverse modes vanishes.

Appendix of Chapter 6

Appendix 6.A. Signal-to-Noise Ratio

In this appendix we provide a brief outline of the derivation of the SNR eq. (6.2) based on the reviews [282–284] as well as ref. [313]. To relate the SGWB power spectrum to its response in a detector, we here start from the expression for the corresponding metric perturbation h_{ab}, and then derive the pairwise-correlated optimal-filter SNR for a network of detectors.

The plane wave expansion of a GW in transverse traceless (TT) gauge is given by

$$h_{ab}(t,\vec{x}) = \int_{-\infty}^{\infty} \mathrm{d}f \int_{S^2} \mathrm{d}^2\hat{k} \sum_{A=+,\times} h_A(f,\hat{k})\, \epsilon^A_{ab}(\hat{k})\, e^{2\pi i f(t-\hat{k}\cdot\vec{x}/c)}\,, \tag{6.25}$$

where $\hat{k}$ is the unit vector in the direction of propagation, ϵ^A_{ab} are the polarization tensors for the $+$ and $\times$ polarization, and $h_A(f,\hat{k})$ are the corresponding Fourier modes. In the case of a SGWB satisfying the assumptions from section 6.1, the latter are random fields whose ensemble averages satisfy $\left\langle h_A(f,\hat{k})\right\rangle = 0$ and[9]

$$\left\langle h^*_A(f,\hat{k})\, h_{A'}(f',\hat{k}')\right\rangle = \frac{1}{16\pi}\,\delta(f-f')\,\delta_{AA'}\,\delta^2(\hat{k}-\hat{k}')\,S_h(f)\,, \tag{6.26}$$

where $S_h(f)$ is the one-sided strain power-spectral density (PSD). Then, using that h_{ab} is real and therefore $h^*_A(f,\hat{k}) = h_A(-f,\hat{k})$, as well as $\epsilon_{A\,ab}(\hat{k})\epsilon^{ab}_{A'}(\hat{k}) = 2\delta_{AA'}$,

$$\left\langle h_{ab}(t,\vec{x})h^{ab}(t,\vec{x})\right\rangle = \int_{-\infty}^{\infty} \mathrm{d}f\, S_h(f) = 2\int_{-\infty}^{\infty} \mathrm{d}(\log f)\, h_c^2(f)\,, \tag{6.27}$$

defining the characteristic strain amplitude $h_c(f) = \sqrt{f S_h(f)}$. Finally, the energy density of a GW is [344]

$$\rho_{\mathrm{GW}} = \frac{M_P^2}{4}\left\langle \dot{h}_{ab}(t,\vec{x})\dot{h}^{ab}(t,\vec{x})\right\rangle = \frac{M_P^2}{2}\int_{-\infty}^{\infty} \mathrm{d}(\log f)\,(2\pi f)^2\, h_c^2(f)\,, \tag{6.28}$$

and therefore, using eq. (6.1), we can relate the GW power spectrum to the characteristic strain and the strain PSD by

$$\Omega_{\mathrm{GW}}(f) = \frac{2\pi^2}{3H^2} f^2 h_c^2(f) = \frac{2\pi^2}{3H^2} f^3 S_h(f)\,. \tag{6.29}$$

[9]Regarding the definitions of $S_h(f)$ and $h_c(f)$ we here follow ref. [313].

Now consider the response $h(t)$ of a detector at position $\vec{x}$ to an incoming GW. The detector response may for instance be the GW-induced phase difference in an interferometer or the timing residuals in a PTA. For weak signals it is linear in the perturbation and therefore given by

$$h(t) = \int_{-\infty}^{\infty} \mathrm{d}t' \int \mathrm{d}^3x' \, R^{ab}(t', \vec{x}') \, h_{ab}(t - t', \vec{x} - \vec{x}') \, , \tag{6.30}$$

where $R^{ab}(t, \vec{x})$ is the impulse response of the detector (see ref. [284] for further details). For a plane wave we correspondingly obtain

$$h(f) = \int_{S^2} \mathrm{d}^2\hat{k} \sum_{A=+,\times} R^A(f, \hat{k}) \, h_A(f, \hat{k}) \tag{6.31}$$

in frequency space, with[10] $R^A(f, \hat{k}) = \epsilon^A_{ab}(\hat{k}) R^{ab}(f, \hat{k}) \, e^{-2\pi i f \, \hat{k}\cdot\vec{x}/c}$ describing the detector response to a sinusodial plane GW from direction $\hat{k}$ with frequency f and polarization A. The output d of the detector is then composed of the GW signal h and the respective noise n, i.e. $d(f) = h(f) + n(f)$.

Let us now suppose that we have a time series of measurements $d_i(t)$ from a network of detectors located at positions $\vec{x}_i$. Furthermore, assume that the noise in each detector is stationary (i.e. its variance is time-independent) and Gaussian, as well as statistically independent of the noise in the other detectors and the GW signal. In the frequency domain, it is then characterized by the mean $\langle n_i(f) \rangle = 0$ and the (co-)variances

$$\left\langle n_i(f) \, n_j^*(f') \right\rangle = \frac{1}{2} \, \delta(f - f') \, \delta_{ij} \, P_{ni}(f) \, , \tag{6.32}$$

where $P_{ni}(f)$ is the noise PSD in detector i. For the signal on the other hand, eqs. (6.26) and (6.31) yield

$$\left\langle h_i(f) \, h_j^*(f') \right\rangle = \frac{1}{2} \, \delta(f - f') \, \Gamma_{ij} \, S_h(f) \, , \tag{6.33}$$

where $\Gamma_{ij} = \int \mathrm{d}^2\hat{k} \sum_A R^A_i(f, \hat{k}) R^{A*}_j(f, \hat{k})$ is the so-called overlap reduction function.

We now take advantage of the fact that the GW signal is correlated between the detectors, whereas the noise is not. Therefore, the signal can be extracted by considering correlations between the detector outputs. We thus define the pair-wise correlated detector output $D_{ij} = \int_{-\infty}^{\infty} \mathrm{d}f \, d_i(f) d_j^*(f) Q_{ij}(f)$, where $Q_{ij}(f)$ is a filter function which we choose such that is maximizes the SNR. The corresponding SNR is given by $\rho_{ij} = \frac{\mu}{\sigma}$ with mean $\mu = \langle S_{ij} \rangle$ and variance $\sigma^2 = \langle S_{ij}^2 \rangle - \langle S_{ij} \rangle^2$. For a weak signal we can neglect the h_i in the variance and we obtain (details of the calculation can be found in refs. [282–284])

$$\rho_{ij}^2 = T_{\mathrm{obs}} \frac{\left[\int_{-\infty}^{\infty} \mathrm{d}f \, Q_{ij}(f) \, \Gamma_{ij}(|f|) \, S_h(|f|) \right]^2}{\int_{-\infty}^{\infty} \mathrm{d}f \, |Q_{ij}(f)|^2 \, P_{ni}(|f|) P_{nj}(|f|)} = 2 \, T_{\mathrm{obs}} \int_0^{\infty} \mathrm{d}f \, \frac{\Gamma_{ij}(f) S_h^2(f)}{P_{ni}(f) P_{nj}(f)} \, , \tag{6.34}$$

[10] We here adapt the definition of ref. [284] for $R^A(f, \hat{k})$, which includes the exponential factor. $R_{ab}(f, \hat{k})$ denotes the Fourier transform of $R_{ab}(t, \vec{x})$.

where we maximized the SNR setting $Q_{ij}(f) = \frac{\Gamma_{ij}(|f|)\, S_h(|f|)}{P_{ni}(|f|)\, P_{nj}(|f|)}$ in the second step. The total squared SNR of the network is simply obtained by summing over all detector pairs, $\rho^2 = \sum_{i>j} \rho_{ij}^2$. Rewriting $S_h(f)$ in terms of the fractional energy density $h^2\Omega_{\rm GW}$ using eq. (6.29), and defining the effective noise of the detector network

$$\Omega_{\rm eff}(f) = \frac{2\pi^2}{3H^2} f^3 \left[\sum_{i>j} \frac{\Gamma_{ij}(f)}{P_{ni}(f) P_{nj}(f)}\right]^{-\frac{1}{2}}, \tag{6.35}$$

we arrive at the expression eq. (6.2).

In the case of a single detector such as *LISA*, a cross-correlated analysis is of course not possible. For *LISA* one can however form combinations of the data from its six laser links, in which the signal is highly suppressed and the noise can be measured, employing a technique called time delay interferometry (TDI) [345, 346]. The noise can then be subtracted, and the corresponding auto-correlated SNR is given by [313]

$$\rho^2 = T_{\rm obs} \int_{f_{\rm min}}^{f_{\rm max}} {\rm d}f \left[\frac{h^2\Omega_{\rm GW}(f)}{h^2\Omega_n(f)}\right]^2. \tag{6.36}$$

Here, $\Omega_n(f) = \frac{2\pi^2 f^3 P_n(f)}{3H^2 \mathcal{R}(f)}$, where $P_n(f)$ is again the detector noise PSD and $\mathcal{R}(f) = \Gamma_{ii}(f)$ is the polarization- and sky-averaged detector response.

Appendix 6.B. Further Details on the Effective Potential

This appendix provides further details on the effective potential. Appendix 6.B.1 gives a formal definition, while appendices 6.B.2 and 6.B.3 sketch the derivation of the zero- and finite-temperature one-loop corrections.

6.B.1. Formal Definition

The effective potential for QFTs was first introduced by Heisenberg and Euler [347], as well as Schwinger [348], and applied to SSB by Jona-Lasinio [349]. It is the generating functional for one-particle irreducible (1PI) Green's functions at zero-momentum [350].

The generating functional $W(J)$ for connected Green's functions[11] is defined through the path integral via

$$Z(J) = \langle 0^+|0^-\rangle_J = \int \mathcal{D}\phi \, \exp\left[iS(\phi) + iJ\cdot\phi\right] = \exp\left[iW(J)\right], \tag{6.37}$$

where $|0^\pm\rangle$ denote the vacuum state at $t = \pm\infty$, ϕ and J are fields and sources, and we use the notation $J\cdot\phi = \int {\rm d}^4x\, \phi(x)J(x)$. We here consider the case of a single field only, following refs. [340, 350, 351], but the generalization is straight forward, see ref. [352].

[11] I.e. when expanding $W(J)$ in powers of J in the functional sense, the corresponding expansion coefficients are the sum of all connected Feynman diagrams with the respective number and types of external legs.

Now, classical fields are given by

$$\phi_c(x) = \frac{\langle 0^+ | \phi(x) | 0^- \rangle_J}{\langle 0^+ | 0^- \rangle_J} = \frac{\delta W(J)}{\delta J(x)} \tag{6.38}$$

and we can define the effective action $\Gamma(\phi_c)$ as the Legendre transform of $W(J)$, i.e. $\Gamma(\phi_c) = W(J) - J \cdot \phi_c$, which generates 1PI Green's functions $\Gamma^{(n)}(x_1, \ldots, x_n)$,

$$\begin{aligned}
\Gamma(\phi_c) &= \sum_{n=0}^{\infty} \frac{1}{n!} \int \mathrm{d}x_1 \ldots \mathrm{d}x_n \, \Gamma^{(n)}(x_1, \ldots, x_n) \, \phi_c(x_1) \ldots \phi_c(x_n) \\
&= \sum_{n=0}^{\infty} \int \prod_{i=1}^{n} \left[\frac{\mathrm{d}\, p_i}{(2\pi)^4} \tilde{\phi}_c(-p_i) \right] (2\pi)^4 \delta^{(4)}(p_1 + \cdots + p_n) \, \Gamma^{(n)}(p_1, \ldots p_n) \,,
\end{aligned} \tag{6.39}$$

where we changed to Fourier modes $\tilde{\phi}_c(p) = \int \mathrm{d}^4x \, e^{-ip\cdot x} \, \phi_c(x)$ in the second line. Let us now consider a vacuum state that is constant in space-time, $\phi_c(x) = \phi_0$. Then, the effective potential can be defined via

$$\Gamma(\phi_0) = (2\pi)^4 \, \delta^{(4)}(0) \sum_{n=0}^{\infty} \Gamma^{(n)}(0, \ldots, 0) \, \phi_0^n = -\int \mathrm{d}^4x \, V_{\text{eff}}(\phi_0) \,. \tag{6.40}$$

Using that $\int \mathrm{d}^4x = (2\pi)^4 \, \delta^{(4)}(0)$ is just the space-time volume factor, we can identify the effective potential as the sum of all 1PI Green's functions at zero-momentum.

Note that, when calculating the effective potential, we cannot simply expand in powers of couplings, as diagrams with internal massless particles become more infrared (IR) divergent when the number of external legs (and thereby the power of the couplings) is increased [352]. One instead typically expands in the number of loops [340, 352], which is equivalent to expanding in powers of $\hbar$ and provides the additional advantage that this expansions is invariant under shifts of the fields $\phi \to \phi + \bar{\phi}$. Using this expansion, the effective potential can be represented diagrammatically as

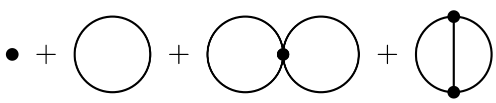

$$+ \, \mathcal{O}(\hbar^3) \,. \tag{6.41}$$

In finite temperature quantum field theory (FTQFT) the effective potential can be defined in the same way, going from Minkowski to Euclidean time (where we now define $Z(J) = \exp\left[-W(J)\right]$, with '$-$' instead of '$i$') and replacing the integrals $\int \mathrm{d}^4x_E$ by $\int_0^\beta \mathrm{d}\tau \int \mathrm{d}^3x$ with $\beta = 1/T$ [314, 351].

Note that a simpler derivation of the effective potential was presented in ref. [353], where the fields are shifted by a their zero-momentum component ϕ_0 (i.e. a constant background field), $\phi(x) = \phi_0 + \phi'(x)$, and V_{eff} is defined via the generating functional at vanishing external source, $Z(0) = \int_{-\infty}^{\infty} \mathrm{d}\phi_0 \, \exp\left[-i \int \mathrm{d}^4x \, V_{\text{eff}}(\phi_0)\right]$, such that

$$\exp\left[-i \int \mathrm{d}^4x \, V_{\text{eff}}(\phi_0)\right] = \int \mathcal{D}\phi' \exp\left[iS(\phi_0 + \phi')\right] \,. \tag{6.42}$$

6.B.2. The One-Loop Effective Potential at Zero-Temperature

Let us now very briefly recapitulate the derivation of the zero-temperature one-loop effective potential eq. (6.21). It was first calculated diagrammatically by Coleman and Weinberg in 1972 [340, 352] and is hence often referred to as Coleman-Weinberg potential. A computation based on functional methods was presented in by 1974 by Jackiw [350]. We here illustrate the calculation in $\lambda\phi^4$ theory following the diagrammatic approach, considering a real scalar field ϕ with the tree-level potential

$$V(\phi) = \frac{m_0^2}{2}\phi^2 + \frac{\lambda}{4!}\phi^4 \,. \tag{6.43}$$

Further details of the calculation can be found in refs. [340, 351, 352].

As mentioned above, the effective potential is calculated expanding in the number of loops, with an infinite series of diagrams contributing at each loop-level. For the potential eq. (6.43), the Feynman diagrams contributing at one-loop are

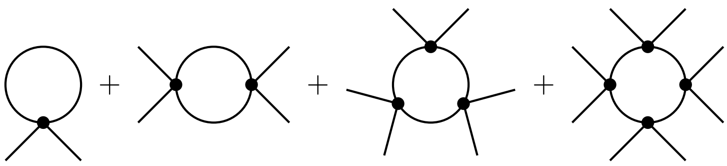

$$+ \dots \,, \tag{6.44}$$

where there external legs correspond to classical background fields with zero momentum. As the theory only features a quartic interaction, all diagrams have an even number of external legs.

Each diagram in eq. (6.44) contributes to the one-loop potential with a term given by the respective amplitudemultiplied by $\phi^{2n}/(2n)!$, where $2n$ is the number of external legs. The corresponding diagram then has n internal vertices and propagators, so that the expression for the diagram is $(-i\lambda)^n \times \left[i/(p^2 - m_0^2)\right]^n$, where we leave the $+i\varepsilon$ in the propagator implicit. We further need to take into account a combinatoric factor from the different ways of assigning momenta to the external lines. There are $(2n)!$ ways to assign the momenta. Interchanging the two momenta at any of the n vertices however does not change the diagram, so that we need to multiply by a symmetry factor $1/2^n$. Furthermore, momentum assignments related by rotations or reflections of the diagram are equivalent, giving another symmetry factor $1/(2n)$. Summing over all diagrams and using dimensional regularization we then obtain

$$\begin{aligned} V_{\mathrm{CW}}(\phi) &= \sum_{n=1}^{\infty} \mu_R^{D-4} \int \frac{\mathrm{d}^D p}{(2\pi)^D} \frac{i}{2n} \left[\frac{\lambda/2\,\phi^2}{p^2 - m^2 + i\varepsilon}\right]^n \\ &= \frac{1}{2}\,\mu_R^{D-4} \int \frac{\mathrm{d}^D p_E}{(2\pi)^D} \log\left[p_E^2 + m^2(\phi) - i\varepsilon\right] \,, \end{aligned} \tag{6.45}$$

where μ_R is the renormalization scale and D is the number of dimensions. For the second equality, we have performed a Wick rotation, identified the infinite sum as the series representation of the logarithm, $\log(1+x) = \sum_{n=1}^{\infty}(-1)^{n-1}x^n/n$, and dropped ϕ-independent terms. Performing the integration we then obtain [351]

$$V_{\mathrm{CW}}(\phi) = \frac{m^4(\phi)}{64\pi^2}\left[\log\left(\frac{m^2(\phi)}{\mu_R^2}\right) - \frac{3}{2} - \Delta\right] \,, \tag{6.46}$$

where $\Delta = \frac{2}{4-D} - \gamma_E + \log 4\pi$ and we defined $m^2(\phi) = m_0^2 + \lambda\phi^2/2$. In the $\overline{\text{MS}}$ renormalization scheme, the term proportional to Δ is subtracted, giving the result in eq. (6.21) for a single scalar DOF ($n_i = 1$).

If N scalars with identical mass are considered, we further recover the factor $n_i = N$ from the number of DOFs in eq. (6.21). A similar calculation can be carried out for fermions propagating in the loop. The Feynman rule for fermion loops then gives an additional over-all negative sign, so that the η_i factor in eq. (6.21) arises. The Dirac trace further yields a factor corresponding to the number of spin DOFs, i.e. $n_i = 4$ (2) for Dirac (Weyl) fermions. The equivalent calculation for gauge bosons in the loop is typically carried out in Landau gauge ($\xi = 0$) as the contributing diagrams are then simply given by the ones in eq. (6.44) with internal lines replaced by gauge boson propagators, and proceeds in analogy to the scalar case. In other gauges, additional diagrams with internal ghost fields would contribute.[12] The contraction of Lorentz indices then gives a factor $\text{Tr}(\eta^{\mu\nu} - \frac{p^\mu p^\nu}{p^2}) = D - 1$ from the numerator of the gauge boson propagator, which can be rewritten as $D - 1 = 3(1 + (D-4)/3)$. Taking $D \to 4$, we see that each gauge boson contributes with $n_i = 3$ DOFs. The trace further combines with the $2/(4-D)$ divergence in Δ, and we obtain that for gauge bosons $C_i = 5/6$ in eq. (6.21). Note that, since we are working Landau gauge, the would-be Nambu-Goldstone bosons also contribute as scalar DOFs.

While we cured UV divergences using dimensional regularization, eq. (6.21) may still suffer from IR singularities in its second derivative generated by fields that become massless for certain values of ϕ. These divergences are particularly problematic when imposing renormalization conditions on the second derivative of the potential in the broken vacuum, where the Goldstone masses vanish. The Goldstone divergences can be treated in different ways, e.g. including the one-loop zero-momentum self-energy of the Goldstone bosons in their squared masses in eq. (6.21) [355], or including the self-energy of the background field, which suffers from the same divergence, in the renormalization condition [356]. We follow the latter approach in chapter 7, whereas we simply numerically regularize the singularity in chapter 8.

6.B.3. The One-Loop Effective Potential at Finite-Temperature

The thermal one-loop effective potential can be obtained in the same manner as the zero-temperature one, evaluating the Feynman diagrams in FTQFT. An introduction to FTQFT can for instance be found in refs. [314, 351, 357] and is clearly beyond the scope of this work. For the following it shall be sufficient to state that the path integral representation of the partition function in the imaginary time formalism of FTQFT can be obtained from its zero-temperature QFT equivalent via the following steps [314].

1. Perform a wick rotation $t \to -i\tau$.
2. Introduce the Euclidean Lagrangian $\mathcal{L}_E = -\mathcal{L}(t{=}-i\tau)$.
3. Restrict τ to the interval $(0, \beta)$, where $\beta = 1/T$.

[12] See e.g. chapter 21 of ref. [21] for gauge-fixing in spontaneously broken gauge theories. The effective potential of scalar electrodynamics in arbitrary R_ξ gauges is for instance discussed in ref. [354].

4. Require periodicity (anti-periodicity) in τ for bosonic (fermionic) fields, i.e. $\phi(\beta) = \phi(0)$ $(\psi(\beta) = -\psi(0))$.

We then obtain a path integral representation similar to eq. (6.37), but with iS replaced by $-S_E$ and imposing the respective boundary conditions on the fields. Here, the Euclidean action is given by $S_E = \int_0^\beta \mathrm{d}\tau \int \mathrm{d}x^3\, \mathcal{L}_E$. The corresponding Feynman rules can be derived from $\mathcal{L}_E$ in analogy to the zero-temperature case.

This recipe can be motivated comparing the quantum mechanics (QM) partition function $Z(T)$ to the vacuum matrix element $\langle 0, t_f | 0, t_i \rangle$ between times t_i and t_f,

$$Z(T) = \mathrm{Tr} \exp\left[-\beta \hat{H}\right] \qquad \text{and} \qquad \langle 0, t_f | 0, t_i \rangle = \langle 0 | \exp\left[-i\left(t_f - t_i\right)\hat{H}\right] |0\rangle \,. \tag{6.47}$$

Defining $\Delta\tau = i(t_f - t_i)$ the exponential in the matrix element becomes $\exp(-\Delta\tau \hat{H})$. We can then identify β with $\Delta\tau$, motivating the Wick rotation. The negative sign in the definition of $\mathcal{L}_E$ is just convention.[13] Furthermore, we usually send $t_{f/i} \to \pm\infty$ in the matrix element, such that the time variable t is not restricted. In the thermal case however, β is fixed and we need to restrict $\tau \in (0, \beta)$. Finally, since the trace evaluates the exponential at equal final and initial states, we have to impose periodic boundary conditions in τ on bosonic fields, whereas fermionic fields are anti-periodic due to their anti-commutativity.

Due to the restriction of the imaginary time variable τ to the finite interval $(0, \beta)$, the zero-component of the Euclidean four-momentum can only take discrete values given by $\omega_n = 2\pi n T$ for bosons and $\omega_n = (2n+1)\pi T$ for fermions, respectively, where n is an integer. These are called Matsubara frequencies. The p^0 integrals then turn into sums over the Matsubara modes, $\int \frac{p^0}{2\pi} f(p^0) \to T \sum_n f(p^0 = i\omega_n)$.

Using theses rules, the one-loop potential at finite-temperature summing the diagrams in eq. (6.44) becomes

$$V_{\text{1-loop}}(\phi, T) = \frac{1}{2}\, \mu_R^{D-4}\, T \sum_{n=-\infty}^{\infty} \int \frac{\mathrm{d}^{D-1} p}{(2\pi)^{D-1}} \log\left[\omega_n^2 + \omega^2\right] , \tag{6.48}$$

where $\omega^2 = \vec{p}^{\,2} + m^2(\phi)$. The Matsubara sum can be evaluated analytically, giving a temperature-independent part that reproduces the Coleman-Weinberg potential, and a part that contains the thermal corrections. The latter was first calculated in 1974 by Jackiw and Dolan [341] in a functional approach and by Weinberg [358] (the other one)[14] with diagrammatic methods. The finite-temperature part is UV-finite, so that we can execute the limit $D \to 4$. One obtains, after integration over the solid angle [341, 351, 358],

$$V_{\mathrm{T}}(\phi, T) = \sum_i \eta_i\, n_i\, \frac{T}{2\pi^2} \int_0^\infty \mathrm{d}p\, p^2 \log\left[1 - \eta_i e^{-\beta\omega_i}\right] = \sum_i n_i \frac{T^4}{2\pi^2} J_{\bar{\eta}_i}\left(\frac{m_i^2(\phi)}{T^2}\right) , \tag{6.49}$$

where we now sum over all contributing species i with n_i DOFs, and $\omega = \sqrt{\vec{p}^{\,2} + m_i^2(\phi)}$. We recover eq. (6.22). Again, $\eta_i = +1$ (-1) for bosons (fermions), and $\bar{\eta}_i = -\eta_i$.

[13]With this convention, the Euclidean Lagrangian for a scalar field is $\mathcal{L} = \frac{1}{2}\left[(\partial_\tau\phi)^2 + (\nabla\phi)^2 + V(\phi)\right]$.

[14]The finite-temperature corrections [358] were calculated by Steven Weinberg, whereas the Coleman-Weinberg potential [340] is due to Erick Weinberg.

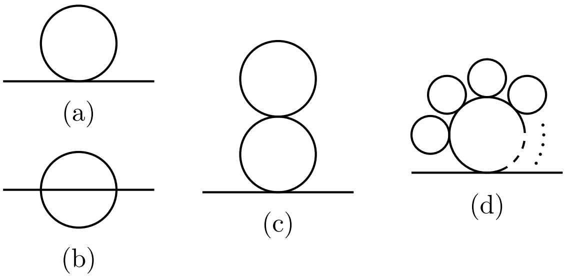

Figure 6.6: One- (a), two- (b+c) and dominant multi-loop (d) contributions to the ϕ^2 vertex.

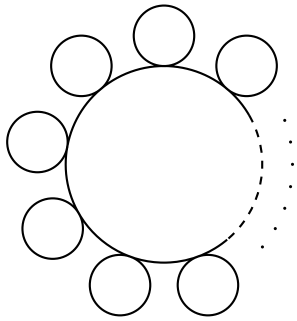

Figure 6.7: Daisy or ring diagram.

We have defined the thermal loop functions for bosons (J_-) and fermions (J_+)

$$J_\mp(x^2) = \pm \int_0^\infty \mathrm{d}y\, y^2 \log\left[1 \mp \exp\left(-\sqrt{y^2 + x^2}\right)\right] . \tag{6.50}$$

These admit the high-temperature expansions [341, 351, 357]

$$\begin{aligned} J_-(x^2) &= -\frac{\pi^4}{45} + \frac{\pi^2}{12}x^2 - \frac{\pi}{6}\left(x^2\right)^{\frac{3}{2}} - \frac{x^4}{32}\log\left(\frac{x^2}{a_-}\right) + \mathcal{O}\left(x^6\right) , && (6.51\text{a}) \\ J_+(x^2) &= -\frac{7\pi^4}{360} + \frac{\pi^2}{48}x^2 + \frac{x^4}{32}\log\left(\frac{x^2}{a_+}\right) + \mathcal{O}\left(x^6\right) , && (6.51\text{b}) \end{aligned}$$

where $a_- = 16\, a_+ = 16\pi^2 \exp(3/2 - 2\gamma_E)$.

Note that the $x^4 \log(x^2)$ terms in eq. (6.51) combine with the $m^4 \log(m^2)$ terms in the zero-temperature part eq. (6.21), so that the only non-analytic dependence on ϕ is in the $(x^2)^{3/2}$ term in eq. (6.51a). The latter term becomes imaginary for negative squared masses, indicating a breakdown of the perturbative expansion due to IR singularities in the zero Matsubara modes of the bosonic contributions [351, 359]. Indeed, the breakdown of fixed-order perturbation theory in the restoration of spontaneously broken theories can be expected, since the thermal loop-corrections overpower the tree-level potential, and is related to the fact that FTQFT has two scales, the mass scale m and temperature T, so that large ratios T/m need to be resummed [360]. This can be achieved resumming the most-IR-divergent higher-loop corrections [360–362].

Let us inspect the higher-loop corrections to the first term in eq. (6.44) quadratic in ϕ, cf. fig. 6.6, in $\lambda\phi^4$ theory. The high-temperature behavior can be derived from the superficial degree of divergence d of the diagrams [351, 360]. Diagrams with $d > 0$ scale with T^d, whereas diagrams with $d \leq 0$ scale linearly in T due to the T prefactor of the Matsubara sum. The one-loop diagram fig. 6.6a has $d = 2$ and therefore behaves like λT^2. The two-loop correction from the sunrise diagram fig. 6.6b has two logarithmically divergent loops (each contributing a factor T) and scales like $\lambda^2 T^2$, whereas the diagram in fig. 6.6c has a quadratically divergent loop stacked on a logarithmically divergent loop, and hence goes like $\lambda^2 T^3/m$, where factors of m are added on dimensional grounds. Thus, in the high-temperature limit, the dominant two-loop correction to the two-point function comes from adding a quadratically divergent loop to the one-loop diagram, i.e. fig. 6.6c. Similarly, at the $N+1$ loop level, the dominant contribution originates from the diagram in which N bubbles are attached to the main loop, see fig. 6.6d, which behaves like $\lambda T(\lambda T^2)^N/m^{2N-1} = \lambda T m(\lambda T^2/m^2)^N$.

The N-loop corrections to the higher-point contributions can be obtained by attaching additional external legs to the loop diagrams of the two-point function. One again finds that the dominant contributions are the ones adding bubbles to the main loop, where each additional quadratically divergent loop contributes a factor $f = \lambda T^2/m^2$ at high temperatures. At the critical temperature, the thermal corrections to the potential are on the order of the tree-level contributions, so that we expect $f \sim 1$. Hence, powers of f need to be resummed to all orders. This corresponds to resumming multi-loop contributions to the effective potential of the form depicted in fig. 6.7, called daisy or ring diagrams, where the small loops are evaluated in the high-temperature limit.

Daisy resummation is achieved by resumming the one-loop thermal self-energy corrections $\Pi_i(T)$, called Debye mass, to the propagator at high-temperature and vanishing external momentum (i.e. in the IR limit). This amounts to replacing $m_i^2(\phi)$ in the effective potential by $m_i^2(\phi) + \Pi_i(T)$.[15] Performing this replacement in the full one-loop potential however requires the introduction of temperature-dependent counter-terms [356]. To avoid this problem, the shift is only carried out in the zero-modes. To this end, we rewrite the logarithm in eq. (6.48) as [342]

$$\log\left[\omega_n^2 + \omega^2 + \Pi_i\right] = \log\left[\omega_n^2 + \omega^2\right] + \log\left[1 + \frac{\Pi_i}{\omega_n^2 + \omega^2}\right] . \tag{6.52}$$

The first term then gives the usual one-loop potential, whereas the second one is evaluated only for the bosonic $n = 0$ Matsubara mode, yielding

$$\int_0^\infty \mathrm{d}p\, p^2 \log\left[1 + \frac{\Pi_i}{p^2 + m_i^2}\right] = -\frac{\pi}{3}\left[(m_i^2 + \Pi_i)^{\frac{3}{2}} - m_i^3\right] , \tag{6.53}$$

where divergent but field-independent terms have been dropped. We thus obtain the ring correction eq. (6.24). The second term in eq. (6.53) then cancels with the cubic term in the high-temperature expansion eq. (6.51a).

A few comments are in order. First, note that thermal corrections to fermion masses are not resummed as there is no fermionic Matsubara zero-mode. However, the fermionic one-loop self-energy diagrams are at worst logarithmically divergent, and can therefore be neglected as they only scale linearly in T. Further note that for gauge bosons only the longitudinal modes receive a thermal mass correction $\Pi \sim T^2$, so that the Daisy correction vanishes for the transverse modes. Finally, it shall be emphasized that the $(m_i^2 + \Pi_i)^{3/2}$ term should actually read $(m^2 + \Pi)_i^{3/2}$, i.e. we need to add the Debye masses first and then diagonalize the corrected mass matrix.

[15] This is done similar to the resummation of 1PI corrections to the propagator in zero-temperature QFT, which leads to the replacement $m_0^2 \to m_R^2 - i m_R \Gamma$.

7. Gravitational Wave Signatures from Lepton Number Breaking

This chapter is based on the sections 5 to 7 as well as appendices A and B of the paper [1]. It contains text composed by the author taken verbatim from the publication. Minor modifications have been made to fit the structure, conventions and style of this dissertation.

Let us now return to the model of gauged lepton number introduced in chapter 5 and investigate whether the lepton number breaking phase transition (PT) can be arranged to be sufficiently strongly first-order to be detectable by *LISA* or other future gravitational wave (GW) observatories. Since we set the vacuum expectation value (VEV) of the lepton number Higgs, which roughly determines the overall scale of the transition, to $v_\Phi = 2\,\mathrm{TeV}$ to satisfy *LEP* constraints, we can expect transition temperatures in the TeV range. A potential stochastic gravitational wave background (SGWB) generated in the transition will therefore end up in the frequency range accessible to space-based experiments. This first-order PT could further provide the out-of-equilibrium condition necessary for successful baryogenesis, as was demonstrated recently in a model of non-abelian gauged lepton number [363].

In the following we aim to identify the regions of parameter space of the model in which the lepton number PT generates a detectable SGWB while at the same time being consistent with the collider and dark matter (DM) constraints discussed previously in chapter 5. The assumption of producing DM as a thermal relic in particular implies thermal equilibrium between the dark lepton sector and the Standard Model (SM). The scenario of a decoupled dark sector is studied in a general context in chapter 8. Nonetheless, the breaking of lepton number occurs separated from the electroweak PT (EWPT) for a large part of the viable parameter space, with a GW spectrum independent of the nature of the latter. Indeed, the EWPT mostly proceeds as a weak cross-over, like it is also the case in the pure SM.

In section 7.1 we discuss the nature of the lepton number breaking PT. We calculate the effective potential and determine the regions of parameter space in which the PT is of first order. The corresponding SGWB and its detectability are evaluated in section 7.2. Conclusions are presented in section 7.3.

7.1. The Lepton Number Breaking Phase Transition

In the early Universe, the spontaneously broken symmetries, viz. the electroweak (EW) and lepton number gauge symmetries, are typically restored due to thermal effects induced by finite-temperature corrections to the effective potential of the scalar fields whose VEVs break the symmetries. These are the scalar $\hat{\phi}$ breaking the $U(1)_\ell$ lepton number gauge symmetry, and the Higgs field $\hat{h}$ which breaks $SU(2)_W \otimes U(1)_Y$. As a consequence, during its history the Universe must have undergone the corresponding PTs associated with the breaking of these symmetries.

At high temperatures, the global minimum of the finite-temperature effective potential is at the origin, i.e. $SU(2)_W \otimes U(1)_Y \otimes U(1)_\ell$ is unbroken. When the temperature drops, the potential changes and at some point develops a minimum at non-vanishing field values. Whether both fields develop non-zero VEVs at the same time or independently at different temperatures depends on the parameters of the model. Since the portal interaction between the two scalars is restricted to be small (see sections 5.2.2 and 5.3.2), and due to the hierarchy of the VEVs ($v_H = 246\,\mathrm{GeV}$, $v_\Phi \gtrsim 1.9\,\mathrm{TeV}$), the lepton number breaking PT however typically occurs first at temperatures in the TeV range, leaving the EW symmetry unbroken. EW symmetry breaking subsequently proceeds like in the SM at a temperature of $T \simeq 160\,\mathrm{GeV}$ [34].

While the EWPT then mostly proceeds as a cross-over, the lepton number PT can be first-order and may therefore generate GWs. In the following, we will thus briefly discuss the full finite-temperature effective potential of the lepton number and EW Higgs fields, and then focus on the lepton number breaking scalar only, neglecting interactions with the SM fields.

7.1.1. Finite-Temperature Effective Potential

The daisy-resummed one-loop finite-temperature effective potential takes the form (cf. eq. (6.20))

$$V_{\mathrm{eff}}(h,\phi,T) = V_{\mathrm{tree}}(h,\phi) + V_{\mathrm{CW}}(h,\phi) + \Delta V_{\mathrm{ct}}(h,\phi) + V_{\mathrm{T}}(h,\phi,T) + V_{\mathrm{ring}}(h,\phi,T)\,, \quad (7.1)$$

where h and ϕ are the classical background fields. Note that these in general do not coincide with the mass eigenstates but with the gauge interaction eigenstates $\hat{h}$ and $\hat{\phi}$. We here however drop the hats for convenience.

The corresponding tree-level potential is

$$V_{\mathrm{tree}}(h,\phi) = -\frac{1}{2}\mu_H^2 h^2 - \frac{1}{2}\mu_\Phi^2\phi^2 + \frac{1}{4}\lambda_H h^4 + \frac{1}{4}\lambda_\Phi\phi^4 + \frac{1}{4}\lambda_p h^2\phi^2\,. \quad (7.2)$$

The non-$\overline{\mathrm{MS}}$ parts of the counter-terms are

$$\Delta V_{\mathrm{ct}}(h,\phi) = -\frac{1}{2}\delta\mu_H^2 h^2 - \frac{1}{2}\delta\mu_\Phi^2\phi^2 + \frac{1}{4}\delta\lambda_H h^4 + \frac{1}{4}\delta\lambda_\Phi\phi^4 + \frac{1}{4}\delta\lambda_p h^2\phi^2\,, \quad (7.3)$$

which we fix by imposing that the VEV as well as the mass-squared matrix of h and ϕ in the broken vacuum remain at the tree-level values.

The general expressions for the Coleman-Weinberg, thermal one-loop and daisy-resummation potentials are given in section 6.5. The field-dependent masses are obtained by diagonalizing the mass matrices eqs. (5.4), (5.10) and (5.16), as well as the corresponding mass matrices for the SM fermions, replacing v_H and v_Φ by h and ϕ, respectively. The Debye masses for the scalars and the lepton number gauge boson are given further below in eq. (7.6), while the corresponding corrections for the SM gauge bosons can be found in [342]. To consider effects of kinetic mixing, the thermal masses must be corrected for the mixing in eq. (5.2).

In fig. 7.1 we show the effective potential at different temperatures, to illustrate the individual steps of the symmetry breaking process. The model parameters are given in the figure caption.

At high temperatures, the global minimum of the effective potential is in the symmetric (unbroken) vacuum $(h, \phi) = (0, 0)$. As the Universe cools down, a second minimum starts to form at non-vanishing values of ϕ. At $T_c \simeq 835\,\mathrm{GeV}$, the two minima are degenerate. At lower temperatures, the second minimum $(h, \phi) \sim (0, 1.1\,\mathrm{TeV})$ is the global minimum and breaks lepton number, whereas the EW symmetry remains unbroken. This minimum is separated from the symmetric minimum by a potential barrier. Thus, to transition to the global minimum, the field has to tunnel (or remain in the symmetric vacuum until the barrier disappears).

As the Universe cools further, the minimum at the origin disappears at some point, and the global minimum moves towards the zero-temperature lepton-number-breaking VEV $(h, \phi) = (0, 2\,\mathrm{TeV})$. Subsequently, at $T \lesssim 160\,\mathrm{GeV}$, the minimum starts to shift to non-vanishing Higgs field values, breaking the EW symmetry in a cross-over transition. Eventually, the Universe ends up in today's vacuum $(h, \phi) \simeq (246\,\mathrm{GeV}, 2\,\mathrm{TeV})$.

7.1.2. A First-Order Lepton-Number-Breaking Phase Transition

In this section, we examine the lepton number breaking PT in the limit of negligible portal coupling λ_p between the SM Higgs and the scalar Φ. Further assuming that the kinetic mixing of the gauge bosons as well as the exotic Yukawa couplings c_i and y_i of the dark leptons are small, we can study a simplified version of the effective potential in which only the lepton number breaking scalar and the lepton number gauge boson are considered.

In this case, the tree-level potential simplifies to

$$V_{\text{tree}}(\phi) = -\frac{1}{2}\mu_\Phi^2\phi^2 + \frac{1}{4}\lambda_\Phi\phi^4 \,. \tag{7.4}$$

Setting the lepton number breaking VEV to $v_\Phi = 2\,\mathrm{TeV}$, in agreement with the *LEP* constraint, the model is therefore fully specified by $m_{Z'}$ and m_ϕ.

The field dependent masses of the scalar, the gauge boson, and the Goldstone boson are given by

$$m_\phi^2 = -\mu_\Phi^2 + 3\lambda_\Phi\phi^2 \,, \quad m_{\omega^0}^2 = -\mu_\Phi^2 + \lambda_\Phi\phi^2 \,, \quad \text{and} \quad m_{Z'}^2 = 9g_\ell^2\phi^2 \,. \tag{7.5}$$

The thermal mass corrections are $(\Pi_\phi = \Pi_{\omega^0} = \Pi_\Phi)$

$$\Pi_\Phi = \left(\frac{1}{3}\lambda_\Phi + \frac{9}{4}g_\ell^2\right)T^2 \quad \text{and} \quad \Pi_{Z'_L} = 3g_\ell^2T^2 + \frac{2}{3}g_\ell^2T^2\left(3 + L'^2 + L''^2\right) , \tag{7.6}$$

where the first part of $\Pi_{Z'_L}$ comes from the scalar, and the second part from the SM and exotic leptons. The subscript L of $\Pi_{Z'_L}$ indicates that only the longitudinal part of the Z' boson receives a thermal correction.

We further use an on-shell scheme, imposing the conditions

$$\left.\frac{\partial\left(V_{\text{CW}} + \Delta V_{\text{ct}}\right)}{\partial\,\phi}\right|_{\phi=v_\Phi} = 0 \qquad \text{and} \qquad \left.\frac{\partial^2\left(V_{\text{CW}} + \Delta V_{\text{ct}}\right)}{\partial\,\phi^2}\right|_{\phi=v_\Phi} = -\Delta\Sigma \,. \tag{7.7}$$

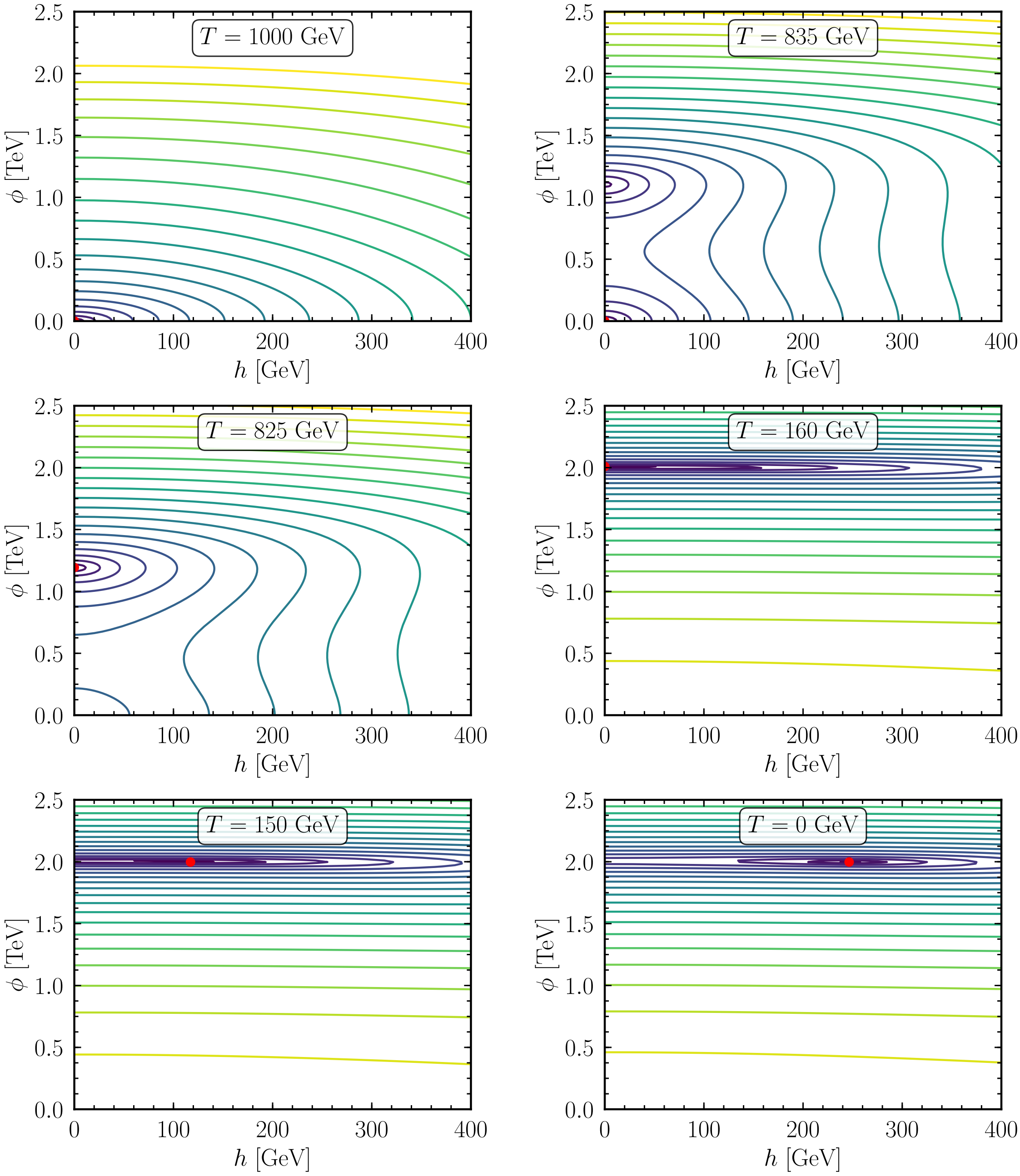

Figure 7.1: Effective potential as a function of temperature. The colored equipotential lines correspond to $V_{\text{eff}} = (30\,\text{GeV})^4, (60\,\text{GeV})^4, (90\,\text{GeV})^4, \ldots, (600\,\text{GeV})^4$ (from dark-purple to yellow). The red dot denotes the global minimum of the potential at $V_{\text{eff}} = 0\,\text{GeV}^4$. The model parameters are $v_\Phi = 2\,\text{TeV}$, $m_\phi = 500\,\text{GeV}$, $\sin\theta_H = 0.05$, $m_{Z'} = 1.5\,\text{TeV}$, $\epsilon = 0$, $m_{\text{DM}} = 590\,\text{GeV}$, $\sin\theta_{\text{DM}} = 0$, $m_{e_4} = m_{e_5} = 650\,\text{GeV}$, and $L' = -1/2$.

This ensures that the VEV and the scalar mass at zero temperature remain at their tree-level values. Here, $\Delta\Sigma \equiv \Sigma(m_\phi^2) - \Sigma(0)$ is the difference of the scalar self-energy evaluated at the tree-level mass and at zero-momentum, see appendix 7.A. The second derivative of the Coleman-Weinberg potential in the vacuum suffers from logarithmic divergences originating from the vanishing Goldstone masses. These are infrared (IR) divergencies and are due to the fact that the effective potential is evaluated at vanishing external momentum. However, the scalar self-energy at zero-momentum suffers from the same divergences, hence its presence in the second condition above [356]. The divergences in $\Delta\Sigma$ and $\partial^2 V_{\text{CW}}/\partial\phi^2$ then cancel, ensuring that we obtain (IR-)finite counter-terms.

We use the numerical package CosmoTransitions [364] to evaluate the effective potential and to analyze the PT. Fixing the VEV to $v_\Phi = 2\,\text{TeV}$ (and setting the renormalization scale to $\mu_R = v_\Phi$), we identify the region in the $m_\phi - m_{Z'}$ parameter space at which a first-order PT occurs.

In this model, the potential barrier between the vacua is generated by thermal corrections from gauge boson loops (note the cubic term in the high-T expansion of the bosonic thermal contribution in eq. (6.23)), i.e. the larger the gauge coupling (and hence also the Z' mass) the higher and wider the barrier. Increasing the scalar mass on the other hand increases the quartic coupling, which in turn reduces (the relative size of) the barrier. Thus, first-order PTs can be obtained for $m_{Z'} \gtrsim m_\phi$; strong transitions occur for $m_{Z'} \gtrsim 2m_\phi$. The term "strong" here refers to transitions in which the VEV (or more precisely the distance between the two degenerate minima in field space) at the critical temperature is larger than the critical temperature itself, i.e. $\langle\phi\rangle_c / T_c \gtrsim 1$, where $\langle\phi\rangle_c = \langle\phi(T_c)\rangle$. This measure is often employed in the context of baryogenesis [351].

Figure 7.2a shows the regions in the $m_\phi - m_{Z'}$ plane in which the effective potential develops degenerate minima at a critical temperature T_c for $L' = -1/2$. The colors indicate the corresponding T_c. In the colored region above the black line, the measure $\langle\phi\rangle_c / T_c$ implies strong transitions. The parameter points which actually lead to a first-order PT through bubble nucleation are shown in fig. 7.2b along with the corresponding nucleation temperature, again for $L' = -1/2$. Here, the black line indicates $\langle\phi\rangle_n / T_n \gtrsim 1$ evaluated at the nucleation temperature.

Although the renormalization conditions eq. (7.7) ensure that the zero-temperature potential has a minimum at $\phi = v_\Phi$, this minimum is not necessarily the global minimum. In particular, if the gauge boson mass $m_{Z'}$ is much bigger than the scalar mass m_ϕ, the potential develops a global zero-temperature minimum at $\phi = 0$, i.e. the Coleman-Weinberg corrections restore the symmetry already at $T = 0$.[1] This is the case in the white area labeled by "$\langle\phi\rangle_0 = 0$" above the colored region in fig. 7.2a (and above the dotted line in fig. 7.2b), which is of course excluded since it would imply the existence of a second massless gauge boson with significant couplings to leptons. Furthermore, even a global minimum at $\phi = v_\Phi$ does not automatically ensure that today's Universe has transitioned to the true vacuum. If the barrier is very large with a small potential difference between the two vacua, which is the case close to the region in which the

[1] Of course, the physical scalar and Z' masses become $m_\phi = 0$ and $m_{Z'} = 0$ in this region. Hence, the x and y axes should be interpreted as $\sqrt{2\lambda_\Phi v_\Phi^2}$ and $3g_\ell v_\Phi$ respectively, where $v_\Phi = 2\,\text{TeV}$ then has no physical meaning.

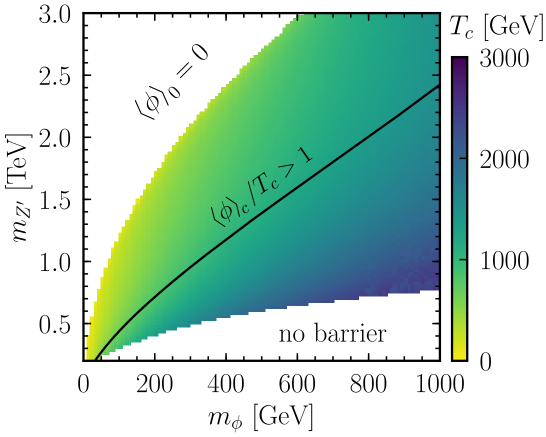

(a) Critical temperature T_c

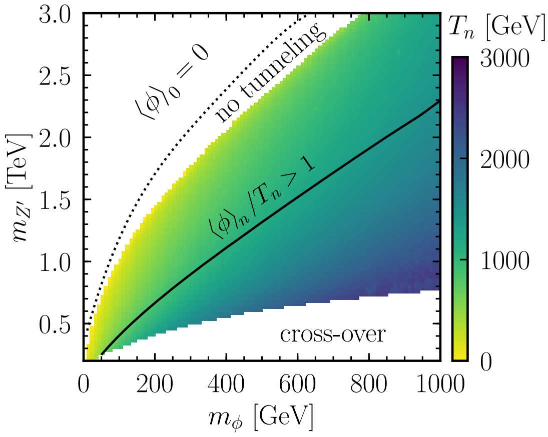

(b) Nucleation temperature T_n

Figure 7.2: Parameter points with two phases separated by a potential barrier at a critical temperature T_c (left), and points that give rise to a cosmological first-order PT with a nucleation temperature T_n (right). The colored regions above the solid black line feature strong transitions with $\langle\phi(T)\rangle/T > 1$ at T_c or T_n, respectively. The dotted line in the right plot denotes the border at which $\phi = 0$ becomes a global minimum.

potential has a global zero-temperature minimum at $\phi = 0$, the tunneling probability is too low. Therefore the field is stuck in the false vacuum and does not tunnel. This corresponds to the parameter region labeled “no tunneling” in fig. 7.2b.[2]

On the other hand, for $m_{Z'} \lesssim m_\phi$ no significant barrier is induced and there is no temperature at which the potential has degenerate minima. Also, if the potential barrier separating the phases is very shallow, it might disappear before bubbles are nucleated. In both cases the transition occurs without tunneling as a cross-over[3] and no gravitational waves are generated. This happens in the areas labeled “no barrier” or “cross-over” in fig. 7.2.

So far, to simplify the parameter space to two dimensions, we neglected the contributions from the dark Yukawa couplings of the fourth and fifth generation leptons to the effective potential. However, if the leptons are heavy, the Yukawa couplings are large and the potential can be modified significantly. This is in particular the case for large Z' masses, where the exotic leptons are required to be heavy in order to obtain the correct DM relic abundance.

[2] Note that CosmoTransitions only evaluates the thermal tunneling probability. Quantum tunneling is not taken into account.

[3] We here rely on the ability of CosmoTransitions to identify cross-over transitions. A proper determination of whether a transition is cross-over may involve non-perturbative calculations and is beyond the scope of this work. Here, we are mainly interested in the region where strong first-order transitions occur.

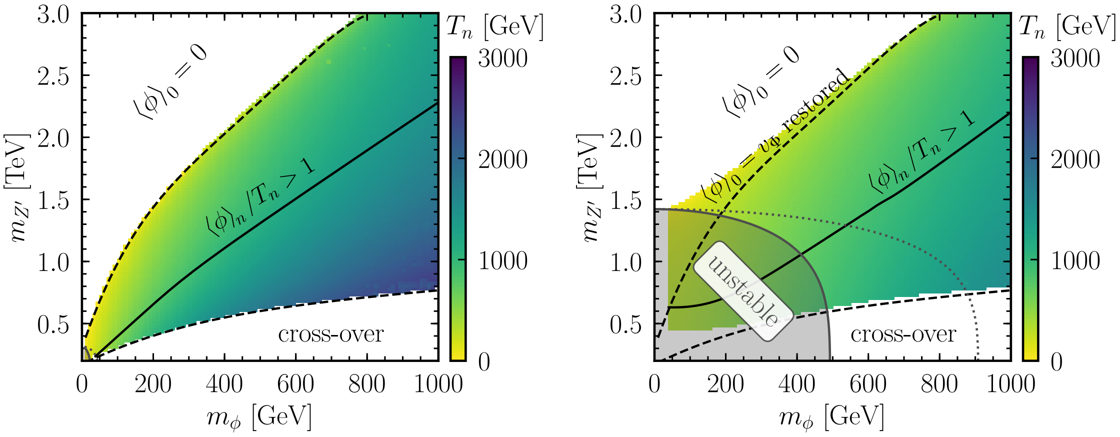

(a) $m_{\mathrm{DM}} = 200\,\mathrm{GeV}$, $m_{\mathrm{HL}} = 210\,\mathrm{GeV}$

(b) $m_{\mathrm{DM}} = 500\,\mathrm{GeV}$, $m_{\mathrm{HL}} = 1\,\mathrm{TeV}$

Figure 7.3: Parameter points giving rise to a cosmological first-order PT with a nucleation temperature T_n, including the contribution from DM and the exotic leptons. The dashed lines indicate the corresponding region neglecting the fermion contributions (cf. fig. 7.2b). In the gray shaded region, the potential becomes unstable below $\phi = 100\,\mathrm{GeV}$; above the gray dotted line it is stable up to $\phi = 10^6\,\mathrm{TeV}$.

For simplicity, we here again assume that the exotic electrons and the exotic neutrino have equal masses, $m_{\mathrm{HL}} \equiv m_{e_4} = m_{e_5} = m_{\nu_4}$, i.e. that the SM Higgs Yukawa couplings y_ν and y_e in eq. (5.14) vanish. The field dependent masses are then given by

$$m_{\mathrm{DM}} = \frac{c_\nu}{\sqrt{2}}\phi \ , \qquad m_{\mathrm{HL}} = \frac{c_\ell}{\sqrt{2}}\phi \ . \tag{7.8}$$

The Yukawa couplings further contribute to the scalar thermal mass correction eq. (7.6), which becomes

$$\Pi_\Phi = \left(\frac{1}{3}\lambda_\Phi + \frac{9}{4}g_\ell^2 + \frac{1}{12}c_\nu^2 + \frac{1}{4}c_\ell^2\right)T^2 \ . \tag{7.9}$$

Figure 7.3 shows the values of the scalar and Z' masses that lead to a first-order PT with the corresponding nucleation temperature, for two different choices of the DM and heavy lepton (HL) masses. The region that gives rise to a first-order PT for vanishing fermion couplings (cf. fig. 7.2b) is indicated by the dashed lines.

As expected, for light HLs (i.e. low Yukawa couplings) the situation changes only marginally with respect to the case assuming vanishing Yukawas. However, for higher fermion masses, the region that yields a first-order PT changes, and the nucleation temperature decreases.

In the parameter region labeled "$\langle\phi\rangle_0 = v_\Phi$ restored" in fig. 7.3b, the bosonic loop corrections to the zero-temperature potential induce a global minimum at $\phi = 0$ in the absence of fermions. If the dark sector leptons are included, their contributions have the opposite sign and partially cancel the bosonic ones, and the global minimum at $\phi = v_\Phi$ is restored. Hence, the region allowing for a first-order PT is extended. On the other hand, if the fermionic corrections overcome the bosonic ones at high field-values, the potential

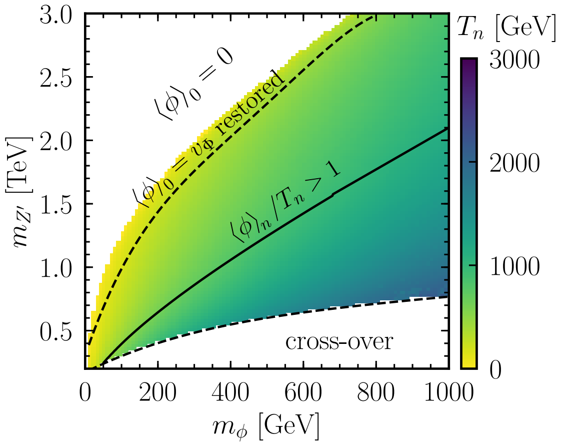

Figure 7.4: Same as fig. 7.3, but at each parameter point the DM mass is set to a value that yields the correct relic abundance. The masses of e_4, e_5, and ν_4 are set to $m_{\rm HL} = 1.5 \times m_{\rm DM}$.

is destabilized as it is not bounded from below. This occurs for low Z' and ϕ masses. The gray shaded regions are excluded since the potential becomes unstable at field values below $\phi = 100\,\text{TeV}$, i.e. $V_{\rm eff}(100\,\text{TeV}) < V_{\rm eff}(\langle\phi\rangle_0)$ at $T = 0$. Above the gray dotted curve the potential is stable even up to $\phi = 10^6\,\text{TeV}$. Note however that a reliable evaluation of the potential at such high field values requires the inclusion of renormalization group (RG) effects.

At high temperatures, the loop corrections from the fermions give a positive contribution $\sim \phi^2 T^2$, whereas they do not contribute to the cubic terms (note that there is no $(m^2/T^2)^{3/2}$ term in the fermionic sum of eq. (6.23)). As a consequence, the finite-temperature corrections restore the symmetric minimum at lower temperatures, reducing the nucleation temperature.

Finally, to properly connect to the DM picture, let us require that the DM candidate has the correct thermal abundance.[4] Figure 7.4 shows the nucleation temperature for the corresponding PT, assuming that $m_{\rm HL} = 1.5 \times m_{\rm DM}$. At each parameter point in the $m_\phi - m_{Z'}$ plane we use micrOMEGAs to find the value of the DM mass that yields the measured abundance, picking the value below the Z' resonance (i.e. we are sitting on the upper branch of the blue line in fig. 5.3). Again, the dashed lines indicate the parameter region that provides a first-order PT if the fermions are neglected.

As the DM mass required to obtain the correct abundance increases with the Z' mass and is mostly independent of the scalar mass, the effects of including the dark leptons are stronger for larger Z' masses. Hence, the fermionic corrections restore the $T = 0$ minimum at $\phi = v_\Phi$ for high $m_{Z'}$, whereas this effect is absent in the low $m_{Z'}$ range. Furthermore, since $m_{\rm DM} < m_{Z'}/2$ (and $m_{\rm HL} = 1.5 \times m_{\rm DM}$), the bosonic contributions are sufficiently large to circumvent the destabilizing effects of the fermionic corrections in the full parameter space shown in fig. 7.4.

[4]Note that the DM in fig. 7.3a already has the measured abundance by co-annihilation for most values of $m_{Z'}$, cf. the green line in fig. 5.4.

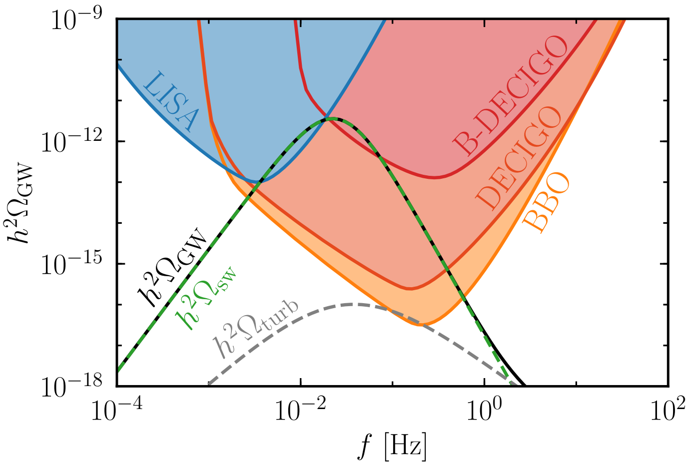

m_ϕ	200 GeV
$m_{Z'}$	1.4 TeV
v_Φ	2 TeV
L'	$-\frac{1}{2}$
T_c	487 GeV
T_n	198 GeV
α	0.18
β/H_*	570

Figure 7.5: GW spectrum (black solid line) from the $U(1)_\ell$ breaking phase transition for $m_\phi = 200\,\text{GeV}$ and $m_{Z'} = 1.4\,\text{TeV}$. The contributions from different production mechanisms are indicated by the dashed green and gray lines. The colored regions indicate the power-law integrated (PLI) sensitvity of *LISA* (blue), *B-DECIGO* (red), *DECIGO* (dark orange), and *BBO* (orange).

7.2. Gravitational Waves Signature

Having explored the parameter regions that give rise to a first-order PT, we now calculate the remaining transition parameters, to wit, the energy budget α and the relative transition scale β/H_*, and determine the corresponding GW spectrum as well as its detectability at future GW experiments. As the scalar field ϕ is coupled to the lepton number gauge boson, the corresponding friction prevents the bubbles from entering the runaway regime [325]. Therefore, only the plasma contributions to the spectrum are considered throughout this chapter, assuming a turbulent fraction of $\varepsilon_{\rm turb} = 5\,\%$. We further take $v_w = 1$ in this section, discussing the impact of the wall velocity in appendix 7.B.

An example of the GW spectrum generated by the lepton number breaking PT for a scalar mass of $m_\phi = 200\,\text{GeV}$ and a gauge boson mass of $m_{Z'} = 1.4\,\text{TeV}$ (with $v_\Phi = 2\,\text{TeV}$ and $L' = -1/2$, neglecting the dark lepton contributions) is shown in fig. 7.5 (black curve). The contributions from acoustic production (green) and magnetohydrodynamic (MHD) turbulence (gray) are indicated by dashed lines. For this choice of parameters, the transition occurs at a nucleation temperature of $T_n \sim 200\,\text{GeV}$ with a peak frequency of the spectrum of $f \sim 22\,\text{mHz}$.

Figure 7.5 also shows the sensitivity curves of the future space-based GW interferometer *LISA* and its potential successors *(B-)DECIGO* and *BBO* as colored regions. Note that these curves are not the noise curves, but the PLI curves defined in eq. (6.4), which indicate that a GW background should be detectable by the experiment if the spectrum touches or reaches into the region above the respective sensitivity curve. Thus, the spectrum shown in the figure can be probed by all four experiments.

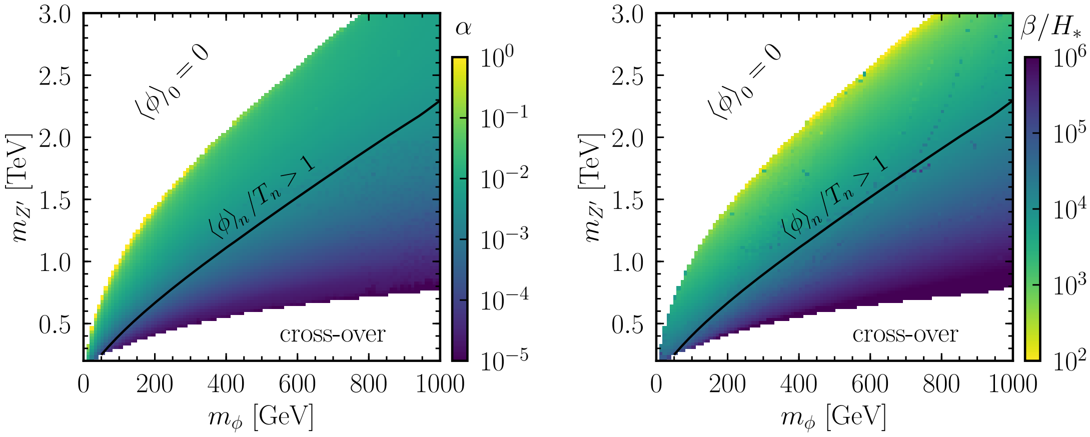

(a) energy budget α (b) relative transition scale β/H_*

Figure 7.6: Energy budget α and inverse relative time scale β/H_* as a function of the $U(1)_\ell$ breaking scalar mass m_ϕ and the $U(1)_\ell$ gauge boson mass $m_{Z'}$ in the case of negligible portal coupling λ_p.

While the specific parameter point depicted in fig. 7.5 exhibits good prospects for observing the generated SGWB at GW experiments, the majority of the parameter regions with a first-order PT gives rise to transitions which are too weak for a detection. Nonetheless, a significant fraction of the parameter space may be probed at least at the far-future observatories *DECIGO* and *BBO*, as we will demonstrate in the following.

Figure 7.6 shows the parameters α and β/H_* for the lepton number breaking PT as a function of the ϕ and Z' mass in the simplified case of negligible portal coupling λ_p considered in section 7.1.2, calculated using CosmoTransitions [364]. Most choices of masses give rise to a rather short first-order PT (high β/H_*) with few energy released (low α). However, large values of α and small values of β/H_* can be obtained in the $m_{Z'} \gtrsim 2m_\phi$ region, which is the region we identified to give rise to strong first-order PTs in section 7.1.2. As the amplitude of the sound-wave contribution to the GW spectrum 6.14b is proportional to $\alpha^2/(1+\alpha)^2$ and H_*/β, this is indeed the region in which the stochastic background can be expected to be detectable.

The corresponding parameter points for which the SGWB generated by the lepton number breaking PT is accessible to space-based GW interferometers are depicted in fig. 7.7a. The blue, red, dark orange, and orange regions can be detected by *LISA*, *B-DECIGO*, *DECIGO*, and *BBO*, respectively, whereas in the gray region the generated GW background is not detectable. If a parameter point is detectable by more than one experiment, the color corresponds to the experiment named first in the list above.

If the ϕ Yukawa couplings (and the Higgs portal coupling) are neglected, *LISA* and *B-DECIGO* are only sensitive in the $m_{Z'} \gg m_\phi$ margin of the parameter space that has a first-order PT. *DECIGO* can probe a small portion of the parameter space, also only close to the $m_{Z'} \gg m_\phi$ edge, *BBO* is slightly more sensitive. Still, the majority of the parameter space is inaccessible to GW experiments.

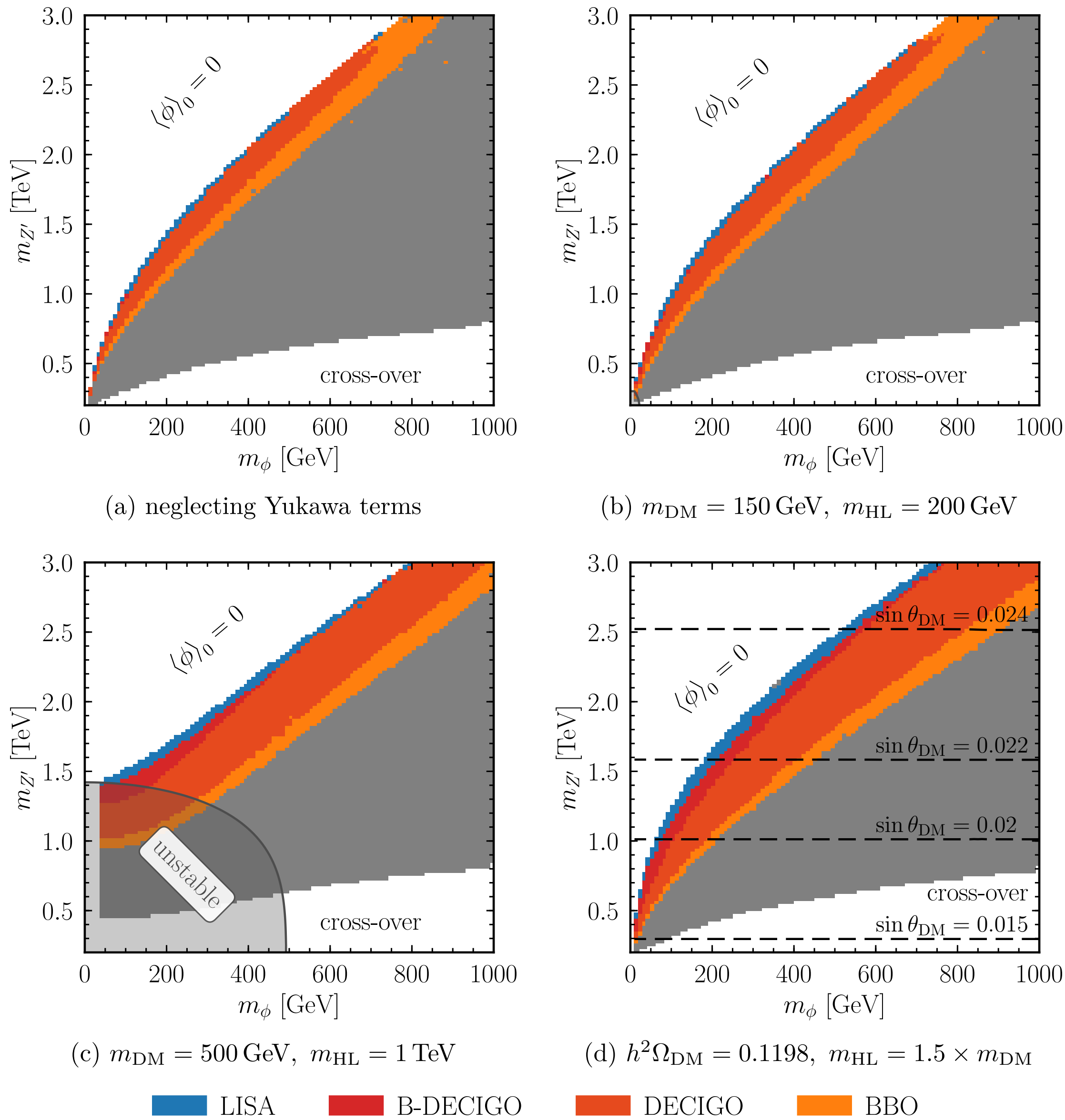

Figure 7.7: Sensitivity of space-based GW observatories to the stochastic background from the lepton number breaking PT (for negligible portal couplings) in the $m_\phi - m_{Z'}$ plane. In the colored regions, the SGWB can be detected by *LISA* (blue), *B-DECIGO* (red), *DECIGO* (dark orange), and *BBO* (orange), respectively. In the gray region, the stochastic background is not detectable. The gray shaded regions (below the dark-gray solid line) in figs. 7.7b and 7.7c are excluded as the potential is unstable. In fig. 7.7d, the DM mass is set to a value reproducing the measured DM abundance at each parameter point. The dashed lines indicate the exclusion reach of *XENON1T* for different values of the DM mixing angle $\theta_{\rm DM}$.

So far we neglected the contributions of the dark leptons to the effective potential. Including them can significantly improve the detection prospects. The detectability of the SGWB for two different choices of exotic lepton masses are shown in figs. 7.7b and 7.7c. For light dark leptons (small Yukawas) with $m_{\rm DM} = 200\,{\rm GeV}$ and $m_{\rm HL} = 210\,{\rm GeV}$ ($m_{\rm HL} \equiv m_{e_4} = m_{e_5} = m_{\nu_4}$), the detectable part of the parameter space barely changes. For heavier leptons with $m_{\rm DM} = 0.5\,{\rm TeV}$ and $m_{\rm HL} = 1\,{\rm TeV}$ however, a significant fraction of the first-order transitions can be probed. Still, the sensitivity of *LISA* is restricted to a band near the $m_{Z'} \gg m_\phi$ edge of the PT region, the size of the detectable region however increases notably compared to the case with vanishing Yukawa couplings. *B-DECIGO* can probe additional parameter points, mostly for low scalar masses. *DECIGO* and *BBO* can reach $m_{Z'} \gtrsim 1\,{\rm TeV}$ for $m_\phi \sim 50\,{\rm GeV}$ and $m_{Z'} \gtrsim 2.8\,{\rm TeV}$ for $m_\phi \sim 1\,{\rm TeV}$.

Last but not least, fig. 7.7d shows the detectability of the SGWB from the lepton number breaking PT requiring that the DM accounts for the full thermal abundance measured by *Planck*, assuming $m_{\rm HL} = 1.5 \times m_{\rm DM}$ as in fig. 7.4. Again, the effects of the dark leptons significantly enhance the parameter space to which future space-based GW observatories are sensitive. The dashed lines indicate the exclusion reach of *XENON1T* (cf. fig. 5.5b) for DM mixing angles of $\sin\theta_{\rm DM} = 0.015$, 0.02, 0.22 and 0.024. The white region in the upper left part of the plot is excluded as the lepton number gauge group remains unbroken. Although not specifically mentioned, this applies to all sub-figures of fig. 7.7.

7.3. Conclusion

In this chapter we have continued our study of the gauged lepton number model introduced in chapter 5, investigating the lepton number breaking PT in the early Universe. If the portal coupling between the SM and dark Higgs is sufficiently small, the lepton number and EW PTs happen independently from one another. Due to the VEV hierarchy imposed by the *LEP* constraints, the former typically occurs first. We found that in a large fraction of the parameter space the lepton number transition is first order. It can thus generate a stochastic background of GWs. We calculated the corresponding GW spectrum and evaluated the detection prospects for future space-based GW observatories.

While *LISA* can only probe a rather small fraction of the parameter space, its possible successors *BBO* and *DECIGO* are able to explore a significant fraction of the parameter points that give rise to a first-order PT. Notably, the exotic leptons significantly enhance the detection prospects, particularly when requiring that the measured relic abundance is reproduced. This is due to two effects. First, the presence of additional particles lowers the nucleation temperature, and second, the fermionic contributions restore the broken minimum in a part of the parameter space in which the bosonic corrections alone would shift the vacuum back to the origin.

Further interesting effects may arise if one considers non-vanishing portal couplings between the dark and SM scalar sectors. The transition can then proceed diagonally in field space, breaking the EW and lepton number gauge groups simultaneously. We leave this subject for future work. Another possible direction would be the investigation of the phase transition in the context of Baryogenesis.

Appendix of Chapter 7

Appendix 7.A. Goldstone Divergences

In this appendix we address the cancellation of the IR divergence in the second derivative of the effective potential, originating from the vanishing Goldstone mass in Landau gauge. We follow the treatment in ref. [356]. This leads to the renormalization condition eq. (7.7). We calculate the self-energy $\Sigma(p^2)$ of the lepton number breaking scalar ϕ in Landau gauge, using dimensional regularization in $D = 4 - 2\epsilon$ dimensions. More precisely, we are interested in the difference of the self-energy evaluated at the scalar mass $p^2 = m_\phi^2$ and at $p^2 = 0$, $\Delta\Sigma \equiv \Sigma(m_\phi^2) - \Sigma(0)$, where p^2 is the external momentum squared.

7.A.1. Scalar Self-Energy

We consider the Lagrangian

$$\mathcal{L} = \mathrm{D}_\mu \Phi^\dagger \mathrm{D}^\mu \Phi + \mu_\Phi^2 \Phi^\dagger \Phi - \lambda_\Phi \left(\Phi^\dagger \Phi\right)^2 , \tag{7.10}$$

where $\mathrm{D}_\mu \Phi = \partial_\mu \Phi - i g_\ell L_\Phi Z' \Phi$. We rewrite the complex scalar Φ in terms of its real and imaginary parts and its VEV v_Φ as $\Phi = \frac{1}{\sqrt{2}}\left(v_\Phi + \phi + i\omega^0\right)$.

The (bare) self-energy of ϕ receives contributions from loops of ϕ itself, the Goldstone boson ω^0, and the gauge boson Z'. As the tadpole diagrams depicted in fig. 7.8 are independent of the external momentum, we only need to evaluate the remaining bubble diagrams. These are

$-i\Sigma_0^S(p^2) =$ 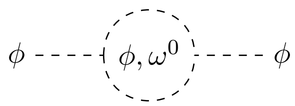 , (7.11)

$-i\Sigma_0^{Z'}(p^2) =$ 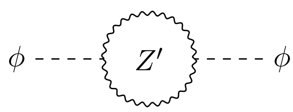 + 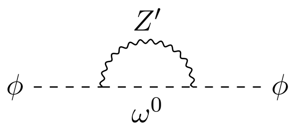 . (7.12)

We perform the Passarino-Veltman reduction [365] of the corresponding integrals using FeynCalc 9.3.0 [366, 367], yielding

$$\Sigma_0^S(p^2) = -\frac{\lambda_S^2 v_\Phi^2}{32\pi^2} B_0\left(p^2, m_S^2, m_S^2\right) , \tag{7.13}$$

$$\begin{aligned}\Sigma_0^{Z'}(p^2) = -\frac{L_\Phi^2 g_\ell^2}{32\pi^2 m_{Z'}^2}\Big\{ &\left[p^4 - 4m_{Z'}^2 p^2 + 12 m_{Z'}^4\right] B_0\left(p^2, m_{Z'}^2, m_{Z'}^2\right) \\ &- p^4 B_0\left(p^2, 0, 0\right) - 2p^2 A_0\left(p^2\right) - 8m_{Z'}^4 \Big\} ,\end{aligned} \tag{7.14}$$

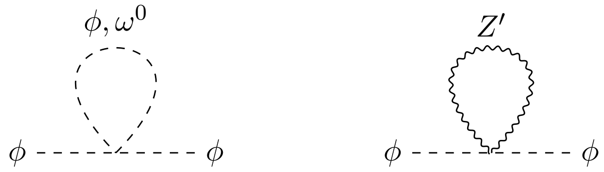

Figure 7.8: Tadpole diagrams contributing to the self-energy of ϕ.

where $\lambda_S = 6\lambda_\Phi$ for $S = \phi$ and $\lambda_S = 2\lambda_\Phi$ for $S = \omega^0$, respectively. The scalar one- and two-point functions A_0 and B_0 are defined by

$$A_0\left(m^2\right) = \frac{(2\pi\mu_R)^{4-D}}{i\pi^2} \int \mathrm{d}^D q \, \frac{1}{q^2 - m^2 + i\varepsilon}\,, \tag{7.15}$$

$$B_0\left(p^2, m_1^2, m_2^2\right) = \frac{(2\pi\mu_R)^{4-D}}{i\pi^2} \int \mathrm{d}^D q \, \frac{1}{q^2 - m_1^2 + i\varepsilon} \frac{1}{(q+p)^2 - m_2^2 + i\varepsilon}\,, \tag{7.16}$$

where μ_R is the renormalization scale. The full self-energy is then given by

$$\Sigma_0\left(p^2\right) = \Sigma_0^\phi\left(p^2\right) + \Sigma_0^{\omega^0}\left(p^2\right) + \Sigma_0^{Z'}\left(p^2\right) + \text{tadpole contributions}\,. \tag{7.17}$$

The renormalized self-energy is related to the bare one by

$$\Sigma_R\left(p^2\right) = \Sigma_0\left(p^2\right) + \delta m^2 - p^2 \delta Z\,, \tag{7.18}$$

where δm^2 and δZ are the mass and field renormalization counter-terms for ϕ,

$$\mathcal{L} \supset \frac{1}{2}\delta Z \partial_\mu \phi \partial^\mu \phi - \frac{1}{2}\delta m^2 \phi^2\,. \tag{7.19}$$

When calculating $\Delta\Sigma$, δm^2 cancels in the difference but δZ remains, i.e.

$$\Delta\Sigma = \Sigma_0\left(m_\phi^2\right) - \Sigma_0(0) - m_\phi^2 \delta Z\,. \tag{7.20}$$

In particular, this means that $\Delta\Sigma$ is independent of the renormalization conditions we impose on the counter-terms δm^2 and $\delta\lambda$ when calculating the effective potential. We can now fix δZ by requiring canonical normalization of the field ϕ, i.e.

$$\frac{\partial\, \Sigma_R}{\partial\, p^2}\left(m_\phi^2\right) = 0 \qquad \Longrightarrow \qquad \delta Z = \frac{\partial\, \Sigma_0}{\partial\, p^2}\left(m_\phi^2\right)\,. \tag{7.21}$$

Again, the tadpole diagrams in fig. 7.8 do not contribute as they are independent of p^2.

Finally, the difference in the self-energy used in the renormalization condition eq. (7.7) is obtained by plugging eqs. (7.17) and (7.21) into eq. (7.20). We use LoopTools 2.13 [368, 369] to evaluate the finite part of the scalar integrals and their derivatives.

7.A.2. On-Shell Renormalization of the Effective Potential

The momentum-dependent mass of ϕ is given by

$$m_\phi^2\left(p^2\right) = m_{\phi,R}^2 + \Sigma_R\left(p^2\right)\,, \tag{7.22}$$

where $m_{\phi,R}$ is the renormalized mass parameter in the Lagrangian, which is related to the physical (pole) mass $m_\phi^2 \equiv m_\phi^2(m_\phi^2)$ by

$$m_{\phi,R}^2 = m_\phi^2 - \Sigma_R\left(m_\phi^2\right)\,. \tag{7.23}$$

Since the effective potential is defined at vanishing external momentum, we now impose the conditions

$$\left.\frac{\partial\, V_{\rm eff}(\phi, T=0)}{\partial\,\phi}\right|_{\phi=v_\Phi} = 0\,, \tag{7.24}$$

$$\left.\frac{\partial^2\, V_{\rm eff}(\phi, T=0)}{\partial\,\phi^2}\right|_{\phi=v_\Phi} = m_\phi^2(0) = m_\phi^2 - \Delta\Sigma\,. \tag{7.25}$$

We further want the VEV v_Φ and the scalar mass m_ϕ to be identical to the values inferred from the tree-level potential, i.e.

$$\left.\frac{\partial\, V_{\rm tree}(\phi)}{\partial\,\phi}\right|_{\phi=v_\Phi} = 0\,, \qquad \left.\frac{\partial^2\, V_{\rm tree}(\phi)}{\partial\,\phi^2}\right|_{\phi=v_\Phi} = m_\phi^2\,, \tag{7.26}$$

hence, using $V_{\rm eff}(\phi, T=0) = V_{\rm tree}(\phi) + V_{\rm CW}(\phi) + \Delta V_{\rm ct}(\phi)$, we obtain the renormalization conditions in eq. (7.7).

Note that $\Delta\Sigma$ has an IR divergence coming from the Goldstone contribution eq. (7.13) to the self-energy at zero-momentum,

$$\Sigma_0^{\omega^0}(0) = -\frac{\lambda_\Phi^2 v_\Phi^2}{8\pi^2} B_0\left(0, m_{\omega^0}^2, m_{\omega^0}^2\right)\,. \tag{7.27}$$

In Landau gauge $m_{\omega^0} = 0$, but we keep it as a regulator. Taking the analytic expression for the scalar two-point function from refs. [370, 371],

$$B_0\left(0, m_{\omega^0}^2, m_{\omega^0}^2\right) = \Delta - \log\frac{m_{\omega^0}^2 - i\varepsilon}{\mu_R^2}\,, \tag{7.28}$$

where $\Delta = \frac{1}{\epsilon} - \gamma_E + \log 4\pi$, we obtain the IR divergent part

$$-\,\Delta\Sigma = \frac{\lambda_\Phi^2 v_\Phi^2}{8\pi^2}\log\frac{m_{\omega^0}^2}{\mu_R^2} + \text{finite terms}\,. \tag{7.29}$$

On the other hand, the Goldstone contribution to the Coleman-Weinberg potential eq. (6.21) is given by

$$V_{\rm CW}(\phi) \supset \frac{m_{\omega^0}^4(\phi)}{64\pi^2}\left[\log\frac{m_{\omega^0}^2(\phi)}{\mu_R^2} - \frac{3}{2}\right]\,, \tag{7.30}$$

where $m^2_{\omega^0}(\phi) = \lambda_\Phi \phi^2 - \mu_\Phi^2$ with $\mu_\Phi^2 = \lambda_\Phi v_\Phi^2$, and its derivatives are

$$\frac{\partial V_{\text{CW}}}{\partial \phi} \supset \frac{\lambda_\Phi \phi \, m^2_{\omega^0}(\phi)}{16\pi^2} \left[\log \frac{m^2_{\omega^0}(\phi)}{\mu_R^2} - 1\right], \tag{7.31}$$

$$\frac{\partial^2 V_{\text{CW}}}{\partial \phi^2} \supset \frac{\lambda_\Phi m^2_{\omega^0}(\phi)}{16\pi^2} \left[\log \frac{m^2_{\omega^0}(\phi)}{\mu_R^2} - 1\right] + \frac{\lambda_\Phi^2 \phi^2}{8\pi^2} \log \frac{m^2_{\omega^0}(\phi)}{\mu_R^2}. \tag{7.32}$$

Whereas the parts with the square brackets go to zero when taking the limit $\phi \longrightarrow v_\Phi$, the second part in the second derivative gives the same IR divergence we encountered in eq. (7.29). Hence, the IR divergences on both sides of the second condition in eq. (7.7) cancel and we obtain IR-finite counter-terms.

Appendix 7.B. Bubble Wall Velocity

The wall velocity is rather difficult to compute and can in general not be determined from the finite-T effective potential alone, as it involves out-of-equilibrium dynamics. It can be obtained by a microscopic treatment of the fluid solving Boltzmann equations or at the macroscopic level adding an effective friction term to the scalar equation of motion, see refs. [321, 322] and references therein for more details, or ref. [323] for recent results. Assuming Chapman-Jouget detonations [372], v_w can be calculated as a function of α, yielding values ranging from the speed of sound $c_s = \frac{1}{\sqrt{3}}$ in the plasma to the speed of light. However, this assumption is not justified and typically incorrect [373].

Since we expect that the bubbles do not run away in our model, the GW spectrum is given by $h^2\Omega_{\text{GW}}(f) = h^2\Omega_{\text{sw}}(f) + h^2\Omega_{\text{turb}}(f)$. For both, sound wave and turbulence contribution, cf. eqs. (6.14b) and (6.14c), the amplitudes of the spectra are proportional to v_w and the peak frequencies shift as $1/v_w$, i.e. order one changes in the wall velocity only have an order one effect on the spectrum and peak frequencies. Hence, the detectability of the generated stochastic background eventually only has a mild dependence on v_w. As a detectable signal further typically requires strong transitions with large wall velocities, we simply take the most optimistic estimate $v_w = 1$.

Figure 7.9 shows the dependence of the detectability on the bubble wall velocity in the case of negligible portal and Yukawa couplings. Compared to fig. 7.7a above, where $v_w = 1$ was assumed, we here show the sensitivity for a slightly lower wall velocity ($v_w = 0.9$), a wall velocity close to the speed of sound ($v_w = 0.6$), and subsonic bubbles ($v_w = 0.3$ and $v_w = 0.1$). Again, the colored regions are detectable by *LISA* (blue), *B-DECIGO* (red), *DECIGO* (dark orange) and *BBO* (orange). The GW spectra generated by the first-order PTs in the gray region are not detectable. For supersonic bubbles, the detectable regions barely change when varying v_w. Taking v_w to subsonic values decreases the sensitivity visibly.

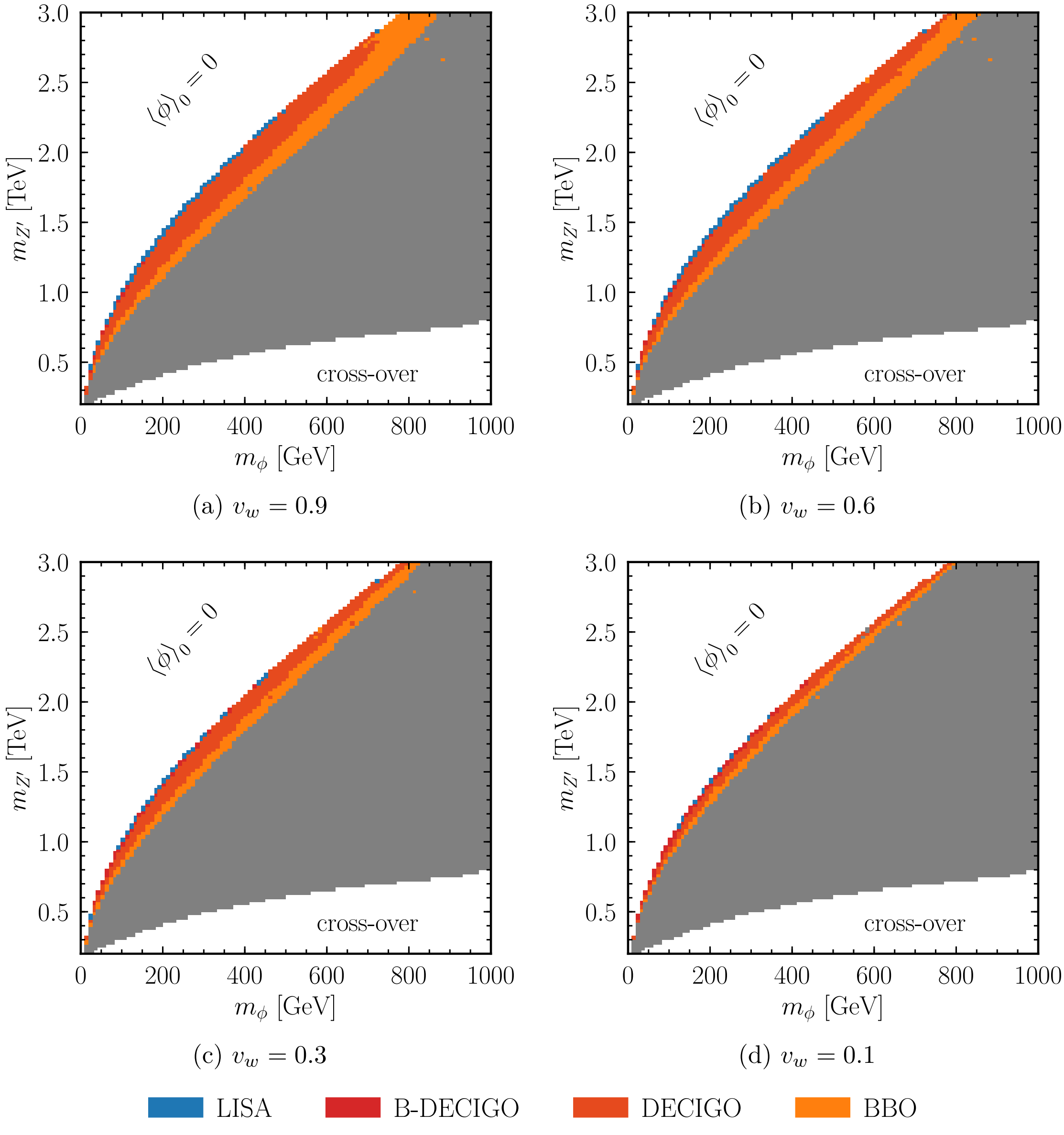

Figure 7.9: Same as fig. 7.7a, but with different wall velocities. Figure 7.7a assumes a wall velocity of $v_w = 1$.

8. Constraining Secluded Hidden Sectors with Gravitational Waves

This chapter is based on work conducted in collaboration with Moritz Breitbach, Joachim Kopp, Toby Opferkuch, and Pedro Schwaller [2]. It closely resembles the publication.

So far we have only considered phase transitions (PTs) occurring within the Standard Model (SM) itself or in sectors beyond the Standard Model (BSM) that are in thermal equilibrium with the SM. This assumption is however not necessarily true. In this chapter, we will discuss the case of PTs in hidden sectors that are decoupled from the SM.

Despite the strong motivation for new physics, the extensive search for beyond the Standard Model (BSM) phenomena at the *LHC* did not provide any clear hints for the existence of new particles so far. We can therefore conclude that the BSM states are either too heavy to be produced at the energy scales currently accessible, or too weakly coupled to be generated at a detectable rate. This provides motivation for so-called hidden or dark sectors, i.e. a group of particles that interact only very weakly, maybe even only gravitationally, with the SM. While such a sector is typically very challenging to detect directly, gravitational waves (GWs) from a PT within the sector may provide a possibility to assess these models. In particular, if the sector interacts with the SM via gravity only, GW probes may be the only way to study such a case.

In this chapter, we will mainly focus on sub-MeV hidden sectors. While PTs at such low temperatures have the advantage that there are less degrees of freedom (DOFs) contributing to the radiation energy density in eq. (6.8), so that the relative amount of energy released into GWs is typically larger than at high temperatures, hidden sectors featuring additional particles with sub-MeV masses are subject to strong constraints on the effective number of neutrino species N_{eff}. These constraints require light hidden sectors to be decoupled from the SM and to be colder than the photon bath at low temperatures. We discuss how this affects the stochastic gravitational wave background (SGWB) generated by a first-order PT in such a sector and its detectability. Due to the low temperatures considered here, the GW spectrum is peaked at frequencies accessible through pulsar timing arrays (PTAs).

To assess whether it is possible to construct sub-MeV hidden sector models that generate an observable SGWB while at the same time consistent with N_{eff} constraints, two simple benchmark models are considered. The first model consists of two SM singlet scalars, the other one is a Higgsed dark photon model. As the number of additional DOFs at low temperatures is strongly constrained, these two models should cover a large fraction of the model space for the relevant DOFs in sub-MeV sectors.

This chapter is structured as outlined below. We first provide an introduction to decoupled hidden sectors in section 8.1, reviewing the decoupling of neutrinos in the SM in section 8.1.1, as well as constraints from the effective number of neutrino species in section 8.1.2. In section 8.1.3 we describe the hidden sector scenarios considered in this chapter. Section 8.2 then discusses how the the SGWB of a first-order PT is altered if it occurs in a secluded sector. The dependence of the parameters characterizing the transition on the temperature ratio between the two sectors is elaborated in section 8.2.1, and section 8.2.2 presents the corresponding effect on the detectability of the spectrum. In section 8.3 we finally demonstrate that decoupled hidden sectors that satisfy the cosmological constraints on N_{eff} may still feature a first-order PT observable via GWs by considering two toy models. We then conclude in section 8.4.

8.1. Decoupled Hidden Sectors

As already stated above, the radiation energy density of BSM sectors at temperatures below an MeV is rather strongly constrained. These constraints are typically phrased in terms of the effective number of neutrino species, N_{eff}. It parametrizes the new physics' contributions to the energy density of the early Universe as if these were originating from additional neutrino generations. In other words, the energy density is rewritten by splitting off the photon contribution and treating all other species as neutrinos,

$$\rho_{\text{rad}}(T) = \frac{\pi^2}{30}\sum_i g_i T_i^4 = \left[1 + \frac{7}{8}\left(\frac{4}{11}\right)^{\frac{4}{3}} N_{\text{eff}}\right]\rho_\gamma(T)\,. \tag{8.1}$$

Here, the sum runs over all relativistic species, which can in principle all have different temperatures T_i, and g_i are the respective effective number of DOFs. As the energy, entropy and number density of relativistic fermions is by a factor of $\frac{7}{8}$ lower than the one of a boson, the effective DOFs for fermions include this $\frac{7}{8}$ factor.

As we will argue in the following, the constraints on N_{eff} require sub-MeV hidden sectors to be decoupled from the photon bath, so that they can have a different temperature. The constraints can then be evaded by assigning the hidden sector a lower temperature. Since the radiation energy density goes with the fourth power of temperature, this suppresses the new physics contribution to N_{eff} quite efficiently. We therefore define the temperature ratio ξ_h as the ratio of the hidden sector to the photon temperature,

$$\xi_h = \frac{T_h}{T_\gamma} \tag{8.2}$$

and consider $\xi_h < 1$ in the following.

To understand the process of particle decoupling as well as how the temperature ratio $\xi_\nu^3 = 4/11$ in eq. (8.1) arises, we will first briefly recapitulate the decoupling of neutrinos in the SM in section 8.1.1. Subsequently, we will review N_{eff} and the various constraints on this parameter in section 8.1.2. Finally, section 8.1.3 is devoted to the different hidden sector scenarios we are going to consider.

8.1.1. Neutrino Decoupling and Electron-Positron Annihilation

In order to maintain equilibrium, the interactions between a given particle species and the other particles in the plasma of the early Universe have to occur sufficiently fast to compete against the Hubble expansion. A species therefore decouples from the plasma when its interaction rate Γ drops below the Hubble rate H. Recall from our discussion of the decoupling of gravity in the beginning of chapter 6 that the interaction rate is given by $\Gamma = n\sigma v$. For neutrinos, these interactions are annihilation to and scattering off SM leptons with $\sigma \propto G_F^2$, where G_F is Fermi's constant. Due to their extremely low mass, neutrinos are still relativistic upon decoupling, such that $n \sim T^3$, $v = c$, and $\sigma \sim G_F^2 T^2$ on dimensional grounds. Further taking $H \sim T^2/M_P$ we obtain that neutrinos decouple at a temperature around

$$T_{\nu-\text{dec.}} \sim \left(G_F^2 M_P\right)^{-\frac{1}{3}} \sim 1\,\text{MeV}\,. \tag{8.3}$$

After decoupling, the decoupled species and the particles in the thermal bath can in principle have different temperatures. These are determined by the conservation of co-moving entropy density, which is conserved separately in the two sectors. In the case of neutrino decoupling

$$a^3 s_\nu = a^3\,\frac{2\pi^2}{45}\,g_\nu\,T_\nu^3 = \text{const} \qquad \text{and} \qquad a^3 s_\text{th} = a^3\,\frac{2\pi^2}{45}\,g_\text{th}\,T_\text{th}^3 = \text{const}\,, \tag{8.4}$$

where T_ν (T_th) and g_ν (g_th) are the temperature and effective number of DOFs of the neutrinos (thermal bath), respectively. Then $g_\nu = \frac{7}{8} \times N_\nu \times 2 = \frac{21}{4}$, where $N_\nu = 3$ is the number of SM neutrino generations, and the remaining thermal bath is composed of photons and electrons, i.e. $g_\text{th} = 2 + \frac{7}{8} \times 4 = \frac{11}{2}$.

As the neutrinos and the bath have the same temperature at decoupling, they will also have the same temperature directly after decoupling. This however changes as soon as some particle species becomes non-relativistic and annihilates, altering the effective number of DOFs. The entropy of the annihilating species is then transferred to the remaining particles, causing the temperature of the sector to drop slower than corresponding to the usual $1/a$ dependence. Indeed, electrons and positrons become non-relativistic at $T \simeq m_e = 511\,\text{keV}$, just after neutrino decoupling, causing g_th to drop to $g_\gamma = 2$. As the photons are the last particles remaining in the thermal bath, we will always characterize it in terms of the photon temperature $T_\text{th} = T_\gamma$ from now on.

Let us now compare the photon bath just before $e^\pm$ annihilation (with quantities indexed by '(1)') and at the time when the annihilation has completed (with quantities indexed by '(2)'). If we assume that the heating of the photon bath due to the entropy transfer from the annihilating electrons and positrons is quasi-instantaneous, we can neglect the change of the scale factor a of the Universe during this process. Conservation of co-moving entropy in the bath then implies that the photon temperature has changed by

$$\frac{T_\gamma^{(2)}}{T_\gamma^{(1)}} = \left(\frac{g_\text{th}^{(1)}}{g_\text{th}^{(2)}}\right)^{\frac{1}{3}} = \left(\frac{11}{4}\right)^{\frac{1}{3}}\,. \tag{8.5}$$

In the neutrino sector on the other hand, the number of effective DOFs remains constant, and so does the temperature, i.e. $T_\nu^{(2)} = T_\nu^{(1)} = T_\gamma^{(1)}$. Therefore, they now have a temperature different from the one of the photons, with a temperature ratio of

$$\xi_\nu \equiv \frac{T_\nu^{(2)}}{T_\gamma^{(2)}} = \frac{T_\gamma^{(1)}}{T_\gamma^{(2)}} = \left(\frac{4}{11}\right)^{\frac{1}{3}}\,. \tag{8.6}$$

After $e^{\pm}$ annihilation, the temperatures of photons and neutrinos again evolve as $T \sim 1/a$, and the temperature ratio of $(4/11)^{1/3}$ is preserved.

Note that we have assumed that neutrino decoupling happens (quasi-)instantaneously, and that the full electron entropy is dumped into photons. However, as the time at which electrons become non-relativistic is very close to the time of neutrino decoupling, this is not entirely true. When electrons and positrons annihilate, the neutrinos are not completely decoupled yet, and a small fraction of the electron entropy is also transferred to the neutrinos. As a result, the neutrino spectra feature small non-thermal distortions [374].

8.1.2. Effective Number of Neutrino Species

Let us now consider the energy density of the Universe after $e^{\pm}$ annihilation,

$$\rho_{\text{rad}} = \frac{\pi^2}{30}\left(g_\gamma T_\gamma^4 + g_\nu T_\nu^4\right) = \left[1 + \frac{g_\nu}{g_\gamma}\frac{T_\nu^4}{T_\gamma^4}\right]\rho_\gamma = \left[1 + \frac{7}{8}N_\nu\left(\frac{4}{11}\right)^{\frac{4}{3}}\right]\rho_\gamma\,. \tag{8.7}$$

We can now interpret additional relativistic DOFs in terms of additional neutrino generations, defining the effective number of neutrino species as

$$N_{\text{eff}} = \frac{8}{7}\frac{\rho_{\text{rad}} - \rho_\gamma}{\rho_\gamma}\left(\frac{11}{4}\right)^{\frac{4}{3}}\,. \tag{8.8}$$

In the SM we have $N_{\text{eff}}^{\text{SM}} = 3.046$ [374], where the deviation from $N_\nu = 3$ originates from entropy leakage due to non-instantaneous neutrino decoupling.

As the effective number of neutrino species parameterizes new physics' contributions to the radiation energy density, it directly effects the expansion rate of the Universe. It is therefore cosmologically constrained from two types of observations: measurements of the relative abundance of light elements at the time of Big Bang Nucleosynthesis (BBN), and the power spectrum of the cosmic microwave background (CMB) [60, 375].

The production of light elements, in particular of ^{4}He, from free neutrons and protons in the early Universe occurred at temperatures around $T_{\text{BBN}} \sim 1\,\text{MeV}$. This process of BBN [376] is well understood [377–379] and provides the earliest stage of our Universe that we have probed reliably [68, 380]. As eventually all free neutrons end up bound in ^{4}He nuclei to a good approximation, the final helium abundance (relative to the total nucleon abundance) is essentially determined by the neutron-to-proton ratio at BBN. This ratio depends on the time or temperature at which the interactions interconverting neutrons and protons freeze out, which in turn is sensitive to the Hubble rate around $T \sim 1\,\text{MeV}$. Additional relativistic species lead to a higher freeze-out temperature and thereby a larger neutron-to-proton ratio, increasing the helium abundance. Measurements of the relative abundance of ^{4}He can therefore be used to put limits on the effective number of neutrino species [381, 382], imposing a 95 % confidence level (CL) constraint of [60]

$$N_{\text{eff}} = 2.95^{+0.56}_{-0.52} \qquad (\text{BBN})\,, \tag{8.9}$$

assuming that N_{eff} is constant during BBN [236, 378, 379, 381] (see e.g. ref. [383] for the impact of relaxing this assumption).

Complementary constraints on N_{eff} around the time of recombination at $T_{\text{rec}} \sim 0.3\,\text{eV}$ can be extracted from the temperature and polarization power spectrum of the CMB. Deviations from $N_{\text{eff}}^{\text{SM}}$ lead to changes in the heights and positions of the acoustic peaks, as well as in the damping tail of the CMB spectrum. These modifications are caused by an increase of the photon diffusion scale (Silk damping scale) at recombination as well as the temperatures of photon decoupling and matter-radiation-equality due to the presence of additional relativistic DOFs [68, 270]. The current 95 % CL constraint from 2018 *Planck* data including polarization and baryon acoustic oscillation (BAO) measurements is [60]

$$N_{\text{eff}} = 2.99^{+0.34}_{-0.33} \qquad (\text{CMB})\,. \tag{8.10}$$

Further taking into account data from local measurements of the Hubble rate H_0 today [112], which provide a value for H_0 that is conflict with the one determined by *Planck*, the CMB 95 % CL limit on N_{eff} relaxes to [60]

$$N_{\text{eff}} = 3.27 \pm 0.30 \qquad (\text{CMB}+H_0)\,. \tag{8.11}$$

8.1.3. Hidden Sector Cosmology

The N_{eff} bounds discussed above strongly constrain the relativistic particle content of hidden sector models at sub-MeV temperatures. In the following, we will review various generic scenarios for such models and the corresponding constraints. The effective number of relativistic DOFs in the hidden sector shall be denoted by g_h. For the case of sectors that are decoupled from the photon bath, let ξ_h further be the ratio of the hidden-sector to photon temperature, as defined in eq. (8.2).

Hidden sectors in thermal contact with the SM

Any additional relativistic DOF that is in thermal equilibrium with the photon bath throughout the BBN (and $e^{\pm}$ annihilation) epoch is inconsistent with the bounds on N_{eff}. Even a single real scalar DOF ($g_h = 1$) would produce a deviation of N_{eff} from the SM value of $\Delta N_{\text{eff}} = 2.2$ and thereby be in conflict with the limits from eqs. (8.9) to (8.11). We therefore discard this scenario in the following.

If, however, around the time of neutrino decoupling thermal contact between the hidden sector and the SM is predominantly established via its interactions with the neutrinos, the hidden sector will decouple from the photon bath along with the neutrinos, remaining in thermal equilibrium with the latter. In this case $\xi_h = \xi_\nu = (4/11)^{1/3}$ after $e^{\pm}$ annihilation, and N_{eff} is modified to[1]

$$N_{\text{eff}} = N_{\text{eff}}^{\text{SM}} \left(1 + \frac{g_h}{g_\nu}\right)\,. \tag{8.12}$$

Once the hidden sector particles become non-relativistic, they annihilate and transfer their entropy into neutrinos. This heats the neutrino sector, modifying the neutrinos' temperature ratio by a factor $[(g_h + g_\nu)/g_\nu]^{1/3}$, i.e. [384]

$$N_{\text{eff}} = N_{\text{eff}}^{\text{SM}} \left(1 + \frac{g_h}{g_\nu}\right)^{\frac{4}{3}}\,. \tag{8.13}$$

[1]Throughout this chapter, we will use $N_{\text{eff}}^{\text{SM}} = 3.046$ instead of $N_\nu = 3$ despite neglecting the entropy leakage in our calculations, such that we reproduce the SM value in the limit $g_h \to 0$.

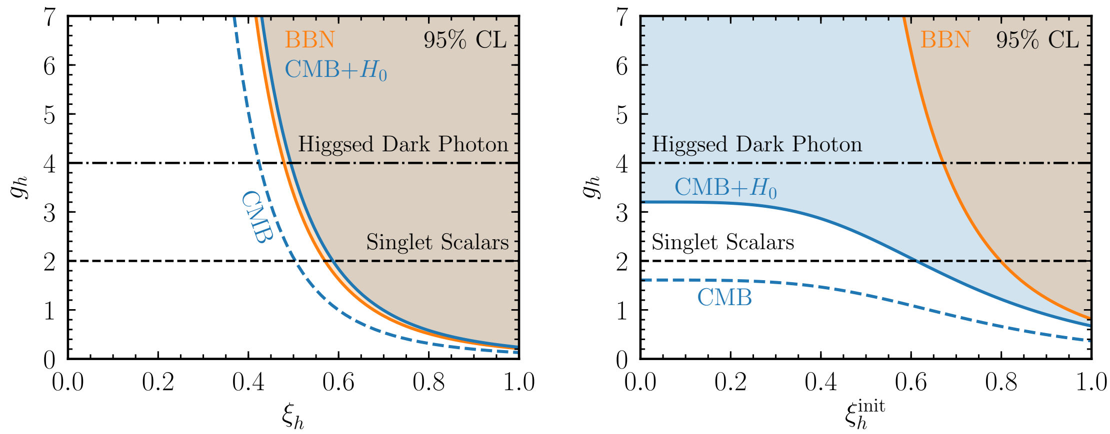

(a) decoupled hidden sector

(b) ν-quilibration

Figure 8.1: 95 % CL limits on N_{eff} from BBN (eq. (8.9), orange shaded region), CMB (eq. (8.10), blue dashed line), and CMB+H_0 (eq. (8.10), blue shaded region) in the decoupled hidden sector (left) and ν-quilibration (right) scenario, as a function of the hidden-sector effective number of DOFs g_h and temperature ratio ξ_h. The dashed and dash-dotted line indicate the value of g_h in the singlet scalars (section 8.3.1) and Higgsed dark photon (section 8.3.2) toy model, respectively.

Even the least stringent 95 % CL constraint considered here, eq. (8.11), limits the number of hidden sector DOFs to $g_h \lesssim 0.90$ (0.66) if they are (non-)relativistic at recombination. As a consequence, no additional light DOF can remain in thermal equilibrium with the SM (with neither photons nor neutrinos) after neutrino decoupling.

Completely decoupled hidden sectors

Let us therefore consider the case that the hidden sector is completely decoupled from the SM with an arbitrary temperature ratio ξ_h. This scenario can arise if the the hidden sector and the SM never were in equilibrium at all, in which case the temperature ratio is determined by the initial conditions after inflation, or if it decoupled from the SM early on (well before BBN), so that ξ_h is set via subsequent annihilation processes of non-relativistic species in the two sectors. We then obtain

$$N_{\text{eff}} = N_{\text{eff}}^{\text{SM}} + \frac{4}{7}\left(\frac{11}{4}\right)^{\frac{4}{3}} g_h\, \xi_h^4\,. \tag{8.14}$$

Note that, when the particles of such a sector become non-relativistic, they typically need to annihilate into a form of dark radiation to avoid over-closure of the Universe.

The BBN and CMB constraints on the temperature ratio ξ_h and number of effective relativistic DOFs in a fully decoupled hidden sector are shown in fig. 8.1a. The solid orange and blue lines depict the 95 % CL bound from BBN (eq. (8.9)) and CMB+H_0 (eq. (8.11)), respectively, the CMB only limit (eq. (8.10)) is shown as the dashed blue line. As can be seen in the plot, even with only a single additional relativistic DOF ($g_h = 1$), the hidden

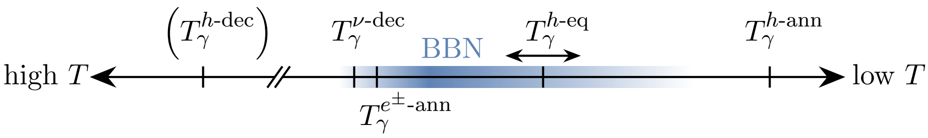

Figure 8.2: Sequence of events in the ν-quilibration scenario, labeled by the corresponding temperature T_γ of the photon bath. In chronological order: hidden sector decoupling ($T_\gamma^{h-\mathrm{dec}}$, if ever in thermal contact with the photons), neutrino decoupling ($T_\gamma^{\nu-\mathrm{dec}}$) and electron-positron annihilation ($T_\gamma^{e^\pm-\mathrm{ann}}$), hidden sector-neutrino (re-)equilibration ($T_\gamma^{h-\mathrm{eq}}$), and hidden sector annihilation ($T_\gamma^{h-\mathrm{ann}}$).

sector is required to be at least a factor of $\xi_h \simeq 0.6 - 0.7$ colder than the visible sector in order to satisfy the constraints.

Hidden sectors equilibrating with neutrinos (ν-quilibration)

While we established above that the hidden sector cannot be in thermal equilibrium with the SM neutrinos around the time of BBN, it may still equilibrate with the latter after they decoupled from the photon bath. This scenario, dubbed ν-quilibration in the following, has been considered in refs. [385, 386] and has the advantage that the hidden sector can annihilate into neutrinos when becoming non-relativistic, as we will discuss later. Let us consider the sequence of events depicted in fig. 8.2.[2]

The hidden sector either never was in thermal contact with the photon bath, or decoupled from it well before BBN at the (photon) temperature $T_\gamma^{h-\mathrm{dec}}$, and may therefore have a temperature different from the visible sector. We denote the hidden sector temperature ratio at the time of neutrino decoupling (at the photon temperature $T_\gamma^{\nu-\mathrm{dec}}$) by ξ_h^{init}. Shortly after that, electrons and positrons become non-relativistic and annihilate at $T_\gamma^{e^\pm-\mathrm{ann}}$, heating up the photon bath. Neglecting the leakage of entropy from the electrons into the neutrinos, this process changes the temperature ratio of the neutrinos from $\xi_\nu = 1$ to the SM value $\xi_\nu = \xi_\nu^{\mathrm{SM}} = (4/11)^{1/3}$ determined in eq. (8.6). The hidden sector temperature ratio is modified in the same way to $\xi_h = \xi_\nu^{\mathrm{SM}}\, \xi_h^{\mathrm{init}}$.

Subsequently, towards the end of the BBN era or later, the hidden sector (re-)enters equilibrium with the neutrinos at the photon temperature $T_\gamma^{h-\mathrm{eq}}$. For simplicity we assume that no hidden sector DOFs have become non-relativistic after neutrino decoupling, so that ξ_h is only modified by $e^\pm$ annihilation. Further assuming that equilibration occurs quasi-instantaneously, the process is governed by conservation of energy. This implies that $g_\nu T_\nu^4 + g_h T_h^4 = (g_\nu + g_h) T_{\nu+h}^4$, where T_ν and T_h are the neutrino and hidden sector temperature at the beginning of equilibration, and $T_{\nu+h}$ is the temperature of the com-

[2] Since we neglect the leakage of entropy from $e^\pm$ annihilation into neutrinos, it actually does not matter whether the equilibration occurs between neutrino decoupling and $e^\pm$ annihilation or shortly after the latter event: the thermalization process does not care about the photon bath, and the photon heating due to annihilation is independent of the decoupled sectors. The resulting N_{eff} constraints are therefore identical.

bined sector after the process has completed. The corresponding temperature ratio $\xi_{\nu+h}$ is then given by

$$\xi_{\nu+h} = \left[\frac{g_\nu \left(\xi_\nu^{\mathrm{SM}}\right)^4 + g_h \left(\xi_\nu^{\mathrm{SM}}\xi_h^{\mathrm{init}}\right)^4}{g_\nu + g_h}\right]^{\frac{1}{4}} = \xi_\nu^{\mathrm{SM}} \left[1 + \frac{g_h}{g_\nu}\right]^{-\frac{1}{4}} \left[1 + \frac{g_h}{g_\nu}\left(\xi_h^{\mathrm{init}}\right)^4\right]^{\frac{1}{4}} . \tag{8.15}$$

With respect to the SM, the effective number of neutrino species is then modified by a factor $(\xi_{\nu+h}/\xi_\nu^{\mathrm{SM}})^4$ accounting for the different temperature ratio, and by a factor $(g_h + g_\nu)/g_\nu$ from the additional DOFs. Therefore, after the hidden sector thermalized with the neutrinos,

$$N_{\mathrm{eff}} = N_{\mathrm{eff}}^{\mathrm{SM}} \left[1 + \frac{g_h}{g_\nu}\left(\xi_h^{\mathrm{init}}\right)^4\right] . \tag{8.16}$$

Subsequently, the hidden sector particle content will become non-relativistic at some temperature $T_\gamma^{h-\mathrm{ann}}$. If the hidden sector had lost thermal contact to the neutrino bath by then, it would have frozen-out while still relativistic, and therefore most likely overclose the Universe. We will hence assume that the hidden sector is still in equilibrium with the neutrinos when becoming non-relativistic. Its entropy is then transferred to the neutrino bath, heating it by a factor $[(g_\nu + g_h)/g_\nu]^{1/3}$. The temperature ratio of the neutrinos after hidden sector annihilation then becomes

$$\xi_\nu = \left[\frac{g_\nu + g_h}{g_\nu}\right]^{\frac{1}{3}} \xi_{\nu+h} = \xi_\nu^{\mathrm{SM}} \left[1 + \frac{g_h}{g_\nu}\right]^{\frac{1}{12}} \left[1 + \frac{g_h}{g_\nu}\left(\xi_h^{\mathrm{init}}\right)^4\right]^{\frac{1}{4}} . \tag{8.17}$$

Unless the hidden sector contains sub-eV particles, annihilation will occur before the time of recombination, and the value of N_{eff} constrained by the CMB is

$$N_{\mathrm{eff}} = N_{\mathrm{eff}}^{\mathrm{SM}} \left[1 + \frac{g_h}{g_\nu}\right]^{\frac{1}{3}} \left[1 + \frac{g_h}{g_\nu}\left(\xi_h^{\mathrm{init}}\right)^4\right] . \tag{8.18}$$

The BBN (orange shaded region) and CMB (blue shaded region and blue dashed line) 95 % CL constraints on N_{eff} in this scenario are shown in fig. 8.1b. The abscissa shows the hidden sector temperature ratio ξ_h^{init} before the $e^\pm$ annihilation, and the ordinate is the effective number of hidden sector DOFs g_h. We employ eqs. (8.16) and (8.18) for the BBN and CMB limits, respectively, assuming that the hidden sector annihilates after BBN[3] and before recombination.

8.2. Gravitational Waves from Decoupled Hidden Sectors

We will now explore how first-order PTs as well as their respective GW signal and its detectability are modified if they occur in a decoupled hidden sector with a temperature different from the one of the photon bath. While all properties of the hidden sector are naturally described in terms of its temperature T_h, we assume that our Universe remains dominated by the visible sector, so that it is more intuitive to characterize the latter

[3] More precisely: after the initial formation of light elements (D and ^{4}He) at $T_\gamma \sim 0.1\,\mathrm{MeV}$ [387].

in terms of the photon temperature T_γ. In particular, we usually express the radiation energy density of the Universe, which eventually determines the Hubble rate, in terms of T_γ, i.e.

$$\rho_{\rm rad}(T_\gamma) = \frac{\pi^2}{30}\, g_\star(T_\gamma)\, T_\gamma^4\,, \qquad \text{with} \qquad g_\star(T_\gamma) = g_\star^{\rm SM}(T_\gamma) + g_h\, \xi_h^4\,. \tag{8.19}$$

We will mostly consider PTs occurring between the epoch of BBN and before recombination, so the the effective number of relativistic DOFs is then given by $g_\star = g_\gamma + g_\nu\, \xi_\nu^4 + g_h\, \xi_h^4$. Similarly, we express the total entropy density of the Universe in terms of the photon temperature, $s(T_\gamma) = \frac{2\pi^2}{45} g_{\star S}(T_\gamma)\, T_\gamma^3$ with $g_{\star S} = g_\gamma + g_\nu\, \xi_\nu^3 + g_h\, \xi_h^3$ at low temperatures.

A phenomenologically important consequence of a decoupled hidden sector is that it cannot interact efficiently with the SM plasma. Whereas this could in principle mean that the vacuum bubbles run away, and that the corresponding SGWB is generated from the vacuum-bubble collisions only, we will assume in the following that the models considered here feature a hidden plasma which exerts friction on the vacuum bubbles and in which sound waves can be induced in the same way as in the SM plasma. We therefore work on the premise that the formulae for the plasma contributions to the GW spectrum (at the time of production) presented in section 6.4.3 still apply. With respect to hidden sectors in equilibrium with the SM but otherwise identical internal properties, the spectrum is then only altered through the change of the parameters entering the calculation of the spectrum and modifications of the red-shifting, derived in the following.

8.2.1. Temperature Ratio Dependence

To facilitate comparison with the case of a hidden sector in thermal contact with the photon bath ($\xi_h = 1$), we here express all PT parameters in terms of the hidden sector temperature T_h and the temperature ratio ξ_h. All parameters internal to the dark sector (i.e. masses, couplings, etc.) are kept fixed.

The effective potential $V_{\rm eff}(\phi, T_h)$, the critical bounce action $S_{E,3}(T_h)/T_h$, and the thermal tunneling rate per unit volume $\Gamma(T_h) \sim T_h^4 \exp\left(-S_{E,3}/T_h\right)$ only depend on the hidden sector properties. They therefore do not require any changes in their definition (apart from making clear that they should be considered as functions of the hidden sector temperature T_h). The first modification required for decoupled hidden sectors is therefore in the nucleation condition eq. (6.9). Recall that the nucleation temperature is defined as the temperature at which $\Gamma(T_{n,h}) \sim H^4(T_{n,\gamma})$, i.e. by comparing the nucleation rate to the Hubble rate. Here, $T_{n,h}$ and $T_{n,\gamma}$ are the temperatures of the hidden and visible sector, respectively, at the time of nucleation. As $H \sim T_\gamma^2$ we therefore pick up a factor ξ_h^8 when expressing everything in terms of the hidden sector temperature, so that eq. (6.9) is modified to

$$\frac{S_{E,3}(T_{n,h})}{T_{n,h}} \sim 146 - 4\log\left(\frac{T_{n,h}}{100\,\text{GeV}}\right) - 2\log\left(\frac{g_{\star,n}}{100}\right) - 8\log\xi_h\,, \tag{8.20}$$

where $g_{\star,n} = g_\star(T_{n,\gamma}) = g_\star(\xi_h^{-1}\, T_{n,h})$ is the effective number of radiative DOFs at nucleation. Due to the weak logarithmic dependence on ξ_h, the corresponding change in the nucleation temperature is typically negligible.

The most prominent effect on the SGWB stems from the energy budget given by eq. (6.10). Recall that the latent heat $\mathcal{E}$ is defined in terms of the effective potential, and therefore natively depends on the hidden sector temperature. The radiation energy density on the other hand is given by eq. (8.19). Thus, compared to the case of a hidden sector in equilibrium with the SM, the energy budget is suppressed by the fourth power of the temperature ratio if we keep $\mathcal{E}$ and $T_{n,h}$ fixed, i.e.

$$\alpha \equiv \frac{\mathcal{E}(T_{n,h})}{\rho_{\mathrm{rad}}(T_{n,\gamma})} \approx \frac{\mathcal{E}(T_{n,h})}{\rho_{\mathrm{rad}}(T_{n,h})\,\xi_h^{-4}} = \xi_h^4\,\alpha_h\,, \tag{8.21}$$

where $\alpha_h \equiv [\alpha]_{\xi_h=1}$ is the energy budget if both sectors have the same temperature, and we neglected potential changes in $g_\star$.

The inverse time scale of the PT normalized to the Hubble rate, β/H_*, on the other hand, is independent of the temperature ratio. This can be easily seen from eq. (6.11). Once normalized to the Hubble rate, the time derivative in the definition of $\beta = \dot{\Gamma}/\Gamma$ can be traded for a derivative with respect to the scale factor a. As co-moving entropy is conserved in the hidden and visible sector separately, the scale-factor derivative can be expressed as a derivative with respect to either temperature, so that we can take

$$\frac{\beta}{H_*} = \left[T_h \frac{\mathrm{d}}{\mathrm{d}T_h}\frac{S_{E,3}}{T_h}\right]_{T_h=T_{n,h}}\,. \tag{8.22}$$

Beside the input parameters which characterize the PT discussed above, the temperature ratio also modifies the amount of red-shifting the GW spectrum experiences. While the temperature factors in the red-shifting of the amplitude in eq. (6.17b) cancel, the frequency red-shift times the Hubble rate at the time of the transition is proportional to the nucleation temperature in the photon bath, and therefore picks up a factor of $1/\xi_h$ compared to the $\xi_h = 1$ case. Adapting the normalization to the temperature range considered here, and keeping the differentiation between $g_\star$ and $g_{\star S}$ as these differ due to decoupling, eq. (6.17) becomes

$$h_* = 68.8\,\mathrm{pHz}\left(\frac{T_{n,h}}{1\,\mathrm{MeV}}\right)\left(\frac{g_{\star S}^0}{g_{\star S}^*}\right)^{\frac{1}{3}}\left(\frac{g_\star^*}{2}\right)^{\frac{1}{2}}\xi_h^{-1}\,, \tag{8.23a}$$

$$\mathcal{R} = 2.473\times 10^{-5}\left(\frac{g_{\star S}^0}{g_{\star S}^*}\right)^{\frac{4}{3}}\left(\frac{g_\star^*}{2}\right)\,. \tag{8.23b}$$

Note that in the effective number of entropic DOFs today (or, to be more precise, at matter-radiation equality), $g_{\star S}^0 = 2 + \frac{7}{4}N_\nu(\xi_\nu^0)^3 + g_h(\xi_h^0)^3$, the values of the temperature ratios ξ_ν^0 and ξ_h^0 may differ from the values at the time of the PT if a species becomes non-relativistic and transfers its entropy to the remaining particles. Further note that, if the hidden sector decouples from the photon bath before the PT and remains decoupled until today, it is sufficient to consider the SM entropic DOFs only, as co-moving entropy is then conserved separately in each sector.

Finally, in the definition of the run-away criterion we need to take into account that the explicit temperature dependence displayed in eq. (6.12) is on $T_{n,h}$, whereas ρ_{rad} implicitly depends on $T_{n,\gamma}$. Therefore, the ratio α/α_∞ is independent of the temperature ratio.

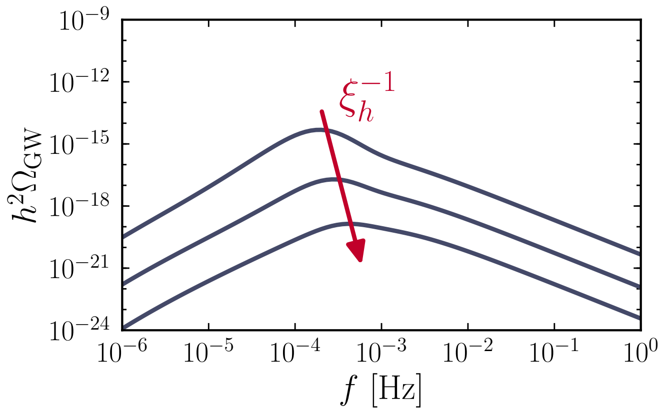

Figure 8.3: Illustration of the dependence of the SGWB from a hidden sector PT on the temperature ratio $\xi_h = T_h/T_\gamma$, keeping $T_{n,h}$, β/H_* and α_h fixed.

The impact of increasing the photon temperature with respect to the hidden sector temperature is illustrated in fig. 8.3. When the nucleation temperature $T_{n,h}$ in the hidden sector, the latent heat release (i.e. the energy budget in the case that $\xi_h = 1$, α_h), and the inverse time scale normalized to the Hubble rate, β/H_*, are kept constant, and the temperature ratio ξ_h is decreased, the GW spectrum is affected in two ways. First, the amplitude recedes due to the ξ_h^4 suppression of the energy budget α in eq. (8.21). Second, the spectrum is shifted to slightly higher frequencies by the ξ_h^{-1} dependence of the peak frequency from red-shifting through eq. (8.23a).

8.2.2. Sensitivity

As discussed in section 8.1, constraints on the effective number of neutrino species require sub-MeV hidden sectors to be colder than the photon bath. We will therefore now discuss how the detectability of first-order PTs in hidden sectors via GWs is affected if the hidden sector is decoupled from the SM with a temperature ratio $\xi_h < 1$.

Figure 8.4 depicts the sensitivity of various GW observatories to the SGWB produced in a PT occurring at a nucleation temperature $T_{n,h}$ in a decoupled hidden sector with temperature ratio ξ_h. The colored regions can be probed by the respective experiments. We present the projected regions of sensitivity for *SKA*, *LISA*, *(B-)DECIGO*, *BBO*, and *ET*. For *SKA* we assume observation periods of 5, 10 and 20 years. The hidden sector temperature around which BBN occurs, i.e. corresponding to a photon temperature of $T_\gamma^{\rm BBN} = 1\,\text{MeV}$, and below which $N_{\rm eff}$ constraints apply, is indicated by the black line.[4] Throughout this chapter we assume that the SGWB from super-massive black hole binaries (SMBHBs) will be resolved and subtracted from our signal, otherwise the sensitivity of *SKA* is diminished significantly.

The left panel of fig. 8.4 shows the case of a runaway transition, whereas the right plot considers a non-runaway GW spectrum dominated by the sound wave and turbulence contributions in a hidden plasma. We fix the latent heat and the transition rate divided by the Hubble rate such that $\alpha_h = 0.1$ and $\beta/H_* = 10$, where α_h is the corresponding value of α assuming equal temperatures in the hidden and visible sector, and assume

[4]Note that the jagged features in the sensitivity curves, such as the particularly distinct spike close to the BBN line, are due to approximating the SM number of relativistic DOFs by a step function.

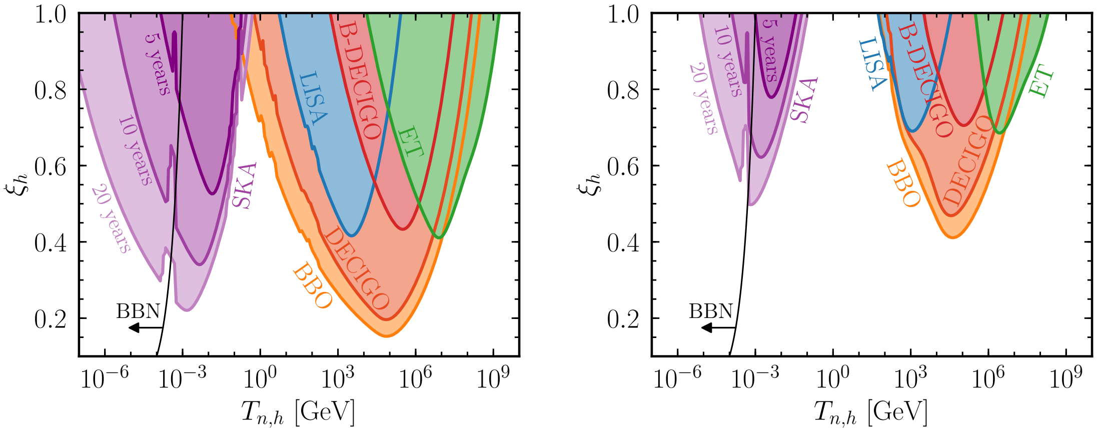

(a) runaway bubbles with $\alpha \gg \alpha_\infty$

(b) non-runaway bubbles ($\alpha < \alpha_\infty$)

Figure 8.4: Projected sensitivity reach (colored regions) of PTAs (*SKA*), space-based (*LISA*, *(B-)DECIGO*, *BBO*), and ground-based (*ET*) GW observatories as a function of the nucleation temperature $T_{n,h}$ in the hidden sector and the temperature ratio ξ_h. The *SKA* limits are shown for 5, 10, and 20 years of observation. The black lines indicate the hidden sector temperature below which BBN occurred and N_{eff} constraints apply. The left (right) panel assumes a (non-)runaway transition. We fix $\alpha_h = 0.1$ and $\beta/H_* = 10$ (see text for details).

$g_h \ll g_\star^{\text{SM}}$. Note that fixing these parameters corresponds to fixing the properties of the hidden sector, whereas $\alpha \sim \xi^4 \alpha_h$ also depends on the visible sector temperature. We further optimistically take the fraction of bulk motion converted into turbulence to be $\varepsilon_{\text{turb}} = 10\,\%$, and assume a bubble wall velocity of $v_w = 1$ in both cases. The latter two assumptions will be retained throughout this chapter.

If the hidden sector has the same temperature as the photon bath, an ample range of nucleation temperatures can be probed. In particular, in the runaway case the entire range $100\,\text{eV} \lesssim T_{n,h} \lesssim 10^6\,\text{TeV}$ is accessible for the parameter values considered in fig. 8.4. However, once the hidden sector temperature is reduced with respect to the photon bath, the sensitivity recedes, mostly due to the ξ_h^4 suppression of the energy budget. For very low temperature ratios $\xi_h \lesssim 0.15$, the SGWB produced in the PT becomes undetectable even in the most optimistic scenario.

As we are interested in the interplay between GW and N_{eff} constraints, let us now focus on PTs occurring after the onset of BBN, with a nucleation temperature in the photon bath below $T_{n,\gamma} \lesssim 1\,\text{MeV}$. Since this is the region in which PTAs are sensitive, we only consider projections for *SKA* in the following.

We have shown that decreasing the temperature ratio ξ_h reduces the prospects for observing the SGWB from hidden sector PTs. Let us therefore adopt the maximal value

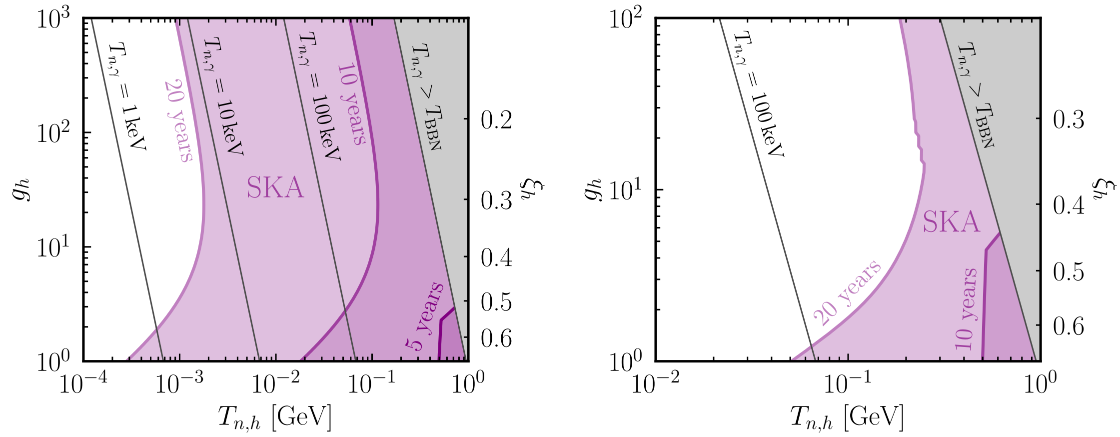

(a) runaway bubbles with $\alpha \gg \alpha_\infty$

(b) non-runaway bubbles ($\alpha < \alpha_\infty$)

Figure 8.5: Range of nucleation temperatures $T_{n,h}$ and numbers of relativistic DOFs g_h in completely decoupled hidden sectors featuring PTs observable through GWs with *SKA* (purple regions) after an observation period of 5, 10, and 20 years, respectively, assuming $\alpha_h = 0.1$ and $\beta/H_* = 10$. The temperature ratio ξ_h is set to the maximal value complying with the BBN constraint on N_{eff} in eq. (8.9), see eq. (8.24). The constraint does not pertain to the gray colored region where the PT occurs before BBN.

of ξ_h consistent with the BBN constraints on N_{eff}, eq. (8.9). Assuming a completely decoupled hidden sector, we can solve eq. (8.14) for ξ_h, yielding

$$\xi_h = \left(\frac{4}{11}\right)^{\frac{1}{3}} \left(\frac{7}{4}\frac{\Delta N_{\mathrm{eff}}}{g_h}\right)^{\frac{1}{4}} , \tag{8.24}$$

where the 95 % CL upper limit from BBN is $\Delta N_{\mathrm{eff}} < 0.46$.

The values of the nucleation temperature $T_{n,h}$ and number of relativistic DOFs g_h in the hidden sector that give rise to a GW signal observable in *SKA*, saturating the N_{eff} limit eq. (8.9) from BBN[5] are shown in fig. 8.5. We again assume $\alpha_h = 0.1$ and $\beta/H_* = 10$. The left (right) plot considers a transition with (non-)runaway bubble walls. The regions shaded in purple can be probed by *SKA* after 5, 10, and 20 years of observation, respectively. In the gray colored region, the PT occurs before the onset of BBN and is therefore unconstrained by N_{eff}.

For transitions in the runaway regime, hidden sectors with only few relativistic DOFs and nucleation temperatures $T_{n,h} \sim 1\,\mathrm{MeV}$ may be probed by *SKA* after only 5 years of observation, whereas in the non-runaway case, even hidden sectors with a single relativistic DOF require observation periods of at least 10 years. The observational prospects are most promising for early transitions close to the beginning of BBN. PTs at lower temperatures require longer observation periods.

Whereas it appears odd at first sight that, according to fig. 8.5, for PTs close to BBN, *SKA* is able to probe models with arbitrarily many additional DOFs, this is just an

[5] I.e. sitting on top of the orange line in fig. 8.1a.

artifact of saturating the N_{eff} bound. Equation (8.24) keeps $g_h\,\xi_h^4$ (and thereby N_{eff} and the total energy density of the Universe) fixed. Furthermore, keeping α_h (the energy budget for $\xi_h = 1$) constant does no longer correspond to fixing the latent heat $\mathcal{E}$ because we vary g_h. As $\rho_{\mathrm{rad}} \propto (g_\star^{\mathrm{SM}} + g_h)T_{n,h}^4$ for $\xi_h = 1$, the actual value of α is not suppressed by ξ_h^4, but approaches a constant for large g_h, i.e.

$$\alpha = \frac{\mathcal{E}}{\frac{\pi^2}{30}\,(g_\star^{\mathrm{SM}} + g_h\,\xi_h^4)\,T_{n,\gamma}^4} = \frac{(g_\star^{\mathrm{SM}} + g_h)\,\xi_h^4\,\alpha_h}{g_\star^{\mathrm{SM}} + g_h\,\xi_h^4} \xrightarrow{g_h \gg g_\star^{\mathrm{SM}}} \frac{g_h\,\xi_h^4}{g_\star^{\mathrm{SM}} + g_h\,\xi_h^4}\,\alpha_h\,. \tag{8.25}$$

With eq. (8.9) we obtain $g_h\,\xi_h^4 = 0.21$ and $\alpha = 0.059$ (for $\alpha_h = 0.1$). Since we further fix β/H_*, the spectrum depends on ξ_h only via the red-shifting in eq. (8.23). Again, saturating the N_{eff} bound keeps $g_\star$ constant, so that the only dependence on g_h is in the frequency red-shift.[6] As a result, for $g_h \gg g_\star^{\mathrm{SM}}$ the GW spectrum does not change along lines of constant $T_{n,\gamma}$, where $T_{n,\gamma} = T_{n,h}/\xi_h \sim T_{n,h}\,g_h^{1/4}$.

8.3. Toy Models

To assess the question whether it is possible to construct cosmologically viable (i.e. satisfying the constraints on the effective number of neutrino species) sub-MeV hidden sector models that feature a first-order PT observable through the corresponding SGWB, let us explore the situation on the example of concrete benchmark models. We will consider two simple toy models in the following. The first hidden sector consists of two singlet scalars with two hidden DOFs and a potential barrier at tree-level, whereas the second model is a Higgsed dark photon model with four DOFs and a loop-induced barrier. To let the hidden sectors thermally decouple from the photon bath as required by the N_{eff} constraints, we neglect all portals to the visible sector. A discussion of the potential size of the portal couplings can be found in ref. [388]. As N_{eff} severely limits the number of relativistic DOFs at the MeV scale, we expect that the models considered here provide a low-temperature effective description of most viable, perturbative, ultraviolet (UV) complete models with non-trivial sub-MeV dynamics.

8.3.1. Singlet Scalars

Our first toy model consists of two scalar particles that are singlets under the SM. In this case, a barrier between two phases can be generated a tree-level from a cubic coupling in the potential. As we will see in the following, the second scalar is required to let the Universe first evolve into the false vacuum, so that it can subsequently tunnel into the true one, producing a first-order PT. The model therefore introduces two hidden sector DOFs.

The simplest possible hidden sector model would consist of only a single real scalar particle S with tree-level potential

$$V_{\mathrm{tree}}(S) = \frac{\mu_S^2}{2}\,S^2 + \frac{\kappa_S}{3}\,S^3 + \frac{\lambda_S}{4}\,S^4 = -\frac{\kappa_S v_S + \lambda_S v_S^2}{2}\,S^2 + \frac{\kappa_S}{3}\,S^3 + \frac{\lambda_S}{4}\,S^4\,, \tag{8.26}$$

[6] Recall that for decoupled sectors co-moving entropy is conserved in each sector. Therefore, in the $g_{\star S}$ factors we only need to consider the SM entropic DOFs.

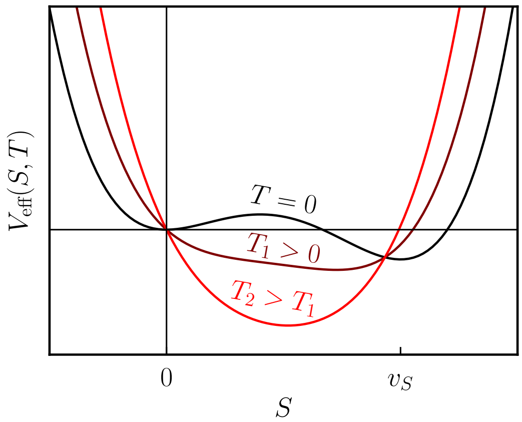

(a) single real scalar field

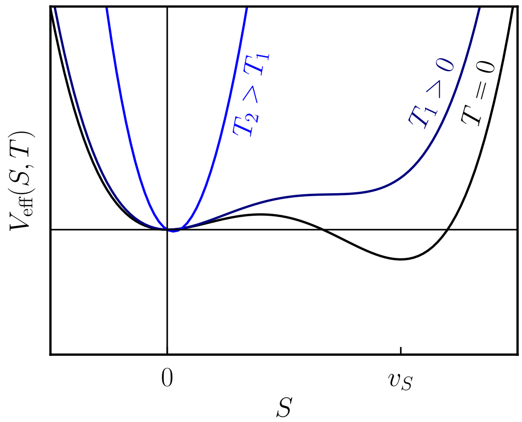

(b) two real scalars

Figure 8.6: Sketch of the effective potential and its evolution with temperature for a single real scalar field (left, eq. (8.26)) and two real scalars (right, eq. (8.27)) as a function of the field S.

where we imposed that the potential has a minimum at $S = v_S > 0$ and used the minimum condition $V'_{\text{tree}}(v_S) = 0$ to eliminate μ_S^2. We need to require $\lambda_S > 0$ for the potential to be bounded from below. The field dependent mass is $m_S^2(S) = \kappa_S\,(2S - v_S) + \lambda_S\,(3S^2 - v_S^2)$, so that $\kappa_S > -2\lambda_S v_S$ in order for $S = v_S$ to be a minimum. The potential further also has extrema at $S = 0$ and $S = -(\kappa_S + \lambda_S v_S)/\lambda_S$. At high temperatures, the potential is approximately given by $V_{\text{eff}} \simeq V_{\text{T}} \sim T_h^2\, m_S^2$, cf. eq. (6.23). It therefore only has a single minimum at $S = -\frac{\kappa_S}{3\lambda_S}$.

We can now distinguish two cases. In the first case, $S = 0$ also corresponds to a minimum. This requires $\kappa_S < -\lambda_S v_S$. The global minimum is at $S = v_S$ for $\kappa_S > -\frac{3}{2}\lambda_S v_S$, and at $S = 0$ otherwise. In the other case, the origin is a maximum, i.e. $\kappa_S > -\lambda_S v_S$. Then, the global minimum is at $S = v_S$ for $\kappa_S < 0$ and at $S < 0$ otherwise. Now, comparing the position of the high-temperature minimum to the position of the maximum, we see that in both cases the high-temperature minimum is always at the same side of the barrier as the global minimum of the tree-level potential. Therefore, as the Universe cools down, the high-temperature minimum will always evolve into the true vacuum and no first-order PT occurs.

This behavior is illustrated in fig. 8.6a. At high temperatures (red line), the effective potential $V_{\text{eff}}(S,T)$ only has a single minimum. Due to the cubic term in eq. (8.26), this minimum is displaced from the origin. As the temperature drops (dark red line), the minimum shifts towards $S = v_S$ and the potential develops a barrier between the minimum and the origin. Finally, the temperature dependent vacuum evolves into the global minimum of the zero-temperature potential (black line) at $S = v_S$. The Universe always resides in the true vacuum and no PT occurs.

To obtain a first-order PT we therefore need to add additional fields. Their field-dependent masses can then be arranged such that the high-temperature minimum evolves into the false vacuum, so that the field subsequently has tunnel to reach the true vacuum.

Thus, let us consider a hidden sector with two real scalar fields, S and A, both singlets under the SM. For simplicity we impose a $\mathbb{Z}_2$ symmetry under which S is even and A is odd. The corresponding potential reads

$$V_{\text{tree}}(S, A) = \frac{\mu_S^2}{2} S^2 + \frac{\kappa_S}{3} S^3 + \frac{\lambda_S}{4} S^4 + \frac{\mu_A^2}{2} A^2 + \frac{\lambda_A}{4} A^4 + \kappa_{SA} S A^2 + \frac{\lambda_{SA}}{2} S^2 A^2 \,. \quad (8.27)$$

To simplify the analysis of the potential, we now only let S acquire a vacuum expectation value (VEV), $\langle S\rangle = v_S$, while $\langle A\rangle = 0$ so that the $\mathbb{Z}_2$ symmetry remains unbroken. Hence, we impose μ_A^2, $\kappa_{SA} \geq 0$, as well as λ_S, $\lambda_A > 0$ to ensure stability of the potential. We fix $A = 0$ at all temperatures for the remainder of this chapter and treat the potential as function of S alone. We checked that this is indeed valid for the parameter values considered here.

The field dependent masses are given by

$$m_S^2(S) = \mu_S^2 + 2\kappa_S S + 3\lambda_S S^2 \qquad \text{and} \qquad m_A^2(S) = \mu_A^2 + 2\kappa_{SA} S + \lambda_{SA} S^2 \,, \quad (8.28)$$

and from the minimum condition $\frac{\partial V_{\text{tree}}}{\partial S}(v_S) = 0$ we can eliminate $\mu_S = -(\kappa_S + \lambda_S\, v_S)\, v_S$. At high temperatures, the potential now behaves as $V_{\text{eff}} \simeq V_{\text{T}} \sim T_h^2(m_S^2 + m_A^2)$. The high-temperature minimum is at $S = -(\kappa_S + \kappa_{SA})/(3\lambda_S + \lambda_{SA})$, so we can adjust κ_{SA} and λ_{SA} to shift it towards the origin and obtain a first-order PT, as depicted in fig. 8.6b. At high temperatures, the minimum of the potential (blue line) is close to the origin. When the temperature decreases (dark blue line), a second minimum develops. At zero temperature (black line), this new minimum has become the global one, whereas the original high-temperature minimum still persists. We therefore now obtain a first-order PT.

For a quantitative investigation of the PT in this model we use the numerical code CosmoTransitions [364], implementing the daisy-resummed one-loop thermal effective potential eq. (6.20). The counter-term potential is given by

$$\Delta V_{\text{ct}}(S) = \frac{\delta\mu_S^2}{2} S^2 + \frac{\delta\kappa_S}{3} S^3 + \frac{\delta\lambda_S}{4} S^4 \,, \quad (8.29)$$

on which we impose the renormalization conditions

$$\left.\frac{\partial\,(V_{\text{CW}} + \Delta V_{\text{ct}})}{\partial\, S}\right|_{S=v_S} = 0 \qquad \text{and} \qquad \left.\frac{\partial^2\,(V_{\text{CW}} + \Delta V_{\text{ct}})}{\partial\, S^2}\right|_{S=v_S} = 0 \,, \quad (8.30)$$

to ensure that the scalar VEV v_S and mass m_S remain at their tree-level values. We additionally require

$$V_{\text{CW}}(v_S) - V_{\text{CW}}(0) + \Delta V_{\text{ct}}(v_S) - \Delta V_{\text{ct}}(0) = 0 \quad (8.31)$$

to fix the vacuum structure. However, as the one-loop quantum corrections shift the local minimum at $S = 0$ slightly away from the origin, the latter condition may not be sufficient if the minima are almost degenerate. Finally, the thermal masses of S and A entering the daisy corrections V_{ring} are

$$\Pi_S(T_h) = \left[\frac{\lambda_S}{4} + \frac{\lambda_{SA}}{12}\right] T_h^2 \qquad \text{and} \qquad \Pi_A(T_h) = \left[\frac{\lambda_A}{4} + \frac{\lambda_{SA}}{12}\right] T_h^2 \,. \quad (8.32)$$

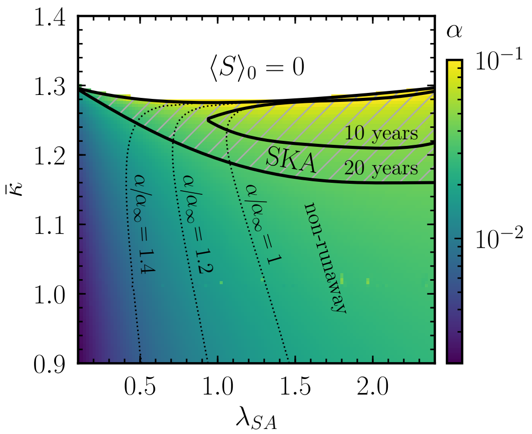

(a) energy budget α

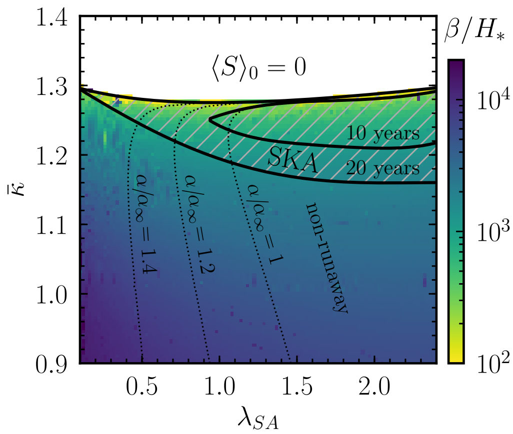

(b) inverse time scale β/H_*

Figure 8.7: Energy budget α (left) and inverse time scale β/H_* (right) for the singlet scalars model in the $\bar{\kappa}$ vs. λ_{SA} plane, where $\bar{\kappa} \equiv -\kappa_S/(\lambda_S v_S)$. We assume $v_S = 50\,\text{keV}$ and $\xi_h = 0.66$, complying with the N_eff constraints in the ν-quilibration scenario (cf. figs. 8.1b and 8.8). The remaining model parameters are set to $\lambda_S = \lambda_A = 0.1$ and $\mu_A = \kappa_{SA} = 0.1\,v_S$. The hatched regions enclosed by the solid black contours can be probed by *SKA* after 10 and 20 years of observation, respectively. The dotted lines are contours of constant α/α_∞, with a runaway transition occurring for $\alpha/\alpha_\infty > 1$.

The parameter space regions giving rise to a first-order PT as a function of the cubic coupling $\bar{\kappa}$ and the mixed quartic coupling λ_{SA} are shown in fig. 8.7, where we defined $\bar{\kappa} \equiv -\frac{\kappa_S}{\lambda_S v_S}$. Recall that, according to our tree-level analysis of the single-scalar model, the potential has a local minimum at the origin and a global one at $S = v_S$ for $1 < \bar{\kappa} < 3/2$. We assume a scalar VEV of $v_S = 50\,\text{keV}$, as well as $\lambda_S = \lambda_A = 0.1$ and $\mu_A = \kappa_{SA} = 0.1\,v_S$. To avoid tension with the constraints on the effective number of neutrino species, we further assume a temperature ratio of $\xi_h = 0.66$, which saturates the CMB+H_0 bound eq. (8.11) in the ν-quilibration scenario discussed in section 8.1.3.

A first-order PT occurs in the colored regions, where the color-coding in the two panels indicates the respective value of the energy budget α (left panel) and inverse time scale β/H_* (right panel). In the white space above the colored region, the Universe remains in the vacuum at $S = 0$, either because it is trapped in the false vacuum since the tunneling probability is too low, or because quantum corrections render the minimum at $S = 0$ the global minimum. The hatched region enclosed by the solid black lines is accessible by *SKA* with an observation period of 10 and 20 years, respectively.

As $\bar{\kappa}$ corresponds to the cubic self-coupling of S, it controls the height and width of the barrier separating the false- and true-vacuum phase. It therefore provides the primary handle to control the relative transition time scale β/H_*. The higher $\bar{\kappa}$ the wider the barrier, and thus, the slower the PT. Increasing $\bar{\kappa}$ leads to a decrease in β/H_*. For $\bar{\kappa} \gtrsim 1.3$, the Universe is trapped in the $S = 0$ vacuum. The mixed quartic λ_{SA} (as well as the mixed cubic κ_{SA}) on the other hand critically influences the high-temperature behavior of the potential, in particular the location of the high-temperature minimum. Higher values

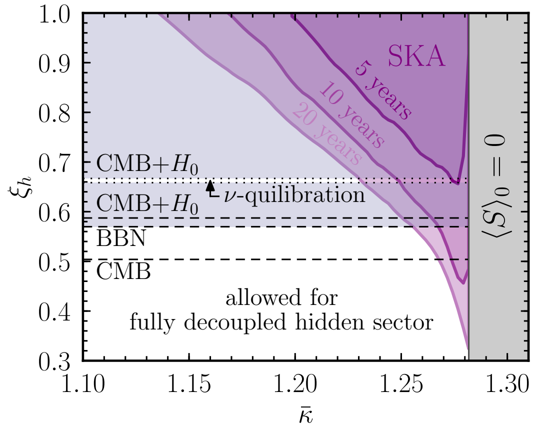

(a) $v_S = 300\,\text{keV}$

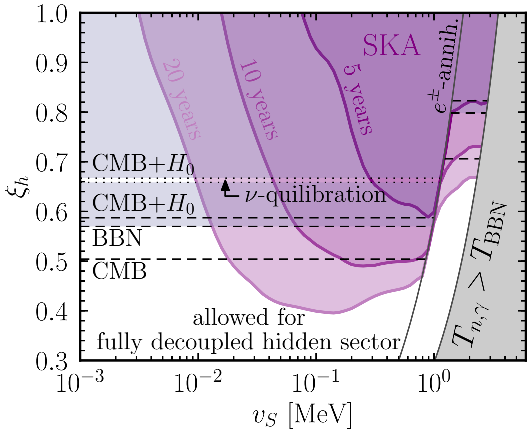

(b) $\bar{\kappa} = 1.275$

Figure 8.8: Impact of the temperature ratio ξ_h at the time of the PT on the sensitivity of *SKA* (purple shaded regions) to first-order PTs in the singlet scalars model as a function of $\bar{\kappa}$ (left, for $v_S = 300\,\text{keV}$) and the VEV of S (right, for $\bar{\kappa} = 1.275$). We set $\lambda_{SA} = 2$, $\lambda_S = \lambda_A = 0.1$, and $\mu_A = \kappa_{SA} = 0.1\,v_S$. The N_{eff} constraints exclude the regions above the respective dashed lines. The regions excluded by the BBN and CMB+H_0 limit are shaded in gray.

of λ_{SA} lower the temperature at which the thermal corrections dominate.[7] It therefore directly influences the critical and nucleation temperature. Increasing λ_{SA} decreases $T_{n,h}$, and thereby rises the energy budget α. Note that the latent heat release required to enter a runaway regime, cf. eq. (6.12), grows as $T_{n,h}^2$, so that runaway transitions occur for lower values of λ_{SA}. Contours of constant α/α_∞ are shown as dotted lines in fig. 8.7.

Figure 8.8 illustrates the impact of the temperature ratio ξ_h at the time of the PT on the detectability of the corresponding SGWB by *SKA* as a function of the cubic coupling $\bar{\kappa}$ (left panel) and the VEV v_S of S (right panel). We fix the mixed quartic coupling to $\lambda_{SA} = 2$, as well as $v_S = 300\,\text{keV}$ and $\bar{\kappa} = 1.275$ in the left and right plot, respectively. The remaining parameters of the model are set as in fig. 8.7. *SKA* is sensitive to the purple colored regions, where the different shades of purple correspond to 5, 10 and 20 years of observation time, respectively. Temperature ratios above the dashed lines are excluded by the respective N_{eff} constraints, cf. eqs. (8.9) to (8.11), if the hidden sector is completely decoupled. The regions excluded by the BBN and CMB+H_0 constraints are further shaded in gray. The white space between the dotted lines is in agreement with N_{eff} limits if the ν-quilibration scenario is assumed. In the gray colored area at the right-hand side of fig. 8.8a, the Universe remains in the vacuum located at the origin and no PT occurs. In fig. 8.8b on the other hand, the gray region in the right corresponds to PTs before BBN, alleviating the constraints on N_{eff}.

While *SKA* may probe a large fraction of the parameter space displayed in fig. 8.8 if the hidden sector has the same temperature as the photon bath, the sensitivity significantly

[7] In the high-temperature limit it contributes as $\sim \lambda_{SA}\, T_h^2\, S^2$ to the potential.

decreases when the temperature ratio is reduced. If we assume that the hidden sector is completely decoupled from the SM throughout the post-BBN evolution of the Universe, the N_{eff} limits, eqs. (8.9) to (8.11), constrain the temperature ratio to values below 0.57 (BBN), 0.59 (CMB+H_0), and 0.50 (CMB), respectively, cf. fig. 8.1a. If, on the other hand, the hidden sector (re-)equilibrates with the neutrino sector between the on-set of BBN and the PT, temperature ratios around $\xi_h \sim 0.66$ can be realized. Note that this value corresponds to the temperature ratio at the time of the transition, which relates to the value before BBN constrained in fig. 8.1b via eq. (8.15). If the PT further occurs between neutrino decoupling and $e^{\pm}$ annihilation, the values of ξ_h constrained by N_{eff} and at the time of the transition also differ in the completely decoupled scenario, with the former related to the latter by a factor ξ_ν^{SM}. The time of $e^{\pm}$ annihilation is indicated by a dark gray line in the right side of fig. 8.8b.

8.3.2. Dark Photon

As a second toy model, let us consider a complex scalar field charged under a dark $U(1)$ gauge group. In contrast to the singlet scalars model, the barrier between the phases here originates from the loop corrections to the potential, in particular from the transverse modes of the dark photon, as can be seen from eq. (6.23) and the fact that barriers from the scalar and the longitudinal modes are cancelled by the corresponding ring corrections in eq. (6.24). This model is very similar to the gauged lepton number model considered in chapter 7. The SGWB from the gauge-symmetry breaking PT in this model has also been studied in refs. [277, 389] for transitions at super-MeV scales, whereas we here focus on sub-MeV PTs. The model features four physical DOFs in the hidden sector.

The most general Lagrangian of the hidden sector including its interactions with the SM is given by

$$\mathcal{L} \supset |\,\mathrm{D}_\mu \mathcal{S}|^2 - \frac{1}{4} F'_{\mu\nu} F'^{\mu\nu} - \frac{\epsilon}{2} F'_{\mu\nu} B^{\mu\nu} - V(\mathcal{S}, H) \tag{8.33}$$

where $\mathcal{S}$ and H are the dark and SM Higgs fields, respectively. The covariant derivative of the complex scalar $\mathcal{S}$ is $\mathrm{D}_\mu \mathcal{S} = (\partial_\mu + i g_D A'_\mu)\,\mathcal{S}$, where A' denotes the dark photon with the corresponding gauge coupling g_D, and $F'_{\mu\nu} = \partial_\mu A'_\mu - \partial_\nu A'_\mu$ is the dark field strength tensor, whereas $B_{\mu\nu}$ is the SM hypercharge field strength. The tree-level potential reads

$$V(S, H) = -\mu_S^2\, |\mathcal{S}|^2 - \mu_H^2\, |H|^2 + \frac{\lambda_S}{2} |\mathcal{S}|^4 + \frac{\lambda_H}{2} |H|^4 + \lambda_{HS} |\mathcal{S}|^2 |H|^2 \,. \tag{8.34}$$

We decompose the dark Higgs into its real and imaginary part, $\mathcal{S} = (S + i\sigma)/\sqrt{2}$, and choose the phase of $\mathcal{S}$ such that it develops a VEV along its real part only, with $\langle S \rangle = v_S$. Since we want the hidden sector to decouple from the SM, the kinetic mixing parameter ϵ and the Higgs portal coupling λ_{HS} need to be negligibly small. We therefore assume $\lambda_{HS} = \epsilon = 0$ in the remainder of this chapter.

The field dependent masses of the dark Higgs boson S, the Goldstone boson σ and the dark photon A' are

$$m_S^2(S) = -\mu_S^2 + \frac{3}{2} \lambda_S\, S^2\,, \quad m_\sigma^2(S) = -\mu_S^2 + \frac{1}{2} \lambda_S\, S^2\,, \quad \text{and} \quad m_{A'}^2(S) = g_D^2 S^2\,, \tag{8.35}$$

where we can eliminate $\mu_S^2 = \frac{\lambda_S}{2} v_S^2$ from the minimum condition $\partial V/\partial S = 0$.

We again use CosmoTransitions [364] to investigate the PT in this model. We impose the renormalization conditions in eq. (8.30) to fix the paramters of the counter-term potential,

$$\Delta V_{\mathrm{ct}}(S) = -\frac{\delta\mu_S^2}{2} S^2 + \frac{\delta\lambda_S}{8} S^4 \,. \tag{8.36}$$

The Debye masses of the scalars and the longitudinal mode A'_L of the dark photon are

$$\Pi_S(T_h) = \Pi_\sigma(T_h) = \left[\frac{\lambda_S}{6} + \frac{g_D^2}{4}\right] T_h^2 \qquad \text{and} \qquad \Pi_{A'_L}(T_h) = \frac{g_D^2}{3} T_h^2 \,. \tag{8.37}$$

Since the bubble wall friction induced by gauge bosons acquiring a mass in a PT, such as the dark photon in the case under consideration, hinder the bubbles from entering the runaway regime [325], we only consider non-runaway bubbles in this model.

In fig. 8.9 the energy budget α (left panel) and inverse relative time scale β/H_* (right panel) are shown as a function of the quartic coupling λ_S and the gauge coupling g_D. The VEV of S is set to $v_S = 40\,\mathrm{keV}$. Since the CMB+H_0 constraints exclude this model if we assume the ν-quilibration scenario, cf. fig. 8.1b, we now consider the case of a completely decoupled hidden sector. The N_{eff} constraints then require a temperature ratio of $\xi_h = 0.48$ at the time of the PT. A first-order PT occurs in the colored regions, where the color indicates the respective value of α and β/H_*. In the white space above the colored region, the dark gauge symmetry remains unbroken, i.e. $\langle S\rangle = 0$ at $T = 0$, whereas in the white area in the lower right corner, the transition is a cross-over. The solid black lines indicate the prospective reach of *SKA* after an observation period of 10 and 20 years, respectively, where the accessible regions are hatched.

As already discussed in the context of the gauged lepton number model in section 7.1.2, the potential barrier is generated by the thermal corrections (cf. eq. (6.23)) from the transverse modes of the dark photon field A'. Therefore, increasing the gauge coupling g_D increases the barrier, such that the transition becomes slower and more energetic. For very large values of g_D, the Universe is stuck in the symmetric phase, whereas for low g_D the barrier is shallow and disappears before tunneling, leading to a smooth cross-over. Increasing the quartic λ_S on the other hand enhances the tree-level potential,[8] and thereby decreases the relative size of the barrier. As a result, a compensating increase of g_D is required to sustain the PT dynamics.

The effect of the temperature ratio ξ_h at the time of the transition is shown in fig. 8.10, varying the dark gauge coupling g_D (left, for $v_S = 300\,\mathrm{keV}$) and VEV v_S (right, for $g_D = 0.7$). The quartic couping is set to $\lambda_S = 0.01$ in both cases. The parameter regions accessible to *SKA* are colored in purple, indicating the required period of observation (5, 10 or 20 years) via the respective shading. The N_{eff} limits on ξ_h, assuming that the hidden sector is decoupled at the time of BBN and thereafter, are indicated by the horizontal dashed back lines. Values of ξ_h above these lines are excluded at 95 % CL by the respective constraint. In the case of the BBN and CMB+H_0 limit, the excluded regions are further shaded in gray.

[8] Since we fix the VEV we can rewrite the tree-level potential as $V_{\mathrm{tree}}(S) = \frac{\lambda_S}{8}(S^2 - 2\,v_S^2)\,S^2$.

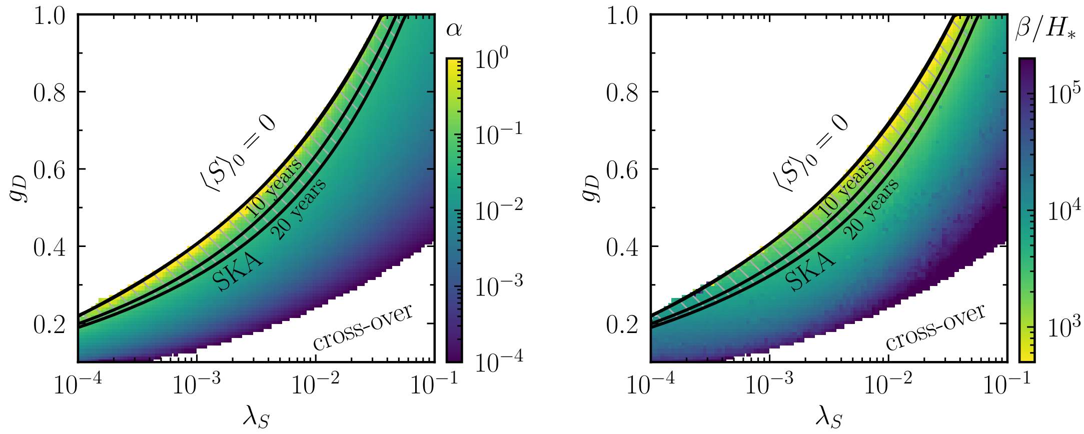

(a) energy budget α (b) inverse time scale β/H_*

Figure 8.9: Energy budget α (left) and inverse time scale β/H_* (right) for the dark photon model in the g_D vs. λ_S plane. We assume $v_S = 40\,\mathrm{keV}$ and $\xi_h = 0.48$, complying with the N_{eff} constraints for a completely decoupled hidden sector (cf. figs. 8.1a and 8.10). The hatched regions enclosed by the solid black contours can be probed by *SKA* after 10 and 20 years of observation, respectively.

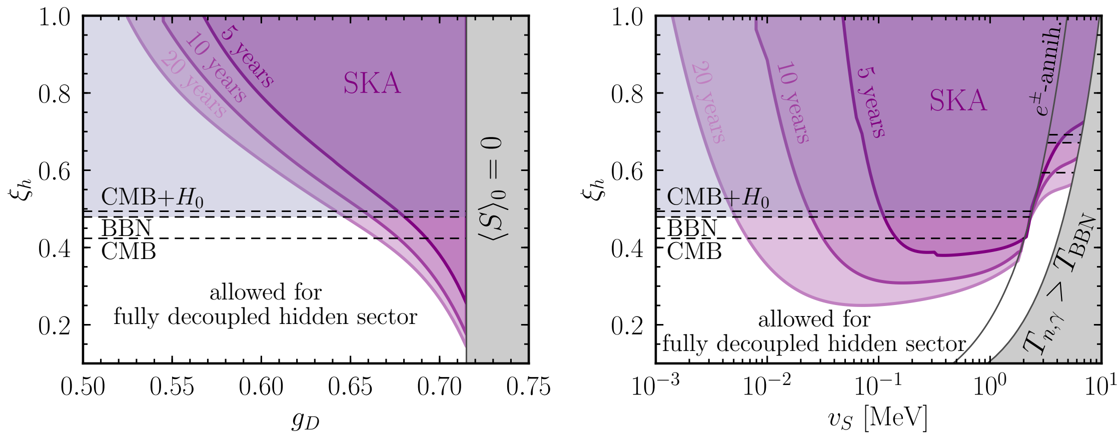

(a) $v_S = 300\,\mathrm{keV}$ (b) $g_D = 0.7$

Figure 8.10: Impact of the temperature ratio ξ_h at the time of the PT on the sensitivity of *SKA* (purple shaded regions) to first-order PTs in the dark photon model as a function of g_D (left, for $v_S = 300\,\mathrm{keV}$) and the VEV of S (right, for $g_D = 0.7$), setting $\lambda_S = 0.01$. The N_{eff} constraints exclude the regions above the respective dashed lines. The regions excluded by the BBN and CMB+H_0 limit are shaded in gray.

Similar to the situation in the singlet scalars model shown in fig. 8.8, fig. 8.10 indicates that *SKA* can access a large fraction of the parameter space displayed in the figure if both sector have the same temperature ($\xi_h = 1$), whereas the sensitivity is reduced as ξ_h decreases. In order to comply with the constraints on N_{eff}, eqs. (8.9) to (8.11), the hidden sector has to be colder than the photon bath by a factor of 0.48 (BBN), 0.49 (CMB+H_0), and 0.42 (CMB), respectively, cf. fig. 8.1a. For $v_S = 300\,\text{keV}$ (and $\lambda_S = 0.01$), detectability by *SKA* then requires $g_D \gtrsim 0.65$, even with 20 years of observation. For $g_D = 0.7$, the PT can be observed for $v_S \gtrsim 100\,\text{keV}$ after 5 years, and for $v_S \gtrsim 5\,\text{keV}$ after 20 years. In the gray area in the right of fig. 8.10b, the PT occurs before BBN, whereas for parameters between the gray region and the solid dark-gray line, the PT occurs between neutrino decoupling and $e^{\pm}$ annihilation, so that the value of ξ_h constrained by N_{eff} is reduced by $\xi_\nu^{\text{SM}} = (4/11)^{1/3}$ compared to the value at the time of the transition.

8.3.3. Parameter Scans

In the discussion of the numerical results for our toy models, we so far only focused on specific slices through the parameter space. To achieve a consideration of the full spectrum of parameters giving rise to first-order PT, let us now present results obtained from random scans over the parameter spaces of the two models.

We calculate the nucleation temperature $T_{n,h}$, the energy budget α_h for $\xi_h = 1$, and the inverse relative time scale β/H_*, scanning 4000 random points for each model. In the singlet scalars model described by eq. (8.27) we scan $0 < \lambda_{SA} < 3$ and $0.7 < \bar{\kappa} < 1.5$ linearly. The remaining parameters, μ_A/v_S, κ_{SA}/v_S, λ_S and λ_A, are scanned logarithmically in the range $10^{-3} - 1$. In the dark photon model, cf. eqs. (8.33) and (8.34), we scan $10^{-4} < \lambda_S < 0.1$ logarithmically and $0 < g_D < 1$ linearly, setting $\lambda_{HS} = \epsilon = 0$. The VEV is kept fixed in the scans. The results are then subsequently rescaled to obtain the desired value of the nucleation temperature.

The corresponding values of the energy budget α and in inverse time scale β/H_* for the scanned parameter points in the toy models are shown in fig. 8.11. Green and blue dots correspond to the singlets scalars and Higgsed dark photon model, respectively. The parameter regions accessible to different GW experiments are indicated by the shaded regions. In the top panel, a temperature ratio of $\xi_h = 1$ is assumed, and the nucleation temperature in the hidden sector is set to $T_{n,h} = 200\,\text{GeV}$ (left) and $T_{n,h} = 50\,\text{keV}$ (right), respectively, whereas the bottom panel takes $T_{n,h} = 50\,\text{keV}$ with temperature ratios $\xi_h = 0.66$ (left) and $\xi_h = 0.48$ (right).

For a nucleation temperature of $T_{n,h} = 200\,\text{GeV}$, cf. fig. 8.11a, the hidden sectors are not affected by the constraints on the effective number of neutrino species, and we can savely assume that they have the same temperature as the photon bath, provided that the hidden sector entropy can be transferred to the SM or dark radiation when becoming non-relativistic. For the chosen transition temperature, the SGWB may be probed by space-based experiments. While a first-order PT in the singlet scalars model remains undetectable for most parameter points, a large fraction of the parameter points in the dark photon model may be probed by *DECIGO* and *BBO*. *LISA* and *B-DECIGO* are mostly insensitive to the toy model PTs at the chosen temperature.

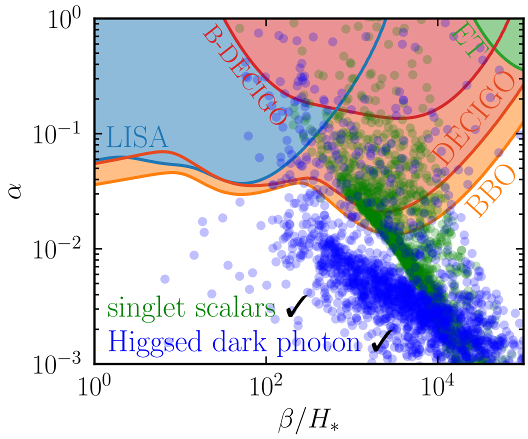

(a) $T_{n,h} = 200\,\mathrm{GeV},\ \xi_h = 1$

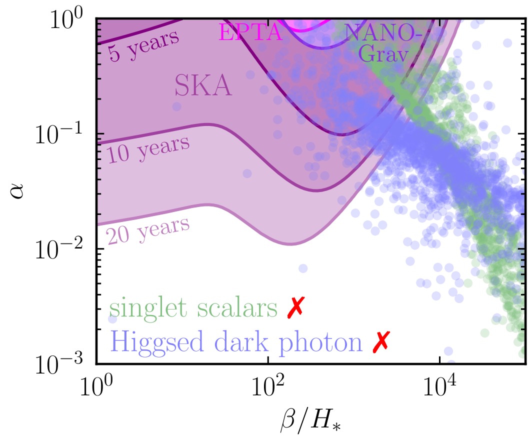

(b) $T_{n,h} = 50\,\mathrm{keV},\ \xi_h = 1$

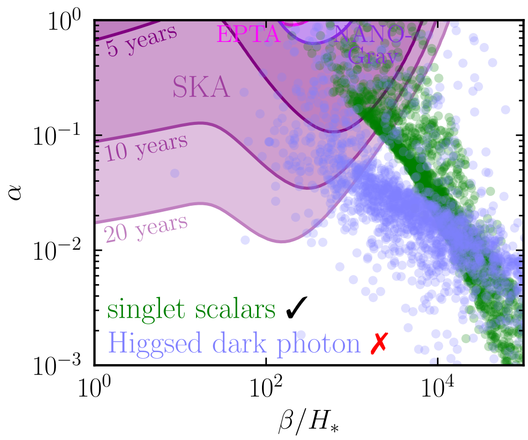

(c) $T_{n,h} = 50\,\mathrm{keV},\ \xi_h = 0.66$

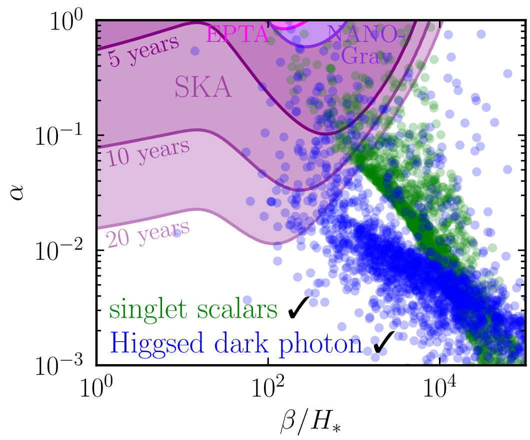

(d) $T_{n,h} = 50\,\mathrm{keV},\ \xi_h = 0.48$

Figure 8.11: Spectrum of GW parameters α and β/H_* covered by the singlet scalars (green dots) and Higgsed dark photon (blue dots) model for the nucleation temperatures $T_{n,h}$ in the hidden sector and temperature ratios ξ_h stated in the respective subcaptions. The SGWB in the shaded regions can be probed by the corresponding future GW observatory. A black tick mark (✓) indicates that the model complies with the N_{eff} constraints (assuming the ν-quilibration scenario in the singlet scalars model and a completely decoupled sector in the dark photon case), whereas a red cross (✗) and a lower opaqueness of the dots denote tension with these limits.

When considering a nucleation temperature of $T_{n,h} = 50\,\mathrm{keV}$ on the other hand, the generated SGWB falls into the region accessible by PTAs. For a temperature ratio of $\xi_h = 1$, cf. fig. 8.11b, both models feature PTs lying within the potential reach of *SKA* after only five years of observation. A small fraction of the parameter space is even excluded by the currently available *EPTA* and *NANOGrav* data. However, for such a low nucleation temperature, our toy models are excluded by N_{eff}.

For a temperature ratio of $\xi_h = 0.66$, as depicted in fig. 8.11c, the singlet scalars model with only two additional DOFs is viable in the ν-quilibration scenario. Comparing figs. 8.11b and 8.11c, we can see how the parameter points are shifted to lower α due to the ξ_h^4 suppression in eq. (8.21). As a result, the parameter space giving rise to an observable PT is reduced, and the detection of the corresponding GW signal in the singlet scalars model now typically requires at least ten years of observation with *SKA*.

In order for the dark photon model, which features four hidden DOFs, to be cosmologically viable, we need to further reduce the temperature ratio to $\xi_h = 0.48$, see fig. 8.11d. The model then complies with the constraints on N_{eff} if the hidden sector is completely decoupled. However, the parameter points are further shifted to lower α, and only very a small portion remains detectable in the dark photon model, whereas the singlet scalars model is now almost undetectable. Still, there are a few parameter points that remain detectable by *SKA* even after only five years of observation.

In conclusion, our toy models indicate that it is possible to have a first-order PT observable via GWs in a sub-MeV scale hidden sector, while at the same time satisfying the BBN and CMB($+H_0$) constraints on the effective number of neutrino species.

8.4. Conclusion

In this chapter we have studied the detectability of SGWBs generated from cosmological first-order PTs occurring in decoupled hidden sectors. Particular focus was put on sub-MeV scale sectors. These are subject to strong constraints from the effective number of neutrino species. We have discussed the corresponding bounds on the number of relativistic DOFs and temperature of the hidden sector. These require the hidden sector to be colder than the photon bath by an $\mathcal{O}(1)$ factor.

We have then investigated the effect of the temperature ratio between the two sectors on the PT in such a hidden sector, finding that a lower hidden sector temperature with respect to the SM mitigates the SGWB generated in the transition, primarily by suppressing the energy budget. The detection prospects at current and future GW observatories are therefore diminished, rendering the transition unobservable if the dark sector if too cold. Nonetheless, it is possible to construct sub-MeV hidden sector models that satisfy the N_{eff} constraints but feature a first-order PT observable in GWs using PTAs.

To corroborate these statements, we have considered two concrete toy realizations of decoupled sub-MeV hidden sectors, to wit, a model with two singlet scalars, and a gauged dark photon model. We find that, even after reducing the hidden sector temperature to a level compatible with N_{eff}, a detectable SGWB can still be obtained in parts of the parameter space in both of these models.

Epilogue

9. Conclusion and Summary

In this thesis, we have studied the phenomenology of various models of physics beyond the Standard Model (BSM). We have predominantly explored two paths to constrain new physics. Part I of this work considered searches at particle (in particular proton) colliders. In part II on the other hand, BSM physics was probed via the generation of gravitational waves (GWs) in cosmological first-order phase transitions (PTs). These two paths provide complementary ways to probe new physics, potentially with an interesting interplay.

We started our discussion of collider studies of new physics in chapter 3 with an investigation of the scalar singlet Higgs-portal dark matter (DM) model at the *LHC*. In contrast to previous works, we here did not only consider the low-mass region in which the Higgs boson can decay invisibly into DM, and the high-mass region where the DM is produced via an off-shell Higgs boson, but also the transition between these two regimes, i.e. $m_S \simeq m_h/2$. We found that, if the kinematic threshold for the decay of an off-shell Higgs boson to a DM pair is very close to the on-shell Higgs mass, the fixed-width approximation in the Breit-Wigner propagator fails. This leads to an unphysical enhancement of the DM production cross-section, potentially exceeding the on-shell Higgs production rate. Therefore, the momentum-dependence of the width in the propagator needs to be retained to obtain consistent results. We then derived the current 95 % confidence level limits on the Higgs-portal coupling as a function of the DM mass, reinterpreting the *CMS* search for invisible decays of the Higgs boson produced in vector-boson fusion [120]. Furthermore, based on the corresponding *HL-LHC* forecast by *CMS* [121], projections for the sensitivity of the high-luminosity and high-energy *LHC* upgrades were presented. Our projections include an estimate of the systematic uncertainties on the background, assuming that the latter is determined by measurements in control regions. Finally, we also presented our bounds as limits on the signal strength of additional Higgs bosons that decay invisibly, which allows for a simple reinterpretation in other dominantly Higgs-mediated DM models, as we illustrated for various effective Higgs-portal models with DM candidates of different spin in the appendix.

In chapter 4, this dissertation then proceeded with an investigation of the prospects to observe the Higgs decay into a Z boson and a photon in top-pair associated production. Due to the low branching ratio of the decay, in particular when leptonic Z decays are considered to allow for an accurate reconstruction of the decay products at hadron colliders, an observation in the dominant Higgs production channels is difficult, even at high luminosities. In top-pair associated production, we however expect that top-tagging techniques can significantly suppress the reducible backgrounds, such that the large Yukawa coupling of the top quark promises a sizable signal-to-background ratio in this channel. Still, an inclusive analysis and high luminosity are required to sustain an observable number of signal events. We have therefore set up a toy analysis searching for the $pp \to \bar{t}th,\ h \to Z\gamma$ process, focusing on the semi-leptonic decay channel of the top-quark pair. Based on Monte Carlo simulations, and an extrapolation to also include the fully-hadronic and fully-leptonic top channels, we found that the process under consideration can contribute significantly to establishing an observation of the $h \to Z\gamma$ decay at the *HL-LHC*, and may allow for precise measurements at the *HE-LHC* and a future 100 TeV FCC_{hh}. We further assessed the indirect constraints that can be put on the contribution of new physics to the $h \to Z\gamma$ decay rate, constraining the corresponding coupling modifier at the level of 15 %, 4 % and 2 % at the *HL-LHC*, *HE-LHC*, and FCC_{hh}, respectively.

Chapter 5 then concluded the part on colliders by presenting a comprehensive study of an extension of the Standard Model (SM) in which lepton number is gauged, exploring the DM and collider phenomenology of the model. The cancellation of lepton number gauge anomalies requires the existence of additional leptons. The lightest of these exotic leptons is stable and establishes a candidate for particle DM. We identified the regions of parameter space in which the model can account for the full DM relic abundance measured by *Planck*, finding that a large range of DM masses from $\mathcal{O}$ (100 GeV) to $\mathcal{O}$ (few TeV) is possible. We also evaluated direct and indirect detection limits, constraining the kinetic and DM mixing parameters. Furthermore, we assessed the bounds from the *LHC* and *LEP* on the Z' lepton number gauge boson, the lepton number breaking scalar field ϕ, as well as the exotic leptons, providing limits on the masses of these particles and their mixing with SM fields. *LEP* data further puts a lower bound on the vacuum expectation value (VEV) of the lepton number Higgs of $v_\Phi \geq 1.88$ TeV.

We then started part II of this thesis after a short introduction to stochastic gravitational wave backgrounds (SGWBs) from cosmological first-order PTs in chapter 6, investigating the lepton number breaking PT of the gauged lepton number model in chapter 7. As the VEV that breaks lepton number is roughly an order of magnitude larger than the SM Higgs VEV, the breaking of lepton number and the electroweak (EW) gauge symmetry typically proceeds via two separate transitions. While the latter remains a cross-over, the former can be of first-order and may be observed with GW observatories. We investigated the parameter regions in which a first-order PT occurs and evaluated the detectability of the corresponding SGWB at *LISA* and other future GW experiments. While the PT is mostly too weak to produce observable GWs if the contributions from the exotic leptons are neglected, the latter significantly enhance the detectability. We assessed the detection prospects in the parameter range where the model accounts for the full DM abundance, finding that a SGWB detectable by *LISA* or possible successor experiments is produced in a large fraction of the viable parameter space.

Finally, we conducted a study of PTs in decoupled dark sectors in chapter 8 with particular focus on sub-MeV hidden sectors. BSM particles with masses at the MeV-scale and below are constrained by limits on the number of relativistic degrees of freedom (DOFs) at the times of Big Bang Nucleosynthesis and photon decoupling. These constraints are typically phrased in terms of the effective number of neutrino species, N_{eff}, and exclude additional relativistic DOFs that are in thermal equilibrium with the SM at temperatures below $\lesssim 1$ MeV. Sub-MeV hidden sectors therefore need to be decoupled from the photon bath. We discussed how this affects potential PTs in such a hidden sector and the detectability of the corresponding SGWB, deriving the dependence of the parameters characterizing the transition on the temperature ratio $\xi_h = T_h/T_\gamma$ between the two sectors. We found that the most prominent effect is a suppression of the energy budget α of the transition by a factor ξ_h^4 if the hidden sector is colder than the photons. As a result, PTs are harder to detect if they occur in cool decoupled sectors. It is however still possible to construct models that comply with the constraints on N_{eff} and still feature a PT observable in GWs using pulsar timing arrays, as we demonstrated on the example of two toy models.

In conclusion, we have presented various searches exploring the phenomenology of new physics at particle colliders and via GWs. Both provide powerful tools for constraining or maybe even discovering BSM physics in the future. With the increase of luminosity and energy at coming colliders, heavier and more weakly coupled particles may be produced directly or observed indirectly via their effects on SM observables. Even in the case that the interactions of new physics with SM particles are too low to be detectable at colliders, GWs may still provide a path for probing such models, for instance via the SGWB generated in a cosmological first-order PT. Given the amount of planned and proposed experiments in both of these directions, the future bears bright prospects for unveiling the nature of physics beyond the Standard Model.

Acknowledgements

All names and personal references were removed from the acknowledgements in the electronic publication of this dissertation.

First and foremost, I would like to express my gratitude towards my thesis advisor for the opportunity to conduct my PhD studies under his supervision, and for his support and advise. I am very happy to say that I do not only appreciate him as a supervisor, but also as a friend, and that I could not imagine a better 'Doktorvater' for myself.

I am further deeply indebted to all my collaborators, from whom I learned a lot over that past years. Moreover, I would like to thank all the great members of the *THEP* working group, who made me feel welcome since the first day in Mainz and who make this group such a kind an enjoyable place. I am truly grateful to all of you, and I could not wish for better colleagues. Furthermore, I am thankful to our invaluable administration who helped me navigating through the jungle of travel request, reimbursement and insurance, as well as any other administrative question I could think of.

I also gratefully acknowledge support from the graduate school "Symmetry Breaking" (DFG/GRK 1581), financially as well as through interesting lectures and a nice summer school and retreat. In addition, I thank the ZDV for the computing time granted at MOGON, and their technical support.

Finally, I would like to thank my non-physicist friends, who helped to keep me entertained and mentally sane over the past months of social distancing, and, last but not least, my parents and my sister, without whose continuous support, motivation and understanding none of this would be possible.

Bibliography

[1] E. Madge and P. Schwaller, *Leptophilic dark matter from gauged lepton number: Phenomenology and gravitational wave signatures*, *JHEP* **02** (2019) 048, [1809.09110].

[2] M. Breitbach, J. Kopp, E. Madge, T. Opferkuch and P. Schwaller, *Dark, Cold, and Noisy: Constraining Secluded Hidden Sectors with Gravitational Waves*, *JCAP* **1907** (2019) 007, [1811.11175].

[3] F. Goertz, E. Madge, P. Schwaller and V. T. Tenorth, *Discovering the $h \to Z\gamma$ Decay in $t\bar{t}$ Associated Production*, *Phys. Rev. D* **102** (2020) 053004, [1909.07390].

[4] J. Heisig, M. Krämer, E. Madge and A. Mück, *Probing Higgs-portal dark matter with vector-boson fusion*, *JHEP* **03** (2020) 183, [1912.08472].

[5] P. Schwaller, T. M. P. Tait and R. Vega-Morales, *Dark Matter and Vectorlike Leptons from Gauged Lepton Number*, *Phys. Rev.* **D88** (2013) 035001, [1305.1108].

[6] http://creativecommons.org/licenses/by/4.0.

[7] S. L. Glashow, *Partial Symmetries of Weak Interactions*, *Nucl. Phys.* **22** (1961) 579–588.

[8] S. Weinberg, *A Model of Leptons*, *Phys. Rev. Lett.* **19** (1967) 1264–1266.

[9] A. Salam, *Weak and Electromagnetic Interactions*, *Conf. Proc.* **C680519** (1968) 367–377.

[10] F. Englert and R. Brout, *Broken Symmetry and the Mass of Gauge Vector Mesons*, *Phys. Rev. Lett.* **13** (1964) 321–323.

[11] P. W. Higgs, *Broken symmetries, massless particles and gauge fields*, *Phys. Lett.* **12** (1964) 132–133.

[12] P. W. Higgs, *Broken Symmetries and the Masses of Gauge Bosons*, *Phys. Rev. Lett.* **13** (1964) 508–509.

[13] G. S. Guralnik, C. R. Hagen and T. W. B. Kibble, *Global Conservation Laws and Massless Particles*, *Phys. Rev. Lett.* **13** (1964) 585–587.

[14] P. W. Higgs, *Spontaneous Symmetry Breakdown without Massless Bosons*, *Phys. Rev.* **145** (1966) 1156–1163.

[15] T. W. B. Kibble, *Symmetry breaking in nonAbelian gauge theories*, *Phys. Rev.* **155** (1967) 1554–1561.

[16] ATLAS collaboration, G. Aad et al., *Observation of a new particle in the search for the Standard Model Higgs boson with the ATLAS detector at the LHC*, *Phys. Lett.* **B716** (2012) 1–29, [1207.7214].

[17] CMS collaboration, S. Chatrchyan et al., *Observation of a New Boson at a Mass of 125 GeV with the CMS Experiment at the LHC*, *Phys. Lett.* **B716** (2012) 30–61, [1207.7235].

[18] E. Rutherford, *The scattering of alpha and beta particles by matter and the structure of the atom*, *Phil. Mag. Ser.6* **21** (1911) 669–688.

[19] LIGO Scientific, Virgo collaboration, B. P. Abbott et al., *Observation of Gravitational Waves from a Binary Black Hole Merger*, *Phys. Rev. Lett.* **116** (2016) 061102, [1602.03837].

[20] LISA collaboration, P. Amaro-Seoane et al., *Laser Interferometer Space Antenna*, 1702.00786.

[21] M. E. Peskin and D. V. Schroeder, *An Introduction to quantum field theory.* Addison-Wesley, Reading, USA, 1995.

[22] M. D. Schwartz, *Quantum Field Theory and the Standard Model.* Cambridge University Press, 2014.

[23] C.-N. Yang and R. L. Mills, *Conservation of Isotopic Spin and Isotopic Gauge Invariance*, *Phys. Rev.* **96** (1954) 191–195.

[24] M. Gell-Mann, *A Schematic Model of Baryons and Mesons*, *Phys. Lett.* **8** (1964) 214–215.

[25] G. Zweig, *An SU(3) model for strong interaction symmetry and its breaking. Version 1*, Preprint CERN-TH-401, CERN, Geneva, Jan, 1964.

[26] H. Fritzsch, M. Gell-Mann and H. Leutwyler, *Advantages of the Color Octet Gluon Picture*, *Phys. Lett.* **47B** (1973) 365–368.

[27] D. J. Gross and F. Wilczek, *Ultraviolet Behavior of Nonabelian Gauge Theories*, *Phys. Rev. Lett.* **30** (1973) 1343–1346.

[28] H. D. Politzer, *Reliable Perturbative Results for Strong Interactions?*, *Phys. Rev. Lett.* **30** (1973) 1346–1349.

[29] G. 't Hooft and M. J. G. Veltman, *Regularization and Renormalization of Gauge Fields*, *Nucl. Phys.* **B44** (1972) 189–213.

[30] N. Cabibbo, *Unitary Symmetry and Leptonic Decays*, *Phys. Rev. Lett.* **10** (1963) 531–533.

[31] M. Kobayashi and T. Maskawa, *CP Violation in the Renormalizable Theory of Weak Interaction*, *Prog. Theor. Phys.* **49** (1973) 652–657.

[32] B. Pontecorvo, *Inverse beta processes and nonconservation of lepton charge*, *Sov. Phys. JETP* **7** (1958) 172–173.

[33] Z. Maki, M. Nakagawa and S. Sakata, *Remarks on the unified model of elementary particles*, *Prog. Theor. Phys.* **28** (1962) 870–880.

[34] M. D'Onofrio and K. Rummukainen, *Standard model cross-over on the lattice*, *Phys. Rev.* **D93** (2016) 025003, [1508.07161].

[35] J. Choi and R. R. Volkas, *Real Higgs singlet and the electroweak phase transition in the Standard Model*, *Phys. Lett.* **B317** (1993) 385–391, [hep-ph/9308234].

[36] J. R. Espinosa, T. Konstandin and F. Riva, *Strong Electroweak Phase Transitions in the Standard Model with a Singlet*, *Nucl. Phys.* **B854** (2012) 592–630, [1107.5441].

[37] J. M. Cline and K. Kainulainen, *Electroweak baryogenesis and dark matter from a singlet Higgs*, *JCAP* **1301** (2013) 012, [1210.4196].

[38] HotQCD collaboration, A. Bazavov et al., *Chiral crossover in QCD at zero and non-zero chemical potentials*, *Phys. Lett.* **B795** (2019) 15–21, [1812.08235].

[39] M. Gyulassy and L. McLerran, *New forms of QCD matter discovered at RHIC*, *Nucl. Phys.* **A750** (2005) 30–63, [nucl-th/0405013].

[40] T. Banks and A. Zaks, *On the Phase Structure of Vector-Like Gauge Theories with Massless Fermions*, *Nucl. Phys.* **B196** (1982) 189–204.

[41] R. D. Pisarski and F. Wilczek, *Remarks on the Chiral Phase Transition in Chromodynamics*, *Phys. Rev.* **D29** (1984) 338–341.

[42] G. 't Hooft, *Naturalness, chiral symmetry, and spontaneous chiral symmetry breaking*, *NATO Sci. Ser. B* **59** (1980) 135–157.

[43] G. F. Giudice, *Naturalness after LHC8*, *PoS* **EPS-HEP2013** (2013) 163, [1307.7879].

[44] N. Arkani-Hamed, A. G. Cohen and H. Georgi, *Electroweak symmetry breaking from dimensional deconstruction*, *Phys. Lett.* **B513** (2001) 232–240, [hep-ph/0105239].

[45] N. Arkani-Hamed, A. G. Cohen, E. Katz and A. E. Nelson, *The Littlest Higgs*, *JHEP* **07** (2002) 034, [hep-ph/0206021].

[46] D. B. Kaplan, H. Georgi and S. Dimopoulos, *Composite Higgs Scalars*, *Phys. Lett.* **136B** (1984) 187–190.

[47] R. Contino, Y. Nomura and A. Pomarol, *Higgs as a holographic pseudoGoldstone boson*, *Nucl. Phys.* **B671** (2003) 148–174, [hep-ph/0306259].

[48] K. Agashe, R. Contino and A. Pomarol, *The Minimal composite Higgs model*, *Nucl. Phys.* **B719** (2005) 165–187, [hep-ph/0412089].

[49] R. Haag, J. T. Lopuszanski and M. Sohnius, *All Possible Generators of Supersymmetries of the s Matrix*, *Nucl. Phys.* **B88** (1975) 257.

[50] P. Fayet, *Supersymmetry and Weak, Electromagnetic and Strong Interactions*, *Phys. Lett.* **64B** (1976) 159.

[51] S. P. Martin, *A Supersymmetry primer*, hep-ph/9709356.

[52] D. Buttazzo, G. Degrassi, P. P. Giardino, G. F. Giudice, F. Sala, A. Salvio et al., *Investigating the near-criticality of the Higgs boson*, *JHEP* **12** (2013) 089, [1307.3536].

[53] J. R. Espinosa, *Implications of the top (and Higgs) mass for vacuum stability*, *PoS* **TOP2015** (2016) 043, [1512.01222].

[54] WMAP collaboration, C. L. Bennett et al., *First year Wilkinson Microwave Anisotropy Probe (WMAP) observations: Preliminary maps and basic results*, *Astrophys. J. Suppl.* **148** (2003) 1–27, [astro-ph/0302207].

[55] A. D. Sakharov, *Violation of CP Invariance, C asymmetry, and baryon asymmetry of the universe*, *Pisma Zh. Eksp. Teor. Fiz.* **5** (1967) 32–35.

[56] V. A. Kuzmin, V. A. Rubakov and M. E. Shaposhnikov, *On the Anomalous Electroweak Baryon Number Nonconservation in the Early Universe*, *Phys. Lett.* **155B** (1985) 36.

[57] A. G. Cohen, D. B. Kaplan and A. E. Nelson, *Baryogenesis at the weak phase transition*, *Nucl. Phys.* **B349** (1991) 727–742.

[58] N. Turok and J. Zadrozny, *Dynamical generation of baryons at the electroweak transition*, *Phys. Rev. Lett.* **65** (1990) 2331–2334.

[59] G. Bertone, D. Hooper and J. Silk, *Particle dark matter: Evidence, candidates and constraints*, *Phys. Rept.* **405** (2005) 279–390, [hep-ph/0404175].

[60] Planck collaboration, N. Aghanim et al., *Planck 2018 results. VI. Cosmological parameters*, 1807.06209.

[61] G. Bertone and D. Hooper, *History of dark matter*, *Rev. Mod. Phys.* **90** (2018) 045002, [1605.04909].

[62] V. C. Rubin and W. K. Ford, Jr., *Rotation of the Andromeda Nebula from a Spectroscopic Survey of Emission Regions*, *Astrophys. J.* **159** (1970) 379–403.

[63] F. Zwicky, *Die Rotverschiebung von extragalaktischen Nebeln*, *Helv. Phys. Acta* **6** (1933) 110–127.

[64] M. Markevitch, A. H. Gonzalez, D. Clowe, A. Vikhlinin, L. David, W. Forman et al., *Direct constraints on the dark matter self-interaction cross-section from the merging galaxy cluster 1E0657-56*, *Astrophys. J.* **606** (2004) 819–824, [astro-ph/0309303].

[65] T. D. Brandt, *Constraints on MACHO Dark Matter from Compact Stellar Systems in Ultra-Faint Dwarf Galaxies*, *Astrophys. J. Lett.* **824** (2016) L31, [1605.03665].

[66] J. Einasto, *Dark Matter*, *Braz. J. Phys.* **43** (2013) 369–374, [1308.2534].

[67] LIGO Scientific, Virgo, Fermi-GBM, INTEGRAL collaboration, B. P. Abbott et al., *Gravitational Waves and Gamma-rays from a Binary Neutron Star Merger: GW170817 and GRB 170817A*, *Astrophys. J. Lett.* **848** (2017) L13, [1710.05834].

[68] Particle Data Group collaboration, M. Tanabashi et al., *Review of Particle Physics*, *Phys. Rev.* **D98** (2018) 030001.

[69] S. D. McDermott, H.-B. Yu and K. M. Zurek, *Turning off the Lights: How Dark is Dark Matter?*, *Phys. Rev.* **D83** (2011) 063509, [1011.2907].

[70] B. Audren, J. Lesgourgues, G. Mangano, P. D. Serpico and T. Tram, *Strongest model-independent bound on the lifetime of Dark Matter*, *JCAP* **1412** (2014) 028, [1407.2418].

[71] S. W. Randall, M. Markevitch, D. Clowe, A. H. Gonzalez and M. Bradac, *Constraints on the Self-Interaction Cross-Section of Dark Matter from Numerical Simulations of the Merging Galaxy Cluster 1E 0657-56*, *Astrophys. J.* **679** (2008) 1173–1180, [0704.0261].

[72] M. Nori, R. Murgia, V. Iršič, M. Baldi and M. Viel, *Lyman α forest and non-linear structure characterization in Fuzzy Dark Matter cosmologies*, *Mon. Not. Roy. Astron. Soc.* **482** (2019) 3227–3243, [1809.09619].

[73] L. Randall, J. Scholtz and J. Unwin, *Cores in Dwarf Galaxies from Fermi Repulsion*, *Mon. Not. Roy. Astron. Soc.* **467** (2017) 1515–1525, [1611.04590].

[74] V. Iršič et al., *New Constraints on the free-streaming of warm dark matter from intermediate and small scale Lyman-α forest data*, *Phys. Rev.* **D96** (2017) 023522, [1702.01764].

[75] H. Baer, K.-Y. Choi, J. E. Kim and L. Roszkowski, *Dark matter production in the early Universe: beyond the thermal WIMP paradigm*, *Phys. Rept.* **555** (2015) 1–60, [1407.0017].

[76] K. Griest and D. Seckel, *Three exceptions in the calculation of relic abundances*, *Phys. Rev.* **D43** (1991) 3191–3203.

[77] L. J. Hall, K. Jedamzik, J. March-Russell and S. M. West, *Freeze-In Production of FIMP Dark Matter*, *JHEP* **03** (2010) 080, [0911.1120].

[78] M. J. Baker and J. Kopp, *Dark Matter Decay between Phase Transitions at the Weak Scale*, *Phys. Rev. Lett.* **119** (2017) 061801, [1608.07578].

[79] M. J. Baker, M. Breitbach, J. Kopp and L. Mittnacht, *Dynamic Freeze-In: Impact of Thermal Masses and Cosmological Phase Transitions on Dark Matter Production*, *JHEP* **03** (2018) 114, [1712.03962].

[80] M. J. Baker and L. Mittnacht, *Variations on the Vev Flip-Flop: Instantaneous Freeze-out and Decaying Dark Matter*, *JHEP* **05** (2019) 070, [1811.03101].

[81] P. Gondolo and G. Gelmini, *Cosmic abundances of stable particles: Improved analysis*, *Nucl. Phys.* **B360** (1991) 145–179.

[82] E. W. Kolb and M. S. Turner, *The Early Universe*, vol. 69 of *Frontiers in Physics*. Westview Press, 1990.

[83] MAGIC, Fermi-LAT collaboration, M. L. Ahnen et al., *Limits to Dark Matter Annihilation Cross-Section from a Combined Analysis of MAGIC and Fermi-LAT Observations of Dwarf Satellite Galaxies*, *JCAP* **1602** (2016) 039, [1601.06590].

[84] Fermi-LAT collaboration, M. Ackermann et al., *Updated search for spectral lines from Galactic dark matter interactions with pass 8 data from the Fermi Large Area Telescope*, *Phys. Rev.* **D91** (2015) 122002, [1506.00013].

[85] H.E.S.S. collaboration, H. Abdallah et al., *Search for dark matter annihilations towards the inner Galactic halo from 10 years of observations with H.E.S.S*, *Phys. Rev. Lett.* **117** (2016) 111301, [1607.08142].

[86] HESS collaboration, L. Rinchiuso, E. Moulin, A. Viana, C. Van Eldik and J. Veh, *Dark matter gamma-ray line searches toward the Galactic Center halo with H.E.S.S. I*, *PoS* **ICRC2017** (2018) 893, [1708.08358].

[87] M. W. Goodman and E. Witten, *Detectability of Certain Dark Matter Candidates*, *Phys. Rev.* **D31** (1985) 3059.

[88] XENON collaboration, E. Aprile et al., *Dark Matter Search Results from a One Ton-Year Exposure of XENON1T*, *Phys. Rev. Lett.* **121** (2018) 111302, [1805.12562].

[89] SuperCDMS collaboration, R. Agnese et al., *First Dark Matter Constraints from a SuperCDMS Single-Charge Sensitive Detector*, *Phys. Rev. Lett.* **121** (2018) 051301, [1804.10697].

[90] DAMIC collaboration, A. Aguilar-Arevalo et al., *Constraints on Light Dark Matter Particles Interacting with Electrons from DAMIC at SNOLAB*, *Phys. Rev. Lett.* **123** (2019) 181802, [1907.12628].

[91] SENSEI collaboration, O. Abramoff et al., *SENSEI: Direct-Detection Constraints on Sub-GeV Dark Matter from a Shallow Underground Run Using a Prototype Skipper-CCD*, *Phys. Rev. Lett.* **122** (2019) 161801, [1901.10478].

[92] CMS collaboration, A. M. Sirunyan et al., *Search for dark matter produced with an energetic jet or a hadronically decaying W or Z boson at $\sqrt{s} = 13$ TeV*, *JHEP* **07** (2017) 014, [1703.01651].

[93] ATLAS collaboration, M. Aaboud et al., *Search for dark matter at $\sqrt{s} = 13$ TeV in final states containing an energetic photon and large missing transverse momentum with the ATLAS detector*, *Eur. Phys. J.* **C77** (2017) 393, [1704.03848].

[94] CMS collaboration, A. M. Sirunyan et al., *Search for new physics in the monophoton final state in proton-proton collisions at $\sqrt{s} = 13$ TeV*, *JHEP* **10** (2017) 073, [1706.03794].

[95] ATLAS collaboration, M. Aaboud et al., *Search for dark matter and other new phenomena in events with an energetic jet and large missing transverse momentum using the ATLAS detector*, *JHEP* **01** (2018) 126, [1711.03301].

[96] Fermi-LAT collaboration, M. Ajello et al., *Fermi-LAT Observations of High-Energy γ-Ray Emission Toward the Galactic Center*, *Astrophys. J.* **819** (2016) 44, [1511.02938].

[97] R. K. Leane and T. R. Slatyer, *Revival of the Dark Matter Hypothesis for the Galactic Center Gamma-Ray Excess*, *Phys. Rev. Lett.* **123** (2019) 241101, [1904.08430].

[98] AMS collaboration, M. Aguilar et al., *Antiproton Flux, Antiproton-to-Proton Flux Ratio, and Properties of Elementary Particle Fluxes in Primary Cosmic Rays Measured with the Alpha Magnetic Spectrometer on the International Space Station*, *Phys. Rev. Lett.* **117** (2016) 091103.

[99] I. Cholis, T. Linden and D. Hooper, *A Robust Excess in the Cosmic-Ray Antiproton Spectrum: Implications for Annihilating Dark Matter*, *Phys. Rev.* **D99** (2019) 103026, [1903.02549].

[100] R. Bernabei et al., *First model independent results from DAMA/LIBRA-phase2*, *Nucl. Phys. Atom. Energy* **19** (2018) 307–325, [1805.10486].

[101] G. Adhikari et al., *An experiment to search for dark-matter interactions using sodium iodide detectors*, *Nature* **564** (2018) 83–86, [1906.01791].

[102] R. J. Crewther, P. Di Vecchia, G. Veneziano and E. Witten, *Chiral Estimate of the Electric Dipole Moment of the Neutron in Quantum Chromodynamics*, *Phys. Lett.* **88B** (1979) 123.

[103] C. A. Baker et al., *An Improved experimental limit on the electric dipole moment of the neutron*, *Phys. Rev. Lett.* **97** (2006) 131801, [hep-ex/0602020].

[104] R. D. Peccei and H. R. Quinn, *Constraints Imposed by CP Conservation in the Presence of Instantons*, *Phys. Rev.* **D16** (1977) 1791–1797.

[105] R. D. Peccei and H. R. Quinn, *CP Conservation in the Presence of Instantons*, *Phys. Rev. Lett.* **38** (1977) 1440–1443.

[106] J. Redondo, *Alternative dark matter candidates: axions and ALPs*, *PoS* **NOW2018** (2019) 083.

[107] D. J. E. Marsh, *Axion Cosmology*, *Phys. Rept.* **643** (2016) 1–79, [1510.07633].

[108] C. S. Machado, W. Ratzinger, P. Schwaller and B. A. Stefanek, *Audible Axions*, *JHEP* **01** (2019) 053, [1811.01950].

[109] C. S. Machado, W. Ratzinger, P. Schwaller and B. A. Stefanek, *Gravitational wave probes of axion-like particles*, 1912.01007.

[110] A. Boyarsky, M. Drewes, T. Lasserre, S. Mertens and O. Ruchayskiy, *Sterile Neutrino Dark Matter*, *Prog. Part. Nucl. Phys.* **104** (2019) 1–45, [1807.07938].

[111] E. Di Valentino, A. Melchiorri and J. Silk, *Cosmological constraints in extended parameter space from the Planck 2018 Legacy release*, *JCAP* **2001** (2020) 013, [1908.01391].

[112] A. G. Riess et al., *New Parallaxes of Galactic Cepheids from Spatially Scanning the Hubble Space Telescope: Implications for the Hubble Constant*, *Astrophys. J.* **855** (2018) 136, [1801.01120].

[113] KATRIN collaboration, M. Aker et al., *Improved Upper Limit on the Neutrino Mass from a Direct Kinematic Method by KATRIN*, *Phys. Rev. Lett.* **123** (2019) 221802, [1909.06048].

[114] I. Esteban, M. C. Gonzalez-Garcia, A. Hernandez-Cabezudo, M. Maltoni and T. Schwetz, *Global analysis of three-flavour neutrino oscillations: synergies and tensions in the determination of θ_{23}, δ_{CP}, and the mass ordering*, *JHEP* **01** (2019) 106, [1811.05487].

[115] J. Schechter and J. W. F. Valle, *Neutrinoless Double beta Decay in SU(2) x U(1) Theories*, *Phys. Rev.* **D25** (1982) 2951.

[116] P. Minkowski, *$\mu \to e\gamma$ at a Rate of One Out of 10^9 Muon Decays?*, *Phys. Lett.* **67B** (1977) 421–428.

[117] S. Dodelson and L. M. Widrow, *Sterile-neutrinos as dark matter*, *Phys. Rev. Lett.* **72** (1994) 17–20, [hep-ph/9303287].

[118] T. Asaka, S. Blanchet and M. Shaposhnikov, *The nuMSM, dark matter and neutrino masses*, *Phys. Lett.* **B631** (2005) 151–156, [hep-ph/0503065].

[119] T. Asaka and M. Shaposhnikov, *The νMSM, dark matter and baryon asymmetry of the universe*, *Phys. Lett.* **B620** (2005) 17–26, [hep-ph/0505013].

[120] CMS collaboration, A. M. Sirunyan et al., *Search for invisible decays of a Higgs boson produced through vector boson fusion in proton-proton collisions at $\sqrt{s} = 13$ TeV*, *Phys. Lett.* **B793** (2019) 520–551, [1809.05937].

[121] CMS collaboration, *Search for invisible decays of a Higgs boson produced through vector boson fusion at the High-Luminosity LHC*, CMS Physics Analysis Summary CMS-PAS-FTR-18-016, CERN, Geneva, 2018.

[122] B. Patt and F. Wilczek, *Higgs-field portal into hidden sectors*, hep-ph/0605188.

[123] G. Arcadi, A. Djouadi and M. Raidal, *Dark Matter through the Higgs portal*, *Phys. Rept.* **842** (2020) 1–180, [1903.03616].

[124] V. Silveira and A. Zee, *SCALAR PHANTOMS*, *Phys. Lett.* **161B** (1985) 136–140.

[125] J. McDonald, *Gauge singlet scalars as cold dark matter*, *Phys. Rev.* **D50** (1994) 3637–3649, [hep-ph/0702143].

[126] C. P. Burgess, M. Pospelov and T. ter Veldhuis, *The Minimal model of nonbaryonic dark matter: A Singlet scalar*, *Nucl. Phys.* **B619** (2001) 709–728, [hep-ph/0011335].

[127] ATLAS, CMS collaboration, G. Aad et al., *Combined Measurement of the Higgs Boson Mass in pp Collisions at $\sqrt{s} = 7$ and 8 TeV with the ATLAS and CMS Experiments*, *Phys. Rev. Lett.* **114** (2015) 191803, [1503.07589].

[128] A. Cuoco, B. Eiteneuer, J. Heisig and M. Krämer, *A global fit of the γ-ray galactic center excess within the scalar singlet Higgs portal model*, *JCAP* **1606** (2016) 050, [1603.08228].

[129] A. Cuoco, J. Heisig, M. Korsmeier and M. Krämer, *Probing dark matter annihilation in the Galaxy with antiprotons and gamma rays*, *JCAP* **1710** (2017) 053, [1704.08258].

[130] J. A. Casas, D. G. Cerdeño, J. M. Moreno and J. Quilis, *Reopening the Higgs portal for single scalar dark matter*, *JHEP* **05** (2017) 036, [1701.08134].

[131] S. Bhattacharya, P. Ghosh, T. N. Maity and T. S. Ray, *Mitigating Direct Detection Bounds in Non-minimal Higgs Portal Scalar Dark Matter Models*, *JHEP* **10** (2017) 088, [1706.04699].

[132] C. Gross, O. Lebedev and T. Toma, *Cancellation Mechanism for Dark-Matter–Nucleon Interaction*, *Phys. Rev. Lett.* **119** (2017) 191801, [1708.02253].

[133] ATLAS collaboration, M. Aaboud et al., *Search for new high-mass phenomena in the dilepton final state using 36 fb^{-1} of proton-proton collision data at sqrts = 13 TeV with the ATLAS detector*, *JHEP* **10** (2017) 182, [1707.02424].

[134] M. Endo and Y. Takaesu, *Heavy WIMP through Higgs portal at the LHC*, *Phys. Lett.* **B743** (2015) 228–234, [1407.6882].

[135] N. Craig, H. K. Lou, M. McCullough and A. Thalapillil, *The Higgs Portal Above Threshold*, *JHEP* **02** (2016) 127, [1412.0258].

[136] M. Heikinheimo, T. Tenkanen, K. Tuominen and V. Vaskonen, *Observational Constraints on Decoupled Hidden Sectors*, *Phys. Rev.* **D94** (2016) 063506, [1604.02401].

[137] M. Gonderinger, Y. Li, H. Patel and M. J. Ramsey-Musolf, *Vacuum Stability, Perturbativity, and Scalar Singlet Dark Matter*, *JHEP* **01** (2010) 053, [0910.3167].

[138] T. Binder, T. Bringmann, M. Gustafsson and A. Hryczuk, *Early kinetic decoupling of dark matter: when the standard way of calculating the thermal relic density fails*, *Phys. Rev.* **D96** (2017) 115010, [1706.07433].

[139] K. Ala-Mattinen and K. Kainulainen, *Precision calculations of dark matter relic abundance*, 1912.02870.

[140] G. Bélanger, F. Boudjema, A. Goudelis, A. Pukhov and B. Zaldivar, *micrOMEGAs5.0 : Freeze-in*, *Comput. Phys. Commun.* **231** (2018) 173–186, [1801.03509].

[141] G. Belanger, A. Mjallal and A. Pukhov, *Recasting direct detection limits within micrOMEGAs and implication for non-standard Dark Matter scenarios*, 2003.08621.

[142] LUX-ZEPLIN collaboration, D. S. Akerib et al., *Projected WIMP Sensitivity of the LUX-ZEPLIN (LZ) Dark Matter Experiment*, 1802.06039.

[143] DARWIN collaboration, J. Aalbers et al., *DARWIN: towards the ultimate dark matter detector*, *JCAP* **1611** (2016) 017, [1606.07001].

[144] GAMBIT collaboration, P. Athron et al., *Status of the scalar singlet dark matter model*, *Eur. Phys. J.* **C77** (2017) 568, [1705.07931].

[145] P. Athron, J. M. Cornell, F. Kahlhoefer, J. Mckay, P. Scott and S. Wild, *Impact of vacuum stability, perturbativity and XENON1T on global fits of $\mathbb{Z}_2$ and $\mathbb{Z}_3$ scalar singlet dark matter*, *Eur. Phys. J.* **C78** (2018) 830, [1806.11281].

[146] L. Feng, S. Profumo and L. Ubaldi, *Closing in on singlet scalar dark matter: LUX, invisible Higgs decays and gamma-ray lines*, *JHEP* **03** (2015) 045, [1412.1105].

[147] D. R. T. Jones and S. T. Petcov, *Heavy Higgs Bosons at LEP*, *Phys. Lett.* **84B** (1979) 440–444.

[148] R. N. Cahn and S. Dawson, *Production of Very Massive Higgs Bosons*, *Phys. Lett.* **136B** (1984) 196.

[149] O. J. P. Eboli and D. Zeppenfeld, *Observing an invisible Higgs boson*, *Phys. Lett.* **B495** (2000) 147–154, [hep-ph/0009158].

[150] H. Han, J. M. Yang, Y. Zhang and S. Zheng, *Collider Signatures of Higgs-portal Scalar Dark Matter*, *Phys. Lett.* **B756** (2016) 109–112, [1601.06232].

[151] D. Dercks and T. Robens, *Constraining the Inert Doublet Model using Vector Boson Fusion*, *Eur. Phys. J.* **C79** (2019) 924, [1812.07913].

[152] CMS collaboration, A. M. Sirunyan et al., *Measurements of the Higgs boson width and anomalous HVV couplings from on-shell and off-shell production in the four-lepton final state*, *Phys. Rev.* **D99** (2019) 112003, [1901.00174].

[153] J. Alwall, R. Frederix, S. Frixione, V. Hirschi, F. Maltoni, O. Mattelaer et al., *The automated computation of tree-level and next-to-leading order differential cross sections, and their matching to parton shower simulations*, *JHEP* **07** (2014) 079, [1405.0301].

[154] NNPDF collaboration, R. D. Ball et al., *Parton distributions for the LHC Run II*, *JHEP* **04** (2015) 040, [1410.8849].

[155] A. Buckley, J. Ferrando, S. Lloyd, K. Nordström, B. Page, M. Rüfenacht et al., *LHAPDF6: parton density access in the LHC precision era*, *Eur. Phys. J.* **C75** (2015) 132, [1412.7420].

[156] LHC Higgs Cross Section Working Group collaboration, D. de Florian et al., *Handbook of LHC Higgs Cross Sections: 4. Deciphering the Nature of the Higgs Sector*, 1610.07922.

[157] T. Sjöstrand, S. Ask, J. R. Christiansen, R. Corke, N. Desai, P. Ilten et al., *An Introduction to PYTHIA 8.2*, *Comput. Phys. Commun.* **191** (2015) 159–177, [1410.3012].

[158] DELPHES 3 collaboration, J. de Favereau, C. Delaere, P. Demin, A. Giammanco, V. Lemaître, A. Mertens et al., *DELPHES 3, A modular framework for fast simulation of a generic collider experiment*, *JHEP* **02** (2014) 057, [1307.6346].

[159] M. Cacciari, G. P. Salam and G. Soyez, *FastJet User Manual*, *Eur. Phys. J.* **C72** (2012) 1896, [1111.6097].

[160] M. Cacciari, G. P. Salam and G. Soyez, *The anti-k_t jet clustering algorithm*, *JHEP* **04** (2008) 063, [0802.1189].

[161] M. L. Mangano, M. Moretti, F. Piccinini and M. Treccani, *Matching matrix elements and shower evolution for top-quark production in hadronic collisions*, *JHEP* **01** (2007) 013, [hep-ph/0611129].

[162] J. Alwall et al., *Comparative study of various algorithms for the merging of parton showers and matrix elements in hadronic collisions*, *Eur. Phys. J.* **C53** (2008) 473–500, [0706.2569].

[163] O. Cata and A. Ibarra, *Dark Matter Stability without New Symmetries*, *Phys. Rev.* **D90** (2014) 063509, [1404.0432].

[164] O. Catà, *Lurking pseudovectors below the TeV scale*, *Eur. Phys. J.* **C74** (2014) 2991, [1402.4990].

[165] S. Kanemura, S. Matsumoto, T. Nabeshima and N. Okada, *Can WIMP Dark Matter overcome the Nightmare Scenario?*, *Phys. Rev.* **D82** (2010) 055026, [1005.5651].

[166] Y. G. Kim, K. Y. Lee and S. Shin, *Singlet fermionic dark matter*, *JHEP* **05** (2008) 100, [0803.2932].

[167] L. Lopez-Honorez, T. Schwetz and J. Zupan, *Higgs portal, fermionic dark matter, and a Standard Model like Higgs at 125 GeV*, *Phys. Lett.* **B716** (2012) 179–185, [1203.2064].

[168] S. Baek, P. Ko, W.-I. Park and E. Senaha, *Higgs Portal Vector Dark Matter : Revisited*, *JHEP* **05** (2013) 036, [1212.2131].

[169] D. G. E. Walker, *Unitarity Constraints on Higgs Portals*, 1310.1083.

[170] A. Freitas, S. Westhoff and J. Zupan, *Integrating in the Higgs Portal to Fermion Dark Matter*, *JHEP* **09** (2015) 015, [1506.04149].

[171] V. V. Khoze and M. Spannowsky, *Higgsplosion: Solving the Hierarchy Problem via rapid decays of heavy states into multiple Higgs bosons*, *Nucl. Phys.* **B926** (2018) 95–111, [1704.03447].

[172] O. Lebedev, H. M. Lee and Y. Mambrini, *Vector Higgs-portal dark matter and the invisible Higgs*, *Phys. Lett.* **B707** (2012) 570–576, [1111.4482].

[173] J. S. Gainer, W.-Y. Keung, I. Low and P. Schwaller, *Looking for a light Higgs boson in the $Z\gamma \to \ell\ell\gamma$ channel*, *Phys. Rev.* **D86** (2012) 033010, [1112.1405].

[174] A. Freitas and P. Schwaller, *Multi-Photon Signals from Composite Models at LHC*, *JHEP* **01** (2011) 022, [1010.2528].

[175] B. Coleppa, K. Kumar and H. E. Logan, *Can the 126 GeV boson be a pseudoscalar?*, *Phys. Rev.* **D86** (2012) 075022, [1208.2692].

[176] Y. Chen, A. Falkowski, I. Low and R. Vega-Morales, *New Observables for CP Violation in Higgs Decays*, *Phys. Rev.* **D90** (2014) 113006, [1405.6723].

[177] I. Low, J. Lykken and G. Shaughnessy, *Singlet scalars as Higgs imposters at the Large Hadron Collider*, *Phys. Rev.* **D84** (2011) 035027, [1105.4587].

[178] A. Azatov, R. Contino, A. Di Iura and J. Galloway, *New Prospects for Higgs Compositeness in $h \to Z\gamma$*, *Phys. Rev.* **D88** (2013) 075019, [1308.2676].

[179] R. Contino, M. Ghezzi, C. Grojean, M. Muhlleitner and M. Spira, *Effective Lagrangian for a light Higgs-like scalar*, *JHEP* **07** (2013) 035, [1303.3876].

[180] A. Pomarol and F. Riva, *Towards the Ultimate SM Fit to Close in on Higgs Physics*, *JHEP* **01** (2014) 151, [1308.2803].

[181] J. Elias-Miro, J. R. Espinosa, E. Masso and A. Pomarol, *Higgs windows to new physics through d=6 operators: constraints and one-loop anomalous dimensions*, *JHEP* **11** (2013) 066, [1308.1879].

[182] G. Belanger, V. Bizouard and G. Chalons, *Boosting Higgs boson decays into gamma and a Z in the NMSSM*, *Phys. Rev.* **D89** (2014) 095023, [1402.3522].

[183] C. Arina, V. Martin-Lozano and G. Nardini, *Dark matter versus $h \to \gamma\gamma$ and $h \to \gamma Z$ with supersymmetric triplets*, *JHEP* **08** (2014) 015, [1403.6434].

[184] D. Liu, I. Low and Z. Yin, *Universal Relations in Composite Higgs Models*, *JHEP* **05** (2019) 170, [1809.09126].

[185] ATLAS collaboration, G. Aad et al., *A search for the $Z\gamma$ decay mode of the Higgs boson in pp collisions at $\sqrt{s}$ = 13 TeV with the ATLAS detector*, 2005.05382.

[186] ATLAS collaboration, *Projections for measurements of Higgs boson cross sections, branching ratios, coupling parameters and mass with the ATLAS detector at the HL-LHC*, ATLAS Note ATL-PHYS-PUB-2018-054, CERN, Geneva, Dec, 2018.

[187] J. M. No and M. Spannowsky, *A Boost to $h \to Z\gamma$: from LHC to Future e^+e^- Colliders*, *Phys. Rev.* **D95** (2017) 075027, [1612.06626].

[188] CMS collaboration, A. M. Sirunyan et al., *Observation of $\mathrm{t\bar{t}}H$ production*, *Phys. Rev. Lett.* **120** (2018) 231801, [1804.02610].

[189] ATLAS collaboration, M. Aaboud et al., *Observation of Higgs boson production in association with a top quark pair at the LHC with the ATLAS detector*, *Phys. Lett.* **B784** (2018) 173–191, [1806.00425].

[190] CMS collaboration, A. M. Sirunyan et al., *Measurements of $\mathrm{t\bar{t}}H$ production and the CP structure of the Yukawa interaction between the Higgs boson and top quark in the diphoton decay channel*, 2003.10866.

[191] CMS collaboration, *First constraints on invisible Higgs boson decays using* $\mathrm{t\bar{t}H}$ *production at* $\sqrt{s} = 13$ *TeV*, CMS Physics Analysis Summary CMS-PAS-HIG-18-008, CERN, Geneva, 2019.

[192] ATLAS collaboration, *Search for* $t\bar{t}H$ *production in the* $H \to \gamma\gamma$ *channel at* $\sqrt{S} = 8$ *TeV with the ATLAS detector*, ATLAS Note ATLAS-CONF-2013-080, CERN, Geneva, Jul, 2013.

[193] ATLAS collaboration, M. Aaboud et al., *Measurement of the cross section for isolated-photon plus jet production in pp collisions at* $\sqrt{s} = 13$ *TeV using the ATLAS detector*, *Phys. Lett.* **B780** (2018) 578–602, [1801.00112].

[194] V. Hirschi and O. Mattelaer, *Automated event generation for loop-induced processes*, *JHEP* **10** (2015) 146, [1507.00020].

[195] J. Butterworth et al., *PDF4LHC recommendations for LHC Run II*, *J. Phys.* **G43** (2016) 023001, [1510.03865].

[196] FCC collaboration, A. Abada et al., *HE-LHC: The High-Energy Large Hadron Collider*, *Eur. Phys. J. ST* **228** (2019) 1109–1382.

[197] FCC collaboration, A. Abada et al., *FCC-hh: The Hadron Collider*, *Eur. Phys. J. ST* **228** (2019) 755–1107.

[198] M. Cepeda et al., *Report from Working Group 2*, *CERN Yellow Rep. Monogr.* **7** (2019) 221–584, [1902.00134].

[199] R. Contino et al., *Physics at a 100 TeV pp collider: Higgs and EW symmetry breaking studies*, *CERN Yellow Rep.* (2017) 255–440, [1606.09408].

[200] LHC Higgs Cross Section Working Group collaboration, J. R. Andersen et al., *Handbook of LHC Higgs Cross Sections: 3. Higgs Properties*, 1307.1347.

[201] G. Durieux, C. Grojean, J. Gu and K. Wang, *The leptonic future of the Higgs*, *JHEP* **09** (2017) 014, [1704.02333].

[202] Q.-H. Cao, H.-R. Wang and Y. Zhang, *Probing* $HZ\gamma$ *and* $H\gamma\gamma$ *anomalous couplings in the process* $e^+e^- \to H\gamma$, *Chin. Phys.* **C39** (2015) 113102, [1505.00654].

[203] P. J. Fox and E. Poppitz, *Leptophilic Dark Matter*, *Phys. Rev.* **D79** (2009) 083528, [0811.0399].

[204] S. Chang, R. Edezhath, J. Hutchinson and M. Luty, *Leptophilic Effective WIMPs*, *Phys. Rev.* **D90** (2014) 015011, [1402.7358].

[205] N. F. Bell, Y. Cai, R. K. Leane and A. D. Medina, *Leptophilic dark matter with* Z' *interactions*, *Phys. Rev.* **D90** (2014) 035027, [1407.3001].

[206] P. Agrawal, Z. Chacko and C. B. Verhaaren, *Leptophilic Dark Matter and the Anomalous Magnetic Moment of the Muon*, *JHEP* **08** (2014) 147, [1402.7369].

[207] Y. Bai and J. Berger, *Lepton Portal Dark Matter*, *JHEP* **08** (2014) 153, [1402.6696].

[208] A. Freitas and S. Westhoff, *Leptophilic Dark Matter in Lepton Interactions at LEP and ILC*, *JHEP* **10** (2014) 116, [1408.1959].

[209] H.-S. Lee, *Muon g-2 anomaly and dark leptonic gauge boson*, *Phys. Rev.* **D90** (2014) 091702, [1408.4256].

[210] Q.-H. Cao, C.-R. Chen and T. Gong, *Leptophilic dark matter confronts AMS-02 cosmic-ray positron flux*, *Chin. J. Phys.* **55** (2017) 10–15, [1409.7317].

[211] J. Kile, A. Kobach and A. Soni, *Lepton-Flavored Dark Matter*, *Phys. Lett.* **B744** (2015) 330–338, [1411.1407].

[212] A. Aranda, E. Jiménez and C. A. Vaquera-Araujo, *Electroweak phase transition in a model with gauged lepton number*, *JHEP* **01** (2015) 070, [1410.7508].

[213] Y. S. Jeong, C. S. Kim and H.-S. Lee, *Constraints on the $U(1)_L$ gauge boson in a wide mass range*, *Int. J. Mod. Phys.* **A31** (2016) 1650059, [1512.03179].

[214] L. A. Cavasonza, H. Gast, M. Krämer, M. Pellen and S. Schael, *Constraints on leptophilic dark matter from the AMS-02 experiment*, *Astrophys. J.* **839** (2017) 36, [1612.06634].

[215] F. D'Eramo, B. J. Kavanagh and P. Panci, *Probing Leptophilic Dark Sectors with Hadronic Processes*, *Phys. Lett.* **B771** (2017) 339–348, [1702.00016].

[216] S. Dutta, D. Sachdeva and B. Rawat, *Signals of Leptophilic Dark Matter at the ILC*, *Eur. Phys. J.* **C77** (2017) 639, [1704.03994].

[217] G. H. Duan, L. Feng, F. Wang, L. Wu, J. M. Yang and R. Zheng, *Simplified TeV leptophilic dark matter in light of DAMPE data*, *JHEP* **02** (2018) 107, [1711.11012].

[218] C.-Y. Chen, J. Kozaczuk and Y.-M. Zhong, *Exploring leptophilic dark matter with NA64-μ*, *JHEP* **10** (2018) 154, [1807.03790].

[219] R. Foot, G. C. Joshi and H. Lew, *Gauged Baryon and Lepton Numbers*, *Phys. Rev.* **D40** (1989) 2487–2489.

[220] P. Fileviez Perez and M. B. Wise, *Baryon and lepton number as local gauge symmetries*, *Phys. Rev.* **D82** (2010) 011901, [1002.1754].

[221] T. R. Dulaney, P. Fileviez Perez and M. B. Wise, *Dark Matter, Baryon Asymmetry, and Spontaneous B and L Breaking*, *Phys. Rev.* **D83** (2011) 023520, [1005.0617].

[222] P. Fileviez Perez and M. B. Wise, *Breaking Local Baryon and Lepton Number at the TeV Scale*, *JHEP* **08** (2011) 068, [1106.0343].

[223] M. Duerr, P. Fileviez Perez and M. B. Wise, *Gauge Theory for Baryon and Lepton Numbers with Leptoquarks*, *Phys. Rev. Lett.* **110** (2013) 231801, [1304.0576].

[224] W. Chao, *Pure Leptonic Gauge Symmetry, Neutrino Masses and Dark Matter*, *Phys. Lett.* **B695** (2011) 157–161, [1005.1024].

[225] W.-F. Chang and J. N. Ng, *Study of Gauged Lepton Symmetry Signatures at Colliders*, *Phys. Rev.* **D98** (2018) 035015, [1805.10382].

[226] W.-F. Chang and J. N. Ng, *Alternative Perspective on Gauged Lepton Number and Implications for Collider Physics*, *Phys. Rev.* **D99** (2019) 075025, [1808.08188].

[227] P. Fileviez Perez, S. Ohmer and H. H. Patel, *Minimal Theory for Lepto-Baryons*, *Phys. Lett.* **B735** (2014) 283–287, [1403.8029].

[228] S. Ohmer and H. H. Patel, *Leptobaryons as Majorana Dark Matter*, *Phys. Rev.* **D92** (2015) 055020, [1506.00954].

[229] K. S. Babu, C. F. Kolda and J. March-Russell, *Implications of generalized $Z - Z'$ mixing*, *Phys. Rev.* **D57** (1998) 6788–6792, [hep-ph/9710441].

[230] A. Alloul, N. D. Christensen, C. Degrande, C. Duhr and B. Fuks, *FeynRules 2.0 - A complete toolbox for tree-level phenomenology*, *Comput. Phys. Commun.* **185** (2014) 2250–2300, [1310.1921].

[231] CTA collaboration, J. Carr et al., *Prospects for Indirect Dark Matter Searches with the Cherenkov Telescope Array (CTA)*, *PoS* **ICRC2015** (2016) 1203, [1508.06128].

[232] Fermi-LAT collaboration, E. Charles et al., *Sensitivity Projections for Dark Matter Searches with the Fermi Large Area Telescope*, *Phys. Rept.* **636** (2016) 1–46, [1605.02016].

[233] A. Olivares-Del Campo, C. Bœhm, S. Palomares-Ruiz and S. Pascoli, *Dark matter-neutrino interactions through the lens of their cosmological implications*, *Phys. Rev.* **D97** (2018) 075039, [1711.05283].

[234] I. Esteban, M. C. Gonzalez-Garcia, M. Maltoni, I. Martinez-Soler and J. Salvado, *Updated Constraints on Non-Standard Interactions from Global Analysis of Oscillation Data*, *JHEP* **08** (2018) 180, [1805.04530].

[235] M. Carena, A. Daleo, B. A. Dobrescu and T. M. P. Tait, *Z' gauge bosons at the Tevatron*, *Phys. Rev.* **D70** (2004) 093009, [hep-ph/0408098].

[236] Particle Data Group collaboration, C. Patrignani et al., *Review of Particle Physics*, *Chin. Phys.* **C40** (2016) 100001.

[237] ALEPH, DELPHI, L3, OPAL, LEP Electroweak collaboration, S. Schael et al., *Electroweak Measurements in Electron-Positron Collisions at W-Boson-Pair Energies at LEP*, *Phys. Rept.* **532** (2013) 119–244, [1302.3415].

[238] A. Belyaev, N. D. Christensen and A. Pukhov, *CalcHEP 3.4 for collider physics within and beyond the Standard Model*, *Comput. Phys. Commun.* **184** (2013) 1729–1769, [1207.6082].

[239] CMS collaboration, A. M. Sirunyan et al., *Search for high-mass resonances in dilepton final states in proton-proton collisions at $\sqrt{s} = 13$ TeV*, *JHEP* **06** (2018) 120, [1803.06292].

[240] A. Hook, E. Izaguirre and J. G. Wacker, *Model Independent Bounds on Kinetic Mixing*, *Adv. High Energy Phys.* **2011** (2011) 859762, [1006.0973].

[241] CMS collaboration, *Combined measurements of the Higgs boson's couplings at $\sqrt{s} = 13$ TeV*, CMS Physics Analysis Summary CMS-PAS-HIG-17-031, CERN, Geneva, 2018.

[242] A. Djouadi, *The Anatomy of electroweak symmetry breaking. I: The Higgs boson in the standard model*, *Phys. Rept.* **457** (2008) 1–216, [hep-ph/0503172].

[243] P. Bechtle, O. Brein, S. Heinemeyer, O. Stål, T. Stefaniak, G. Weiglein et al., HiggsBounds $-$ 4*: Improved Tests of Extended Higgs Sectors against Exclusion Bounds from LEP, the Tevatron and the LHC*, *Eur. Phys. J.* **C74** (2014) 2693, [1311.0055].

[244] ALEPH, DELPHI, L3, OPAL, LEP Working Group for Higgs Boson Searches collaboration, S. Schael et al., *Search for neutral MSSM Higgs bosons at LEP*, *Eur. Phys. J.* **C47** (2006) 547–587, [hep-ex/0602042].

[245] OPAL collaboration, G. Abbiendi et al., *Decay mode independent searches for new scalar bosons with the OPAL detector at LEP*, *Eur. Phys. J.* **C27** (2003) 311–329, [hep-ex/0206022].

[246] CMS collaboration, *Update on the search for the standard model Higgs boson in pp collisions at the LHC decaying to W^+W^- in the fully leptonic final state*, CMS Physics Analysis Summary CMS-PAS-HIG-13-003, CERN, Geneva, 2013.

[247] CMS collaboration, *Properties of the Higgs-like boson in the decay $H \to ZZ$ to 4ℓ in pp collisions at $\sqrt{s} = 7$ and 8 TeV*, CMS Physics Analysis Summary CMS-PAS-HIG-13-002, CERN, Geneva, 2013.

[248] CMS collaboration, V. Khachatryan et al., *Search for a Higgs boson in the mass range from 145 to 1000 GeV decaying to a pair of W or Z bosons*, *JHEP* **10** (2015) 144, [1504.00936].

[249] ATLAS collaboration, G. Aad et al., *Search for an additional, heavy Higgs boson in the $H \to ZZ$ decay channel at $\sqrt{s} = 8$ TeV in pp collision data with the ATLAS detector*, *Eur. Phys. J.* **C76** (2016) 45, [1507.05930].

[250] CMS collaboration, *Combination of standard model Higgs boson searches and measurements of the properties of the new boson with a mass near 125 GeV*, CMS Physics Analysis Summary CMS-PAS-HIG-12-045, CERN, Geneva, 2012.

[251] ATLAS collaboration, M. Aaboud et al., *Measurement of the Higgs boson coupling properties in the $H \to ZZ^* \to 4\ell$ decay channel at $\sqrt{s} = 13$ TeV with the ATLAS detector*, JHEP **03** (2018) 095, [1712.02304].

[252] ATLAS collaboration, M. Aaboud et al., *Measurements of Higgs boson properties in the diphoton decay channel with 36 fb^{-1} of pp collision data at $\sqrt{s} = 13$ TeV with the ATLAS detector*, Phys. Rev. **D98** (2018) 052005, [1802.04146].

[253] ATLAS, CMS collaboration, G. Aad et al., *Measurements of the Higgs boson production and decay rates and constraints on its couplings from a combined ATLAS and CMS analysis of the LHC pp collision data at $\sqrt{s} = 7$ and 8 TeV*, JHEP **08** (2016) 045, [1606.02266].

[254] L3 collaboration, P. Achard et al., *Search for heavy neutral and charged leptons in e^+e^- annihilation at LEP*, Phys. Lett. **B517** (2001) 75–85, [hep-ex/0107015].

[255] ATLAS collaboration, M. Aaboud et al., *Search for electroweak production of supersymmetric particles in final states with two or three leptons at $\sqrt{s} = 13$ TeV with the ATLAS detector*, Eur. Phys. J. **C78** (2018) 995, [1803.02762].

[256] CMS collaboration, A. M. Sirunyan et al., *Combined search for electroweak production of charginos and neutralinos in proton-proton collisions at $\sqrt{s} = 13$ TeV*, JHEP **03** (2018) 160, [1801.03957].

[257] C. Han, A. Kobakhidze, N. Liu, A. Saavedra, L. Wu and J. M. Yang, *Probing Light Higgsinos in Natural SUSY from Monojet Signals at the LHC*, JHEP **02** (2014) 049, [1310.4274].

[258] P. Schwaller and J. Zurita, *Compressed electroweakino spectra at the LHC*, JHEP **03** (2014) 060, [1312.7350].

[259] H. Baer, A. Mustafayev and X. Tata, *Monojets and mono-photons from light higgsino pair production at LHC14*, Phys. Rev. **D89** (2014) 055007, [1401.1162].

[260] Z. Han, G. D. Kribs, A. Martin and A. Menon, *Hunting quasidegenerate Higgsinos*, Phys. Rev. **D89** (2014) 075007, [1401.1235].

[261] M. Low and L.-T. Wang, *Neutralino dark matter at 14 TeV and 100 TeV*, JHEP **08** (2014) 161, [1404.0682].

[262] R. Mahbubani, P. Schwaller and J. Zurita, *Closing the window for compressed Dark Sectors with disappearing charged tracks*, JHEP **06** (2017) 119, [1703.05327].

[263] A. Einstein, *Näherungsweise Integration der Feldgleichungen der Gravitation*, *Sitzungsber. Preuss. Akad. Wiss. Berlin (Math. Phys.)* **1916** (1916) 688–696.

[264] A. Einstein, *Über Gravitationswellen*, *Sitzungsber. Preuss. Akad. Wiss. Berlin (Math. Phys.)* **1918** (1918) 154–167.

[265] J. H. Taylor, L. A. Fowler and P. M. McCulloch, *Measurements of general relativistic effects in the binary pulsar PSR 1913+16*, *Nature* **277** (1979) 437–440.

[266] R. A. Hulse and J. H. Taylor, *Discovery of a pulsar in a binary system*, *Astrophys. J.* **195** (1975) L51–L53.

[267] D. R. Lorimer, *Binary and millisecond pulsars*, *Living Rev. Rel.* **1** (1998) 10.

[268] J. H. Taylor and J. M. Weisberg, *A new test of general relativity: Gravitational radiation and the binary pulsar PS R 1913+16*, *Astrophys. J.* **253** (1982) 908–920.

[269] J. M. Weisberg and Y. Huang, *Relativistic Measurements from Timing the Binary Pulsar PSR B1913+16*, *Astrophys. J.* **829** (2016) 55, [1606.02744].

[270] D. Baumann, *Primordial Cosmology*, *PoS* **TASI2017** (2018) 009, [1807.03098].

[271] C. Caprini and D. G. Figueroa, *Cosmological Backgrounds of Gravitational Waves*, *Class. Quant. Grav.* **35** (2018) 163001, [1801.04268].

[272] P. Schwaller, *Gravitational Waves from a Dark Phase Transition*, *Phys. Rev. Lett.* **115** (2015) 181101, [1504.07263].

[273] J. Jaeckel, V. V. Khoze and M. Spannowsky, *Hearing the signal of dark sectors with gravitational wave detectors*, *Phys. Rev.* **D94** (2016) 103519, [1602.03901].

[274] M. Chala, G. Nardini and I. Sobolev, *Unified explanation for dark matter and electroweak baryogenesis with direct detection and gravitational wave signatures*, *Phys. Rev.* **D94** (2016) 055006, [1605.08663].

[275] A. Addazi, *Limiting First Order Phase Transitions in Dark Gauge Sectors from Gravitational Waves experiments*, *Mod. Phys. Lett.* **A32** (2017) 1750049, [1607.08057].

[276] I. Baldes, *Gravitational waves from the asymmetric-dark-matter generating phase transition*, *JCAP* **1705** (2017) 028, [1702.02117].

[277] A. Addazi and A. Marciano, *Gravitational waves from dark first order phase transitions and dark photons*, *Chin. Phys.* **C42** (2018) 023107, [1703.03248].

[278] K. Tsumura, M. Yamada and Y. Yamaguchi, *Gravitational wave from dark sector with dark pion*, *JCAP* **1707** (2017) 044, [1704.00219].

[279] M. Aoki, H. Goto and J. Kubo, *Gravitational Waves from Hidden QCD Phase Transition*, *Phys. Rev.* **D96** (2017) 075045, [1709.07572].

[280] D. Croon, V. Sanz and G. White, *Model Discrimination in Gravitational Wave spectra from Dark Phase Transitions*, *JHEP* **08** (2018) 203, [1806.02332].

[281] I. Baldes and C. Garcia-Cely, *Strong gravitational radiation from a simple dark matter model*, *JHEP* **05** (2019) 190, [1809.01198].

[282] B. Allen and J. D. Romano, *Detecting a stochastic background of gravitational radiation: Signal processing strategies and sensitivities*, *Phys. Rev.* **D59** (1999) 102001, [gr-qc/9710117].

[283] M. Maggiore, *Gravitational wave experiments and early universe cosmology*, *Phys. Rept.* **331** (2000) 283–367, [gr-qc/9909001].

[284] J. D. Romano and N. J. Cornish, *Detection methods for stochastic gravitational-wave backgrounds: a unified treatment*, *Living Rev. Rel.* **20** (2017) 2, [1608.06889].

[285] N. Christensen, *Stochastic Gravitational Wave Backgrounds*, *Rept. Prog. Phys.* **82** (2019) 016903, [1811.08797].

[286] J. Weber, *Detection and Generation of Gravitational Waves*, *Phys. Rev.* **117** (1960) 306–313.

[287] J. Weber, *Observation of the Thermal Fluctuations of a Gravitational-Wave Detector*, *Phys. Rev. Lett.* **17** (1966) 1228–1230.

[288] J. Weber, *Evidence for discovery of gravitational radiation*, *Phys. Rev. Lett.* **22** (1969) 1320–1324.

[289] LIGO Scientific collaboration, G. M. Harry, *Advanced LIGO: The next generation of gravitational wave detectors*, *Class. Quant. Grav.* **27** (2010) 084006.

[290] https://ligo.org/.

[291] Virgo collaboration, F. Acernese, *The Advanced Virgo detector*, *J. Phys. Conf. Ser.* **610** (2015) 012014.

[292] http://www.virgo-gw.eu/.

[293] KAGRA collaboration, K. Somiya, *Detector configuration of KAGRA: The Japanese cryogenic gravitational-wave detector*, *Class. Quant. Grav.* **29** (2012) 124007, [1111.7185].

[294] https://gwcenter.icrr.u-tokyo.ac.jp/en/.

[295] B. Sathyaprakash et al., *Scientific Objectives of Einstein Telescope*, *Class. Quant. Grav.* **29** (2012) 124013, [1206.0331].

[296] D. Reitze et al., *Cosmic Explorer: The U.S. Contribution to Gravitational-Wave Astronomy beyond LIGO*, *Bull. Am. Astron. Soc.* **51** (2019) 035, [1907.04833].

[297] W.-R. Hu and Y.-L. Wu, *The Taiji Program in Space for gravitational wave physics and the nature of gravity*, *Natl. Sci. Rev.* **4** (2017) 685–686.

[298] TianQin collaboration, J. Luo et al., *TianQin: a space-borne gravitational wave detector*, *Class. Quant. Grav.* **33** (2016) 035010, [1512.02076].

[299] J. Crowder and N. J. Cornish, *Beyond LISA: Exploring future gravitational wave missions*, *Phys. Rev.* **D72** (2005) 083005, [gr-qc/0506015].

[300] N. Seto, S. Kawamura and T. Nakamura, *Possibility of direct measurement of the acceleration of the universe using 0.1-Hz band laser interferometer gravitational wave antenna in space*, *Phys. Rev. Lett.* **87** (2001) 221103, [astro-ph/0108011].

[301] S. Sato et al., *The status of DECIGO*, *J. Phys. Conf. Ser.* **840** (2017) 012010.

[302] S. Isoyama, H. Nakano and T. Nakamura, *Multiband Gravitational-Wave Astronomy: Observing binary inspirals with a decihertz detector, B-DECIGO*, *PTEP* **2018** (2018) 073E01, [1802.06977].

[303] R. D. Ferdman et al., *The European Pulsar Timing Array: current efforts and a LEAP toward the future*, *Class. Quant. Grav.* **27** (2010) 084014, [1003.3405].

[304] L. Lentati et al., *European Pulsar Timing Array Limits On An Isotropic Stochastic Gravitational-Wave Background*, *Mon. Not. Roy. Astron. Soc.* **453** (2015) 2576–2598, [1504.03692].

[305] F. Jenet et al., *The North American Nanohertz Observatory for Gravitational Waves*, 0909.1058.

[306] NANOGRAV collaboration, Z. Arzoumanian et al., *The NANOGrav 11-year Data Set: Pulsar-timing Constraints On The Stochastic Gravitational-wave Background*, *Astrophys. J.* **859** (2018) 47, [1801.02617].

[307] R. N. Manchester et al., *The Parkes Pulsar Timing Array Project*, *Publ. Astron. Soc. Austral.* **30** (2013) 17, [1210.6130].

[308] G. Hobbs et al., *The international pulsar timing array project: using pulsars as a gravitational wave detector*, *Class. Quant. Grav.* **27** (2010) 084013, [0911.5206].

[309] R. N. Manchester, *The International Pulsar Timing Array*, *Class. Quant. Grav.* **30** (2013) 224010, [1309.7392].

[310] G. Janssen et al., *Gravitational wave astronomy with the SKA*, *PoS* **AASKA14** (2015) 037, [1501.00127].

[311] SKA collaboration, D. J. Bacon et al., *Cosmology with Phase 1 of the Square Kilometre Array: Red Book 2018: Technical specifications and performance forecasts*, *Publ. Astron. Soc. Austral.* **37** (2020) e007, [1811.02743].

[312] J. Simon and S. Burke-Spolaor, *Constraints on Black Hole/Host Galaxy Co-evolution and Binary Stalling Using Pulsar Timing Arrays*, *Astrophys. J.* **826** (2016) 11, [1603.06577].

[313] E. Thrane and J. D. Romano, *Sensitivity curves for searches for gravitational-wave backgrounds*, *Phys. Rev.* **D88** (2013) 124032, [1310.5300].

[314] M. Laine and A. Vuorinen, *Basics of Thermal Field Theory*, *Lect. Notes Phys.* **925** (2016) pp.1–281, [1701.01554].

[315] D. A. Kirzhnits and A. D. Linde, *Macroscopic Consequences of the Weinberg Model*, *Phys. Lett.* **42B** (1972) 471–474.

[316] S. R. Coleman, *The Fate of the False Vacuum. 1. Semiclassical Theory*, *Phys. Rev.* **D15** (1977) 2929–2936.

[317] C. G. Callan, Jr. and S. R. Coleman, *The Fate of the False Vacuum. 2. First Quantum Corrections*, *Phys. Rev.* **D16** (1977) 1762–1768.

[318] A. D. Linde, *Fate of the False Vacuum at Finite Temperature: Theory and Applications*, *Phys. Lett.* **100B** (1981) 37–40.

[319] A. D. Linde, *Decay of the False Vacuum at Finite Temperature*, *Nucl. Phys.* **B216** (1983) 421.

[320] J. Ellis, M. Lewicki and J. M. No, *On the Maximal Strength of a First-Order Electroweak Phase Transition and its Gravitational Wave Signal*, 1809.08242.

[321] J. R. Espinosa, T. Konstandin, J. M. No and G. Servant, *Energy Budget of Cosmological First-order Phase Transitions*, *JCAP* **1006** (2010) 028, [1004.4187].

[322] T. Konstandin, G. Nardini and I. Rues, *From Boltzmann equations to steady wall velocities*, *JCAP* **1409** (2014) 028, [1407.3132].

[323] G. C. Dorsch, S. J. Huber and T. Konstandin, *Bubble wall velocities in the Standard Model and beyond*, *JCAP* **1812** (2018) 034, [1809.04907].

[324] D. Bodeker and G. D. Moore, *Can electroweak bubble walls run away?*, *JCAP* **0905** (2009) 009, [0903.4099].

[325] D. Bodeker and G. D. Moore, *Electroweak Bubble Wall Speed Limit*, *JCAP* **1705** (2017) 025, [1703.08215].

[326] E. Witten, *Cosmic Separation of Phases*, *Phys. Rev.* **D30** (1984) 272–285.

[327] C. J. Hogan, *Gravitational radiation from cosmological phase transitions*, *Mon. Not. Roy. Astron. Soc.* **218** (1986) 629–636.

[328] A. Kosowsky and M. S. Turner, *Gravitational radiation from colliding vacuum bubbles: envelope approximation to many bubble collisions*, *Phys. Rev.* **D47** (1993) 4372–4391, [astro-ph/9211004].

[329] S. J. Huber and T. Konstandin, *Gravitational Wave Production by Collisions: More Bubbles*, *JCAP* **0809** (2008) 022, [0806.1828].

[330] M. Hindmarsh, S. J. Huber, K. Rummukainen and D. J. Weir, *Numerical simulations of acoustically generated gravitational waves at a first order phase transition*, *Phys. Rev.* **D92** (2015) 123009, [1504.03291].

[331] C. Caprini, R. Durrer and G. Servant, *The stochastic gravitational wave background from turbulence and magnetic fields generated by a first-order phase transition*, *JCAP* **0912** (2009) 024, [0909.0622].

[332] P. Binetruy, A. Bohe, C. Caprini and J.-F. Dufaux, *Cosmological Backgrounds of Gravitational Waves and eLISA/NGO: Phase Transitions, Cosmic Strings and Other Sources*, *JCAP* **1206** (2012) 027, [1201.0983].

[333] D. J. Fixsen, *The Temperature of the Cosmic Microwave Background*, *Astrophys. J.* **707** (2009) 916–920, [0911.1955].

[334] L. Husdal, *On Effective Degrees of Freedom in the Early Universe*, *Galaxies* **4** (2016) 78, [1609.04979].

[335] D. Cutting, M. Hindmarsh and D. J. Weir, *Gravitational waves from vacuum first-order phase transitions: from the envelope to the lattice*, *Phys. Rev.* **D97** (2018) 123513, [1802.05712].

[336] D. Cutting, M. Hindmarsh and D. J. Weir, *Vorticity, kinetic energy, and suppressed gravitational wave production in strong first order phase transitions*, 1906.00480.

[337] J. Ellis, M. Lewicki, J. M. No and V. Vaskonen, *Gravitational wave energy budget in strongly supercooled phase transitions*, *JCAP* **1906** (2019) 024, [1903.09642].

[338] J. Ellis, M. Lewicki and J. M. No, *Gravitational waves from first-order cosmological phase transitions: lifetime of the sound wave source*, 2003.07360.

[339] F. Giese, T. Konstandin and J. van de Vis, *Model-independent energy budget of cosmological first-order phase transitions*, 2004.06995.

[340] S. R. Coleman and E. J. Weinberg, *Radiative Corrections as the Origin of Spontaneous Symmetry Breaking*, *Phys. Rev.* **D7** (1973) 1888–1910.

[341] L. Dolan and R. Jackiw, *Symmetry Behavior at Finite Temperature*, *Phys. Rev.* **D9** (1974) 3320–3341.

[342] M. E. Carrington, *The Effective potential at finite temperature in the Standard Model*, *Phys. Rev.* **D45** (1992) 2933–2944.

[343] H. H. Patel and M. J. Ramsey-Musolf, *Baryon Washout, Electroweak Phase Transition, and Perturbation Theory*, *JHEP* **07** (2011) 029, [1101.4665].

[344] E. E. Flanagan and S. A. Hughes, *The Basics of gravitational wave theory*, *New J. Phys.* **7** (2005) 204, [gr-qc/0501041].

[345] J. W. Armstrong, F. B. Estabrook and M. Tinto, *Time-delay interferometry for space-based gravitational wave searches*, *Astrophys. J.* **527** (1999) 814–826.

[346] M. Muratore, D. Vetrugno and S. Vitale, *Revisitation of time delay interferometry combinations that suppress laser noise in LISA*, 2001.11221.

[347] W. Heisenberg and H. Euler, *Consequences of Dirac's theory of positrons*, *Z. Phys.* **98** (1936) 714–732, [physics/0605038].

[348] J. S. Schwinger, *On gauge invariance and vacuum polarization*, *Phys. Rev.* **82** (1951) 664–679.

[349] G. Jona-Lasinio, *Relativistic field theories with symmetry breaking solutions*, *Nuovo Cim.* **34** (1964) 1790–1795.

[350] R. Jackiw, *Functional evaluation of the effective potential*, *Phys. Rev.* **D9** (1974) 1686.

[351] M. Quiros, *Finite temperature field theory and phase transitions*, in *Proceedings, Summer School in High-energy physics and cosmology: Trieste, Italy, June 29-July 17, 1998*, pp. 187–259, 1999, hep-ph/9901312.

[352] E. J. Weinberg, *Radiative corrections as the origin of spontaneous symmetry breaking*, Ph.D. thesis, Harvard U., 1973. hep-th/0507214.

[353] R. Fukuda and E. Kyriakopoulos, *Derivation of the Effective Potential*, *Nucl. Phys.* **B85** (1975) 354–364.

[354] L. Dolan and R. Jackiw, *Gauge Invariant Signal for Gauge Symmetry Breaking*, *Phys. Rev.* **D9** (1974) 2904.

[355] J. Elias-Miro, J. R. Espinosa and T. Konstandin, *Taming Infrared Divergences in the Effective Potential*, *JHEP* **08** (2014) 034, [1406.2652].

[356] C. Delaunay, C. Grojean and J. D. Wells, *Dynamics of Non-renormalizable Electroweak Symmetry Breaking*, *JHEP* **04** (2008) 029, [0711.2511].

[357] J. I. Kapusta and C. Gale, *Finite-temperature field theory: Principles and applications*. Cambridge Monographs on Mathematical Physics. Cambridge University Press, 2011, 10.1017/CBO9780511535130.

[358] S. Weinberg, *Gauge and Global Symmetries at High Temperature*, *Phys. Rev.* **D9** (1974) 3357–3378.

[359] K. Takahashi, *Perturbative Calculations at Finite Temperatures*, *Z. Phys.* **C26** (1985) 601–613.

[360] D. Curtin, P. Meade and H. Ramani, *Thermal Resummation and Phase Transitions*, *Eur. Phys. J.* **C78** (2018) 787, [1612.00466].

[361] R. R. Parwani, *Resummation in a hot scalar field theory*, *Phys. Rev.* **D45** (1992) 4695, [hep-ph/9204216].

[362] P. B. Arnold and O. Espinosa, *The Effective potential and first order phase transitions: Beyond leading-order*, *Phys. Rev.* **D47** (1993) 3546, [hep-ph/9212235].

[363] B. Fornal, Y. Shirman, T. M. P. Tait and J. R. West, *Asymmetric dark matter and baryogenesis from $SU(2)_\ell$*, *Phys. Rev.* **D96** (2017) 035001, [1703.00199].

[364] C. L. Wainwright, *CosmoTransitions: Computing Cosmological Phase Transition Temperatures and Bubble Profiles with Multiple Fields*, *Comput. Phys. Commun.* **183** (2012) 2006–2013, [1109.4189].

[365] G. Passarino and M. J. G. Veltman, *One Loop Corrections for e+ e- Annihilation Into mu+ mu- in the Weinberg Model*, *Nucl. Phys.* **B160** (1979) 151–207.

[366] R. Mertig, M. Bohm and A. Denner, *FeynCalc: Computer algebraic calculation of Feynman amplitudes*, *Comput. Phys. Commun.* **64** (1991) 345–359.

[367] V. Shtabovenko, R. Mertig and F. Orellana, *New Developments in FeynCalc 9.0*, *Comput. Phys. Commun.* **207** (2016) 432–444, [1601.01167].

[368] T. Hahn and M. Perez-Victoria, *Automatized one loop calculations in four-dimensions and D-dimensions*, *Comput. Phys. Commun.* **118** (1999) 153–165, [hep-ph/9807565].

[369] G. J. van Oldenborgh and J. A. M. Vermaseren, *New Algorithms for One Loop Integrals*, *Z. Phys.* **C46** (1990) 425–438.

[370] G. 't Hooft and M. J. G. Veltman, *Scalar One Loop Integrals*, *Nucl. Phys.* **B153** (1979) 365–401.

[371] A. Denner, *Techniques for calculation of electroweak radiative corrections at the one loop level and results for W physics at LEP-200*, *Fortsch. Phys.* **41** (1993) 307–420, [0709.1075].

[372] P. J. Steinhardt, *Relativistic Detonation Waves and Bubble Growth in False Vacuum Decay*, *Phys. Rev.* **D25** (1982) 2074.

[373] M. Laine, *Bubble growth as a detonation*, *Phys. Rev.* **D49** (1994) 3847–3853, [hep-ph/9309242].

[374] G. Mangano, G. Miele, S. Pastor, T. Pinto, O. Pisanti and P. D. Serpico, *Relic neutrino decoupling including flavor oscillations*, *Nucl. Phys.* **B729** (2005) 221–234, [hep-ph/0506164].

[375] Planck collaboration, P. A. R. Ade et al., *Planck 2015 results. XIII. Cosmological parameters*, *Astron. Astrophys.* **594** (2016) A13, [1502.01589].

[376] R. A. Alpher, H. Bethe and G. Gamow, *The origin of chemical elements*, *Phys. Rev.* **73** (1948) 803–804.

[377] R. V. Wagoner, W. A. Fowler and F. Hoyle, *On the Synthesis of elements at very high temperatures*, *Astrophys. J.* **148** (1967) 3–49.

[378] V. F. Shvartsman, *Density of relict particles with zero rest mass in the universe*, *Pisma Zh. Eksp. Teor. Fiz.* **9** (1969) 315–317.

[379] R. J. Scherrer and M. S. Turner, *Primordial Nucleosynthesis with Decaying Particles. 1. Entropy Producing Decays. 2. Inert Decays*, *Astrophys. J.* **331** (1988) 19–32.

[380] B. D. Fields, P. Molaro and S. Sarkar, *Big-Bang Nucleosynthesis*, *Chin. Phys.* **C38** (2014) 339–344, [1412.1408].

[381] G. Steigman, D. N. Schramm and J. E. Gunn, *Cosmological Limits to the Number of Massive Leptons*, *Phys. Lett.* **66B** (1977) 202–204.

[382] A. Peimbert, M. Peimbert and V. Luridiana, *The primordial helium abundance and the number of neutrino families*, *Rev. Mex. Astron. Astrofis.* **52** (2016) 419–424, [1608.02062].

[383] M. Hufnagel, K. Schmidt-Hoberg and S. Wild, *BBN constraints on MeV-scale dark sectors. Part I. Sterile decays*, *JCAP* **1802** (2018) 044, [1712.03972].

[384] C. Boehm, M. J. Dolan and C. McCabe, *Increasing Neff with particles in thermal equilibrium with neutrinos*, *JCAP* **1212** (2012) 027, [1207.0497].

[385] A. Berlin and N. Blinov, *Thermal Dark Matter Below an MeV*, *Phys. Rev. Lett.* **120** (2018) 021801, [1706.07046].

[386] A. Berlin and N. Blinov, *Thermal neutrino portal to sub-MeV dark matter*, *Phys. Rev.* **D99** (2019) 095030, [1807.04282].

[387] R. H. Cyburt, B. D. Fields, K. A. Olive and T.-H. Yeh, *Big Bang Nucleosynthesis: 2015*, *Rev. Mod. Phys.* **88** (2016) 015004, [1505.01076].

[388] M. Fairbairn, E. Hardy and A. Wickens, *Hearing without seeing: gravitational waves from hot and cold hidden sectors*, *JHEP* **07** (2019) 044, [1901.11038].

[389] K. Hashino, M. Kakizaki, S. Kanemura, P. Ko and T. Matsui, *Gravitational waves from first order electroweak phase transition in models with the $U(1)_X$ gauge symmetry*, *JHEP* **06** (2018) 088, [1802.02947].

[390] M. Dohse, *TikZ-FeynHand: Basic User Guide*, 1802.00689.

[391] J. Ellis, *TikZ-Feynman: Feynman diagrams with TikZ*, *Comput. Phys. Commun.* **210** (2017) 103–123, [1601.05437].

[392] J. D. Hunter, *Matplotlib: A 2D graphics environment*, *Computing in Science & Engineering* **9** (2007) 90–95.

List of Abbreviations

1PI one-particle irreducible
ALP axion-like particle
BAO baryon acoustic oscillation
BBN Big Bang Nucleosynthesis
BH black hole
BSM beyond the Standard Model
CB compact binary
CCD charged coupled device
CDM cold dark matter
CKM Cabibbo-Kobayashi-Maskawa
CL confidence level
CMB cosmic microwave background
COVID-19 Coronavirus disease 2019
DM dark matter
DOF degree of freedom
EDM electric dipole moment
EFT effective field theory
EM electromagnetic, electromagnetism
EW electroweak
EWBG electroweak baryogenesis
EWPT electroweak phase transition
EWSB electroweak symmetry breaking
FTQFT finite temperature QFT
GR general relativity
GW gravitational wave
HL heavy lepton
IR infrared
LO leading order
LSP lightest supersymmetric particle
MACHO massive astrophysical compact halo object
MC Monte Carlo
MET missing transverse energy
MHD magnetohydrodynamic
MS minimal subtraction
NLO next-to-leading order
νMSM neutrino minimal SM
NS neutron star
NWA narrow-width approximation
OSSF opposite-sign same-flavor
PBH primordial black hole
PDF parton distribution function
PLI power-law integrated
PMNS Pontecorvo-Maki-Nakagawa-Sakata
PSD power-spectral density
PT phase transition
PTA pulsar timing array
QCD quantum chromodynamics
QFT quantum field theory
QM quantum mechanics
RG renormalization group
SGWB stochastic GW background
SM Standard Model
SMBHB super-massive black hole binary
SNR signal-to-noise ratio
SSB spontaneous symmetry breaking
SUSY supersymmetry
TDI time delay interferometry
TT transverse traceless
UV ultraviolet
VBF vector-boson fusion
VEV vacuum expectation value
WIMP weakly interacting massive particle

List of Experiments

Colliders and Detectors
- **FCC** Future Circular Collider
- **HE-LHC** high-energy LHC
- **HL-LHC** high-luminosity LHC
- **ILC** International Linear Collider
- **LEP** Large Electron-Positron Collider
- **LHC** Large Hadron Collider
  - **ALICE** A Large Ion Collider Experiment
  - **ATLAS** A Toroidal LHC ApparatuS
  - **CMS** Compact Muon Solenoid
  - **LHCb** LHC-beauty
- **RHIC** relativistic heavy ion collider

Dark Matter Experiments
- **direct detection**
  - **CMDS** Cryogenic Dark Matter Search
  - **CRESST** Cryogenic Rare Event Search with Superconducting Thermometers
  - **DAMA/LIBRA** DArk MAtter / Large sodium Iodide Bulk for RAre processes
  - **DAMIC** Dark Matter in CCDs
  - **DARWIN** DARk matter WImp search with liquid xenoN
  - **LUX** Large Underground Xenon dark matter experiment
  - **LZ** *LUX-ZEPLIN*
  - **SENSEI** Sub-Electron-Noise Skipper-CCD Experimental Instrument
  - **XENON1T**
  - **ZEPLIN** ZonEd Proportional scintillation in LIquid Noble gases
- **gamma-ray telescopes (indirect detection)**
  - **CTA** Cherenkov Telescope Array
  - **Fermi-LAT** Fermi Large Area Telescope
  - **H.E.S.S.** High Energy Stereoscopic System
  - **MAGIC** Major Atmospheric Gamma Imaging Cherenkov Telescopes

Gravitational Wave Experiments
- **ground-based observatories**
  - **CE** Cosmic Explorer
  - **ET** Einstein Telescope
  - **KAGRA** Kamioka Gravitational Wave Detector
  - **LIGO** Laser Interferometer Gravitational-Wave Observatory
  - **Virgo**

pulsar timing arrays
- **EPTA** European Pulsar Timing Array
- **IPTA** International Pulsar Timing Array
- **NANOGrav** North American Nanohertz Observatory for Gravitational Waves
- **PPTA** Parkes Pulsar Timing Array
- **SKA** Square Kilometre Array

space-based observatories
- **B-DECIGO** Scaled-down version of *DECIGO*, “B” stands for “Basic” or “Base”
- **BBO** Big Bang Observer
- **DECIGO** DECi-hertz Interferometer Gravitational Wave Observatory
- **LISA** Laser Interferometer Space Antenna

Other
- **CERN** European Council for Nuclear Research
- **KATRIN** KArlsruhe TRItium Neutrino experiment
- **Planck** Planck satellite

This dissertation is typeset with $\LaTeX\,2_\varepsilon$ in the KOMA-Script book class. All Feynman diagrams are drawn using the Ti*k*Z-FeynHand [390, 391] package. Figures 6.4, 6.5 and 8.2 are created with Ti*k*Z. The remaining figures are generated in Python3 using the Matplotlib [392] library.